Design and Field Weakening Analysis of Hybrid Rotor PMSM

– A Unified Model for Synchronous AC Machines

by

Dheeraj Bobba

A dissertation submitted in partial fulfillment of
the requirements for the degree of

Doctor of Philosophy
(Electrical Engineering)

at the
UNIVERSITY OF WISCONSIN – MADISON
2021

Date of final oral examination: 01/14/2021

The dissertation is approved by the following members of the final Oral Committee:

Bulent Sarlioglu, Associate Professor,	Electrical and Computer Engineering
Thomas M. Jahns, Professor,	Electrical and Computer Engineering
Daniel C. Ludois, Associate Professor,	Electrical and Computer Engineering
Rich Schiferl, Adjunct Asst. Professor,	Engineering Professional Development
Gregory F. Nellis, Professor,	Mechanical Engineering

Abstract

In recent years, the electrification of industrial, urban and commercial mobility, e-mobility, has garnered significant attention due to a rapidly growing interest in reducing reliance on fossil fuels and global carbon footprint. Both industrial and traction applications desire to reduce manufacturing costs and modular manufacturing methods. In addition, electric machines that can maintain a wide constant power speed ratio (CPSR) are desired for traction applications. Internal permanent magnet (IPM) machines are widely used in the current industry to meet such wide CPSR requirements. However, achieving wide CPSR using an IPM machine requires an iterative design and validation process due to the co-dependency of crucial machine parameters on the same rotor design features.

Machines that use a combination of rotor types, i.e., hybrid rotor machines, are shown to be effective in producing wide CPSR designs. The arrangement of rotors in a dual rotor machine also gives two additional degrees of freedom in design, individual stack lengths and a relative angle between the rotors. While these degrees of freedom can be used to improve the performance of a hybrid rotor machine, they also introduce additional degree of complexity in analyzing and understanding the performance characteristics.

The focus of this research is to propose and develop analysis and modeling method that considers all available degrees of freedom and propose a design process to achieve wide CPSR using hybrid rotor machines. The proposed analytical model and evaluation method also enables a quick and cost-effective machine design process that can standardize rotor cross-section for the manufacturers while meeting a wide range of system requirements using

combinations of rotor modules. In addition, since a dual rotor machine can use different combinations of rotor types and positions and exhibit the performance characteristics of a wide range of synchronous machine types, the developed analysis unifies the modeling and field weakening theory of synchronous AC machines.

Acknowledgements

This thesis embodies my Ph.D. research and the knowledge gained along the journey at Wisconsin Electric Machines and Power Electronics Consortium (WEMPEC) at the University of Wisconsin – Madison. This research would not have been possible without the guidance, support, and generous help from the faculty, staff, colleagues, friends, and family.

Firstly, I would like to express my sincere gratitude to my research advisor and mentor, Prof. Bulent Sarlioglu, for his dedicated involvement, insightful guidance, and encouragement. He is always willing to help and readily available. His candid feedback taught me to have persistence and optimism in overcoming obstacles and nimbleness in facing uncertainties. Through his experiences and knowledge, I benefited greatly over the years in reaching both my research and personal goals. The wisdom he instilled in me will continue to influence my perception and future endeavors.

I would also like to extend my gratitude to Prof. Thomas Jahns, who, in addition to being my Ph.D. committee member, had also become a mentor through my research project for the past few years. His all-around acumen in dissecting and analyzing complex problems, and his lectures and insights on machine design guided me immensely in shaping this thesis.

I would also like to express my gratitude to my Ph.D. committee members, Prof. Rich Schiferl, Prof. Daniel Ludois, and Prof. Gregory Nellis. Their valuable evaluation and recommendations helped me scrutinize my research and develop a more in-depth perspective. Particularly, I would like to thank Prof. Schiferl for his thorough review and detailed feedback in making this thesis more precise.

My thanks extend to WEMPEC lab manager, Kyle Hanson. The improvements in laboratory equipment and facilities he oversaw were instrumental in manufacturing my prototype machine. I am also grateful for the support and guidance provided by Ryan Halverson and Dave Farnia from Arnold Magnetics, and Stephen Funk from Kollmorgen during the prototype manufacturing process. My special thanks to Matt Woongkul Lee and Pablo Castro Palavicino for their invaluable assistance with the experimental setup, and JSOL Corp. – JMAG Division for providing the simulation and modeling tools used in this research.

On a personal note, I would like to thank the past and current WEMPEC administrative directors, Helene Demont and Kathy Young, former and current fellow WEMPECKERS and UW-Madison student community who made my life wonderful in Madison. I have learned much from this diverse, intellectual, and inspiring community. I am grateful for their friendship and feel privileged to be a part of this extended family.

I am indebted to friends and family who greatly influenced and kept me motivated through tough times; Dave Farnia, Ryoko Imamura, Pablo Palavicino, Dr. Gerd Bramerdorfer, Yingjie Li, Matt Lee, Ju Hyung Kim, Susie Choi, Shang-Chuan Lee, Dan Erato, Patrick Dills, James Swankee and many others.

Last but foremost, I wish to express my deepest gratitude to my parents, my brother, the Kolluri family, and the Bikkina family for their unconditional love and encouragement throughout this time. I would not have been the person I am today without their support.

Dheeraj Bobba
January 07th, 2021

Table of Contents

List of Figures

List of Tables

Chapter 1

1. Introduction

1.1. Background and Motivation

A desire to improve performance and reduce manufacturing costs has always been a driving force in electric machine research. There are different types of electric machines developed over the centuries of the history of electromechanical energy conversion. With varying types of applications and their performance requirements, there is no one best machine type that would meet all requirements. The application's performance requirements can be understood based on the load profile. Some of the commonly found torque and power requirements are shown in Figure 1-1.

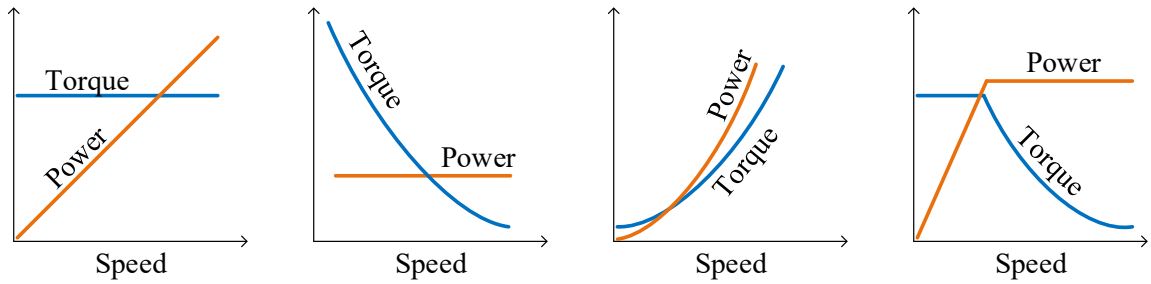

(a) (b) (c) (d)

Figure 1-1. Typical torque, power profiles of industrial applications. (a) Constant torque, (b) Constant power, (c) Variable torque and power, (d) Constant torque and power

Applications such as conveyors or feeders and cranes typically require constant torque and fall under the load type described by Figure 1-1(a). Applications such as drum rollers and rolling mills require constant power, as illustrated by Figure 1-1(b), while fans, centrifugal

pumps, and propulsion applications have characteristics described by Figure 1-1(c). Traction applications, on the other hand, require high starting torque and maintain constant power at higher speeds, as shown in Figure 1-1(d).

Synchronous machines, based on the rotor design and torque production mechanism, can be categorized into wound field synchronous machines (WFSM), permanent magnet synchronous machines (PMSM) and synchronous reluctance machines (SyRM). Including more recent developments, PMSMs can be further classified into surface permanent magnet machine (SPMM), interior permanent magnet machine (IPMM), flux intensifying permanent magnet machines (FIPMM), and variable flux interior permanent magnet machines (VFIPMM). While there are other machine types, such as flux switching machines, their performance and operation can be understood or modeled with one of the aforementioned classifications. In fact, the performance of IPMM and its derivative designs, such as FIPMM and VFIPMM, can also be modeled using a combination of SPMM and SyRM. The typical torque and power characteristics of SPMM, SyRM, and an ideal IPMM, are shown in Figure 1-2. It is noteworthy that with a proper design and some compromise on the power density, SPMM can also achieve a wider constant power region. Comparing the torque and power characteristics of different load types from Figure 1-1 to the characteristics of typical PMSMs shown in Figure 1-2, it can be inferred that PMSMs are an attractive solution for many applications. Furthermore, from the characteristics of individual machines in Figure 1-2, it is evident that the performance of an ideal IPMM lies in between the performance characteristics from SPMM and SyRM. In retrospect, SPMM and SyRM can be considered as the fundamental building blocks of other PMSMs.

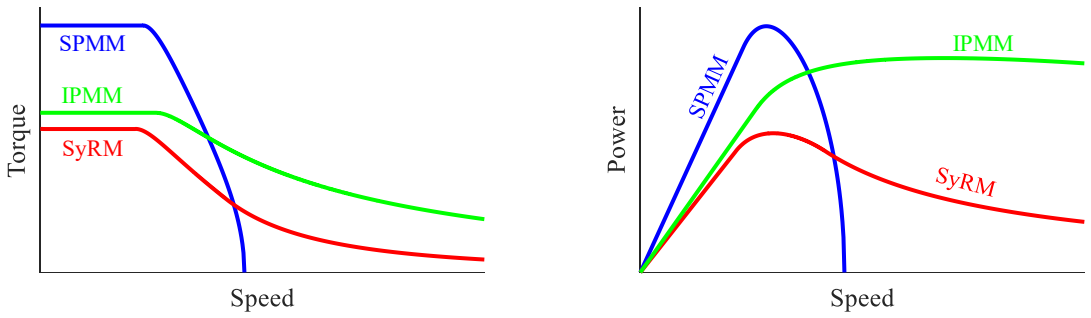

Figure 1-2. Typical performance characteristics of common PMSMs (a) Torque vs. Speed, (b) Power vs. Speed

The sizing and design methods of SPMM are well understood and abundant literature available, making it the most preferred option for the majority of servo applications and even some traction applications. The design of SyRM, although not as straight forward as SPMM, is also well defined since the only design goal is to decrease the reluctance of the flux path in one axis of the rotor. IPMM, on the other hand, poses a delicate balance of PM material position and orientation to obtain desired performance characteristics. While IPMMs are widely used in present-day applications, the designs are rigorously fine-tuned through an iterative design process and optimization techniques to achieve desired torque and power vs. speed characteristics.

Utilizing SPMM and SyRM as building blocks, a simplified design methodology can be established to obtain the characteristics of any PMSM. There have been some promising developments in the past with dual rotor PMSMs that have different rotor sections on a single shaft, hereby referred to as hybrid rotor machines. Simplified cross-section representations of two of the possible hybrid rotor machines are shown in Figure 1-3. The radial hybrid rotor

variant illustrated in Figure 1-3(a) utilizes two rotors, each on the inside and outside of an annular stator. The axial hybrid rotor scheme illustrated in Figure 1-3(b) uses a conventional stator and rotor structure, but with fractional stack lengths of SPM and SyR rotor segments stacked axially on the shaft. In both cases, the positions of SPMM and SyRM are interchangeable.

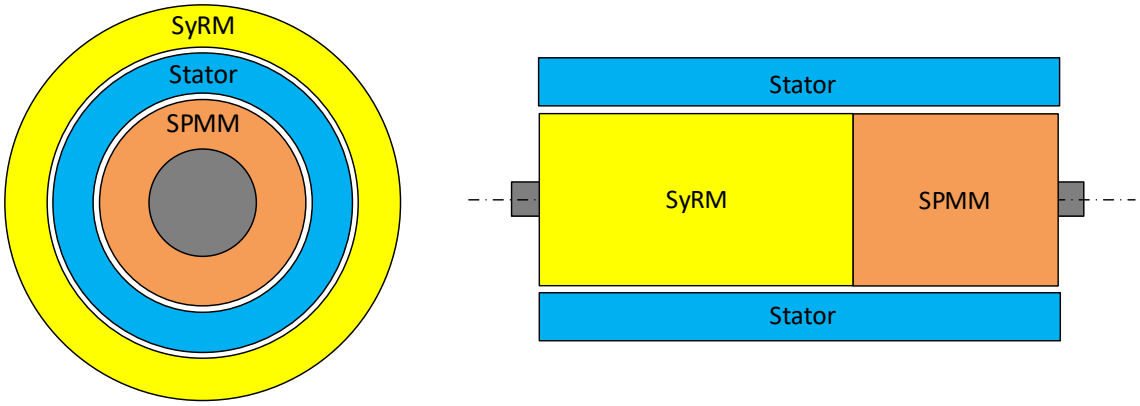

(a) (b)

Figure 1-3. Simplified cross-sectional representation of hybrid rotor PMSMs (a) Radial hybrid rotor PMSM, (b) Axial hybrid rotor PMSM

Although dual rotor machines are studied widely, research into hybrid rotor machines is limited. No clear design principle or analysis that describes the complete spectrum of possible performance characteristics of hybrid rotor PMSM exists so far. The existing synchronous machine analysis models are only partially applicable to hybrid rotor machines since there are additional degrees of freedom, a relative angle between the two different rotor types and the stack length of each rotor. Literature available on hybrid rotor PMSMs thus far has either limited the offset angle such that the design can be analyzed with existing IPMM

models or focused on a limited combination of offset angles and rotor stack lengths in order to understand the performance by experimental methods or finite element analysis (FEA).

1.2. Research Objectives

The goals of this research are to bridge a knowledge gap in the design methodology of hybrid rotor PMSMs to achieve desired performance characteristics and to develop a field weakening analysis model of hybrid rotor PMSMs.

Conventionally, different synchronous machines use different field weakening models to estimate the current command trajectory and predict operating characteristics. Hybrid rotor machines are a combination of different machine types and introduce additional degrees of freedom in the design. Hence, they pose a unique challenge in developing current command trajectories and estimating filed weakening performance characteristics using the existing synchronous AC machine's field weakening models. Therefore, the primary goal is to develop an analytical field weakening model of hybrid rotor PMSMs.

Hybrid rotor machines also offer flexibility to mimic various types of PMSM performance characteristics using simple SPM and SyR rotor combinations. The ability to maintain constant power in the field weakening region is sought after more so than other characteristics. However, it requires an intricate and iterative design process for conventional PMSMs to achieve such performance. Hence in addition to the primary objective, this research also aims at developing practical modeling procedures and sizing analysis for hybrid rotor machines, mainly using SPM and SyR rotor combinations, and to develop design guidelines and parameter selection to achieve constant power operation during field weakening operation.

1.3. Thesis Organization

This thesis consists of ten chapters. The first chapter provides an introduction, a brief overview, and the motivation behind this research work. The objectives and end goals of the research are identified.

Chapter 2 presents a state-of-the-art review of hybrid rotor PMSM. The various IPM machine types that can be mimicked using hybrid rotor PMSM are also introduced. Based on the literature review, the knowledge gaps in the understanding of hybrid rotor PMSMs and research opportunities are summarized at the end of the chapter.

Chapter 3 firstly develops the framework to model the hybrid rotor PMSM operating at a steady-state in the synchronous reference frame. The field weakening analytical model of hybrid rotor PMSM is then developed, and the field weakening performance is characterized. The ability to use the field weakening model to understand any synchronous AC machine performance is explored. Finally, the rotor design parameters to achieve the desired speed, power – torque characteristics using hybrid rotor PMSM are developed.

Chapter 4 provides guidelines on the selection of a slot-pole combination and aspect ratio for hybrid rotor PMSM. Key design considerations are identified, and the design trend in the state-of-the-art are summarized. The sizing equations for the hybrid rotor PMSM are developed. A quantitative comparison between the hybrid rotor PMSM and an equivalent SPMM is presented using the developed sizing equations, and the scalability analysis of a hybrid rotor PMSM is developed.

Chapter 5 focuses on the design of a low power – low speed proof-of-concept hybrid rotor PMSM and implementation using FEA. Individual SPM and SyR machines are initially

sized and analyzed using 2D-FEA. The rotor sections are then combined, and a hybrid rotor PMSM analysis using 3D-FEA is presented.

Chapter 6 proposes a high-fidelity look-up-table (LUT) based modeling method to reduce the computational cost of 3D-FEA based models and aid in evaluating the performance of the hybrid rotor PMSM. The validation of the LUT model is presented by comparing it with 3D-FEA at various operating points. The validation of the proposed analytical field weakening model is performed using the developed LUT model.

Chapter 7 identifies the limitations of the analytical model due to linearized approximations and incorporates the nonlinearities into the analytical model. The nonlinear model is then used to estimate the field weakening performance of the hybrid rotor PMSM and compared with the high fidelity LUT model, further validating the analytical modeling method. Based on the developed analysis, some of the limitations of the modeling methods and the hybrid rotor PMSMs are identified.

Chapter 8 summarizes the design, manufacturing, and assembly of an experimental prototype hybrid rotor PMSM. The prototype machine is tested with each individual SPM and SyR rotors, and the experimental measurements are compared with 2D FEA. A hybrid rotor PMSM is then assembled, and the measured data is compared with LUT based model, thus validating both FEA and LUT based modeling developed in previous chapters.

Chapter 9 is focused on the design of a high power – high speed hybrid rotor PMSM suitable for traction applications and compares the performance with an existing traction machine. Loss calculation LUT for hybrid rotor PMSM using the analytical machine model as reference is developed and validated using 3D-FEA, and efficiency map generated over the

complete operating range. The benefits of hybrid rotor PMSM in the mitigation of torque ripple and demagnetization are evaluated.

Chapter 10 summarizes the conclusions from this research and lays out the research contributions stemming from this work. The recommended future work is summarized at the end.

Chapter 2

2. State-of-the-Art Review

In this chapter, a concise view of the different types of PMSMs found in present-day industrial and traction applications is presented. Based on the machine type identified, different types of IPMMs are introduced. A comprehensive review of the state-of-the-art technology of hybrid rotor machines is presented. The knowledge gap in the design and characterization of hybrid rotor machines and potential research opportunities are identified.

2.1. PMSM in Electric and Battery Electric Vehicles

Historically, the most commonly used machines are asynchronous in nature, i.e., induction machine (IM). There are several advantages to IM due to simple and robust construction and the ability to line start. In fact, until as recently as 2017, Tesla Motors continued to use IM in what could be one of the arguably most advanced commercial electric vehicles (EV) in production. The primary driver for this decision appears to be a manageable cost of material and manufacturing, as well as high starting torque offered by IM. However, IMs suffer from lower power factor and efficiency at high speeds, thus reducing the range.

Synchronous machines, on the other hand, were shown to have better efficiencies at higher speeds along with precise control of the steady-state speed. However, synchronous machines cannot be line started and require a variable frequency drive (VFD), thus limiting their use to specialized applications in the past. Due to the reduction in component and packaging costs, VFDs are more readily available, and concurrently synchronous machines

quickly became popular in the past few decades. While a well-designed IM can compete with PMSM in power density and operation characteristics, the former fares worse in efficiency at high-speed operation. Hence servo and automotive traction applications increasingly migrated towards PMSMs. An extensive review of the trend in electric machine types used in automotive traction application until the year 2016 was performed by Bazzi, et al. [1] and a cumulative trend of machine types shown in Figure 2-1. Focusing on the last decade, hybrid and EV market is dominated by PMSMs (see Figure 2-2).

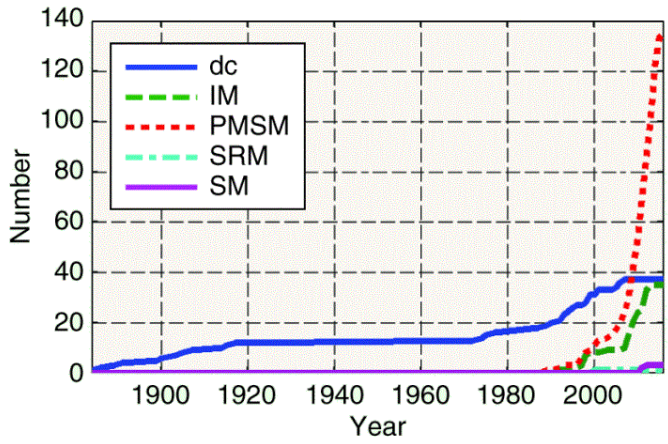

Figure 2-1. Cumulative trend of electric machine technologies in automotive traction application [1]

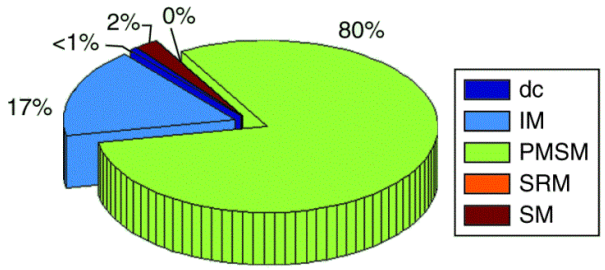

Figure 2-2. Percentage distribution of machine types in automotive traction application over the past decade [1]

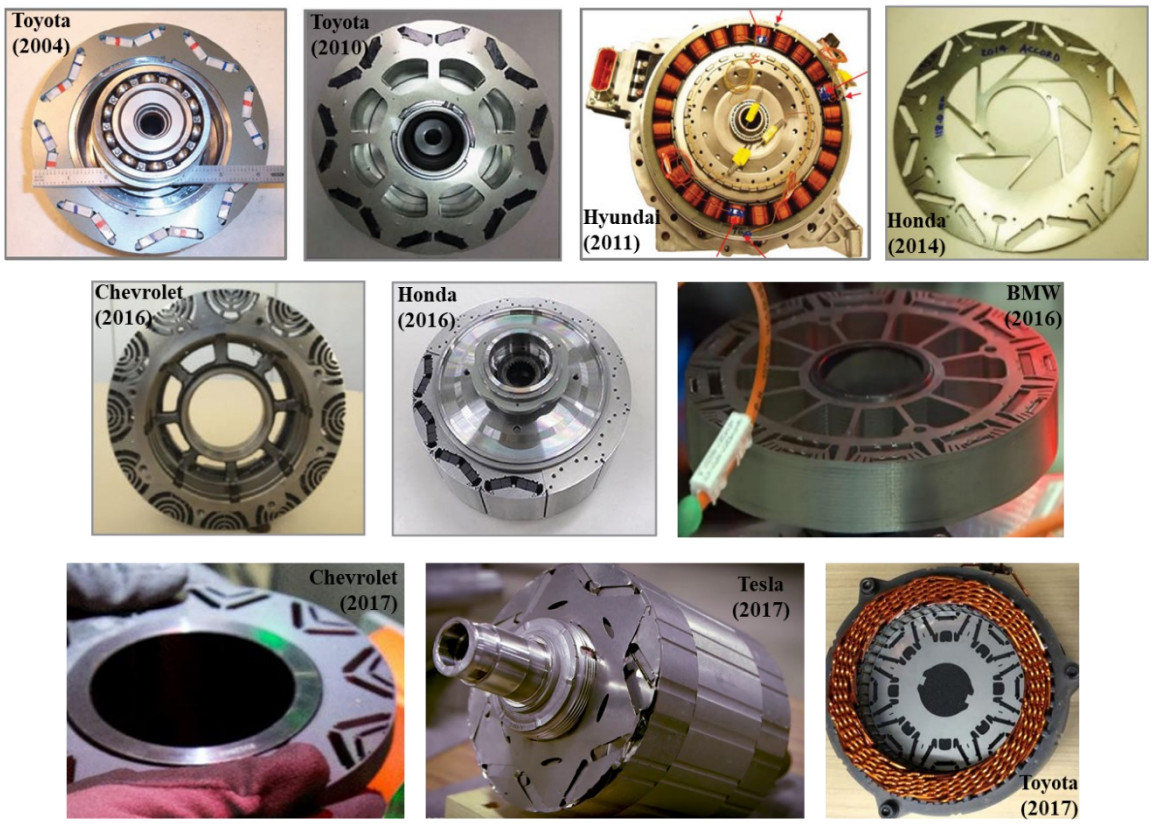

Figure 2-3. Rotor designs of PMSMs used in commercial EV, HEV [2]–[5]

The rotor designs of an array of traction motors used in commercial EV and HEV collected from various sources are shown in Figure 2-3. While some SPMMs could be found in the modern traction applications, it is evident that the current trend, in general, has a penchant for IPM machines. This comes from the fact that an IPM machine can meet torque density targets with better constant power region than SPMM. In addition, IPMM uses lower PM material volume due to the nature of the torque production mechanism, i.e., both PM torque and reluctance torque. In addition, the reduction in PM material aids in achieving a wider constant power speed ratio (CPSR), i.e., a wider speed range at which the power can be held

constant. Furthermore, since the PM material is buried inside the rotor steel, IPM machines have a lower potential for permanent demagnetization due to over current condition.

2.2. PMSM Design for Wide CPSR

While PMSMs offer an attractive advantage with power density due to the passive rotor excitation of the PM material, it also poses a limitation that the PM flux cannot be turned off or reduced. Hence the PMSM that is designed for a specific rated speed will exceed the rated terminal voltage limit at higher speeds. Extended speed operation is achieved by weakening the PM flux, as shown in Figure 2-4(a) [6], thus maintaining the induced voltage within inverter limitation. The behavior of voltage limit locus as speed increases is shown in a current vector plane in Figure 2-4(b) [7].

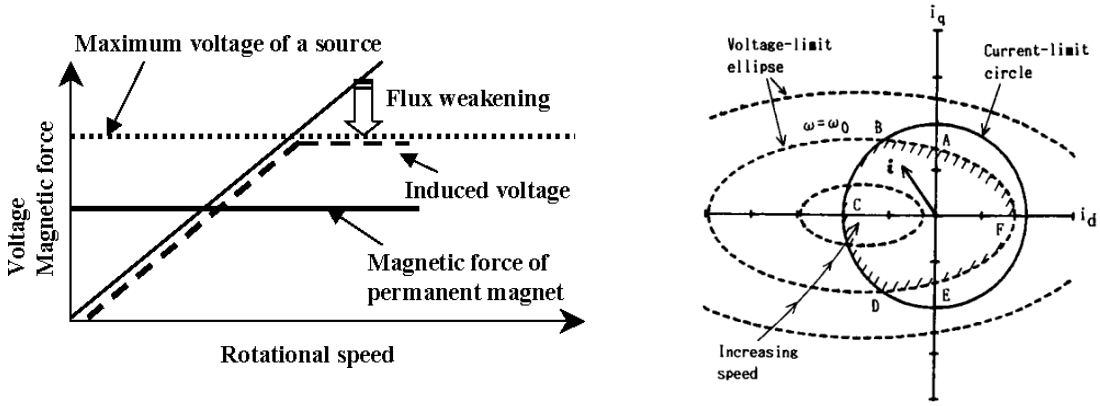

(a) (b)

Figure 2-4. Field weakening process and available current vector command region for PMSM with saliency. [6], [7]

Field weakening is achieved by controlling the current vector command such that the operating point is always within the current limit circle and the voltage limit ellipse (see Figure

2-4(b)). The appropriate current vector trajectories for conventional IPM machines were developed by Morimoto, et al. [7] and shown in Figure 2-5. The appropriate designations of the operating modes and process to identify command current will be discussed in detail in the latter part of this thesis. However, one key aspect to note from Figure 2-5 is the center of the voltage limit ellipse (identified as A4), also referred to as the characteristic current. The amplitude of characteristic current relative to the current limit plays an important role in the determination of field weakening characteristics of PMSMs.

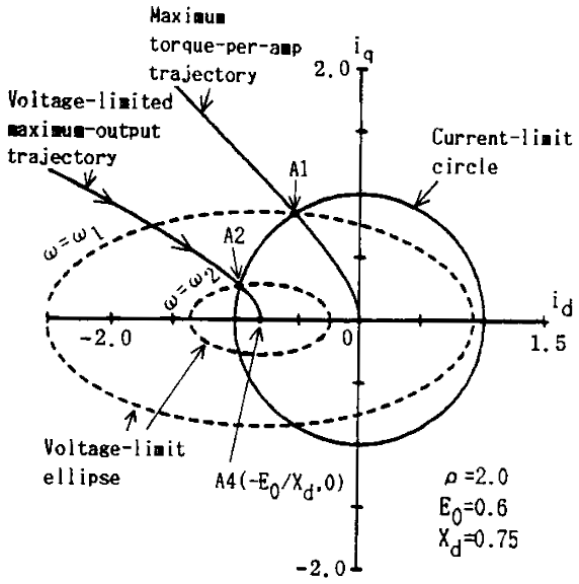

Figure 2-5. Current vector command trajectories for field weakening operation [7].

A very comprehensive work presented by Soong et al. [8] establishes the baseline for achieving wide CPSR using an IPMM. The field weakening performance of an IPM machine is characterized using two independent machine parameters. Based on the normalized PM flux linkage and saliency of the rotor, an ideal IPMM design guideline was proposed by Soong, as

shown in Figure 2-6. It is clear that the two parameters, i.e., PM flux linkage, saliency ratio, are key properties of SPM and SyR rotors, respectively.

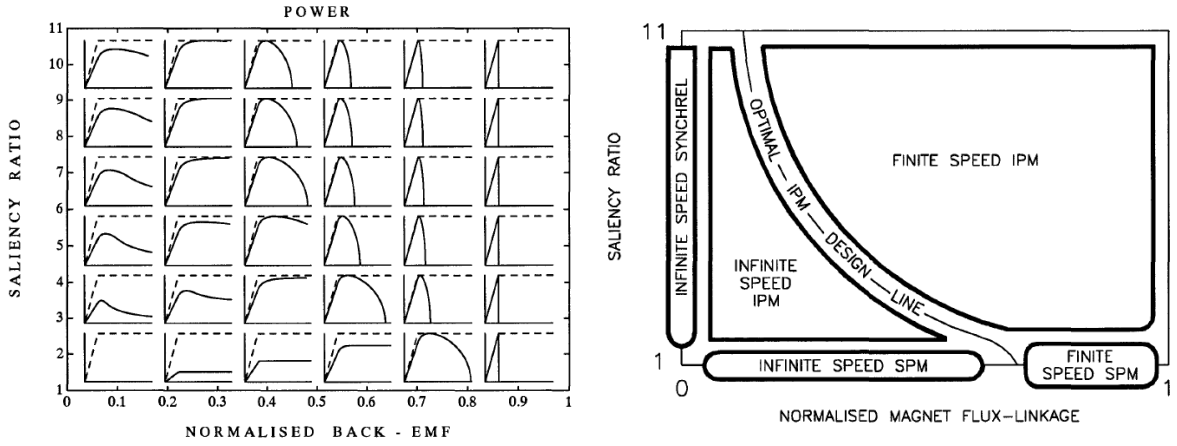

(a) (b)

Figure 2-6. Synchronous machine parameters for obtaining wide CPSR. [8]

It is evident from Figure 2-3 that the rotor geometry and PM material position in the IPM rotors are intricately arranged. A typical initial design process is either focused on improving the saliency ratio of the rotor, i.e., a PM assisted reluctance machine, or on carefully positioning the PM material in the rotor if PM torque component is dominant, i.e., conventional IPMM. Correspondingly, the PM flux linkage or the saliency ratio of the rotor are by-products, respectively. While multi-objective optimization is becoming more common to tackle both PM and reluctance components of a rotor design simultaneously, such analysis is computationally intensive and not always readily accessible. Hence the design life cycles for ideal wide CPSR machines typically spans over a few years including system integration.

2.3. Scalable and Modular Manufacturing

Due to the considerable effort involved in design of machines with desired performance characteristics and torque or power densities, design of a similar line of machines is often achieved by scaling the dimensions or modifying the winding nature to achieve a machine with different rating. Since the manufacturing process of an electric machine involves stamping the stator and rotor laminations and considering the manufacturing equipment costs for such stamping tools, it is preferable to standardize the lamination geometry and scale the machine axially, i.e., only stack length. This process was historically more commonly used for induction machines suitable for a wide range of applications. A more recent example of such study for elevator systems is performed by Alberti et al. [9] as shown in Figure 2-7.

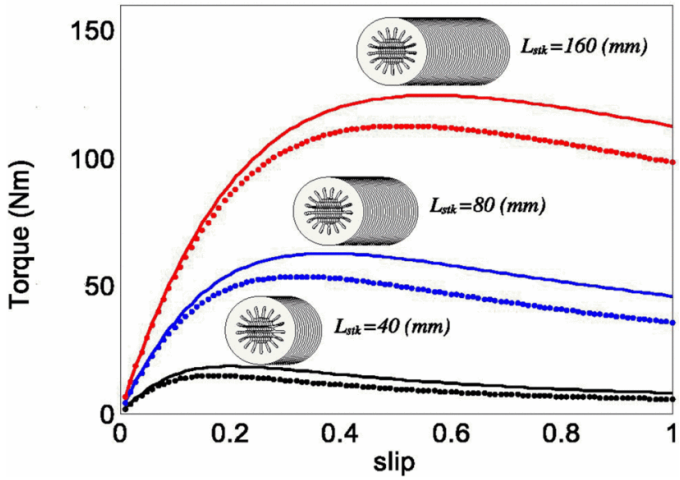

Figure 2-7. Scalable manufacturing for elevator [9]

Among the synchronous machines, such practice is commonly implemented by electric machine manufacturers for servo applications where the business models are increasingly

focused on less development time, smaller component inventories and ability to integrate a vast range of electric drive system requirements.

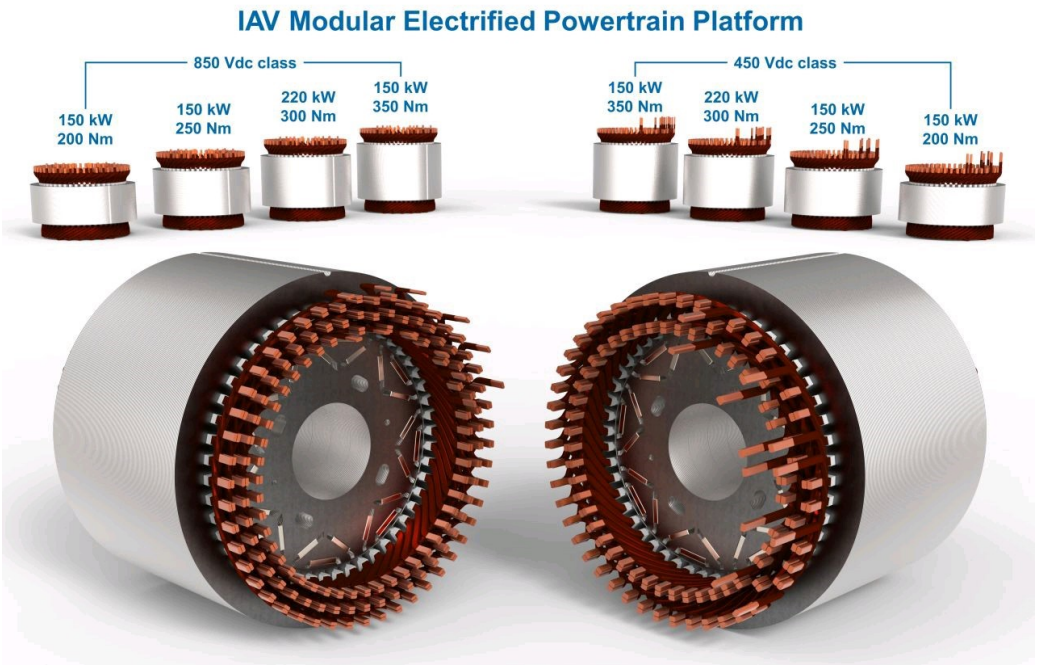

Figure 2-8. Scalable and modular manufacturing for EV, HEV from IAV GmbH [10].

In the recent past for traction industry, the original equipment manufacturer(s) (OEM) and tier 1 suppliers are also inclining to fine tune their business models to scalable and modular product lines due to competition in life cycle and manufacturing costs. In addition to standardizing the laminations, manufacturing in modules of rotor and stator stacks that can either be assembled to produce the desired power or a complete machine design that can be stacked together to compound the shaft power were commercialized in the traction and aerospace industry. An example of the modular powertrain platform for traction applications from IAV GmbH. is shown in Figure 2-8, and stackable high-performance machines for aerospace application from magniX shown in Figure 2-9. Such modular design methodologies

enable OEMs to produce customizable yet cost and demand optimized machines with relatively minimal additional manufacturing costs and time.

Figure 2-9. Modular manufacturing for aviation application form magniX [11]

2.4. Hybrid Rotor PMSM – Dual Rotor Machines

While the authors in [8] refer to the IPM machine characteristics as a hybrid of the SPM and SyR machines, they were referring only to the performance characteristics as a hybrid rather than the rotor design itself. With the physical combination of SPM and SyR rotors, the hybrid rotor machine can replicate the performance of an equivalent IPM machine. The concept of using two rotors with a single stator is quite natural for axial flux machines due to the nature of the stator and rotor arrangement on the shaft. The transition of this idea into radial flux machines can be divided into two parts.

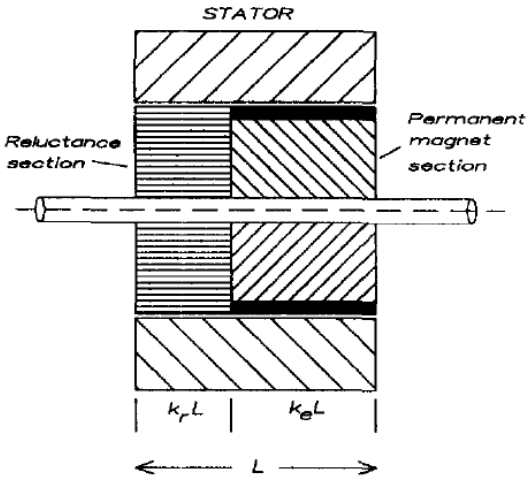

Figure 2-10. Axially stacked hybrid rotor PMSM with SyR and SPM rotor sections [12]

2.4.1. Axial Stacked Dual Rotor Hybrid PMSM

The origins of axially stacked composite/hybrid rotor construction can be traced back more than two decades ago. However, there is limited literature available on such machines. Chalmers et al. [13] and Gosden et al. [12] analyzed such rotor topology and compared its performance against conventional IPM machines and IM. The composite rotor design was achieved by utilizing an axially laminated SyR rotor section and an SPM rotor section axially stacked on a common shaft. A cross-section of axial stacked hybrid rotor PMSM is shown in Figure 2-10.

Chalmers's work in [14], [15] establishes the initial groundwork for analysis of hybrid rotor PMSM with the analytical equations for torque and voltage. The machine's field weakening performance, however, is computed using numerical search methods. Due to the computational cost and possibility of numerous combinations, the analysis was limited to offset angles of 0^o and 90^o. They also identified that by using the 90^o offset, the hybrid rotor PMSM

could achieve inverse saliency ($L_q < L_d$). Gu et al. [16] performed a numerical analysis to identify optimal design space for hybrid rotor PMSM. However, the design metrics focused were limited, and the analysis started with an existing design. Nevertheless, Gu's investigation concluded that to minimize the leakage between the two rotor sections, a non-magnetic separation of 20 times the airgap thickness is necessary (see Figure 2-11). Even with a small airgap machine, such nonmagnetic separation occupies a significant portion of the stack length.

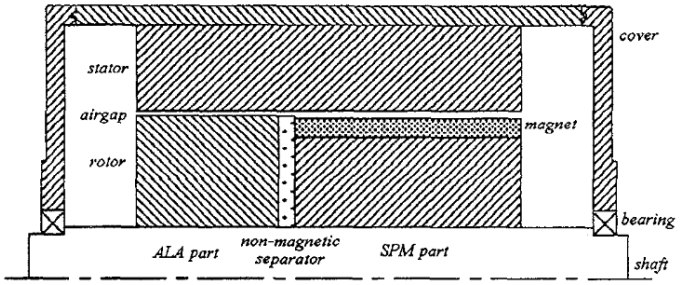

Figure 2-11. Axial cross-section of hybrid rotor PMSM with axially laminated SyR rotor and SPM rotor showing nonmagnetic separation between rotor sections. [17]

Randy [18] attempted to further enhance the design space identification of hybrid rotor PMSM to obtain the desired CPSR. This work also uses a system of nonlinear equations that were solved numerically to identify power-speed curves for different parameter combinations. Despite some limitations on the rotor parameters that can be analyzed, Randy's work shows that hybrid rotor PMSMs can be designed to produce desired CPSR characteristics. Chen et al. performed experimental work on the torque and power characteristics by manufacturing multiple rotors with different rotor offset angles, as shown in Figure 2-12.

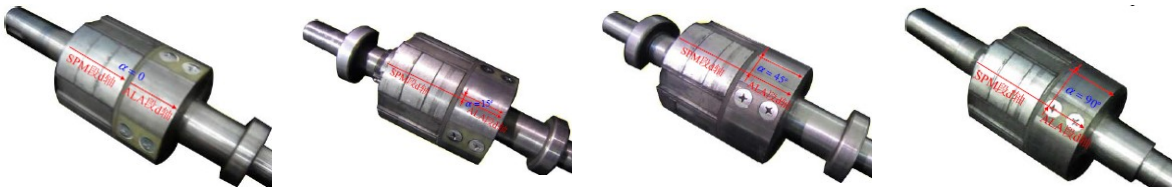

(a)

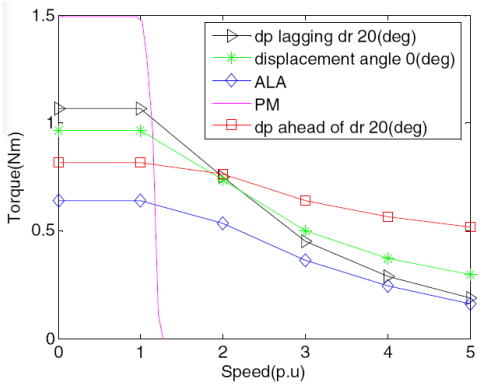

(b)

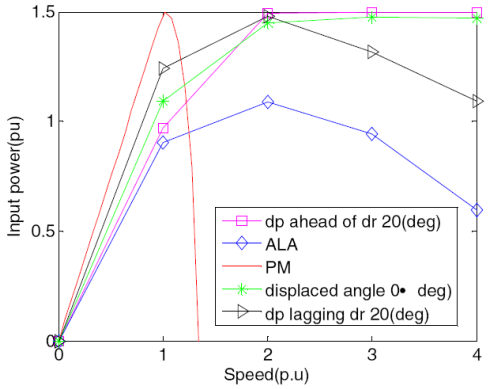

(c)

Figure 2-12. Experimental analysis of hybrid rotor PMSM [19], [20] (a) prototype rotors with different rotor offset angles (b) Torque-speed curve comparison (c) Power-speed curve comparison.

(a)

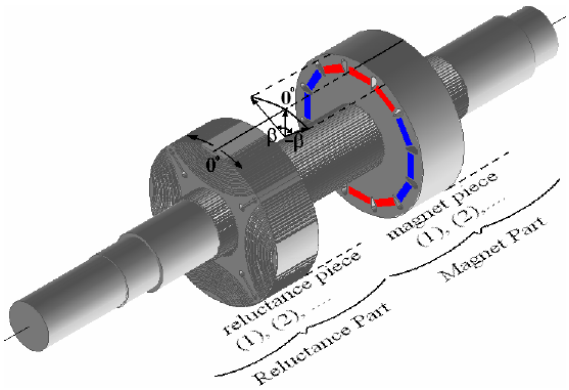

(b)

Figure 2-13. Hybrid rotor PMSM prototype for experimental analysis of a wide range of rotor offset angles [21], [22]

Beser et al. also performed a similar experimental study. The rotor was constructed to be configurable with different rotor section lengths and offset angles using a spline shaft (see Figure 2-13). Nevertheless, the stack lengths of the PM and SyR rotor sections were selected ad-hoc, and the work was limited to comparing the results between FEA simulation and experimental measurements with limited offset angles. While the modularity and reconfigurable nature of the hybrid rotor PMSMs is apparent from this study, a missed opportunity was to identify the advantages or limitations of the available configurations and provide insight and guidelines into rotor configuration selection.

More recently, there has been a renewed interest in the hybrid rotor PMSM due to the increase in transportation electrification. Yang et al. [23] and Zhao et al. [24] have separately revisited the hybrid rotor PMSM configurations and implemented models with conventional SyR rotors, as shown in Figure 2-14. However, the analysis was also limited to FEA models with a single offset angle.

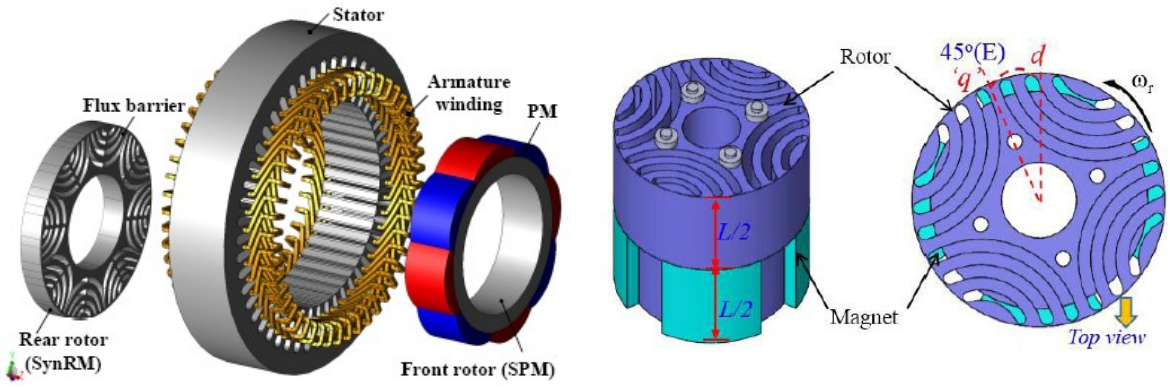

(a) (b)

Figure 2-14. Hybrid rotor PMSM for max. torque in traction [23] and fan [24] applications.

2.4.2. Radial Dual Rotor Hybrid PMSM

Radial dual rotor machine concept, as shown in Figure 1-3(a), was first found to be proposed in an induction machine [25] and similar concept later applied to other rotor types [26]–[28]. However, these machines used the same rotor types for both rotors. A hybrid rotor PMSM with different rotor types was proposed by Y. Li [29] and shown in Figure 2-15(a), the rotor offset angle is identified in Figure 2-15(b). The advantage of increased torque due to the rotor offset angle is addressed, and the machine was analyzed for a traction application in [30]. However, this analysis is only limited to one offset angle. While radial dual rotor machines are shown to improve torque densities, it comes at the expense of manufacturing complexity due to the nature of inner and outer rotor configuration. In addition, the stator winding is not easily accessible for cooling. No known manufactured prototype of radial dual rotor hybrid PMSM was found in the literature thus far.

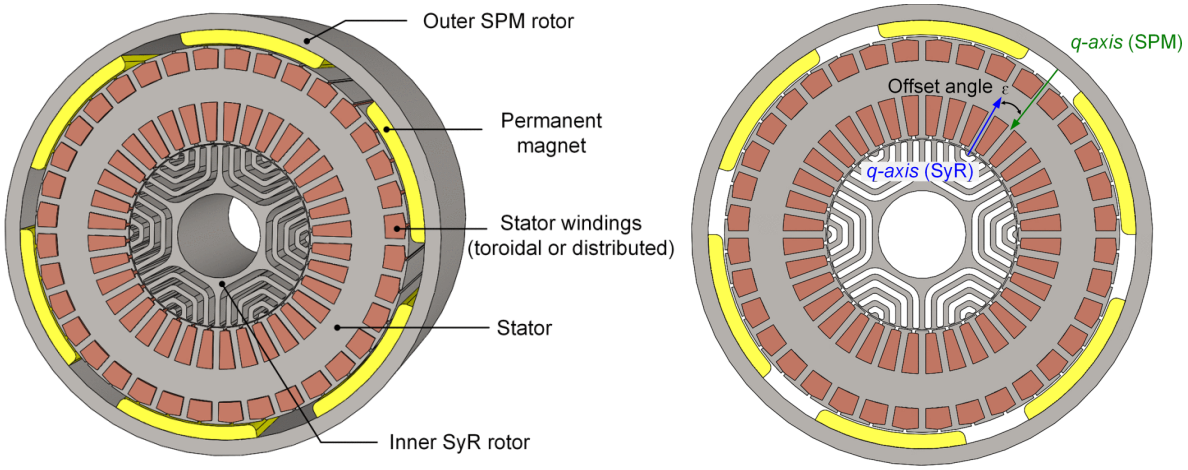

(a) (b)

Figure 2-15. Radial dual-rotor hybrid PMSM with the inner SyR and the outer SPM rotors and toroidal winding [29]

2.5. IPM Machine Types

Since the hybrid rotor PMSM is expected to mimic the operating characteristics of various machine types, it is beneficial to summarize different types of IPMM and their characteristics. From Figure 2-3, it is evident that the IPM rotor designs in traction applications have a range of variation. The IPM machines can be further categorized based on factors such as, the dominant torque component, the nature of reluctance torque production mechanism, and the nature of control in extended speed operation.

2.5.1. Conventional IPM Machines

Most common IPM machines typically use some variation of a 'V' shaped magnet arrangement with high remanence PM material such as NdFeB. Such machines have a high PM torque component and a relatively lower reluctance component. There are several other PM material arrangements such as, spoke type, bar type, delta shape, etc. that can all fall under the umbrella of IPM machines with high PM torque and low reluctance torque.

Alternatively, IPM machines that rely on a dominant reluctance torque component than PM torque component are also possible. Such machines are aptly referred to as PM assisted reluctance machines and usually tend to have multi-layer barrier configuration on the rotor. The barrier space is either mostly filled with lower remanence PM material such as Ferrite or partly filled with high remanence PM material. The driving factor for such designs is reduced material cost either due to cheaper PM material or reduced PM material utilization.

Both IPMM and PM assisted reluctance machines are found in Figure 2-3. However, based on the fundamental torque production mechanism and field weakening control technique, both categories can be referred to as conventional IPMM. There is a wealth of

literature available on such IPM machines, and the details will not be repeated here [31]. A key identifying factor for conventional IPM machines is that the d-axis inductance (L_d) is lower than q-axis inductance (L_q) due to the PM material being in the d-axis flux path.

2.5.2. Flux Intensifying IPM Machines

Conventional IPMM operates with negative *d*-axis current even at the rated operation to produce positive reluctance torque due to the nature of its saliency. Therefore, the PM material in an IPMM is continuously subjected to flux weakening at rated operation.

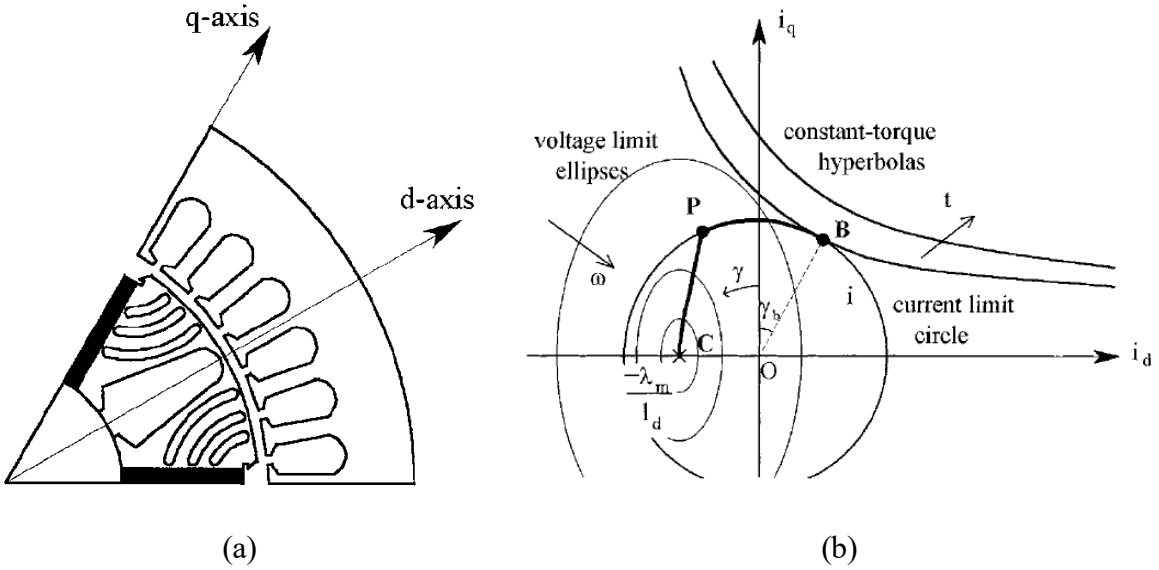

Figure 2-16. FIPMM with $L_q < L_d$ using flux barriers in the q-axis flux path [32]

FIPMMs alleviate this issue at rated operation. The rotor is designed such that $L_q < L_d$ and hence requires positive d-axis current to produce positive reluctance torque, thus aiding and intensifying the PM flux at rated operation [32]–[34]. However, the reduction in L_q is typically achieved by increasing the effective air gap in the q-axis flux path by adding more flux barriers, as shown in Figure 2-16. FIPMM design, while reducing the demagnetizing flux

on the PM material at rated operation, essentially creates a very low inductance machine. Such low inductance leads to limited saliency and a higher current requirement to produce similar torque compared to conventional IPMM [35].

2.5.3. Variable Flux IPM Machines

Typical PMSMs use PM material with a fixed magnetization state, and the machine is designed or operated such that the PM material never sees sufficiently large current to be permanently demagnetized. VFIPMMs, on the other hand, actively alter the magnetization state of the PM material by de/re magnetizing when necessary to maintain the phase voltage within the inverter limit at overrated operating speeds. This is possible by using a low coercive force PM material, such as AlNiCo or SmCo.

VFIPMMs also uses a similar structure as FIPMMs to avoid the subjecting the low coercive force PM material to unintended demagnetizing current at high load operation. Some examples of VFIPMMs are shown in Figure 2-17. While this is an attractive option to reduce overall losses, both magnetic and electric loading of such machines is limited due to the low coercivity of PM material.

The current command trajectory and torque-speed curves for VFIPMM would look similar to a FIPMM, but with the active magnetization state change, they can be adjusted to meet the voltage limit without applying continuous flux weakening. An example of the possible torque-speed envelop with VFIPMM is shown in Figure 2-18.

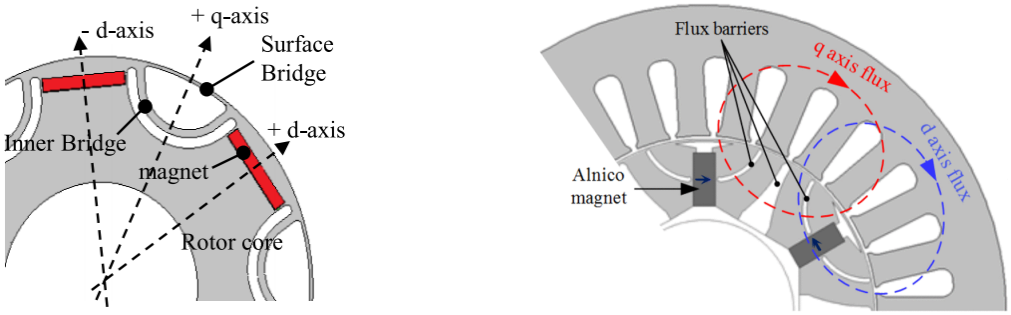

(a) (b)

Figure 2-17. VFIPMM with $L_q < L_d$ using flux barriers in q-axis flux path [36], [37]

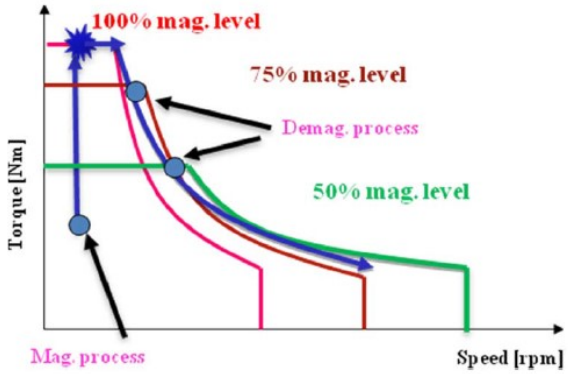

Figure 2-18. Operation area expansion in VFIPMM using magnetization state change [38]

2.5.4. Shifted Reluctance Axis IPM Machines

In the recent past, IPM machines that have the PM material distributed with an offset from the *d*-axis of the rotor are introduced. While there are numerous variations of such machines with complex and intricate rotor structures, some of the first few identified from the literature are shown in Figure 2-19.

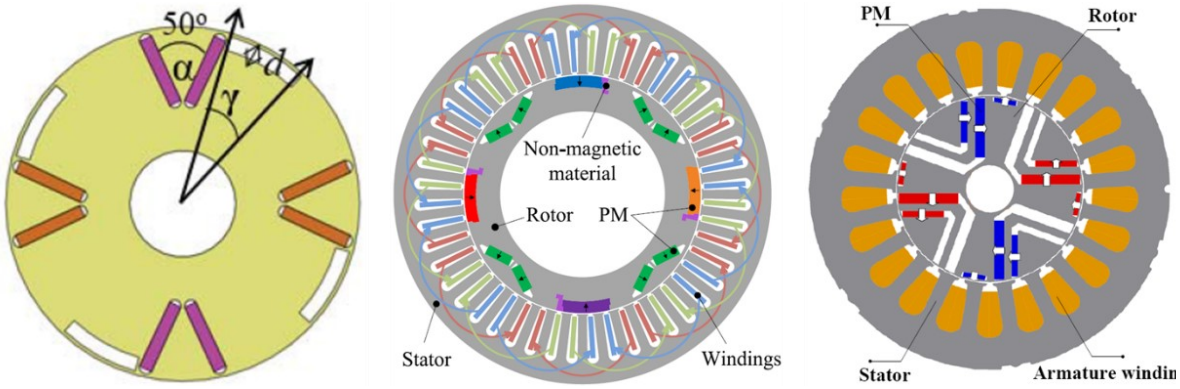

Figure 2-19. Shifted reluctance axis IPM machines [39]–[41]

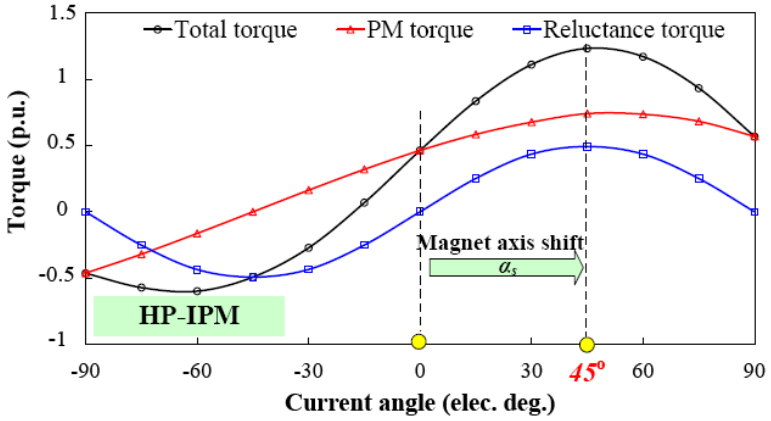

Figure 2-20. Shifted PM torque component to align MTPA with reluctance torque [41]

The primary goal of these designs is to distribute the PM material such that both PM and reluctance torque components are at their maximum simultaneously, as shown in Figure 2-20. With appropriate positioning of PM material and flux barriers, the superposition of PM torque and reluctance torque components results in an overall higher shaft torque. The tradeoff for shifted reluctance axis machines appears in the form of increased harmonic distortion in the back emf due to the non-homogenous PM material distribution. Also, the design of shifted reluctance axis machines to achieve the desired offset angle is complicated and based on a trial-and-error process. Besides, understanding the field weakened performance of shifted

reluctance axis machines also presents a similar complexity with hybrid rotor machines due to the offset angle. However, unlike axial stacked dual rotor hybrid PMSM, the reluctance axis shifted IPM machines have axial symmetry and thus can be analyzed using 2D FEA with less computational cost. Hence available literature thus far on such machines also used numerical methods and FEA to evaluate field weakening operation.

2.6. Summary and Research Opportunities

This chapter presented the state-of-the-art literature review on dual rotor machines that use different rotor types on a single shaft. The key advantage of such hybrid rotor machines is the ability to meet the requirements for a wide range of operation characteristics without a significant redesign of the machine. This is made possible due to additional degrees of freedom available in hybrid rotor machines compared to conventional PMSMs. However, the additional degrees of freedom also make the analysis and defining design parameters more complicated for a PMSM with a hybrid rotor configuration, which will be referred to as hybrid rotor PMSM. With a non-zero rotor offset angle, the torque and voltage vs. current angle characteristics of the hybrid rotor PMSM does not follow the conventional wisdom. Hence it is not possible to develop an overview of the performance characteristics in the field weakening operation region using the existing PMSM theory.

Few researchers have analyzed hybrid rotor machines and hypothesized on the possibility of creating an ideal design with wide CPSR. However, most of the analysis thus far were performed using FEA and the design parameters selected arbitrarily. There is no clear design process available, nor is there a clear understanding of the hybrid rotor PMSM's performance characteristics.

Based on the state-of-the-art literature review, the following research opportunities are identified for hybrid rotor PMSM:

- Develop generalized machine model that accounts for additional degrees of freedom and accurately determine the machines steady state performance.

  Despite the past efforts, there is no simple equivalent machine models that can decompose the machines equivalent parameters into the constituent individual rotor section parameters. A method to determine the overall machine inductances is a crucial aspect in order to determine possible steady state operation before a complete machine is assembled and parameters determined using numerical or experimental methods.

- Develop generalized field weakening operation model to understand the strengths and limitations of hybrid rotor PMSMs.

  The analytical field weakening modeling analysis methods of conventional PMSMs offer a detailed insight into their characteristics and performance during field weakening operation. However, due to the additional degrees of freedom and the added complexity, such field weakening analysis model for hybrid rotor PMSMs does not exist thus far, which led to past analysis in the literature being limited to either computationally costly numerical methods or economically costly experimental methods. While they are more accurate, such methods fail to provide insights and design guidelines to achieve desired performance. Hence a generalized model that accounts the addition degrees of freedom and reliably estimate the field weakening performance of hybrid rotor PMSMs is necessary to understand the strengths and limitations of hybrid rotor PMSMs.

- Develop methodology to determine optimum parameters of individual rotors in a hybrid rotor PMSM to obtain the desired field weakening characteristics.

  The ability to achieve desired field weakening characteristics, particularly a wide CPSR, is hypothesized as one of the advantages of hybrid rotor PMSMs. However, due to the lack of generalized machine model and a generalized field weakening analysis methodology, the investigations found in the literature were limited to studying the performance of fully designed hybrid rotor PMSMs and quantify the performance range. A well-defined methodology to determine the target machine parameters or to select the combination of the rotor sections to achieve desired field weakening performance does not exist.

- Develop accurate and fast modeling method to design and analyze a hybrid rotor PMSM.

  While analytical models give comprehensive insights into the operating principles and provide a good conceptual design, a detailed and high-fidelity analysis method is necessary to validate the analytical predictions. In present day, FEA methods often serve this purpose. For axially staked hybrid dual rotor PMSM, which is the focus of this research, the axial asymmetry requires to use 3D FEA modeling. Despite the improved computational performance, using 3D FEA for field weakening performance analysis, which require hundreds of operating points to be analyzed, is not practical. In addition, the hybrid rotor PMSM configuration generates numerous possible rotor combinations for a given SPM and SyR rotor sections, thus making 3D FEA analysis less practical. Hence a fast and accurate analysis methodology that is comparable with

FEA and enables analyzing any given rotor combination and determine the performance over a wide operating region is necessary.

- Develop sizing and design principles for hybrid rotor PMSMs.

  The designs for hybrid rotor PMSM found in literature thus far relied on existing machine dimensions and develop rotor designs to explore the performance or maintain the material costs. There is no clear design process or design guidelines developed that can be used to design a hybrid rotor PMSM based on given system specifications or application requirements.

- Investigate demagnetization and torque ripple mitigation strategies for hybrid rotor PMSM.

  The modular nature of the hybrid rotor PMSM also allows for some inherent advantages that typically require specific design considerations to be accommodated in conventional PMSM. Toque ripple mitigation and demagnetization resistance are of interest while designing for desired field weakening performance.

Chapter 3

3. Analytical Modeling of Hybrid Rotor PMSM and Field Weakening Operation

The primary objective of this chapter is to develop analytical framework of an equivalent IPM rotor machine for the hybrid rotor configuration, and characterize the performance including the field weakening operation region. It is important to understand the individual rotor characteristics to determine the advantages and limitations of an achievable hybrid rotor machine and to establish which characteristics are desired in the SPM and SyR rotor sections. The characterization of SPM and SyR machines and their theoretical field weakening operation are widely covered in the literature. The initial portion of this chapter re-introduces the *dq* model of the conventional SPM and SyR machines using constant parameters for the sake of completeness. The individual machine models and vector diagrams will be used to derive the hybrid rotor machine parameters. It will be shown that the hybrid rotor PMSM can be regarded as an equivalent IPM machine for practical purposes albeit some differences in the torque profile due to the offset angle between the SPM and SyR rotor sections

3.1. Conventional PMSM Steady State Model

Synchronous AC machines' performance can be defined using a few key parameters such as the number of phases (m), poles (P), inductances in direct and quadrature axis (L_d, L_q), and permanent magnet flux linkage (ψ_m). The available drive limitations, such as DC bus

voltage (V_{DC}) and phase current (I_{ph}), define the limits to which the machine can be theoretically operated. SyR machines will be a subset of this definition where $\psi_m = 0$.

In developing the theoretical analysis in this chapter, a few simplifying assumptions are used:

- The DQ model is assumed to have constant parameters and at steady state
- The drive operates with sinusoidal voltage and current, i.e., spatial and switching harmonic components are neglected
- A lossless linear system can be used to characterize the steady-state performance, i.e., losses and saturation are neglected

Using such assumptions will make decomposing the motor performance using key rotor parameters more manageable but neglects some of the practical aspects of the machine design. Finite element analysis will be used to include the nonlinearities and losses to make the design practical. In addition, normalizing the machine and inverter parameters allows us to interpret and compare the performance of different rotor types in both rated and field weakening operation. The base quantities are set to match the maximum phase voltage and current that can be supplied by the inverter at rated speed and unity power factor. Such normalization will aid in reducing the number of parameters, i.e., voltage and current, of the machine equal to 1 p.u at the rated operation of 1 p.u. speed [42]–[44]. Following that convention, by selecting the desired rated mechanical speed (ω_{base}), rated peak voltage (V_{base}) and rated peak current (I_{base}) values, the remaining base values are defined as,

$$P_{base} = \frac{3}{2} V_{base} I_{base} \qquad \tau_{base} = \frac{P_{base}}{\omega_{base}}$$
$$L_{base} = \frac{V_{base}}{\omega_{base} I_{base}} \qquad \psi_{base} = \frac{T_{base}}{I_{base}} \tag{3.1}$$

where ω_{base} is the base speed in *rad/sec*, τ_{base} is the base torque in *N-m*, L_{base} is the base inductance in *H*, and ψ_{base} is the base flux linkage in *Wb*. With the base quantities determined, the normalized quantities can be defined as,

$$V_n = \frac{V}{V_{base}}; \quad I_n = \frac{I}{I_{base}}; \quad \omega_n = \frac{\omega}{\omega_{base}}; \quad L_n = \frac{L}{L_{base}}; \quad \psi_n = \frac{\psi}{\psi_{base}} \tag{3.2}$$

3.1.1. Surface Permanent Magnet Machine

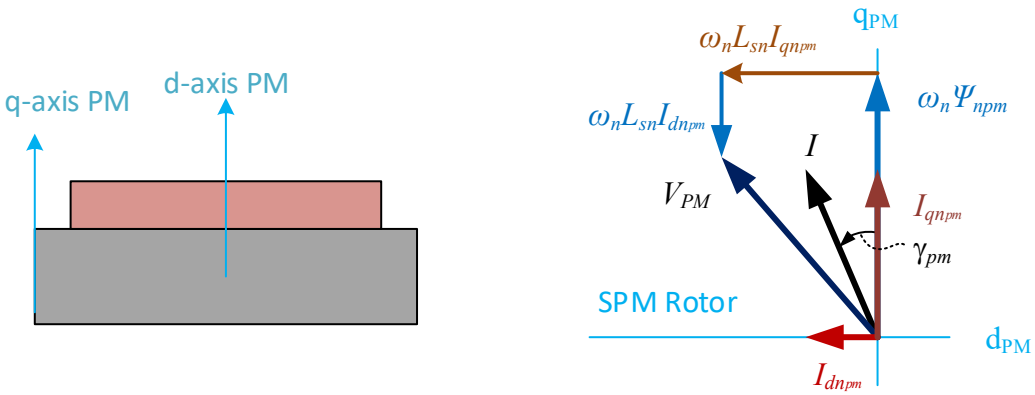

(a) (b)

Figure 3-1. Surface permanent magnet machine rotor structure and vector diagram

For a surface permanent magnet (SPM) machine, the magnets are typically placed on the surface of the rotor as shown in Figure 3-1(a) and held in place by either glue (for lower speed operation) or with the aid of a retaining sleeve (for high-speed operation). The vector diagram for an SPM machine is shown in Figure 3-1(b). For an SPM machine with given

inductance (L), pm flux linkage (ψ_{PM}) and poles (P), the steady-state equations for voltage and torque can be written as,

$$\begin{aligned} V_q &= \omega L_d I_d + \omega \psi_{PM} \\ V_d &= -\omega L_q I_q \\ \tau_{PM} &= \frac{3}{2}\frac{P}{2}\psi_{PM} I_q \end{aligned} \tag{3.3}$$

Since the permeability of PM material is close to air, and the material is uniformly distributed across the airgap in SPM machines, the inductances are nearly identical in d-axis and q-axis. Hence the SPM machines do not exhibit any saliency, and it can be assumed that $L_d = L_q = L_s$. Using the normalization, the voltage and torque equations can be written as,

$$\begin{aligned} V_{dn} &= -\omega_n L_{sn} I_{qn} \\ V_{qn} &= \omega_n L_{sn} I_{dn} + \omega_n \psi_{nm} \\ \tau_n &= \psi_{nm} I_{qn} \end{aligned} \tag{3.4}$$

where the current vectors can be written in terms of current angle 'γ' as,

$$I_{qn} = I_n \cos\left(\gamma_{pm}\right) \quad \text{and} \quad I_{dn} = -I_n \sin\left(\gamma_{pm}\right) \tag{3.5}$$

The voltage loci can be obtained by substituting (3.4) to the voltage limit constraint $V_{qn}^2 + V_{dn}^2 \le V_{n-\max}^2$ and rearranging terms to give,

$$\left(I_{dn} + \frac{\psi_{nm}}{L_{sn}}\right)^2 + I_{qn}^2 \le \frac{V_{n-\max}^2}{\left(\omega_n L_{sn}\right)^2} \tag{3.6}$$

Equation (3.6) represents a circle whose radius is $V_{n-\max}/\left(\omega_n L_{sn}\right)$ and centered at $\left(-\psi_{nm}/L_{sn},\ 0\right)$. From the torque equation in (3.4), it is evident that a maximum SPM machine

torque is obtained when I_{qn} is maximum, i.e., $I_{qn} = I_n$. This is only possible with $I_{dn} = 0$, thus giving the maximum torque per amp (MTPA) current angle as $\gamma_{max} = 0$. The constant voltage limit and constant torque locus along with the current limit circle at rated operation for an SPM are shown in Figure 3-2.

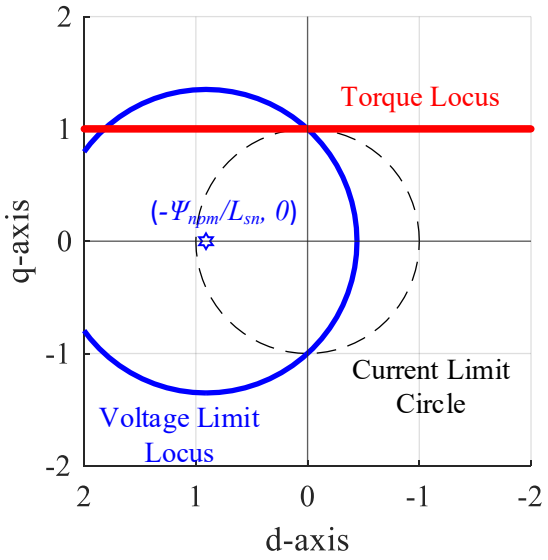

Figure 3-2. Surface permanent magnet machine circle diagram

From (3.6), it can be understood that the radius of the voltage limit circle reduces as the speed increases, and the radius becomes zero at infinite speed. The center of the voltage limit circle, also known as characteristic current, dictates if the SPM machine can reach infinite speed. If the characteristic current is higher than the current limit, the required current vector to achieve infinite speed is not possible.

3.1.2. Synchronous Reluctance Machine

Synchronous reluctance machines do not use any PM material, and the torque is produced due to the difference in the reluctance of d- and q- axis flux paths. Typically, the

rotor axis that produces higher gap flux (i.e., high inductance axis for a SyRM) is designated as d-axis. However, to keep the comparison and equations consistent between SyRM and other PM machines, the d-axis is selected as the least inductance axis in this thesis. A simplified SyR rotor structure is shown in Figure 3-3(a) with the d- and q-axis labeled. The corresponding vector diagram is shown in Figure 3-3(b).

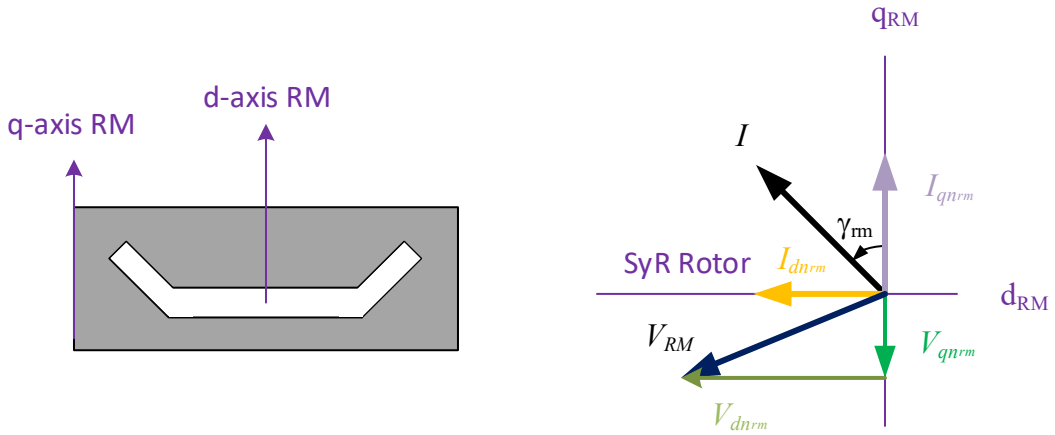

(a) (b)

Figure 3-3. Synchronous reluctance machine rotor structure and vector diagram

Applying the normalization and defining the saliency ratio as $\xi = L_q / L_d$, the steady-state equations for SyRM voltage and torque can be written as,

$$\begin{aligned} V_{dn} &= -\omega_n \xi L_{dn} I_{qn} \\ V_{qn} &= \omega_n L_{dn} I_{dn} \\ \tau_n &= -(\xi - 1) L_{dn} I_{dn} I_{qn} \end{aligned} \tag{3.7}$$

Applying the voltage limit constraints, the constant voltage loci can be obtained as,

$$I_{dn}^2 + (\xi I_{qn})^2 \le \left(\frac{V_{n-\max}}{\omega_n L_{dn}} \right)^2 \tag{3.8}$$

Equation (3.8) represents an ellipse with an ellipticity of ξ with its center at the origin. The constant torque locus can be written as,

$$I_{dn} I_{qn} = \frac{-\tau_n}{(\xi - 1) L_{dn}} \tag{3.9}$$

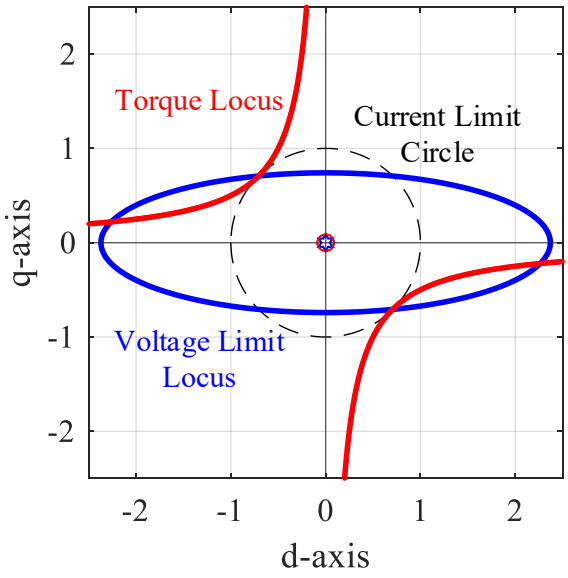

Figure 3-4. Synchronous reluctance machine circle diagram

Equation (3.9) represents a hyperbola with asymptotes $I_{dn} = 0$ and $I_{qn} = 0$, and centered at the origin. The voltage limit locus and constant torque locus along with the current limit circle for a SyR machine at rated operation are shown in Figure 3-4. Also from the torque equation in (3.7), it is evident that for a given saliency, the SyR rotor torque is maximum when the product of I_{dn} and I_{qn} is maximum. From (3.9), the MTPA current angle for a SyR rotor can be calculated as $\gamma_{rm\text{-}max} = \pi/4$. Additionally, the center of the voltage limit ellipse is at the origin, i.e., no characteristic current, and hence SyR rotor machines do not have a theoretical maximum speed.

3.1.3. Interior Permanent Magnet Machine

A conventional IPM machine can be formed by inserting PM material into the rotor flux barriers of the SyR rotor. Hence, both reluctance and PM components of flux linkage and torque are produced. A typical IPM rotor structure is shown in Figure 3-5(a) and the corresponding vector diagram shown in Figure 3-5(b).

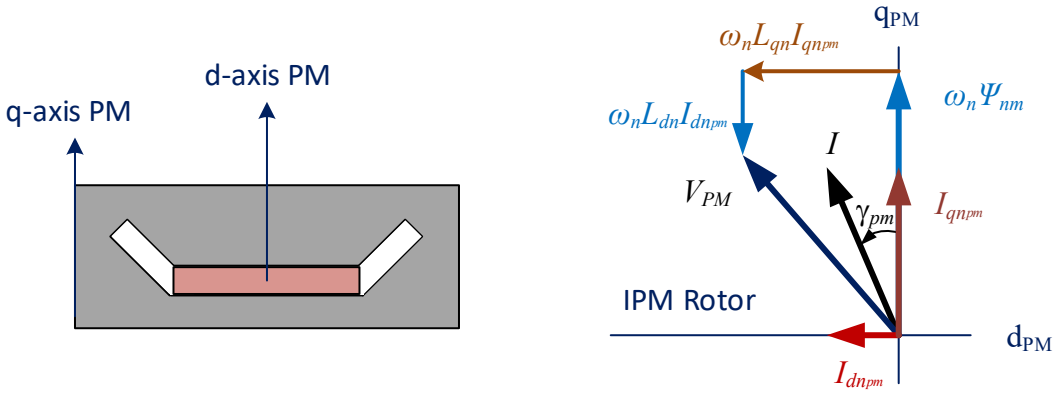

Figure 3-5. Interior permanent magnet machine rotor structure and vector diagram

The normalized steady-state equation for conventional IPM machine can be written as,

$$\begin{aligned} V_{dn} &= -\omega_n L_{qn} I_{qn} \\ V_{qn} &= \omega_n L_{dn} I_{dn} + \omega_n \psi_{nm} \\ \tau_n &= \psi_{nm} I_{qn} - (\xi - 1) L_{dn} I_{dn} I_{qn} \end{aligned} \tag{3.10}$$

Using voltage limit constant, the constant voltage loci can be written as,

$$\left(I_{dn} + \frac{\psi_{nm}}{L_{dn}} \right)^2 + \left(\xi I_{qn} \right)^2 \le \left(\frac{V_{n-\max}}{\omega_n L_{dn}} \right)^2 \tag{3.11}$$

Equation (3.11) also represents an ellipse with an ellipticity of ξ similar to SyRM, but its center is shifted from the origin to $\left(-\psi_{nm}/L_{dn},0\right)$ which is similar to the SPM machine case. Rearranging the terms of the torque equation in (3.10), the constant torque locus is given by,

$$I_{dn}I_{qn} = I_{qn}\frac{\psi_{nm}}{(\xi-1)L_{dn}} - \frac{\tau_n}{(\xi-1)L_{dn}} \tag{3.12}$$

Equation (3.12) also represents a hyperbola similar to the SyRM, but the center of the torque hyperbola is shifted to $\left(\psi_{nm}/(\xi-1)L_{dn},0\right)$. The voltage limit locus and constant torque locus along with the current limit circle for an IPM machine at rated operation are shown in Figure 3-6.

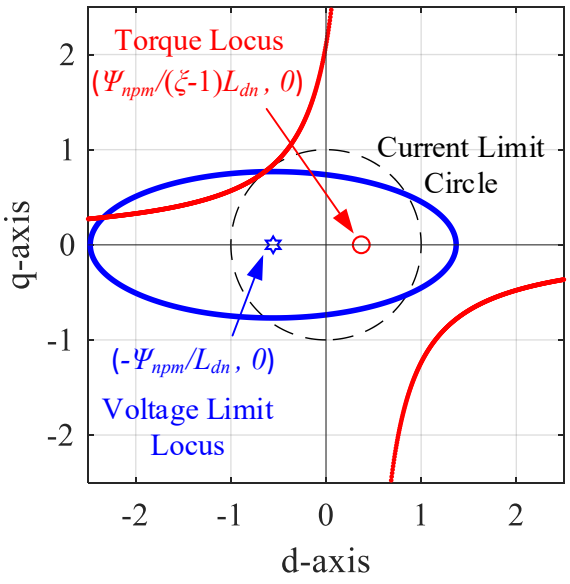

Figure 3-6. Interior permanent magnet machine circle diagram

The MTPA current angle for IPM can be obtained by differentiating the torque equation with respect to γ. The torque equation in terms of current angle can be written as,

$$\tau_n = \psi_{nm} I_n \cos(\gamma) + \frac{1}{2}(\xi - 1) L_{dn} I_n^2 \sin(2\gamma) \tag{3.13}$$

Differentiating the torque equation and equating to zero gives the current angle at which torque will be maximum as,

$$\gamma_{\max} = \sin^{-1}\left(\frac{-\psi_{nm} + \sqrt{\psi_{nm}^2 + 8(\xi - 1)^2 L_{dn}^2}}{4(\xi - 1) L_{dn}} \right) \tag{3.14}$$

The operation at MTPA during low speed is designated as mode 1. The machine can sustain mode 1 operation until the increasing speed causes terminal voltage to reach the DC bus supply limit. Once the terminal voltage reaches its limits, mode 2 operation starts where both current and voltage are at their maximum amplitude with the current angle increasing as speed increases. The speed in mode 2 can be calculated as,

$$\omega_n = \frac{V_{n-\max}}{\sqrt{\left(\xi L_{dn} I_n \cos(\gamma)\right)^2 + \left(-L_{dn} I_n \sin(\gamma) + \psi_{nm}\right)^2}} \tag{3.15}$$

If the center of the voltage limit ellipse, i.e., characteristic current, is within the current limit, then as speed increases, the constant torque hyperbola will become tangential to constant voltage ellipse on the current limit circle. At this point, it is beneficial to reduce current amplitude to achieve maximum torque possible within the voltage constraint, often referred to as mode 3 or maximum torque per volts (MTPV) operation. The mode 3 operating trajectory can be determined by substituting the voltage limit constraint into the torque equation and differentiating with respect to the current angle. The MTPV current command trajectory can be obtained as [7],

$$I_{dn} = -\frac{\psi_{nm}}{L_{dn}} - \Delta I_{dn}$$
$$I_{qn} = \frac{\sqrt{1/\omega_n^2 - \left(L_{dn}\Delta I_{dn}\right)^2}}{\xi L_{dn}} \tag{3.16}$$

where,

$$\Delta I_{dn} = \frac{-\xi\psi_{nm} + \sqrt{\left(\xi\psi_{nm}\right)^2 + 8\left(\xi - 1\right)^2/\omega_n^2}}{4\left(\xi - 1\right)L_{dn}} \tag{3.17}$$

Similar to SPM rotor machines, the ability of an IPM machine to achieve infinite speed is dependent on the characteristic current value being lower than the current limit.

3.2. Hybrid Rotor PM Synchronous Machines

The hybrid rotor is a combination of SPM and SyR rotor on a single shaft. Each rotor section can be arranged with its own arbitrary orientation which introduces a relative rotor offset angle 'α' between the two rotors. To derive the equations for the hybrid rotor, a common reference frame must be selected. An intuitive choice would be to select the PM rotor as the reference frame since the open circuit back EMF gives an ideal frame of reference for practical purposes. However, this will make interpretation of the saliency of SyR rotor dependent on the relative rotor offset angle (α), making the equations more complicated. Selecting the SyR rotor as the reference axis, will avoid arbitrary orientation of saliency but will require break down of PM flux linkage into both *d* and *q* axis. A depiction of the rotor offset angle (α) with the SyR rotor reference fame is shown in Figure 3-7.

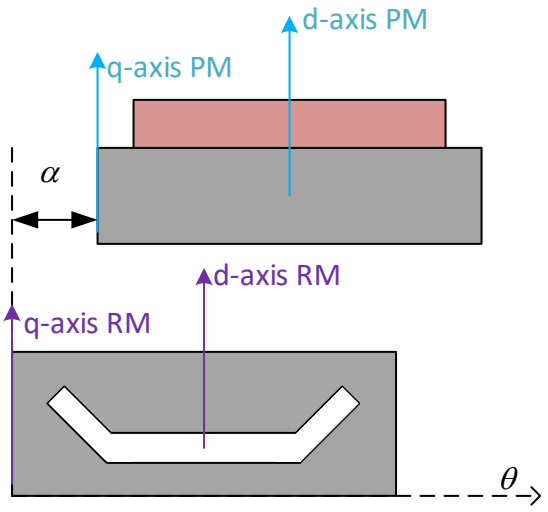

Figure 3-7. Rotor sections in hybrid rotor PMSM with SyR rotor reference frame and SPM rotor offset by arbitrary offset angle 'α'

For convenience, the SyR rotor referenced dq axis will be simply referred to as the d- and q- axis, and the corresponding dq axis of the PM machine will be referred to as d_{pm} and q_{pm} axis. With the SyR rotor as reference axis and considering an arbitrary offset angle of α to the SPM rotor axis, the current, and voltage of SPM must be transformed on to the SyR axis. Taking I_{dpm} and I_{qpm} and transforming on to new reference dq axis as shown in Figure 3-8(a) will generate four components that can be expressed as,

$$\begin{aligned} I_{qn_{pm}-q} &= I_{qn_{pm}}\cos(\alpha); \quad I_{dn_{pm}-q} = I_{dn_{pm}}\sin(\alpha) \\ I_{qn_{pm}-d} &= -I_{qn_{pm}}\sin(\alpha); \quad I_{dn_{pm}-d} = I_{dn_{pm}}\cos(\alpha) \end{aligned} \tag{3.18}$$

Then the transformed current vectors on the SyR reference axis will be,

$$\begin{aligned} I'_{qn_{pm}} &= I_{qn_{pm}-q} + I_{dn_{pm}-q} \\ I'_{dn_{pm}} &= I_{qn_{pm}-d} + I_{dn_{pm}-d} \end{aligned} \tag{3.19}$$

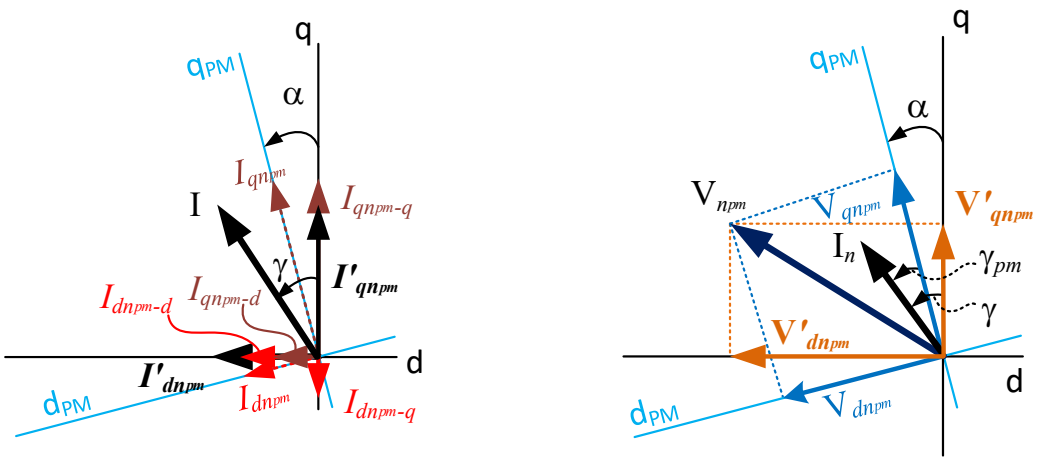

(a) (b)

Figure 3-8. Transformed SPM vectors onto the SyR rotor reference frame (a) Current vector transformation (b) Voltage vector transformation.

Substituting (3.18) into (3.19),

$$\begin{aligned} I'_{qn_{pm}} &= I_n\left[\cos\left(\gamma_{pm}\right)\cos\left(\alpha\right)-\sin\left(\gamma_{pm}\right)\sin\left(\alpha\right)\right] = I_n\cos\left(\gamma_{pm}+\alpha\right) \\ I'_{dn_{pm}} &= -I_n\left[\cos\left(\gamma_{pm}\right)\sin\left(\alpha\right)+\sin\left(\gamma_{pm}\right)\sin\left(\alpha\right)\right] = -I_n\sin\left(\gamma_{pm}+\alpha\right) \end{aligned} \tag{3.20}$$

Based on the rotation convention assumed, $\gamma_{pm}=\gamma-\alpha$. Substituting in (3.20) gives,

$$\begin{aligned} I'_{qn_{pm}} &= I_n\cos\left(\gamma\right) \\ I'_{dn_{pm}} &= -I_n\sin\left(\gamma\right) \end{aligned} \tag{3.21}$$

This can, of course, be deduced from the vector diagram shown in Figure 3-8(a); however, the intermediate equations will be useful in simplifying the voltage equations. Since the current command will be provided from a single stator, the net *d* and *q* axis currents will be the same regardless of the rotor offset angle and hence,

$$\begin{aligned} I_{qn} &= \quad I_n \cos(\gamma) \\ I_{dn} &= -I_n \sin(\gamma) \end{aligned} \tag{3.22}$$

In addition, (3.19) can be written in a matrix from as,

$$\begin{bmatrix} I'_{qn_{pm}} \\ I'_{dn_{pm}} \end{bmatrix} = \begin{bmatrix} \cos(\alpha) & \sin(\alpha) \\ -\sin(\alpha) & \cos(\alpha) \end{bmatrix} \begin{bmatrix} I_{qn_{pm}} \\ I_{dn_{pm}} \end{bmatrix} \tag{3.23}$$

which gives the rotational transformation of the vectors on the PM axis by any arbitrary angle of α. This transformation matrix can be used on the voltage vectors as well, giving,

$$\begin{bmatrix} V'_{qn_{pm}} \\ V'_{dn_{pm}} \end{bmatrix} = \begin{bmatrix} \cos(\alpha) & \sin(\alpha) \\ -\sin(\alpha) & \cos(\alpha) \end{bmatrix} \begin{bmatrix} V_{qn_{pm}} \\ V_{dn_{pm}} \end{bmatrix} \tag{3.24}$$

Substituting and expanding the SPM voltage,

$$\begin{aligned} V'_{qn_{pm}} &= -\begin{bmatrix} I_n \sin(\gamma_{pm}) \cos(\alpha) \omega_n L_{sn} \quad + \\ \qquad I_n \cos(\gamma_{pm}) \sin(\alpha) \omega_n L_{sn} \end{bmatrix} + \omega_n \psi_{n_{pm}} \cos(\alpha) \\ V'_{dn_{pm}} &= \begin{bmatrix} I_n \sin(\gamma_{pm}) \sin(\alpha) \omega_n L_{sn} \quad - \\ \qquad I_n \cos(\gamma_{pm}) \cos(\alpha) \omega_n L_{sn} \end{bmatrix} - \omega_n \psi_{n_{pm}} \sin(\alpha) \end{aligned} \tag{3.25}$$

Using equations (3.20), (3.21) and substituting into (3.25),

$$\begin{aligned} V'_{qn_{pm}} &= -I_n \sin(\gamma) \omega_n L_{sn} + \omega_n \psi_{n_{pm}} \cos(\alpha) \\ V'_{dn_{pm}} &= -I_n \cos(\gamma) \omega_n L_{sn} - \omega_n \psi_{n_{pm}} \sin(\alpha) \end{aligned} \tag{3.26}$$

Applying the voltage limit constraint $V_q^2 + V_d^2 \le V_s^2$ on the transformed voltage equations from (3.26), the constant voltage loci can be obtained as,

$$\left(I_{dn_{pm}}+\frac{\psi_{n_{pm}}\cos(\alpha)}{L_{sn}}\right)^2+\left(I_{qn_{pm}}+\frac{\psi_{n_{pm}}\sin(\alpha)}{L_{sn}}\right)^2\le\left(\frac{V_{sn}}{\omega_n L_{sn}}\right)^2 \tag{3.27}$$

This equation clearly represents a circle with the same radius as (3.6). The center of the transformed voltage loci, however, is now a function of the offset angle and given as,

$$\left(h_{cV-pm},k_{cV-pm}\right)=\left(-\frac{\psi_{n_{pm}}\cos(\alpha)}{L_{sn}},-\frac{\psi_{n_{pm}}\sin(\alpha)}{L_{sn}}\right) \tag{3.28}$$

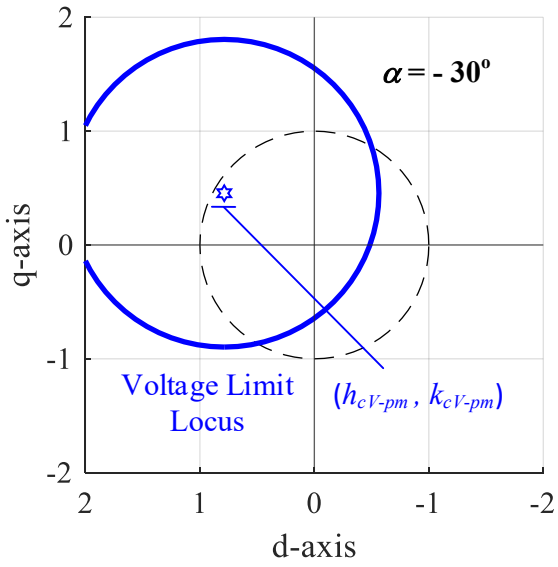

Figure 3-9. Rotated voltage limit locus of SPM rotor in SyR rotor reference frame with an arbitrary offset angle of α = -30°

It can be seen that the center of the voltage limit loci itself has a locus with respect to offset angle in a polar coordinate form, and it represents a circle with radius $\psi_{n_{pm}}/L_{sn}$ and centered at the origin. The transformed SPM voltage limit locus plot is shown in Figure 3-9.

Now that the SPM rotor currents and voltages are transformed on to the SyR rotor reference frame, the voltage vectors can be combined to get the equivalent voltage equations of the hybrid rotor PMSM. Assuming both SPM and SyR rotors have identical d-axis inductance, i.e., $L_{dpm} \approx L_{drm} \approx L_s$, will make the equations simplify further to identify the inductance behavior of the equivalent IPM machine. To combine both rotors on the shaft for an axially stacked hybrid rotor PMSM, a fractional length of each rotor must be used. Hence by defining the SPM rotor length factor as,

$$k_l = \frac{l_{pm}}{l_e} \tag{3.29}$$

the length factor of the SyR rotor becomes $(1-k_l)$. The voltage equations can be written as,

$$\begin{aligned} V_{qn} &= k_l V'_{qn_{pm}} + (1-k_l) V_{qn_{rm}} \\ V_{dn} &= k_l V'_{dn_{pm}} + (1-k_l) V_{dn_{rm}} \end{aligned} \tag{3.30}$$

Substituting (3.26) and (3.7) into (3.30) and simplifying,

$$\begin{aligned} V_{qn} &= -I_n \sin(\gamma)\omega_n \left[k_l L_{sn} + (1-k_l) L_{sn}\right] + k_l \omega_n \psi_{n_{pm}} \cos(\alpha) \\ V_{dn} &= -I_n \cos(\gamma)\omega_n \left[k_l L_{sn} + (1-k_l)\xi L_{sn}\right] - k_l \omega_n \psi_{n_{pm}} \sin(\alpha) \end{aligned} \tag{3.31}$$

Once again, applying the voltage limit constraint and rearranging,

$$\begin{aligned} &\left(I_{dn} + \frac{k_l \psi_{n_{pm}} \cos(\alpha)}{k_l L_{sn} + (1-k_L) L_{sn}} \right)^2 + \left(\frac{k_l L_{sn} + (1-k_l)\xi L_{sn}}{k_l L_{sn} + (1-k_l) L_{sn}} I_{qn} + \frac{k_l \psi_{n_{pm}} \sin(\alpha)}{k_l L_{sn} + (1-k_l) L_{sn}} \right)^2 \\ &\qquad \leq \left(\frac{V_{sn}}{\omega_n \left(k_l L_{sn} + (1-k_l) L_{sn}\right)} \right)^2 \end{aligned} \tag{3.32}$$

Comparing with the voltage equations of a conventional IPM from (3.10), the equivalent d and q axis inductances of the hybrid rotor PMSM can be written as,

$$\begin{aligned} L_{dnEq} &= k_l L_{sn} + (1-k_l) L_{sn} = L_{sn} \\ L_{qnEq} &= k_l L_{sn} + (1-k_l) \xi L_{sn} \end{aligned} \tag{3.33}$$

Equation (3.33) indicates that the inductances of the hybrid rotor PMSM are only dependent on the stack length ratio k_l, and are independent of the rotor offset angle in the chosen reference frame. Defining the equivalent saliency and equivalent PM flux linkage of the resulting hybrid rotor as,

$$\begin{aligned} \xi_{Eq} &= \frac{L_{qnEq}}{L_{dnEq}} = \frac{k_l L_{sn} + (1-k_l)\xi L_{sn}}{k_l L_{sn} + (1-k_l) L_{sn}} = k_l + (1-k_l)\xi \\ \psi_{nEq} &= k_l \psi_{n_{pm}} \end{aligned} \tag{3.34}$$

the voltage limit equation can be written by substituting equivalent inductance and saliency from (3.33) and (3.34) into (3.32),

$$\left(I_{dn} + \frac{\psi_{nEq}\cos(\alpha)}{L_{dnEq}} \right)^2 + \left(\xi_{Eq} I_{qn} + \frac{\psi_{nEq}\sin(\alpha)}{L_{dnEq}} \right)^2 \le \left(\frac{V_{sn}}{\omega_n L_{dnEq}} \right)^2 \tag{3.35}$$

Similar to conventional IPM constant voltage loci, (3.35) represents an ellipse with an ellipticity of ξ_{Eq} with the center of the ellipse as,

$$(h_{cV}, k_{cV}) = \left(-\frac{\psi_{nEq}\cos(\alpha)}{L_{dnEq}}, -\frac{\psi_{nEq}\sin(\alpha)}{\xi_{Eq} L_{dnEq}} \right) \tag{3.36}$$

From (3.36) it can be seen that the center of the voltage ellipse represents its own locus with respect to α. In polar coordinate form, (3.36) represents an elliptical trajectory with

respect to α for the voltage ellipse center. The minor axis and major axis lengths are dependent on L_{dEq} and L_{qEq} values. For $\alpha = 0$, the voltage limit locus becomes identical to a conventional IPM machine.

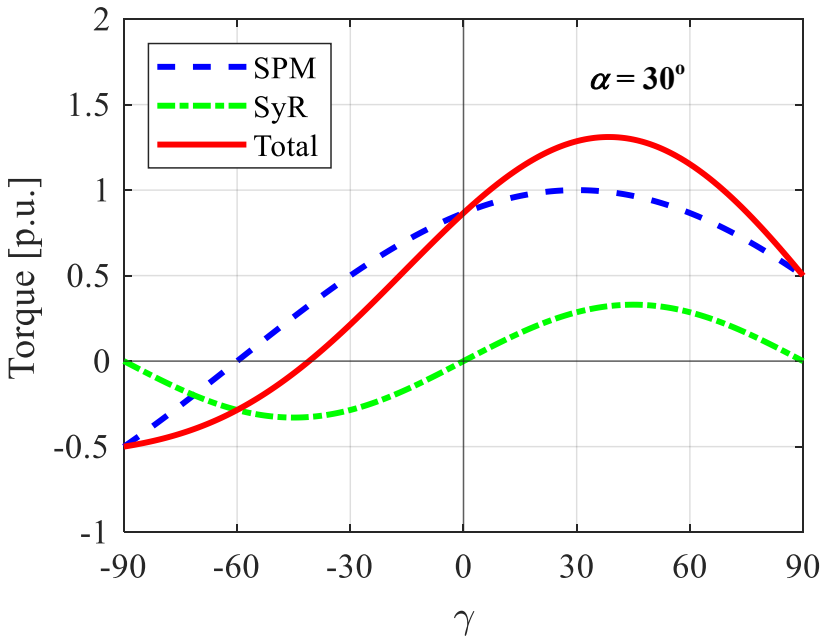

Figure 3-10. Net torque of a hybrid rotor PMSM with a PM rotor offset angle $\alpha = 30^{o}$

The toque of the hybrid rotor IPM can be calculated as,

$$\tau_{nEq} = \frac{V_{qn} I_{qn} + V_{dn} I_{dn}}{\omega_n} \tag{3.37}$$

Substituting voltage and current equations from (3.31) , (3.22) and simplifying,

$$\begin{aligned}\tau_{nEq} &= k_l \psi_{n_{PM}} I_n \cos(\gamma-\alpha) + \frac{1}{2}\begin{pmatrix}\{k_l L_{sn} + (1-k_l)\xi L_{sn}\} \\ -\{k_l L_{sn} + (1-k_l) L_{sn}\}\end{pmatrix} I_n^2 \sin(2\gamma) \\ &= \psi_{nEq} I_n \cos(\gamma-\alpha) + \frac{1}{2} L_{dnEq}(\xi_{Eq}-1) I_n^2 \sin(2\gamma)\end{aligned} \tag{3.38}$$

This torque equation can be compared to the conventional IPM torque from (3.13) and inferred that the PM torque component is simply shifted by α. Separated torque components are plotted as a function of γ and shown in Figure 3-10.

To obtain the constant torque locus, the torque equation is expanded and written in terms of *dq* currents as,

$$\tau_{nEq} = \psi_{nEq}\left[I_{qn}\cos(\alpha) - I_{dn}\sin(\alpha)\right] - L_{dnEq}(\xi_{Eq}-1) I_{dn} I_{qn} \tag{3.39}$$

Rearranging terms, the constant torque locus can be written as,

$$I_{dn} I_{qn} = I_{qn}\frac{\psi_{nEq}\cos(\alpha)}{L_{dnEq}(\xi_{Eq}-1)} - I_{dn}\frac{\psi_{nEq}\sin(\alpha)}{L_{dnEq}(\xi_{Eq}-1)} - \frac{\tau_{nEq}}{L_{dnEq}(\xi_{Eq}-1)} \tag{3.40}$$

The voltage limit locus and constant torque locus, along with the current limit circle for rated operation with an arbitrary rotor offset angle, are shown in Figure 3-11(a). The centers of the torque and voltage loci are also plotted as a function of α and shown in Figure 3-11(b) along with the direction of rotation of the centers.

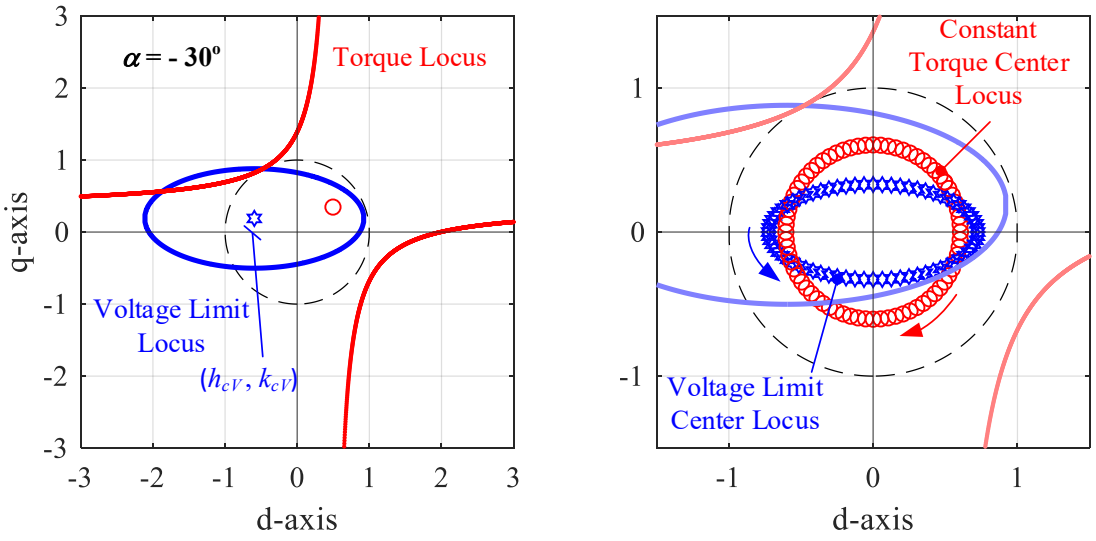

(a) (b)

Figure 3-11. Hybrid rotor PMSM circle diagram (a) Constant voltage and torque locus (b) Loci of centers of constant voltage and torque loci with changing α

3.2.1. Maximum Torque per Amp Operation

Similar to conventional IPM, determining the MTPA value of the current angle γ requires differentiation of torque equation with respect to γ and equating it to zero,

$$\frac{d\tau_{nEq}}{d\gamma} = -\psi_{nEq} I_n \sin(\gamma-\alpha) + L_{dnEq}\left(\xi_{Eq}-1\right) I_n^2 \cos(2\gamma) = 0 \qquad (3.41)$$

However, unlike conventional IPM, since there is an additional offset angle term in the PM torque component, the MTPA cannot be solved as a quadratic equation. Expanding (3.41) and rearranging terms,

$$\begin{aligned}\left(-\psi_{Eq} I_n \sin(\gamma)\cos(\alpha) - L_{dEq}\left(\xi_{Eq}-1\right) I_n^2 \sin^2(\gamma)\right) + \\ \left(\psi_{Eq} I_n \cos(\gamma)\sin(\alpha) + L_{dEq}\left(\xi_{Eq}-1\right) I_n^2 \cos^2(\gamma)\right)\end{aligned} = 0 \qquad (3.42)$$

Using the definition of I_{qn} and I_{dn}, and rearranging terms, we can rewrite (3.42) as,

$$\left(I_{qn}^2 + 2I_{qn}\sigma_n \frac{\psi_{nEq}\sin(\alpha)}{L_{dnEq}} \right) - \left(I_{dn}^2 - 2I_{dn}\sigma_n \frac{\psi_{nEq}\cos(\alpha)}{L_{dnEq}} \right) = 0 \tag{3.43}$$

where,

$$2\sigma_n = \frac{1}{(\xi_{Eq} - 1)} \tag{3.44}$$

Adding and subtracting $\sigma_n^2 \frac{\psi_{nEq}^2 \sin^2(\alpha)}{L_{dnEq}^2}$ and $\sigma_n^2 \frac{\psi_{nEq}^2 \cos^2(\alpha)}{L_{dnEq}^2}$ to the two halves of (3.43) respectively and simplifying,

$$\begin{aligned} &\left(I_{qn} + \sigma_n \frac{\psi_{nEq}\sin(\alpha)}{L_{dnEq}} \right)^2 - \sigma_n^2 \frac{\psi_{nEq}^2 \sin^2(\alpha)}{L_{dnEq}^2} \\ &- \left(I_{dn} - \sigma_n \frac{\psi_{nEq}\cos(\alpha)}{L_{dnEq}} \right)^2 + \sigma_n^2 \frac{\psi_{nEq}^2 \cos^2(\alpha)}{L_{dnEq}^2} \end{aligned} = 0 \tag{3.45}$$

Rearranging the terms, a generalized slope of the torque hyperbola, i.e., MTPA trajectory can be expressed as,

$$\frac{\left(I_{qn} + \sigma_n \frac{\psi_{nEq}\sin(\alpha)}{L_{dnEq}} \right)^2}{\sigma_n^2 \frac{\psi_{nEq}^2}{L_{dnEq}^2}\left(\sin^2(\alpha) - \cos^2(\alpha)\right)} - \frac{\left(I_{dn} - \sigma_n \frac{\psi_{nEq}\cos(\alpha)}{L_{dnEq}} \right)^2}{\sigma_n^2 \frac{\psi_{nEq}^2}{L_{dnEq}^2}\left(\sin^2(\alpha) - \cos^2(\alpha)\right)} = 1 \tag{3.46}$$

Equation (3.46) represents a standard form of a rectangular hyperbola with its center (h_{cMTPA}, k_{cMTPA}) corresponding to the MTPA trajectory center located at,

$$\left(h_{cMTPA}, k_{cMTPA}\right) = \left(\sigma_n \frac{\psi_{nEq}\cos(\alpha)}{L_{dnEq}}, -\sigma_n \frac{\psi_{nEq}\sin(\alpha)}{L_{dnEq}} \right) \tag{3.47}$$

The MTPA trajectory and corresponding center are shown in Figure 3-12(a). It is to be noted that the denominator in (3.46), which represents the length of the semi-major and semi-minor axis, varies between $\pm\sigma_n^2\psi_{nEq}^2 / L_{dnEq}^2$ depending on the value of α. Although a negative or complex axis length does not make sense, this simply means that the symmetricity of the hyperbola changes from *d* axis to *q* axis when the sign becomes negative, as shown in Figure 3-12(b). In addition, the center of the hyperbola has its own locus that is dependent on α and represents a circular trajectory with a radius of $\sigma_n \psi_{nEq}/L_{dnEq}$.

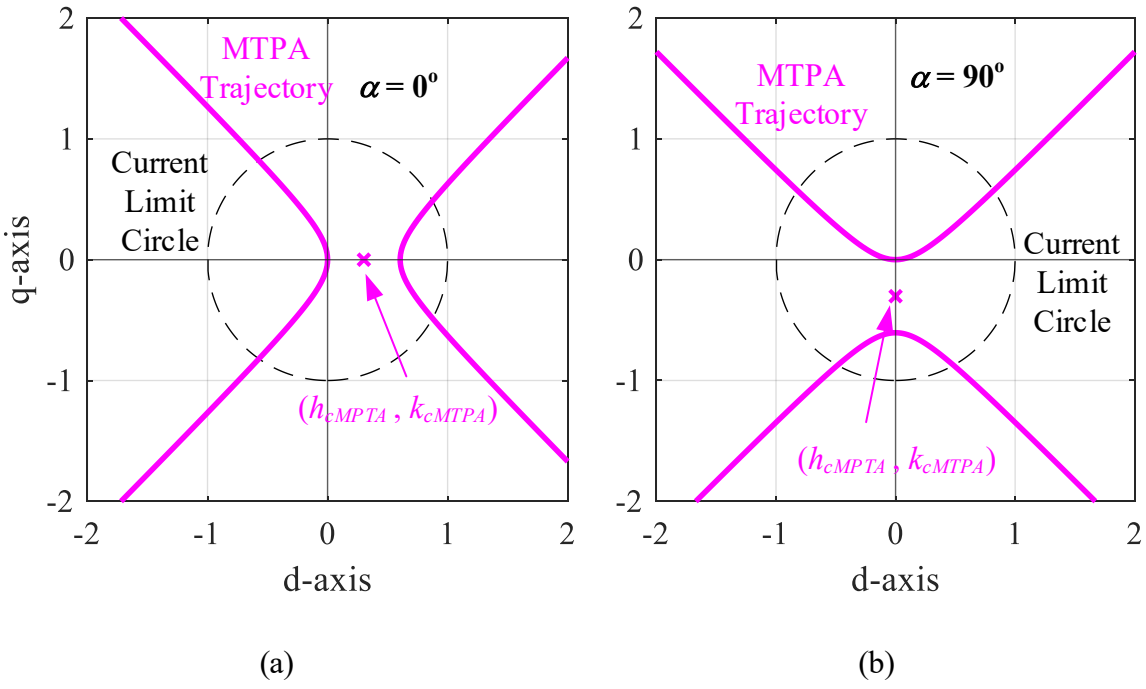

Figure 3-12. Theoretical MTPA trajectories with different rotor offset angles

In order to determine the MTPA current angle for rated operation, the current limit circle can be used as the boundary condition. The intersecting points of (3.46) with the current limit circle will give the MTPA current angle for the rated operation. Depending on the value of σ_n and α, the center of the hyperbola and the axis length will change. This results in either both or only one branch intersecting with the current limit circle. However, only one branch of the hyperbola passes through origin independent of the value of σ_n and α. Since an MTPA value must exist for every current amplitude, the branch of the hyperbola passing through origin will be a feasible MTPA trajectory. Substitution back into the torque equation is necessary to identify the correct MTPA angle for motoring mode.

3.2.2. Maximum Torque per Amp and Volt Operation

The intersection of MTPA trajectory and the current limit circle represents the beginning of Mode 2 operation, i.e., field weakening mode. During mode 2 operation, torque is bound by both voltage limit and current limit, hence the name MTPAV. As speed increases, the voltage limit ellipse shrinks, and the intersection point of the voltage ellipse with the current limit circle will be the operating point. The operating speed during MTPAV can be obtained as,

$$\omega_n = \frac{1}{\sqrt{\left(I_{dn}L_{dn} + \psi_{nEq}\cos(\alpha)\right)^2 + \left(I_{qn}\xi_{Eq}L_{dnEq} + \psi_{nEq}\sin(\alpha)\right)^2}} \tag{3.48}$$

3.2.3. Maximum Torque per Volt Operation

Identifying MTPV trajectory can follow a similar process as the conventional IPM, i.e., substituting (3.35) into (3.39) and differentiating with respect to γ. However, due to the additional degree of freedom introduced by α, using such a process will yield extremely

complicated equations and do not aid in interpreting the behavior of MTPV trajectory. This is one of the primary reasons researchers in the past resorted to numerical optimization to determine the MTPV operating points.

Alternatively, since torque in MTPV region is only dependent on the voltage limit, transforming the torque equation from current *dq* (*I-dq*) plane into corresponding voltage *dq* (*V-dq*) plane reduces some of the complexity. In order to transform the torque to *V-dq* plane, the *d* and *q* axis currents must be expressed as functions of voltages. Using the voltage equations from (3.31), we can write,

$$\begin{aligned} I_{qn} &= -\frac{V_{dn}}{\omega_n L_{qnEq}} - \frac{\psi_{nEq}\sin(\alpha)}{L_{qnEq}} \\ I_{dn} &= \frac{V_{qn}}{\omega_n L_{dnEq}} - \frac{\psi_{nEq}\cos(\alpha)}{L_{dnEq}} \end{aligned} \tag{3.49}$$

Substituting into (3.37), the torque expression becomes,

$$\tau_{nEq} = \frac{V_{dn}V_{qn}}{\omega_n^2}\left(\frac{1}{L_{dnEq}} - \frac{1}{L_{qnEq}}\right) - \frac{1}{\omega_n}\left(V_{dn}\frac{\psi_{nEq}\cos(\alpha)}{L_{dnEq}} - V_{qn}\frac{\psi_{nEq}\sin(\alpha)}{L_{qnEq}}\right) \tag{3.50}$$

Defining the voltage angle with respect to *q*-axis as δ, the *dq* voltages can be defined as,

$$V_{qn} = V_n\cos(\delta) \quad \text{and} \quad V_{dn} = -V_n\sin(\delta) \tag{3.51}$$

Equation (3.51) also indicates that the voltage limit locus is a circle with a constant radius in *V-dq* plane. Substituting (3.51) into (3.50) and simplifying, the torque equation is written as,

$$\tau_{nEq} = \frac{V_n^2}{\omega_n^2}\left(\frac{L_{dnEq}-L_{qnEq}}{L_{dnEq}L_{qnEq}}\right)\frac{\sin(2\delta)}{2} + \frac{V_n\psi_{nEq}}{\omega_n}\left(\sin(\delta)\frac{\cos(\alpha)}{L_{dnEq}}-\cos(\delta)\frac{\sin(\alpha)}{L_{qnEq}}\right) \tag{3.52}$$

On the *V-dq* plane, the maximum torque per voltage trajectory can be obtained by differentiating (3.52) with respect to δ and equating to zero, which gives,

$$\frac{d\tau_{nEq}}{d\delta} = \frac{V_n^2}{\omega_n^2}\left(\frac{L_{dnEq}-L_{qnEq}}{L_{dnEq}L_{qnEq}}\right)\cos(2\delta) + \frac{V_n\psi_{nEq}}{\omega_n}\left(\cos(\delta)\frac{\cos(\alpha)}{L_{dnEq}}+\sin(\delta)\frac{\sin(\alpha)}{L_{qnEq}}\right) = 0 \tag{3.53}$$

Expanding (3.53) and rearranging terms,

$$\left(\frac{V_n^2\cos^2(\delta)}{\omega_n^2}\left(\frac{L_{dnEq}-L_{qnEq}}{L_{dnEq}L_{qnEq}}\right)+\frac{V_n\cos(\delta)}{\omega_n}\frac{\psi_{nEq}\cos(\alpha)}{L_{dnEq}}\right) + \left(\frac{V_n^2\sin^2(\delta)}{\omega_n^2}\left(\frac{L_{dnEq}-L_{qnEq}}{L_{dnEq}L_{qnEq}}\right)+\frac{V_n\sin(\delta)}{\omega_n}\frac{\psi_{nEq}\sin(\alpha)}{L_{qnEq}}\right) = 0 \tag{3.54}$$

using (3.34) and substituting (3.51) into (3.54),

$$\left(\frac{V_{qn}^2}{\omega_n^2}+2\frac{V_{qn}}{\omega_n}\zeta_n\frac{\psi_{nEq}\cos(\alpha)}{L_{dnEq}}\right)-\left(\frac{V_{dn}^2}{\omega_n^2}+2\frac{V_{dn}}{\omega_n}\zeta_n\frac{\psi_{nEq}\sin(\alpha)}{\xi_{Eq}L_{dnEq}}\right) = 0 \tag{3.55}$$

where,

$$2\zeta_n = \frac{L_{dnEq}L_{qnEq}}{\left(L_{dnEq}-L_{qnEq}\right)} = \frac{L_{dnEq}\xi_{Eq}}{\left(1-\xi_{Eq}\right)} \tag{3.56}$$

Adding and subtracting necessary terms on the two halves and simplifying,

$$\left(\frac{V_{qn}}{\omega_n}+\zeta_n\frac{\psi_{nEq}\cos(\alpha)}{L_{dnEq}}\right)^2-\zeta_n^2\left(\frac{\psi_{nEq}\cos(\alpha)}{L_{dnEq}}\right)^2 -\left(\frac{V_{dn}}{\omega_n}+\zeta_n\frac{\psi_{nEq}\sin(\alpha)}{\xi_{Eq}L_{dnEq}}\right)^2+\zeta_n^2\left(\frac{\psi_{nEq}\sin(\alpha)}{\xi_{Eq}L_{dnEq}}\right)^2=0 \tag{3.57}$$

Rearranging terms, a generalized MTPV trajectory in *V-dq* plane can be written as,

$$\left(\frac{V_{qn}}{\omega_n}+\zeta_n\frac{\psi_{nEq}\cos(\alpha)}{L_{dnEq}}\right)^2-\left(\frac{V_{dn}}{\omega_n}+\zeta_n\frac{\psi_{nEq}\sin(\alpha)}{\xi_{Eq}L_{dnEq}}\right)^2=\zeta_n^2\chi_n^2 \tag{3.58}$$

where,

$$\chi_n^2=\frac{\psi_{nEq}^2}{L_{dnEq}^2}\left(\cos^2(\alpha)-\frac{\sin^2(\alpha)}{\xi_{Eq}^2}\right) \tag{3.59}$$

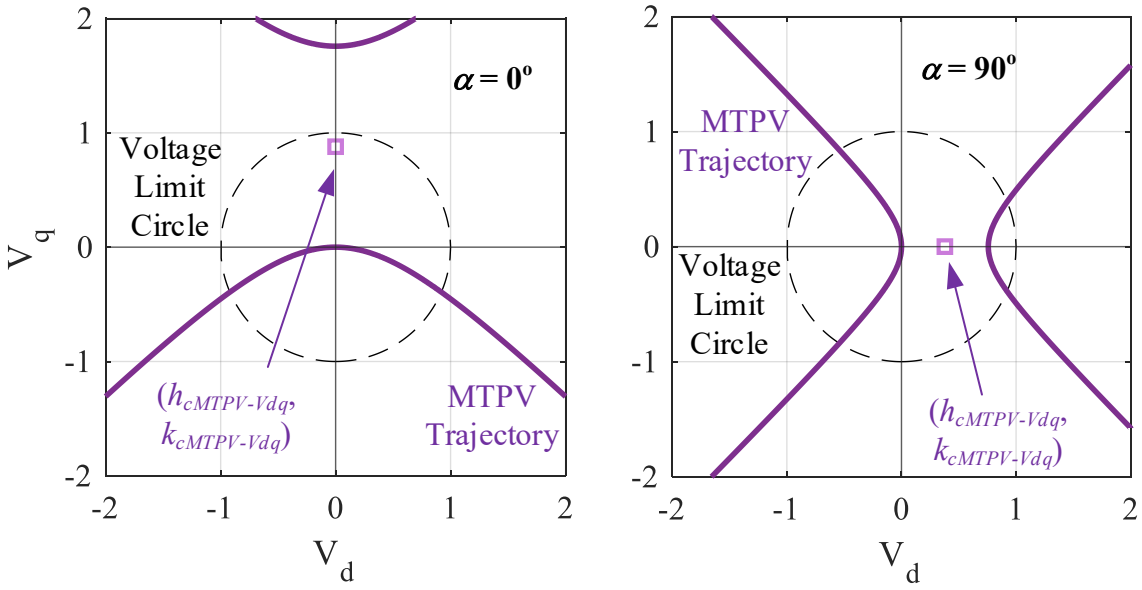

(a) (b)

Figure 3-13. Theoretical MTPV trajectories in *V-dq* plane with different rotor offset angles

This equation represents a rectangular hyperbola for MTPV trajectory in *V-dq* plane, as shown in Figure 3-13(a). The center of MTPV trajectory is,

$$\left(h_{cMTPV-Vdq}, k_{cMTPV-Vdq}\right) = \left(-\omega_n \zeta_n \frac{\psi_{nEq}\sin(\alpha)}{\xi_{Eq} L_{dnEq}}, -\omega_n \zeta_n \frac{\psi_{nEq}\cos(\alpha)}{L_{dnEq}}\right) \tag{3.60}$$

which has its own locus with respect to α and can be identified as an ellipse in polar form. The axis length in (3.58), similar to MTPA trajectory, can be either positive or negative, indicating the symmetricity of MTPV switches between *d* and *q* axis depending on α as shown in Figure 3-13(b).

The intersection of MTPV trajectory with the constant voltage limit circle should give the voltage vector angle at the onset of mode 3 operation. It can be seen from (3.58) that the trajectory is dependent on speed (ω_n). This poses a challenge since the ω_n for mode 3 onset is still an unknown. In order to solve this, one more constraint is required, which in this case is the constant current locus since at the onset of mode 3, the current is still at its rated value. Plotting the current locus from (3.49) on *V-dq* plane and looking for a common intersection point will give the onset of mode 3. However, the current locus is also dependent on ω_n in *V-dq* plane and does not give enough boundary conditions to determine the operating speed.

This can be solved by transforming the MTPV trajectory back into conventional *I-dq* plane. Using (3.31) the voltage equations can be expressed as,

$$\begin{aligned} \frac{V_{dn}}{\omega_n} &= -I_{qn}\xi_{Eq}L_{dnEq} - \psi_{nEq}\sin(\alpha) \\ \frac{V_{qn}}{\omega_n} &= I_{dn}L_{dnEq} + \psi_{nEq}\cos(\alpha) \end{aligned} \tag{3.61}$$

Substituting into (3.57) and simplifying,

$$\left(I_{dn}+\frac{\psi_{nEq}\cos(\alpha)}{L_{dnEq}}\left\{1+\frac{\zeta_n}{L_{dnEq}}\right\}\right)^2 - \left(\xi_{Eq}I_{qn}+\frac{\psi_{nEq}\sin(\alpha)}{L_{dnEq}}\left\{1-\frac{\zeta_n}{\xi_{Eq}L_{dnEq}}\right\}\right)^2 = \frac{\zeta_n^2\chi_n^2}{L_{dnEq}^2} \quad (3.62)$$

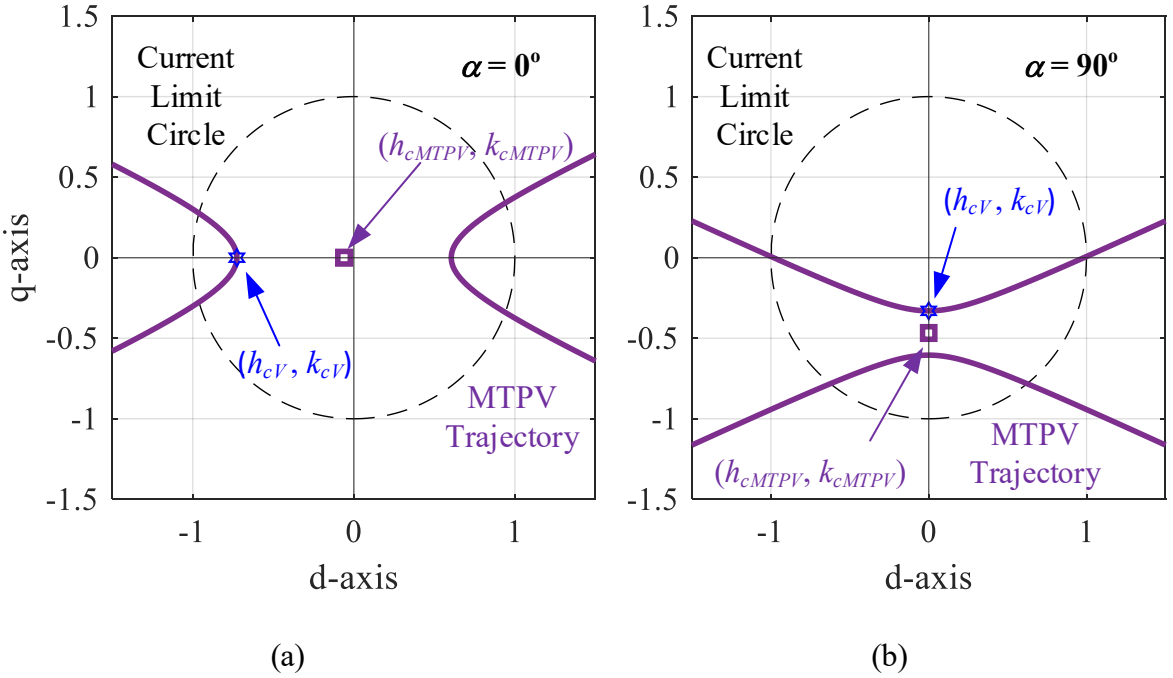

(a) (b)

Figure 3-14. Theoretical MTPV trajectories in *I-dq* plane with different rotor offset angles

It is evident from (3.62) that the MTPV in *I-dq* plane is independent of rotor speed. MTPV in *I-dq* plane represents a standard form of a hyperbola, as opposed to rectangular hyperbola for MPTV in *V-dq* plane. The center of MTPV in *I-dq* plane is,

$$\left(h_{cMPTV},k_{cMTPV}\right)=\left(-\frac{\psi_{nEq}\cos(\alpha)}{L_{dnEq}}\left\{1+\frac{\zeta_n}{L_{dnEq}}\right\},\frac{\psi_{nEq}\sin(\alpha)}{\xi_{Eq}L_{dnEq}}\left\{1-\frac{\zeta_n}{\xi_{Eq}L_{dnEq}}\right\}\right) \quad (3.63)$$

As with the MTPA trajectory, the major and minor axis lengths of MTPV also can be either positive or negative, making the hyperbola symmetric on either d or q axis respectively, as shown in Figure 3-14(a), and Figure 3-14(b). As speed increases, we know that the voltage limit ellipse shrinks to its center. Hence the MTPV trajectory must always pass through the center of the constant voltage limit ellipse shown in (3.36). The voltage limit ellipse center is also shown in Figure 3-14, and it can be seen that only one branch of the MTPV trajectory passes through (h_{cV}, k_{cV}), which yields the feasible MTPV trajectory.

3.3. Hybrid Rotor Operating Characteristics

With the feasible MTPA and MTPV trajectories determined, the current command trajectory and the operating speed can be specified for maximum torque operation throughout the machine's operation speed. The current command trajectory and the three modes of operation of a hypothetical hybrid rotor PMSM with an arbitrary offset angle are shown in Figure 3-15. The corresponding torque and power characteristics for maximum power operation with the three modes of operation highlighted are shown in Figure 3-16.

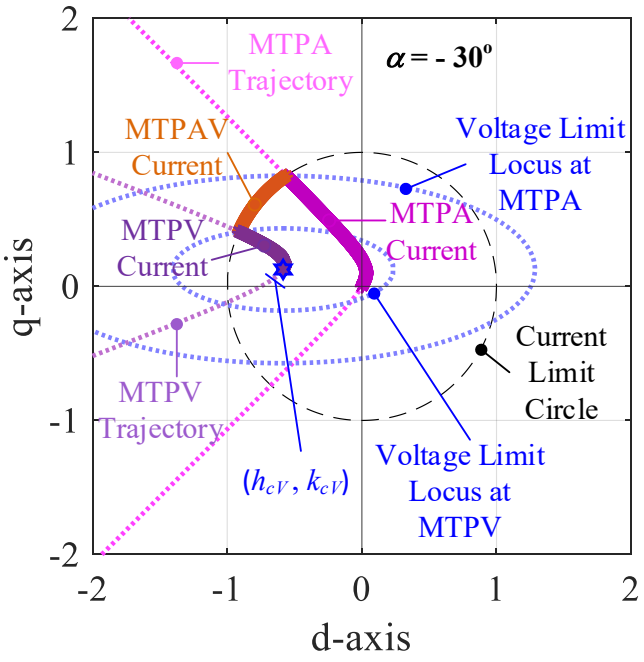

Figure 3-15. Current command trajectory for maximum torque operation of a hypothetical hybrid rotor PMSM with arbitrary offset angle, $\alpha = -30^{o}$

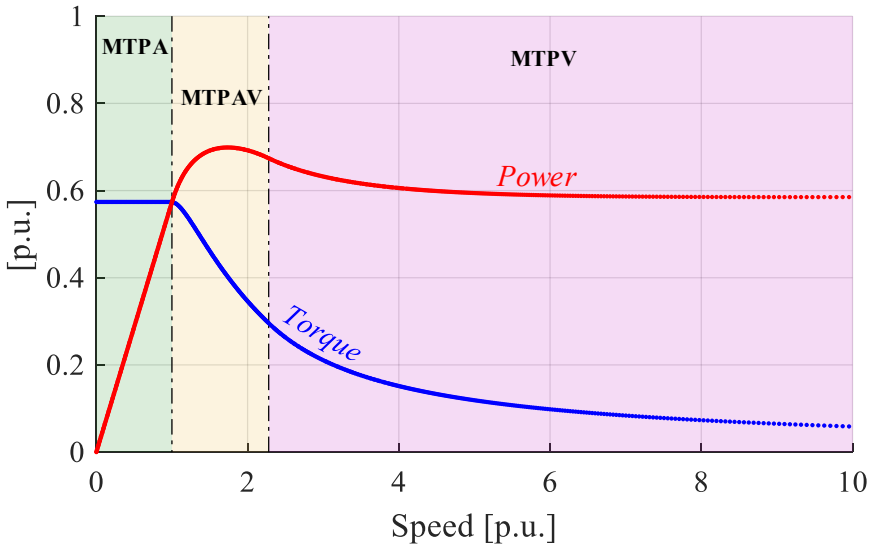

Figure 3-16. Torque and power vs. speed characteristics for maximum power operation of a hypothetical hybrid rotor PMSM with arbitrary offset angle, $\alpha = -30^{o}$

Similar to a conventional PMSM, MTPV operation is only possible when the center of the voltage limit locus lies inside the current limit circle. For a conventional PMSM, this limit is determined by the ratio of normalized PM flux linkage and *d*-axis inductance, also identified as the characteristic current. However, by introducing the offset angle as an additional degree of freedom in the hybrid rotor PMSM, it is shown that the center of voltage limits locus moves in the *I-dq* plane (see Figure 3-11) in an elliptical orbit as a function of α. Hence for a hybrid rotor PMSM, the characteristic current can be represented as two components in *d*- and *q*-axis and can be configured to obtain infinite speed as long as the ratio of normalized flux linkage and *q*-axis inductance lies within the current limit circle. The current command trajectories, as well as the corresponding torque and power characteristics for a hypothetical hybrid rotor PMSM whose *d*-axis characteristic current is higher than current limit, but *q*-axis characteristic current lies within the current limit circle are shown in Figure 3-17 and Figure 3-18.

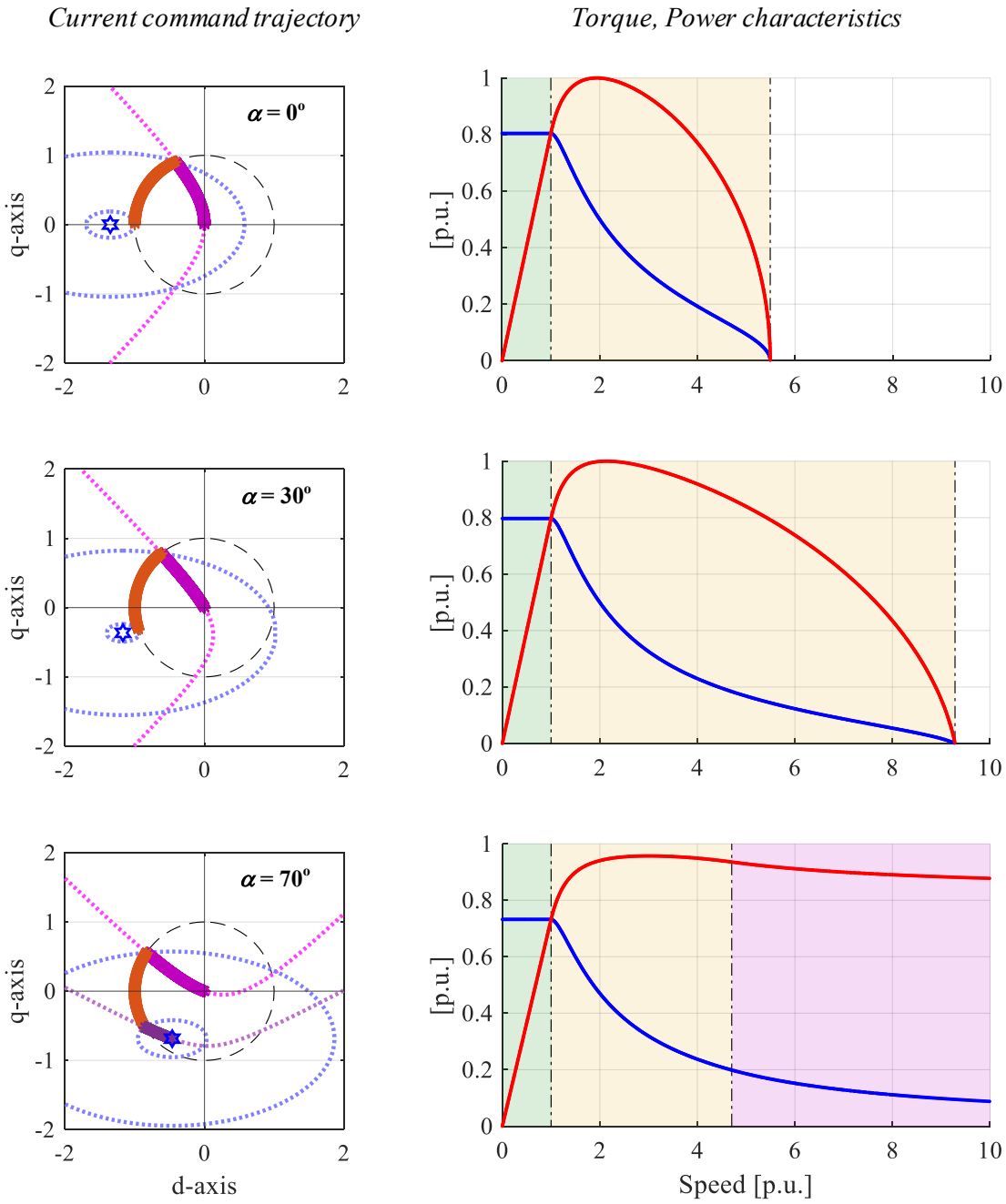

Figure 3-17. Max. torque and max. power characteristics of hybrid rotor PMSM with $\alpha = [0, 30, 70]^{o}$

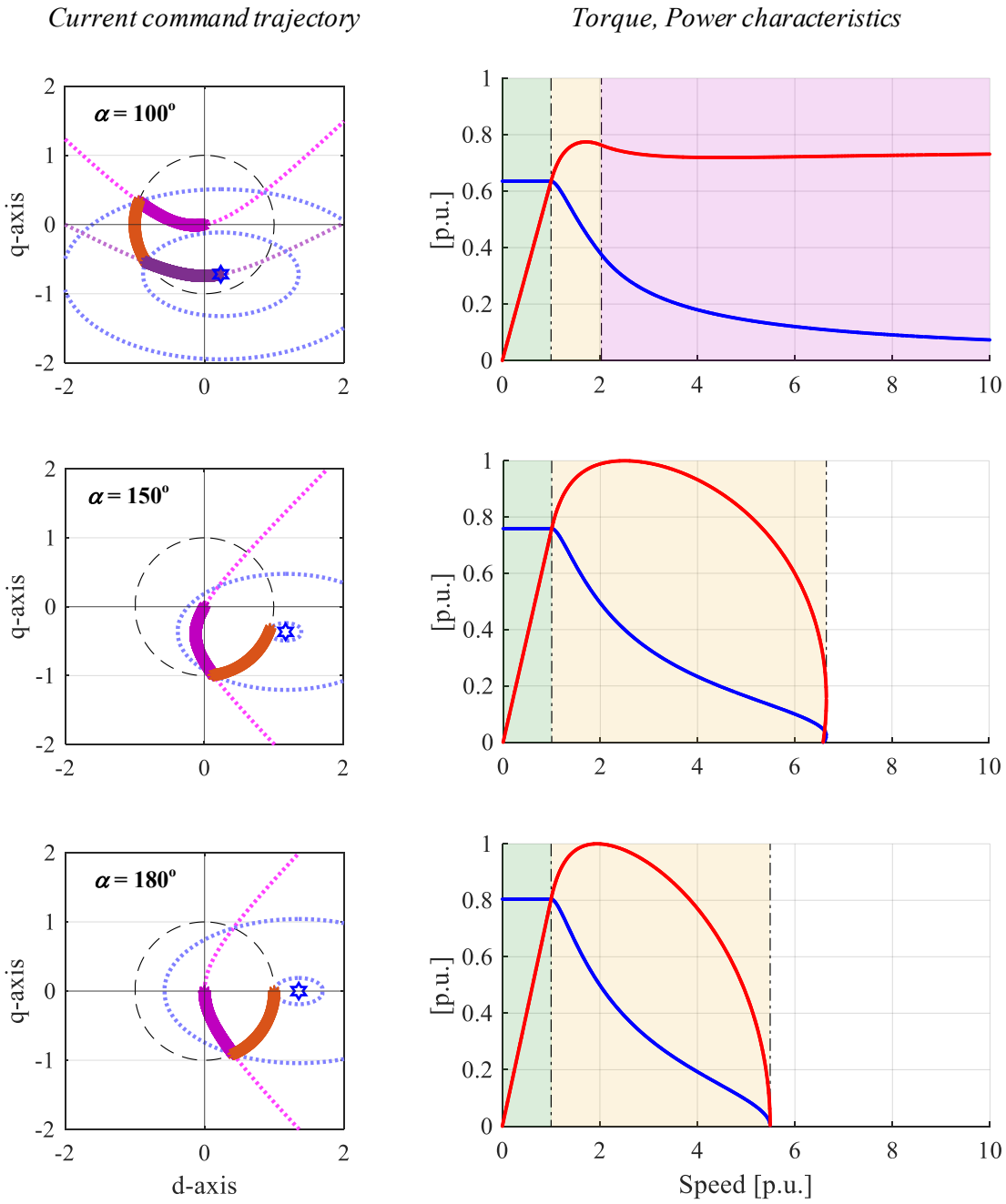

Figure 3-18. Max. torque and max. power characteristics of hybrid rotor PMSM with $\alpha = [100, 150, 180]$ °

It can be seen that there is no feasible MTPV trajectory when the center of voltage ellipse, i.e., characteristic current vector, is outside the current limit circle, and consequently, the speed is limited. When the characteristic current vector amplitude is more dependent on the *q*-axis component (*q*-axis inductance), there is a feasible MTPV trajectory found, and the torque, power characteristics indicate that the machine can theoretically reach infinite speed.

Few noteworthy observations from Figure 3-17 and Figure 3-18, the HRPMSM machine's motoring mode is not limited to only 2 quadrants. Depending on α, the motoring mode shifts through all the quadrants of *I-dq* plane. It is also evident that the machine's performance characteristics are identical at $\alpha = 0^o$ and $\alpha = 180^o$. This is expected since the reluctance torque component is a second-order component with respect to the current angle. Therefore, the performance characteristics observed for rotor offset angles between $\alpha = 0^o$ to 180^o will repeat for $\alpha = -180^o$ to 0^o.

3.4. Infinite CPSR Hybrid Rotor PMSM

It is evident from the current command trajectories and the power-speed curve that if the characteristic current, which is defined by the center of the voltage limit ellipse, is higher than rated value, then the machine has a speed limit where it cannot sustain the voltage limit. However, if the characteristic current is lower than rated current, the machine can have theoretical infinite speed, but the power produced in MPTV operation will be lower due to the reduced current vector amplitude. Hence an ideal machine will have characteristic current equal to rated current and will produce infinite CPSR with maximum possible power, i.e., MTPAV (mode 2) terminates on the center of the voltage limit ellipse.

Using (3.36), the condition for a hybrid rotor PMSM to achieve a theoretical infinite CPSR can be written as,

$$\frac{\psi_{nEq}^2}{\xi_{Eq}^2 L_{dnEq}^2}\sin^2(\alpha)+\frac{\psi_{nEq}^2}{L_{dnEq}^2}\cos^2(\alpha)=1 \tag{3.64}$$

Using (3.64), the optimum α that produces and infinite CPSR can be calculated as,

$$\sin^2(\alpha)=\frac{\frac{\xi_{Eq}^2 L_{dnEq}^2}{\psi_{nEq}^2}-\xi_{Eq}^2}{1-\xi_{Eq}^2} \tag{3.65}$$

Equation (3.65) also establishes another boundary condition. The expression on the right-hand side must be within the bounds of 0 to 1. Another way to interpret this is that the locus of the voltage center ellipse shown in Figure 3-11(b) must have an intersecting point with the current limit circle. Hence, the optimum α and the bounds for the machine parameters to produce a theoretical infinite CPSR can be written using the major and minor axis lengths of the voltage limit center locus as,

$$\alpha=\sin^{-1}\left(\frac{\xi_{Eq}}{\psi_{nEq}}\sqrt{\frac{L_{dnEq}^2-\psi_{nEq}^2}{1-\xi_{Eq}^2}}\right)\ \forall\ \left\{\frac{\psi_{nEq}}{L_{dnEq}}\geq 1\quad \&\quad \frac{\psi_{nEq}}{\xi_{Eq}L_{dnEq}}\leq 1\right\} \tag{3.66}$$

Substituting the equivalent parameter equations from (3.34) into bounds described in (3.66), a design space for hybrid rotor PMSM rotor section stack length to obtain infinite CPSR can be established based on individual SPM and SyR machine parameters as,

$$\frac{L_{sn}}{\psi_{n_{pm}}}\leq k_l\leq\frac{\xi L_{sn}}{\psi_{n_{pm}}+L_{sn}(\xi-1)} \tag{3.67}$$

Since k_I value is bound to be between 0 and 1, it can also be established that the PM rotor must have characteristic current at least greater than 1 p.u. in order to be used for a hybrid rotor PMSM that can sustain infinite CPSR. The optimum α for each k_I can be calculated by substituting the k_I value between the bounds set by (3.67) into (3.66).

3.5. Unified Field Weakening Model

The hybrid rotor PMSM is essentially made up of the fundamental building blocks of IPM machine. With a similar d-axis inductance and the ability to independently design the PM flux linkage, saliency and the rotor offset angle makes the hybrid rotor PMSM model virtually represent any synchronous PMSMs with minor changes to the way hybridization parameters are considered, i.e., k_I and α. To generalize the analytical model, the reluctance rotor stack length ratio must be assigned separately and can be defined as,

$$k_r = \frac{l_r}{l_e} \tag{3.68}$$

where l_r is the stack length of the SyR rotor. The list of machine types and corresponding hybridization parameters are listed in Table 3-1. It is to be noted that since radial hybrid rotor PMSM is a dual rotor configuration, both PM and reluctance occupy the full stack length on either side stator inner and outer diameter and can be modeled as two separate full stack length machines provided there is no magnetic interaction between the two rotors [30].

Table 3-1. Unified field weakening model parameters and equivalent machines

k_l	k_r	α [deg]	Machine Type
1	1	[0, 180] [1]	Radial Hybrid Rotor PMSM
1	0	0	SPMM
0	1	N/A [2]	SyRM
(0, 1)	(1-k_l)	0	IPMM
(0, 1)	(1-k_l)	± 90	FIPMM
[-1, 1]	1	± 90	VFPMM / WFSM

[1] → characteristics repeat from 180° to 360°
[2] → α is eliminated from model with $k_l = 0$

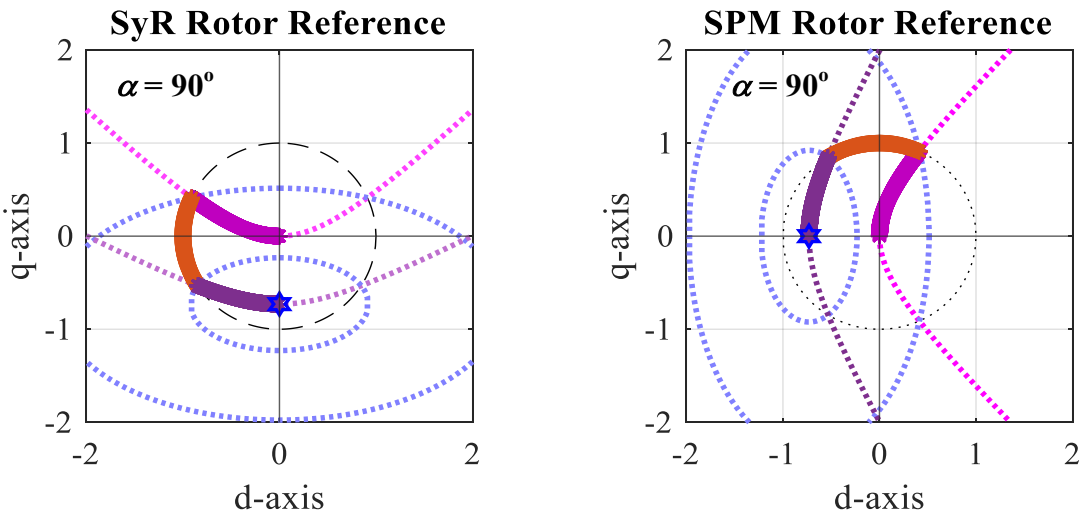

Figure 3-19. FIPMM current command trajectories in (a) SyR rotor reference frame (b) SPM rotor reference frame.

The equations can also be transformed back into the PM rotor reference frame to interpret the current command trajectories and implement current vector control in a conventional manner. For example, the current command trajectory for a FIPMM in both the

SyR rotor reference frame and SPM rotor reference frame is shown in Figure 3-19(a) and Figure 3-19(b), respectively. Based on the MTPA current angle with respect to the SPM rotor reference frame, it can be deduced that, in fact, using the hybrid rotor PMSM, a FIPMM design can be obtained with α ranging from 45^o to 135^o.

3.6. Summary

With the goal of developing a field weakening model for a hybrid rotor PMSM, the vector diagram and field weakening models for SPM, SyR, and IPM machines are revisited at the beginning of this chapter. A transformation of SPM rotor vectors to the SyR reference frame is then developed, and the combined hybrid rotor machine parameters are identified in terms of individual SPM and SyR machine parameters. Using the hybrid rotor machine model, an analytical model to predict the MTPA and MTPV current command trajectories is developed, and a method to identify the feasible trajectories of field weakening operation is proposed. Consequently, an analytical model that accounts for additional degrees of freedom offered by the hybrid rotor PMSM machine design is developed.

It is shown that the proposed model can be used to predict the field weakening operation scheme and the performance characterization of hybrid rotor PMSM with any rotor offset angle and stack length ratio. A methodology to calculate optimum hybrid rotor parameters to achieve theoretical infinite CPSR is developed based on individual SPM and SyR rotor parameters. Finally, it is shown that the proposed unified machine model can be used to model the field weakening characteristics of different types of synchronous AC machines, thus unifying the field weakening theory for synchronous AC machines.

Chapter 4

4. Design Selection and Sizing for Hybrid Rotor PMSM

Since the hybrid rotor PMSM uses a single stator, the stator must be designed to perform optimally for both SPM and SyR rotors. The power, speed, and dimension of the machine are some of the metrics that are often dictated by the application at a system level. The nature of the winding configuration and the choice of the number of phases, stator slots, and rotor poles comes down to the designer but must adhere to more delicate details of the desired application requirements such as fault tolerance, torque, and current ripple limits as well as efficiency. In this chapter, factors for selection of slot-pole combination, aspect ratio are discussed, and appropriate design criteria selection for a hybrid rotor PMSM summarized. The sizing equations for a hybrid rotor PMSM are developed, and the power capability based on the rotor parameters is presented. A scalability analysis based on the sizing equations is developed for maintaining the filed weakening performance.

4.1. Slot – Pole Combinations for PMSM

Depending on the number of phases being used, only certain combinations of slot-pole (S-P) will be feasible. For a typical 3-phase machine, the number of slots must always be a multiple of 3. The nature of an optimum winding configuration for a motor is typically associated with the slot-pole combination using the slot per pole per phase (SPP) number. SPP can be calculated as,

$$SPP = \frac{Q_s}{mp} = \frac{z}{b} \tag{4.1}$$

where, Q_s is the number of stator slots, P is the number of rotor poles, and m is the number of phases of the machine. The SPP can be simplified into a fraction form (z/b) where z, b are natural numbers. If b is equal to 1, then there are an integral number of slots per pole per phase, and SPP is an integer. However, if b is an integer greater than 1, then the rotor pole arc span is different from the stator pole arc leading to fractional slot configurations. With b as an integer greater than 1, if $z < b$, then it is typically a fractional slot concentrated winding (FSCW), and if z > b, then a fractional slot distributed winding (FSDW) both with non-integral SPP.

The choice of the winding, either fractional slot distributed winding (FSDW), or fractional-slot concentrated winding (FSCW), depends on the SPP value and the corresponding maximum achievable winding factor value. The amplitude of the fundamental winding factor (k_{w1}) is one of the important factors to denote the amount of useful stator magneto motive force (MMF). The maximum possible k_{w1} values for various S-P combinations with double-layer windings can be calculated as,

$$k_{w1} = \sin\left(\frac{\pi p C_p}{2Q_s}\right)\frac{1}{2K_f \sin\left(\frac{\pi}{6K_f}\right)} \tag{4.2}$$

where,

$$C_p = \begin{Bmatrix} 1 & \forall \text{ CW} \\ round\left(\frac{Q_s}{P}\right) & \forall \text{ DW} \end{Bmatrix} \quad \& \quad K_f = \frac{Q_s}{m \times GCD\left(Q_s, P\right)} \tag{4.3}$$

where GCD stands for greatest common divisor. The values of maximum possible k_{w1} obtained for various S-P combinations for a 3-phase machine are shown in Table 4-1. The term 'maximum possible' is utilized here since the winding pitch can be varied to select the most optimum configuration that produces the highest k_{w1}. The recommended range of SPP for CW is typically between 0.25 and 0.5 because it can produce both high k_{w1} and short end-windings. If SPP is greater than 0.5, DW is the typically adopted winding configuration.

Table 4-1. Maximum possible fundamental winding factors for slot-pole combinations

Q_s \ P	4	6	8	10
6	0.866		0.866	0.5
9	0.945	0.866	0.945	0.945
12	1		0.866	0.933
15	0.951		0.951	0.866
18	0.945	1	0.945	0.945
21	0.953		0.932	0.953
24	0.966		1	0.925
27	0.954	0.945	0.941	0.941
30	0.951		0.951	1

Fractional Slot Concentrated Winding (FSCW)
Integral Slot Distributed Winding (ISDW)
Fractional Slot Distributed Winding (FSDW)
Not Feasible

The value of K_f can also be used to determine if a slot-pole combination yields any imbalance in the rotor forces. If K_f is a whole number, the combination is balanced, and it is unbalanced otherwise. Other factors, such as the cogging torque, total harmonic distortion (THD), and unbalanced rotor radial forces [45], also influence the selection of S-P combination. Since the frequency of cogging torque is proportional to the least common multiple (LCM), and the amplitude of cogging torque inversely proportional to the LCM of

the slot and pole numbers, a high LCM is preferred. Also, since K_f corresponds to the number of distributed coils, the high value of K_f indicates a low THD of back-EMF. Finally, the unbalanced rotor radial forces, which can be a major source of noise and vibration, can occur if the greatest common divisor (GCD) of slot-pole combinations is 1. As a result, such combinations (e.g., 9S–4P and 15S–4P) should not be selected in the high-speed operation.

Typically, DW machines are better at avoiding excessive harmonic components leading to lower harmonic losses and leakage. However, they are relatively cumbersome to assemble and exhibit higher mutual coupling between phases. CW machines, on the other hand, are easy to manufacture and can achieve higher slot fill factors along with better fault tolerance. However, they have higher harmonic content and leakage [46]. Furthermore, the combinations that have SPP < 0.5 will have significant spatial sub-harmonic components leading to parasitic effects and increased core losses. In fact, all combinations that have SPP not a multiple of 0.5 will have harmonic components that are interacting across different pole pairs on the rotor, causing asymmetrical flux distribution [45]. Hence, while it is beneficial to select an S-P combination that has high k_{w1}, the application requirements and type of rotor dictate which S-P combinations must be avoided.

It is shown in the literature that selecting FSCW configuration with SPP < 0.5 and with high k_{w1}, typically a higher pole number, are beneficial for SPM rotor. However, having FSCW for SyR rotor machines introduces cross-saturation and leads to poor performance. The saliency ratio achievable by a SyR design is inversely proportional to the number of poles, thus leading to designs that have a low pole number. It is apparent that for a hybrid rotor PMSM, both the SPM and SyR rotors must have the same pole number in order to use a single stator

and associated VFD. This adds some unique constraints and design considerations while selecting the S-P combination and winding configuration.

Since FSCW and large pole count is not suitable for SyR rotor, S-P combinations with SPP < 1 and pole number over 8 are not suitable. While choosing SPP = 1 gives the highest k_{w1}, it also leads to relatively high MMF harmonics. A higher SPP typically indicates more sinusoidal MMF, however considering the annular cross-section of the stator that is occupied by stator slots and teeth, i.e., excluding the back iron, the overall copper fill factor decreases due to insulation and manufacturing constraints as SPP increases. An ideal SPP range for a SyR machine would be 1 < SPP < 3.

4.2. Aspect Ratio

Once an appropriate S-P combination is selected, the next step is determining an appropriate aspect ratio before sizing the machine for the desired power output at a specified voltage and current limits.

Defining the aspect ratio of a machine as,

$$K_L = \frac{l_e}{D_g} \tag{4.4}$$

where, D_g is the mean airgap diameter, and l_e is the effective stack length of the machine. The aspect ratio of the machine must be selected based on the applications' requirements. For example, in servo and control applications where a quick dynamic response is expected, a large K_L is beneficial to reduce the rotor inertia. However, the duty cycle of such machines is usually small since large K_L impacts the ability to remove heat from the machine. On the other hand,

in applications where efficiency and continuous operation are more valued, small K_L is preferred, but such machines will have dominant end effects and leakage components, thus increasing the leakage inductance. In addition, since the hybrid rotor PMSM uses multiple rotor sections, the end leakage effects become more prominent if the machine aspect ratio is too small.

To broadly evaluate the impact of aspect ratio on the machine parameters, two different slot-pole combinations are selected from Table 4-1, 18S-4P with FSDW and 6S-4P with FSCW, and SPM machines designed with different aspect ratios for a rating of 400 W at 1,200 RPM. To maintain a coherent comparison of the machine parameters, all machines are designed to have the same shear stress (σ_m) of 10 kPa, which can be expressed as,

$$\sigma_m = \frac{\tau_m}{2V_{rotor}} \tag{4.5}$$

where τ_m is the mechanical torque output, and V_{rotor} is the rotor volume. The slot and stator dimensions are calculated to maintain a constant current density of 3.5 A_{rms}/mm^2 with a fixed phase current of 4 A_{rms} and a terminal voltage of 35 V_{rms}. It is assumed that the slot fill factors are 0.35 and 0.5 for the DW and CW configurations, respectively, while using 16 AWG strands. The designed stator and rotor geometries for the 18S-4P and 6S-4P configurations with different aspect ratios are shown in Figure 4-1 and Figure 4-2, respectively.

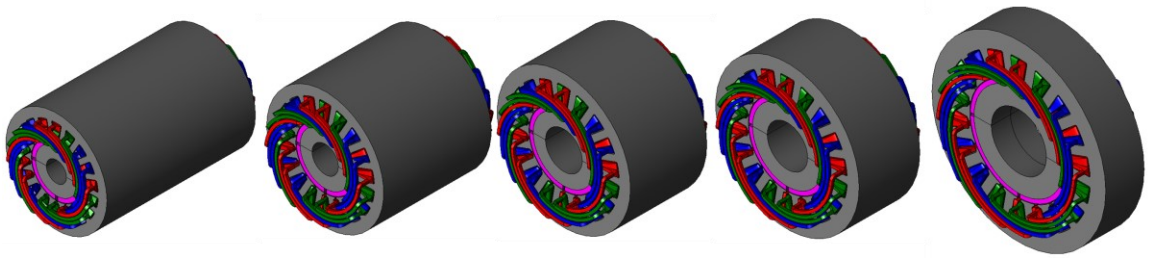

(a) (b) (c) (e) (f)

Figure 4-1. SPM design with 18S – 4P combination (1.5 SPP) for various aspect ratios and same output power. (a) $K_L = 3$, (b) $K_L = 1.85$, (c) $K_L = 1.1$, (d) $K_L = 0.78$, (e) $K_L = 0.4$

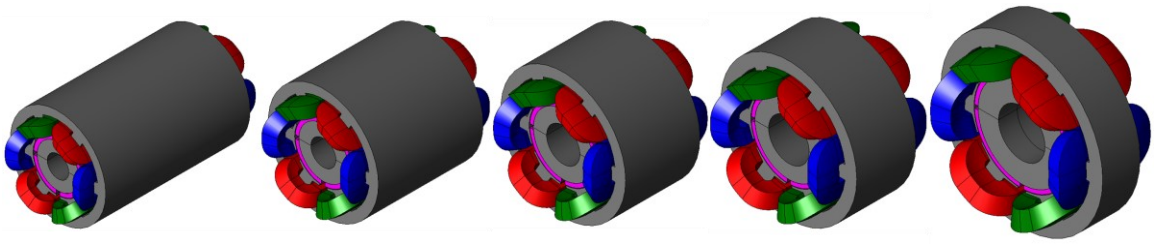

(a) (b) (c) (e) (f)

Figure 4-2. SPM design with 6S – 4P combination (0.5 SPP) for various aspect ratios and same output power. (a) $K_L = 3$, (b) $K_L = 1.85$, (c) $K_L = 1.1$, (d) $K_L = 0.78$, (e) $K_L = 0.4$

Table 4-2. Parameters of SPM machines with different aspect ratios

K_L	D_g [mm]	l_e [mm]	V_{tip} [m/s]	N_c	
				18 Slot	*6 Slot*
0.4	79.6	31.4	5	28	115
0.78	63.3	49.5	4	22	89
1.1	56.5	62.2	3.5	19	74
1.85	47.6	87.7	3	16	61
3	40.6	121	2.5	12	46

The key rotor parameters along with the number of series turns per coil (N_c) for each aspect ratio are summarized in Table 4-2. It can be noted that since all the machines have the same sheer stress and torque output, the rotor volume must be constant, which can be determined using D_g and l_e from Table 4-2 and calculated as $\approx 15.6 \times 10^{-5}$ m^3 for all rotors.

The phase resistances and *dq* inductances of all the machines are calculated and plotted as shown in Figure 4-3. The phase resistance behavior observed in Figure 4-3 (a) does not have a significant variation for CW machines with changing K_L while it is decreasing for DW machines with increasing K_L. Phase resistance is a function of the total coil length in the machine and the cross-section area of the winding. Since all machines are designed for 16 AWG, the cross-section area is constant. The coil length can be divided into two portions: the axial portion occupying the space inside the slots, and the end winding portion. The axial portion of the coil length is equal to l_e and actively contributes to flux linkage and hence phase voltage. As K_L increases, l_e increases and N_c must be decreased to maintain a constant phase voltage for both DW and CW. The end winding length (l_{ew}) however, is dependent on the nature of the winding. The change in l_{ew} with K_L is not significant for CW machines since it is dependent only on the stator tooth pitch. For DW machines, however, l_{ew} is dependent on the pole pitch, which is proportional to D_g. Hence for a DW machine with small K_L, $l_{ew} > l_e$. Since l_e for both DW and CW machines is identical for a given K_L, the difference in end winding length has a dominant effect on the net phase resistance at low K_L. As K_L increases, the difference in l_{ew} diminishes and N_c plays a dominant role in phase resistance magnitude.

The inductance as a function of K_L shown in Figure 4-3(b) indicates that at lower K_L, both CW and DW machines have higher inductance. This is expected due to dominant end

effects and leakage flux for both DW and CL machines. CW machines, in particular, have relatively higher harmonic and slot leakage components [47]. However, as K_L increases, the difference between slot pitch and pole pitch decreases and hence the slot leakage components are expected to be less significant. It is observed that at higher K_L, the inductance of CW configuration asymptotically reaches to similar values as DW configuration.

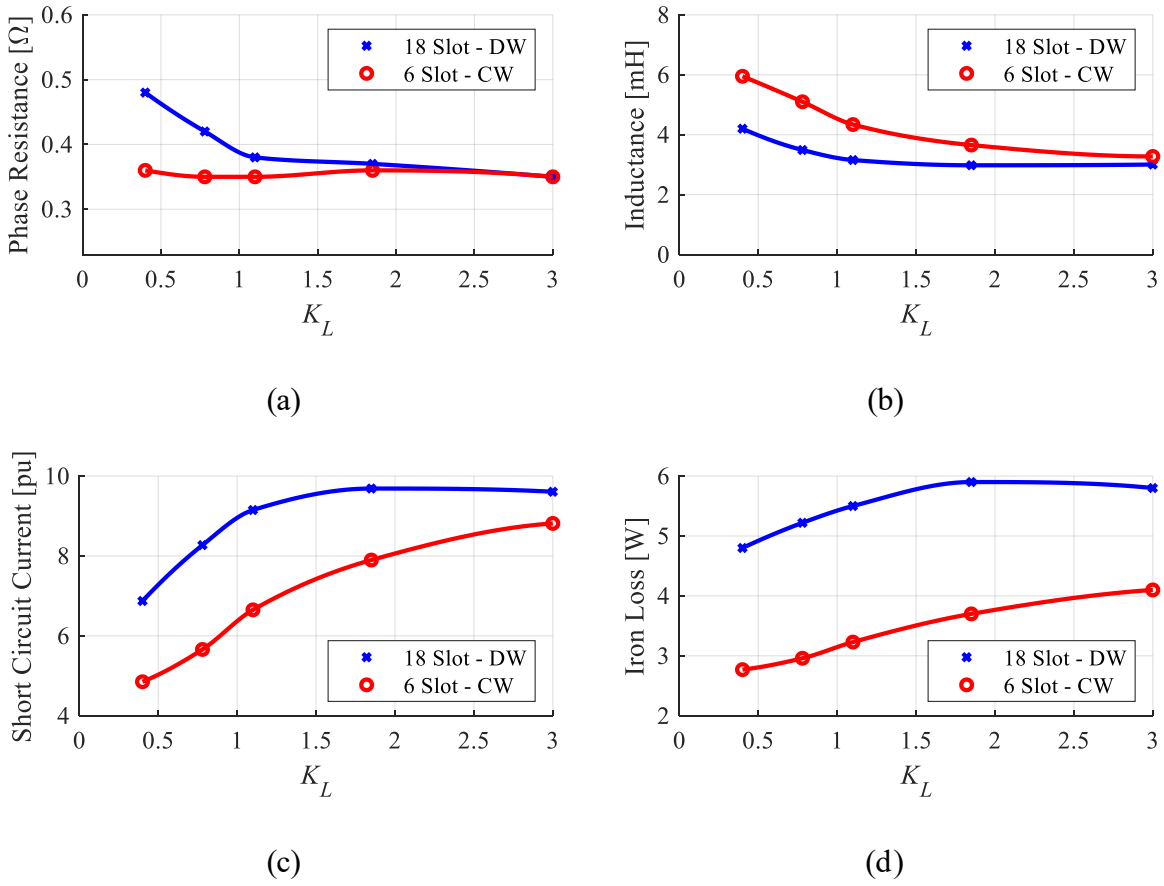

Figure 4-3. Comparison of machine parameters for DW and CW configurations. (a) Phase resistance (b) Inductance (c) Short circuit current (d) Iron Loss

The corresponding short circuit current, which will be equal to the characteristic current, is shown in Figure 4-3(c). Since all the machines are designed for the same terminal

voltage, the short circuit current simply follows the inverse of inductance. Figure 4-3(d) shows the iron loss behavior as a function of the aspect ratio. It can be clearly seen that the iron loss increases as the aspect ratio increases. The iron loss for DW machines is higher than CW machines. Due to the lower slot fill factor and a higher number of slots, the total stator iron material volume for DW machine higher than CW machine, thus resulting in higher iron loss. It must be noted that the machines are configured with an SPM rotor, resulting in nearly DC flux component and minimal losses in the rotor iron. The rotor losses will be more dependent on the rotor iron for a SyR rotor.

Based on the identified influence of K_L on the machine parameters for designs with a given power, current density and voltage constraints, it is evident that with K_L less than 1, the resistance and leakage inductance are higher for DW machines while only inductance is impacted significantly by K_L for CW machines. While the CW appears better than DW in terms of both characteristic current and stator iron loss, reluctance torque and power factor will be significantly impacted with CW stator when used with SyR rotor. Both DW and CW machine parameters appear to plateau around $K_L \approx 1$ and approach same magnitudes at $K_L \approx 3$.

4.3. Design Criteria for Hybrid Rotor PMSM

The key design component of a hybrid rotor PMSM is the rotor. More specifically, designing a combination of individual SPM and SyR rotors to meet the application requirement. The stator can be any design that is applicable to a conventional IPM machine. Nevertheless, that should not diminish the importance of selecting a proper S-P combination and winding configuration that is optimum for both SPM and SyR rotor sections.

If the SPM rotor occupies a dominant portion of the stack length and has a higher pole number, then a CW configuration with higher K_L is more suitable. By contrast, if the SyR rotor is dominant, a DW configuration must be selected, preferably with a low pole number. Based on the application requirements, a preferable design space for hybrid rotor machines will be $1 \leq K_L \leq 3$. A summary of the hybrid rotor PMSM machines found in the literature (grouped by authors) and their S-P configuration and aspect ratio is shown in Table 4-3.

Table 4-3. Hybrid rotor PMSM designs form literature

Literature	Slot-Pole	Rotor Sections		Aspect Ratio
[12], [14], [16], [17], [48]	36-4	SPM	Ax-SyR	1.14
[19], [20], [49]	36-4	SPM	Ax-SyR	NA
[21], [22]	36-4	SPM	Ax-SyR	2
[50]	36-6	SPM	SyR	1.15
[23]	48-8	SPM	SyR	0.32
[24], [51]	6-4	SPM	SyR	1.05
[52]	12-8	SPM	IPM	NA

Based on the literature, the hybrid rotor PMSM designs studied thus far also fall within this category, except for [23]. The aspect ratio is kept small since an existing traction machine was used as a baseline.

It is also noteworthy that the initial proposed hybrid rotor PMSM used an axially laminated SyR (Ax-SyR) rotor. This trend was followed for the majority of the work by early researchers. While Ax-SyR boasts high saliency, they are relatively difficult to model, and manufacture than conventional SyR rotors. An additional drawback, which was addressed by

Chalmers et al. in [17], is that the PM and SyR rotors must be axially separated, preferably at a length of 20 times the airgap length, to avoid leakage flux between the two rotor sections. Such aggressive separation was necessitated by the Ax-SyR lamination structure, facilitating an axial path for the PM flux. Such separation between rotors is only practical for machines where the air gap is extremely small.

Hybrid rotors studied in the recent past have predominantly used conventional SyR rotor sections. The authors explicitly did not point out why a conventional SyR was selected. Still, it can be inferred that a combination of the complexity in modeling Ax-SyR using FEA as well as laborious manufacturing could be the reasons to avoid Ax-SyR rotor. While this presents a trade-off of a lower saliency ratio, it limits the leakage flux between the rotor sections even without any separation due to the nature of the laminated structure of SyR rotor. Hence it is more practical for machines that do not have a very small air gap or have limited stack length.

4.4. Sizing Equations for Hybrid Rotor PMSM

The sinusoidal nature of the flux linkage and back EMF for both SPM and SyR machines facilitates a similar sizing methodology. Since both SPM and SyR rotor sections will be using the same stator, the electrical loading ($A_{s,rms}$) will be identical. Hence, in order to develop a hybrid rotor PMSM, the rotor sections can be sized separately, and the stack length ratios determined based on the operation characteristics desired.

4.4.1. Surface Permanent Magnet Rotor

For the sake of simplicity, neglecting the leakage inductance components and stator resistance, the air gap power of an SPM machine can be written as,

$$P_{out} = \eta m K_p E_{pk} I_{pk} \tag{4.6}$$

where η is the efficiency, E_{pk} and I_{pk} are the peak values of airgap phase back EMF and phase current, respectively. The term K_p is an electrical power waveform factor and can be determined based on the nature of current and voltage waveforms which is defined as,

$$K_p = \frac{1}{T}\int_0^T \frac{e(t)\times i(t)}{E_{pk}\times I_{pk}} dt \tag{4.7}$$

where $e(t)$ and $i(t)$ represent the phase voltage and current. Assuming a sinusoidal excitation, and unity power factor, K_p can be determined as 0.5 for SPM.

The back EMF is dependent on the flux per pole in the air gap (ϕ_g) which can be expressed as,

$$\phi_g = 2B_{g1}\left(\frac{D_g l_e}{p}\right) \tag{4.8}$$

where B_{g1} is the fundamental airgap flux density, D_g is the mean airgap diameter, p is the number of pole pairs. The average gap flux density can be determined based on the rotor type and PM grade. With a net series-connected turns per phase defined as N_s, the back EMF per phase can be calculated as,

$$E_{pk} = 2k_{w1}N_s B_{g1}\frac{f_e}{p} D_g l_e \tag{4.9}$$

where B_{g1} is the fundamental component amplitude of the gap flux density and can be computed from $B_{g\text{-}avg}$.

Similarly, the peak current can be calculated as,

$$I_{pk} = \frac{\pi D_g}{\sqrt{2} m N_s} A_{s,rms} \tag{4.10}$$

Substituting (4.9) and (4.10) into (4.6), the power equation can be expressed as,

$$P_{out} = \sqrt{2}\eta K_p k_{w1} \left(\frac{f_e}{p} \right) B_{g1} A_{s,rms} \pi D_g^2 l_e \tag{4.11}$$

4.4.2. Synchronous Reluctance Rotor

The sizing for SyR rotor also uses a similar method and equations developed for SPM rotor. Few considerations when applying the equations for SyR to keep in mind are that the SyR rotor does not have an active rotor flux component, and torque is produced by the interaction of *d*- and *q*-axis flux linkage components produced by the stator current. This effect can be captured by the power factor and incorporated into sizing. The power factor can be approximated as a function of the saliency of the rotor as [43],

$$\cos(\phi) = \frac{\xi - 1}{\xi + 1} \tag{4.12}$$

Practical machines have saliencies ranging between 2 to 10 and the corresponding power factor between 0.3 to 0.8. Hence the output power equation for a SyR rotor can be written as,

$$P_{out} = \sqrt{2}\eta K_p k_{w1} \left(\frac{f_e}{p} \right) B_{g1} A_{s,rms} \pi D_g^2 l_e \cos(\phi) \tag{4.13}$$

4.4.3. Hybrid Rotor PMSM

With the sizing equations for SPM and SyR rotors, the output power for a hybrid rotor PMSM will be a combination of both equations while keeping D_g constant and scaling the stack length of each section using the length coefficient defined in (3.29). In addition, both sizing equations are derived for rated conditions, i.e., the current angle is assumed to be at its MTPA for each rotor section. Since the rotor sections in hybrid rotor PMSM can have an angular offset 'α' (electrical radians), and using the SyR rotor as a reference, offset angle along with the rated current angle of π/4 for SyR rotor must be added to the SPM sizing equation. Hence the output power of a hybrid rotor PMSM can be written as,

$$P_{out} = \sqrt{2}\eta K_p k_{w1}\left(\frac{f_e}{p}\right) B_{g1} A_{s,rms} \pi D_g^2 l_e \left[k_l \cos\left(\frac{\pi}{4}-\alpha\right)+\left(1-k_l\right)\cos\left(\phi\right)\right] \tag{4.14}$$

The above equation assumes both B_{g1} and $A_{s,rms}$ are equal for both rotor sections. While the $A_{s,rms}$ should be identical, the gap flux density is highly dependent on the grade of the PM material in SPM rotor and the lamination steel properties for SyR rotor. Defining the ratio of magnetic loading factor as,

$$K_B = \frac{B_{g1,rm}}{B_{g1,pm}} \tag{4.15}$$

the combined sizing equation can be written as,

$$P_{out} = \sqrt{2}\eta K_p k_{w1}\left(\frac{f_e}{p}\right) B_{g1,pm} A_{s,rms} \pi D_g^2 l_e \begin{bmatrix} k_l \cos\left(\frac{\pi}{4}-\alpha\right)+ \\ K_B\left(1-k_l\right)\cos\left(\phi\right) \end{bmatrix} \tag{4.16}$$

It is evident that the power output of a hybrid rotor PMSM is similar to that of an SPM rotor and can be compared by taking a ratio of (4.16) to (4.11) giving,

$$\frac{P_{out,HR}}{P_{out,PM}} = k_l \cos\left(\frac{\pi}{4} - \alpha\right) + K_B\left(1 - k_l\right)\cos\left(\phi\right) \tag{4.17}$$

From the above equation, it is clear that the comparison is primarily dependent on the magnetic loading factor and the power factor of the SyR rotor. The relative power ratio as a function of stack length ratio and offset angle for different magnetic loading factors with a practical maximum power factor is shown in Figure 4-4. A low value of K_B corresponds to higher magnetic loading at SPM rotor section, i.e., higher-grade PM material such as NdFeB. As K_B increases, the PM strength decreases, thus making the reluctance torque component dominant. Based on (3.34), k_l corresponds to the PM flux linkage and hence the volume of PM material.

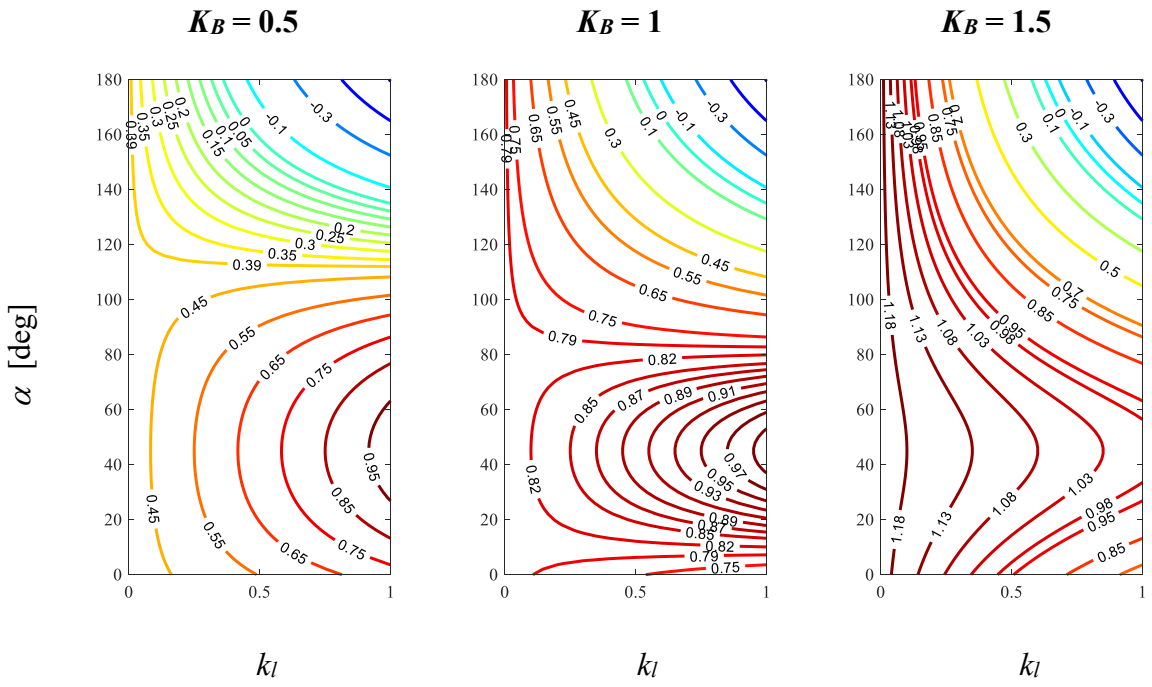

Figure 4-4. Ratio of power output of hybrid rotor PMSM with respect to equivalent SPMM

4.5. Scalability of Field Weakening Operation

Scaling of a machine design is often used to meet higher power and/or higher torque requirements. This is typically achieved by scaling up the machine dimensions uniformly while keeping the aspect ratio constant or linearly increasing either the stack length or diameter of the machine, thereby changing the aspect ratio. Linear increase of stack length is more commonly used to reduce retooling costs involved in lamination stamping. In the case of linear increase of machine diameter, as observed from the analysis presented in section 4.2, the phase resistance and leakage inductance increase as the machines' aspect ratio decreases, thus causing more copper losses and impacting torque density due to loss in cooling capability.

Key metrics to consider in comparing the scalability of a machine would be current density (J), which is governed by the thermal constraints, and magnetic flux density (B) governed by the material's saturation limits. The available machine drive system also establishes constraints on either the current or voltage. The impacts on the machine parameters and performance due to scaling can be estimated used the design equations.

Assuming all the dimensions are scaled uniformly, for a fixed magnetic loading, the flux per pole crossing the airgap is dependent on the pole face surface area as seen by (4.8). Hence the proportionality for the total flux can be written as,

$$\phi_g \propto D_g l_e \tag{4.18}$$

The stator flux linkage and peak voltage will also increase by the same factor if the number of turns is kept constant. However, if the voltage is constrained, then the number of turns must be reduced. Hence the proportionality can be written as,

$$E_{pk} \propto N_s D_g l_e \tag{4.19}$$

For a given RMS current density (J_{RMS}), the stator current can be written as,

$$I_{pk} = \frac{J_{RMS} Q_{slot} A_{slot} k_{cu}}{3\sqrt{2} N_s} \tag{4.20}$$

where A_{slot} is the cross-section area of the slot and k_{cu} is the slot fill factor. Hence the proportionality can be written as,

$$I_{pk} \propto \frac{J_{RMS} D_g^2}{N_s} \tag{4.21}$$

From (4.19) and (4.21), the proportionality for output power and shaft torque can be written as,

$$\tau_m \propto P_{out} \propto J_{RMS} D_g^3 l_e \tag{4.22}$$

Equation (4.22) only indicates the scaling of power output. To understand the field weakening performance of the scaled machines, the scaling of characteristic current must also be considered. The proportionality of the PM flux linkage is similar to total flux linkage and can be written as,

$$\psi_{pm} \propto N_s D_g l_e \tag{4.23}$$

The inductance of the machine, ignoring end winding leakage components, is dependent on the number of turns, gap surface area and the equivalent electromagnetic gap length (g_e). The change in inductance can be written as,

$$L \propto N_s^2 \frac{D_g l_e}{g_e} \tag{4.24}$$

Hence the characteristic current will change as,

$$I_{char} \propto \frac{g_e}{N_s} \tag{4.25}$$

Using equations (4.21) and (4.25) gives an important constraint on how to scale the effective airgap to maintain the field weakening performance, i.e., for a given current density, N_s and voltage rating, if the mean gap diameter is scaled by a factor of k, the air gap must be scaled by k^2 to maintain the same normalized characteristic current.

4.6. Summary

This chapter firstly discusses the merits and demerits of different possible slot-pole combinations of PMSMs and developed a guideline for the selection of slot-pole configuration for a hybrid rotor PMSM. Several DW and CW PMSM designs are designed with different aspect ratios and identical power, voltage, and current rating. Using a detailed analysis of the machine parameters, a rationale for the choice of aspect ratio for hybrid rotor PMSM is also developed.

The sizing equations for individual SPM and SyR machines are introduced, and hybrid rotor PMSM sizing equations are developed. A comparison of the power generation capability of a hybrid rotor PMSM to that of an equivalent SPM machine is performed. It is shown that in terms of peak power, the hybrid rotor PMSM performance is primarily dependent on the magnetic loading of the SPM rotor and the power factor of the SyR rotor. Through scalability

analysis using the sizing equations, it is established that to maintain the field weakening performance of the hybrid rotor PMSM, the effective electromagnetic airgap must be proportional to the square of the scaling factor of the diameter for a given current density.

Chapter 5

5. Design and Performance Analysis of Hybrid Rotor PMSM

In this chapter, the design process is discussed in detail for each individual component of the hybrid rotor machine, i.e., the stator, SPM rotor, and SyR rotor. Individual SPM and SyR machines are thoroughly analyzed, and the key parameters characterized. A proof-of-concept hybrid rotor PMSM is then implemented in 3D FEA using the SPM and SyR rotor. The resulting parameters and torque are characterized as a baseline for further analysis in field weakening region operation.

5.1. Stator Design

For proof of concept and ease in prototyping, a low power, low-speed machine is beneficial. In addition, the low power machine serves as a case study for servo applications. Hence, with the design criteria specified in the previous chapter, an 18 slot – 4 pole configuration with an aspect ratio of 3 is selected. The rated phase voltage and current are selected as 25 V_{rms} and 10 $A_{rms,}$ respectively, with a rated speed of 1200 RPM. The current and speed ratings are chosen primarily based on the available hardware and infrastructure. The design parameters are listed in Table 5-1. The stator design is shown in Figure 5-1. Since the 18S-4P configuration has a periodicity of 2, only half of the stator and rotor model is sufficient to predict the performance.

Table 5-1. Hybrid rotor PMSM design parameters

Parameter	Value
Nominal Power [W]	750
Stator Slots	18
Rotor Poles	4
Phase Voltage [V_{rms}]	25
Nominal Speed [RPM]	1200
Phase Current (I_s) [A_{rms}]	10
Airgap diameter (D_g) [mm]	40.2
Airgap (g) [mm]	0.5
Turns per phase per pole	13
Phase Resistance (R_s) [ohm]	0.39
Stack Length (l_e) [mm]	120

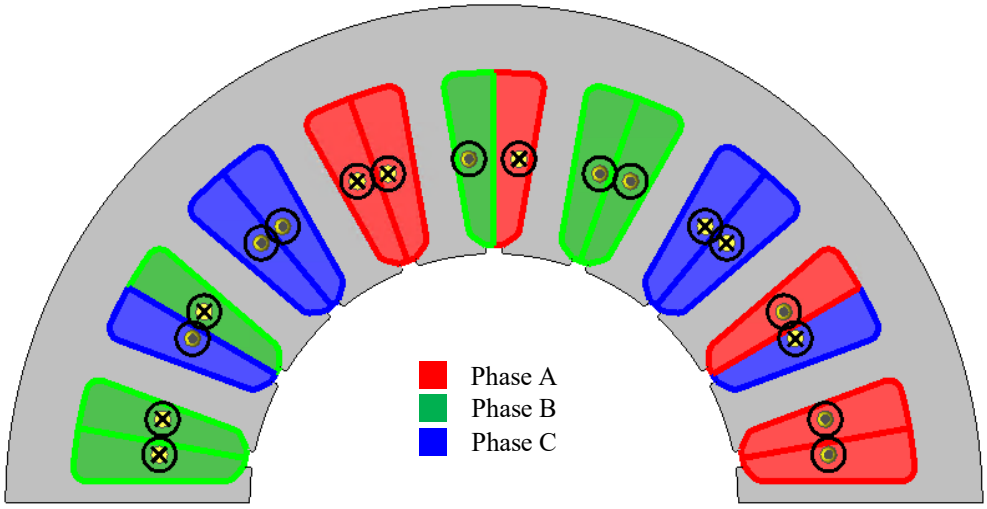

Figure 5-1. Stator design and winding configuration for 18 slot – 4 pole configuration

The saliency of the rotor determines the characteristics of field-weakening performance and power factor; however, the reluctance torque is dependent on the difference of inductances, $\Delta L_{dq} = (L_q - L_d)$. Both inductance components can be expressed as a combination of magnetizing inductance (L_m) in the respective axis and leakage inductance (L_l) component as,

$$\begin{aligned} L_q &= L_{mq} + L_l \\ L_d &= L_{md} + L_l \end{aligned} \tag{5.1}$$

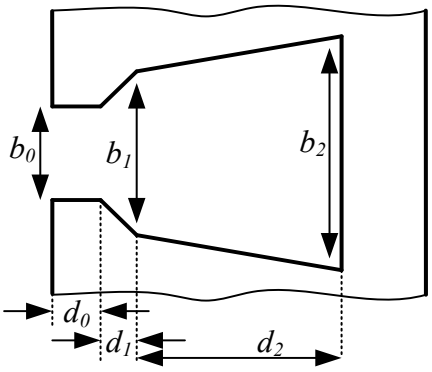

Figure 5-2. Stator slot representation for slot leakage inductance calculation

The end winding and slot leakage are the two leakage inductance components that can be determined from the stator design. Analytical models for calculating end winding leakage inductance exist [53]–[56]. However, since the machine under consideration has a high aspect ratio, it is reasonable to assume that the end winding leakage component is sufficiently small due to the short end winding length compared to the active length of the machine and can be ignored. The slot leakage inductance is primarily dependent on the slot shape close to the airgap and can be approximated as [53],

$$L_l = 4mN_s^2 l_e \frac{P_s}{Q_s} \tag{5.2}$$

where P_s is the total slot permeance ratio. Approximating the slot as a trapezoidal shape, as shown in Figure 5-2, the slot can be divided into three sections. Defining the permeance ratio for each section as P_{s0}, P_{s1}, and $P_{s2,}$ respectively, the total permeance ratio will be, $P_s = P_{s0}+P_{s1}+P_{s2}$. However, slot leakage is typically more sensitive to the permeance ratio near the airgap and insensitive to slot bottom. Hence P_{s2} can be ignored. The permeance ratios for the remaining sections can be written as,

$$\left.\begin{aligned} P_{s0} &= \frac{d_0}{b_0} \\ P_{s1} &= \frac{d_1}{(b_1 - b_0)} \ln\left(\frac{b_1}{b_0}\right) \end{aligned}\right\} \quad P_s = P_{s0} + P_{s1} \tag{5.3}$$

For the stator design shown in Figure 5-1, the slot leakage inductance is calculated as 0.01 [mH] using (5.2) and (5.3).

The magnetizing inductance is dependent on both the stator and rotor designs in the form of the winding function and effective rotor permeance (P_r), respectively. With a predetermined air gap profile, the inductance of any winding can be calculated as,

$$L_{xy} = \mu_0 \frac{D_g}{2} l_e \int \left[W_x(\theta) W_y(\theta) \times P_r(\theta) \right] d\theta \tag{5.4}$$

where μ_0 is the permeability of free space, W_x and W_y are the winding functions of the corresponding windings. For a fixed air gap rotor, such as in the case of an SPM, the rotor permeance can be simply expressed as the inverse of the effective air gap length (g_e). Assuming a smooth air gap, the inductances in stationary reference (*abc*) frame and synchronous reference (*dq*) frame can be calculated as a function of the air gap length. Using this method, one can realize the limits of inductance based on stator winding configuration independent of

the rotor design. The variation of inductance with increasing g_e for the stator design under consideration is plotted in Figure 5-3.

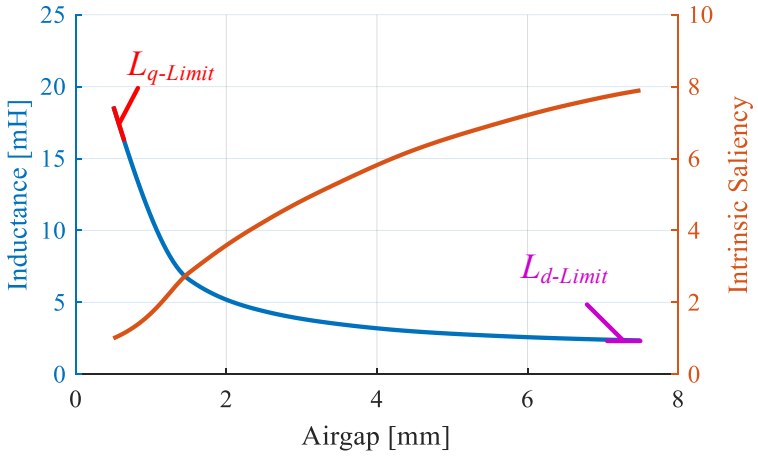

Figure 5-3. Inductance characteristics and intrinsic saliency of the stator winding as a function of air gap

Here, the inductance with minimum possible g_e substituted will serve as a theoretical upper limit for L_q, while the inductances with subsequent increasing g_e values can be considered as L_d assuming such an equivalent air gap can be introduced in the d-axis using appropriate rotor design. An intrinsic saliency value can be calculated as,

$$Intrinsic\ Saliency = \frac{L_{q-Limit}}{L_d(g_e)} \tag{5.5}$$

The intrinsic saliency is also plotted as shown in Figure 5-3. It can be seen that the change in inductance diminishes and is asymptotically approaching a lower limit. Further increasing the airgap would not yield in lower inductance. Hence this can be considered as the theoretical lower limit of *d*-axis inductance, and saliency calculated at this point will be the theoretical

upper limit of saliency possible with this stator design. A more practical saliency ratio limit would be at the knee point of the inductance curve, which is identified as ≈ 3 for this stator.

5.2. Rotor Design

5.2.1. Synchronous Reluctance Rotor

Since the saliency achieved by the SyR rotor plays a crucial role in determining the hybrid rotor PMSM performance, the design of SyR rotor is addressed first. Based on the design selection criteria, salient pole and axially laminated SyR rotor designs are not considered. Hence a multiple internal flux-barrier SyR rotor design will be used. A higher number of flux barrier layers will theoretically increase ΔL_{dq} and, consequently, the average torque. However, if the number of barrier slots at the outer rotor diameter per pole pair is equal to the number of slots per pole pair on the stator, torque ripple will be aggravated due to the interaction of stator and rotor magnetic potential harmonic components [57]. For the selected 18 slot – 4 pole design, with an SPP of 1.5, the number of slots per pole pair is 9 giving rise to 8^{th} and 10^{th} harmonic components on the stator MMF, as shown in Figure 5-4. Hence it is beneficial to avoid 8^{th} and 10^{th} harmonic components on the rotor magnetic potential.

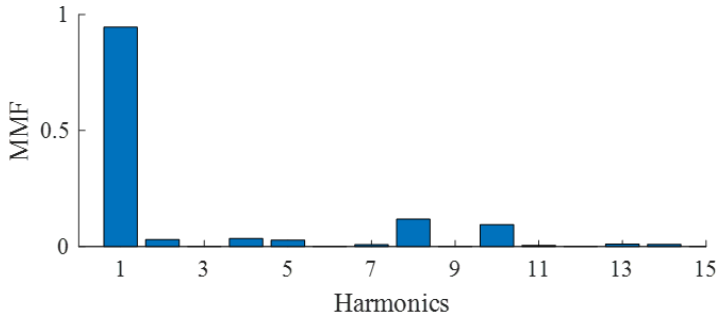

Figure 5-4. Stator MMF harmonics for a 18 slot – 4 pole configuration

On the rotor, each flux barrier will generate four equivalent slots per pole pair. Hence with 2 or 3 layers of flux barriers, the rotor magnetic protentional will have 7^{th} & 9^{th} or 11^{th} and 13^{th} harmonic components, respectively. A 3-layer flux barrier design is desirable for higher average torque; however, with the limited rotor core depth available, too much space is occupied by the barriers, and hence *q*-axis path inductance will reduce due to higher saturation. Therefore, a baseline rotor is designed with a half-open slot is considered which gives ten equivalent rotor slots per pole pair. The design can be further optimized once a baseline is established.

The q-axis high permeability path and hence the barrier shape must be designed to produce as little reluctance as possible. An ideal flux barrier shape can be identified from the flux path observed in the rotor using FEA. The natural flux path for the stator design under consideration is shown in Figure 5-5.

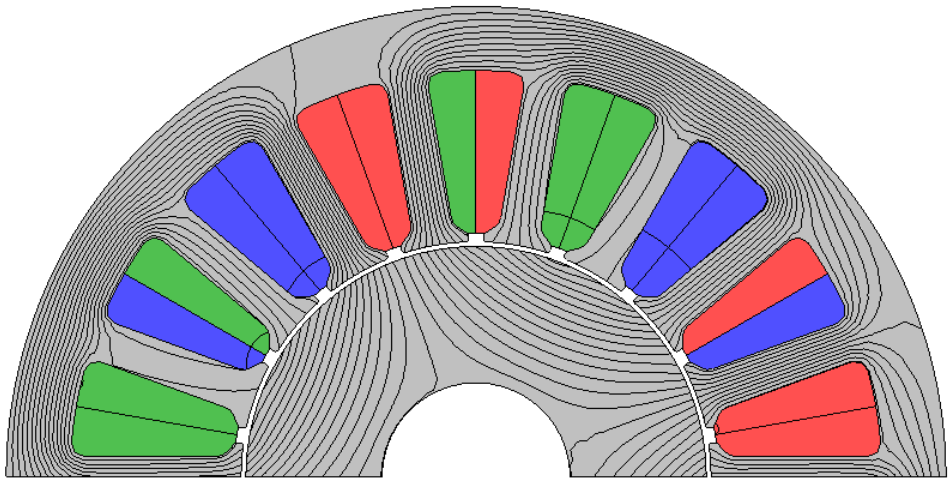

Figure 5-5. Natural flux path in a smooth rotor for the 18 slot - 4 pole configuration

Based on the flux path observed in the above figure, a baseline SyR rotor is designed, as shown in Figure 5-6. The FEA estimated torque and phase voltages along with voltage harmonic components using the baseline rotor with rated current and theoretical MTPA are shown in Figure 5-7 and Figure 5-8, respectively.

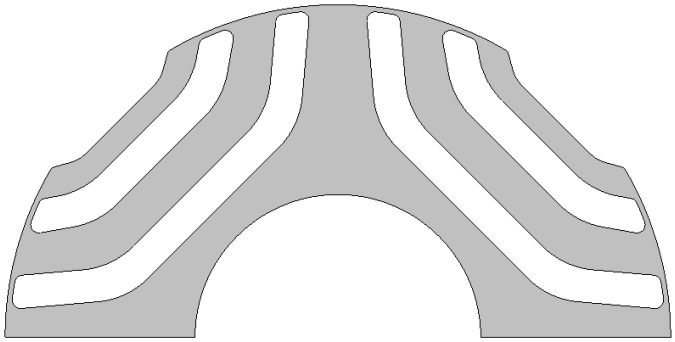

Figure 5-6. Baseline SyR rotor design

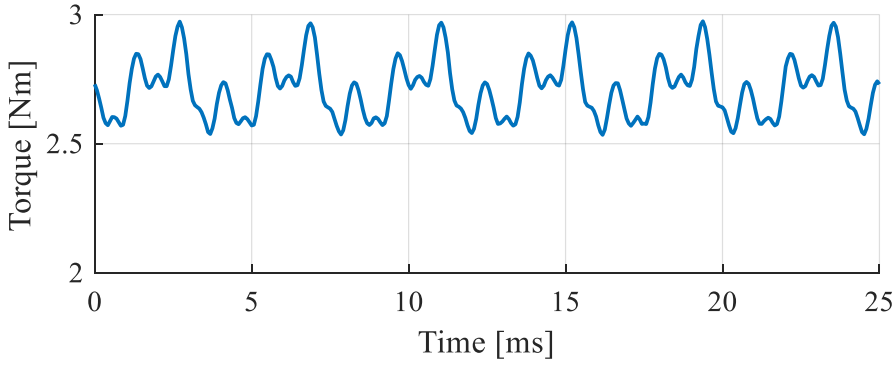

Figure 5-7. Torque waveform at rated operation using baseline SyR rotor design

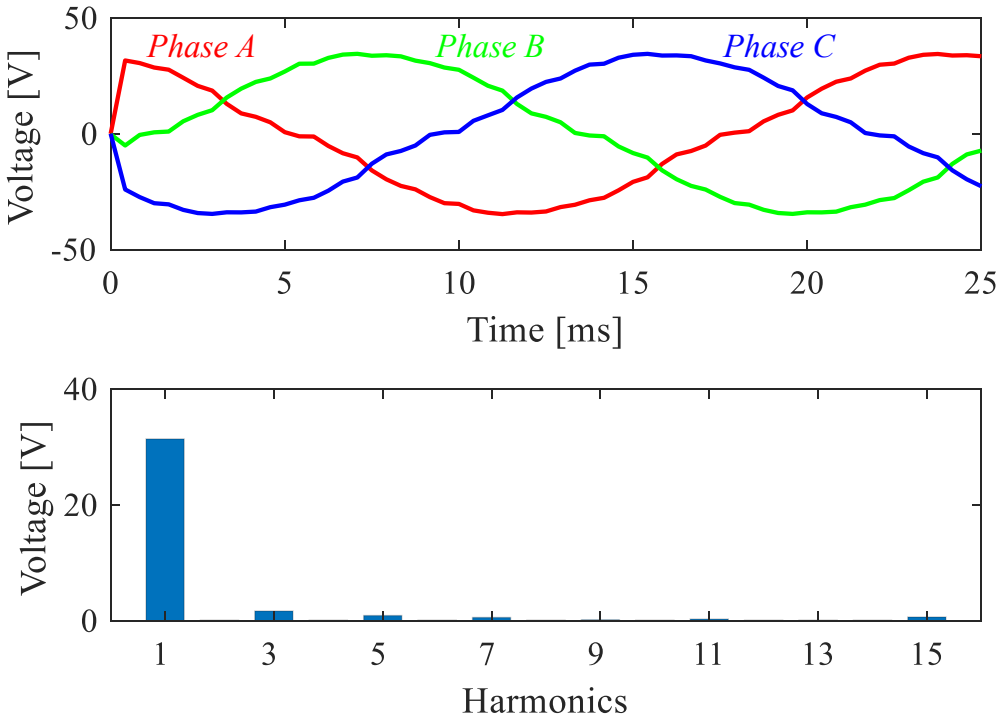

Figure 5-8. Phase voltage waveform and harmonic components at rated operation using Baseline SyR rotor design

The baseline rotor produced an average torque of 2.7 Nm with a torque ripple of 16.1%. The power factor is calculated to be 0.52. The power factor and saliency are also in part, dependent on the bridge thickness. A thicker bridge is beneficial to keep the rotor structurally robust at high-speed operation, but the bridge also acts as a short circuit path for the rotor flux leading to higher leakage flux and lower saliency. Hence it is vital to keep the bridge thickness as low as possible to saturate easily yet be within the material yield strength limit at the maximum operating speed for the application. With a rated speed of 1200 RPM, assuming a CPSR of 5, the SyR rotor must withstand up to 6000 RPM. A structural FEA co-simulation is performed on the baseline rotor with a bridge thickness of 0.4 mm and at 6000 RPM. A typical

Si-steel material has a yield strength of 420 MPa. Owing to any calculation error or manufacturing defects, it is beneficial to consider a safety margin of 20% on the permissible stress in the material.

The meshed rotor and Mises stress contour plot obtained from the structural FEA are shown in Figure 5-9. Since the stress is expected to be the most at the bridges, the mesh is refined locally around the bridges to improve the calculation accuracy while keeping the computation cost at a reasonable level. Form the contour plot; it can be observed the highest stress is indeed at the thin bridges near the outer periphery of the rotor geometry. The magnitude of stress, however, is well under the safety margin. Although this indicates that the bridge thickness can be further reduced, it is not practically feasible to achieve a thinner bridge due to manufacturing limitations.

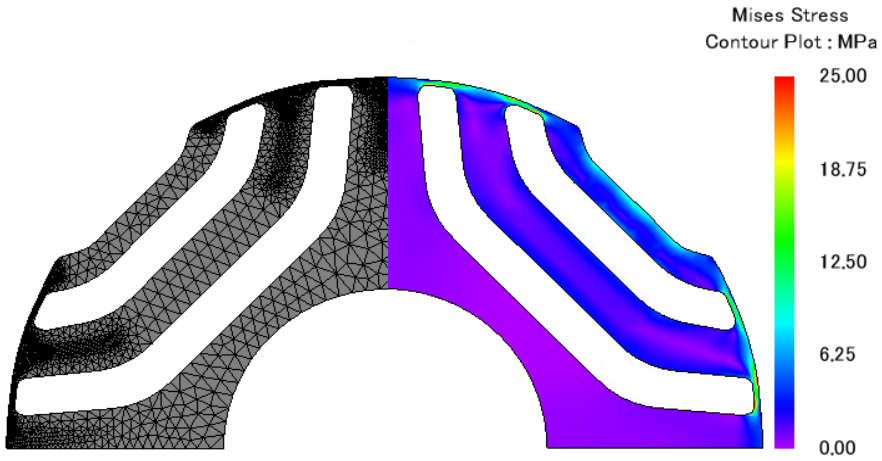

Figure 5-9. Meshed rotor for structural FEA and Mises stress distribution for the baseline SyR rotor

The inductances achieved using the baseline rotor as a function of the phase current are shown in Figure 5-10, and the average torque vs. phase at different current values is shown in Figure 5-11.

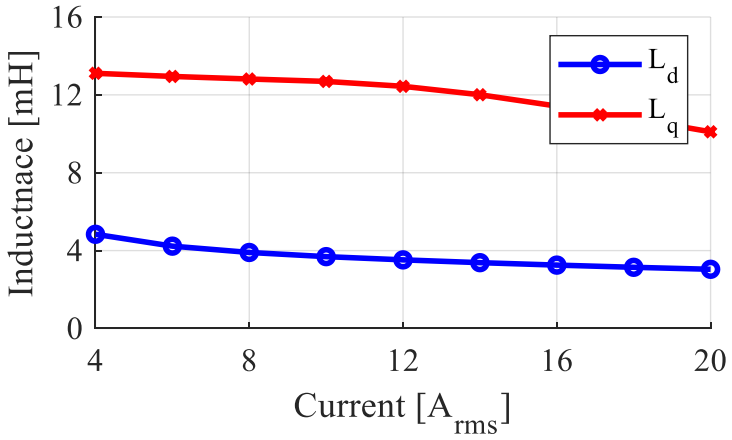

Figure 5-10. Inductance as a function of current calculated using FEA using baseline SyR rotor

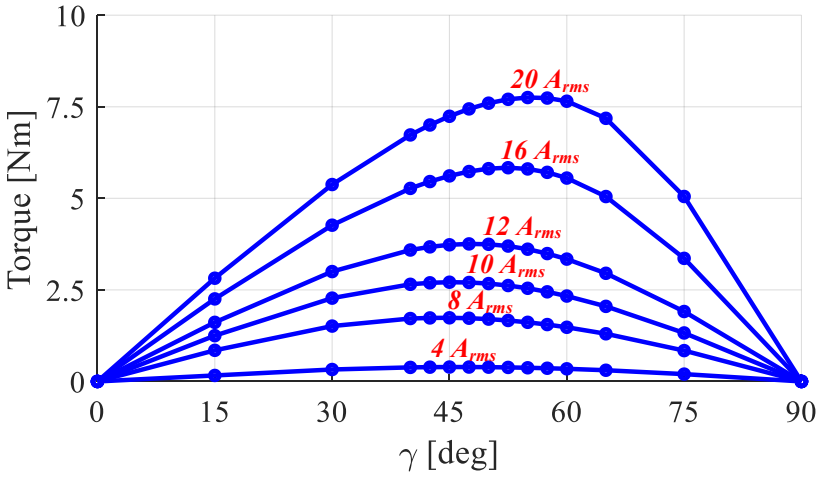

Figure 5-11. Torque as a function of current amplitude and current angle (γ) for baseline SyR rotor

It can be seen that the MTPA phase angle is shifting as the current amplitude increases due to saturation effects. The maximum torque achieved for each current amplitude and the corresponding power factor are plotted, as shown in Figure 5-12. It is evident that the overall power factor for the SyR rotor is low, ranging from 0.52 at rated operation, to 0.57 at peak power.

Since the rotor barrier shape and position will significantly affect the flux path and leakage, the performance of the SyR rotor can be improved by modifying the rotor geometry. Since there are numerous possible shape and size combinations of the rotor barriers, geometric optimization can be used to identify optimum patterns. The geometric parameters that define the barrier shape and position are identified in Figure 5-13 and their ranges listed in Table 5-2.

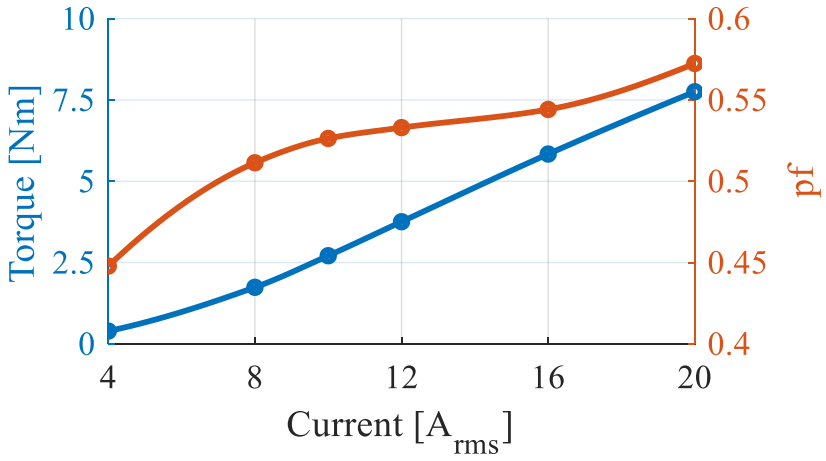

Figure 5-12. Maximum torque and corresponding power factor for baseline SyR rotor

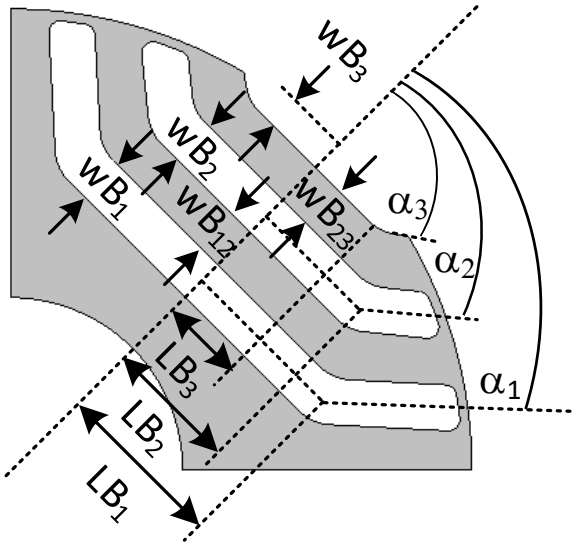

Figure 5-13. Geometric parameters used for the optimization of SyR rotor

Table 5-2. SyR rotor geometric optimization parameter range

Parameter	Baseline	Range
α_1 [deg]	48	45 – 70
α_2 [deg]	51	45 - 70
α_3 [deg]	55	45 - 70
LB_1 [mm]	7.5	5 – 9
LB_2 [mm]	5.75	4 – 8
LB_3 [mm]	4	3 – 7.5
wB_1 [mm]	2	0.5 - 3
wB_{12} [mm]	2	0.3 – 2.5
wB_2 [mm]	2	0.5 – 3
wB_{23} [mm]	2	0.3 – 2.5
wB_3 [mm]	1	0.25 – 1.5

Table 5-3. Objective functions for geometric optimization of SyR rotor

Parameter	Objective	Constraint
Average Torque [Nm]	Maximize	> 2.4
Torque Ripple [%]	Minimize	< 20
Power Factor	Maximize	> 0.6

It is beneficial to optimize the rotor to account for both an increase in saliency and the difference of *dq* inductances since they indicate SyR machines extended speed operation and maximum torque, respectively. However, calculating *dq* inductance from FEA is a post-processing operation which requires additional computation, thus increasing the optimization computation cost and time. Alternatively, the average torque and the power factor can represent the difference in *dq* inductance, and saliency, respectively. Hence, the objective functions and constraints are set as described in Table 5-3.

A differential evolution (DE) based multi-objective optimization algorithm is used with the listed 11 variables describing various rotor barrier shapes and positions. An initial subset of 100 rotor designs are generated using an orthogonal factorial array method for the design of experiments (DoE), and the results are fed to the optimization algorithm as initial data. A total of 5000 designs are generated during the optimization – 100 generations with a population limit of 50 per generation. Due to a large number of parameters, it is not practical to constraint the range of each parameter such that no infeasible geometry is created. Applying such constraints on the parameter range would adversely limit the design space and may not yield useful results. However, it is also important to ensure only structurally sound designs are evaluated and avoid the algorithm to converge onto unfeasible designs. Constraints are placed on some specific combinations of parameters such as,

$$\left(wB_1 + wB_{12} + wB_2 + wB_{23} + wB_3\right) < \left(rR_o - rR_i\right) \tag{5.6}$$

where rR_o is the rotor outer radius, and rR_i is the rotor inner radius. Such constraints will limit the geometries that are infeasible while giving a wider degree of variation for each parameter. Furthermore, additional designs are generated within each generation to be substituted for any failed design during the meshing process in the FEA. This will ensure the population in each generation is adequately diversified up to its population limit.

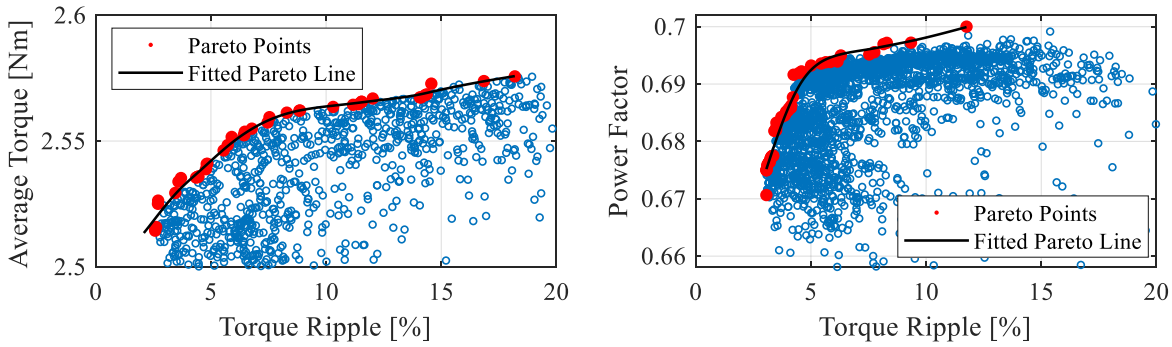

(a) (b)

Figure 5-14. Objective function scatter plot indicating Pareto curves for SyR rotor geometric optimization

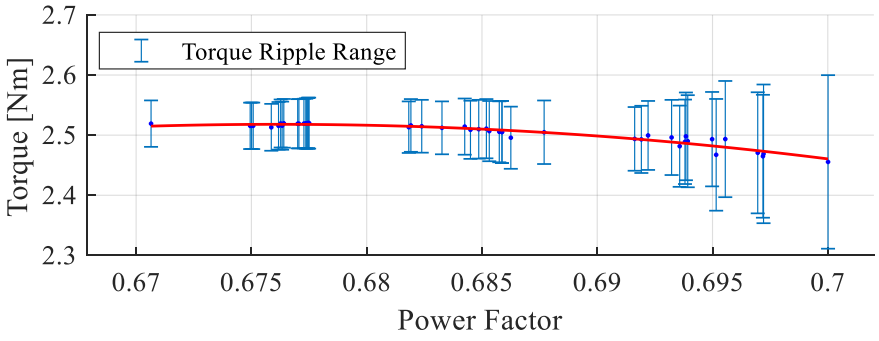

Figure 5-15. Maximum torque and corresponding power factor with the torque ripple range for optimal designs

A scatter plot of the objective values resulting from the optimization along with the corresponding Pareto-curves are plotted and shown in Figure 5-14. It can be seen that the increase in average torque and power factor is limited at the pareto front. However, the torque ripple is reduced considerably, with a minimum of 3%. The overall power factor is also improved from 0.52 to over 0.68 for the designs on the pareto front. This however comes at the expense of a reduction in the average torque. A plot of all the objectives of the designs that are on the pareto curve of all objective functions is shown in Figure 5-15. The torque ripple range is plotted in Nm for each design point as an error bar. This indicates that the power factor increases, the average torque reduces, and the torque ripple increases with a clear tradeoff relation. Using Figure 5-15, an optimum design can be selected such that the torque ripple is under 5% with an average torque > 2.5 Nm and power factor close to 0.7. The selected optimized SyR rotor design is shown in Figure 5-16.

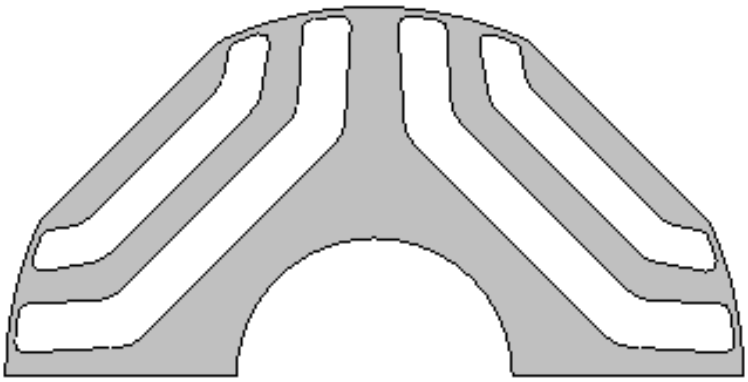

Figure 5-16. Optimized SyR rotor design

The dq inductances as a function of current amplitude and the maximum torque, power factor as a function of current are determined using FEA and plotted in Figure 5-17 and Figure 5-15 respectively. It is evident that the optimized rotor has a slight reduction in the peak torque,

but the overall power factor has significantly improved. The optimized rotor dimensions are listed in Table 5-4.

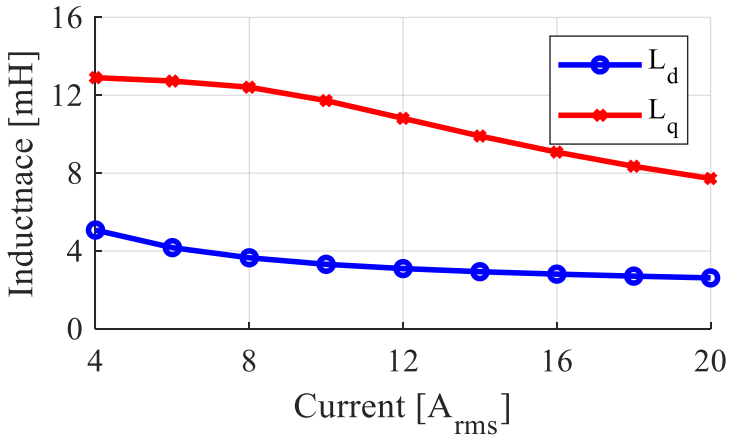

Figure 5-17. Inductance as a function of current calculated using FEA for optimized SyR rotor

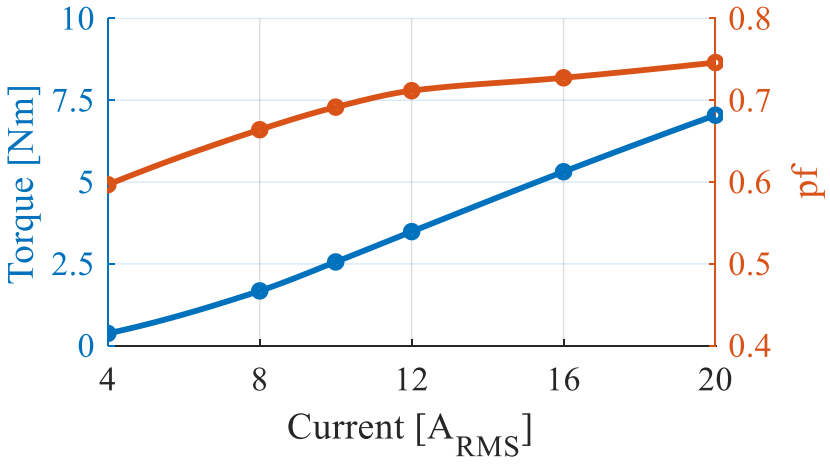

Figure 5-18. Maximum torque and corresponding power factor for optimized SyR rotor

Table 5-4. Optimized SyR rotor parameters

Parameter	Value
α_1 [deg]	45
α_2 [deg]	48.38
α_3 [deg]	55.20
LB_1 [mm]	7.64
LB_2 [mm]	5.7
LB_3 [mm]	6.5
wB_1 [mm]	2.63
wB_{12} [mm]	1.86
wB_2 [mm]	2.15
wB_{23} [mm]	1.78
wB_3 [mm]	1.22

5.2.2. Surface Permanent Magnet Rotor

The design of the SPM rotor is less tedious than the SyR rotor. Since the initial assumption in developing the analytical model was to maintain identical *d*-axis inductance between SPM and SyR rotors, the magnet thickness can be selected based on the d-axis inductance of the SyR rotor. From Figure 5-17, the *d*-axis inductance at rated operation for the SyR rotor is 3.49 mH. Since the relative permeability of PM material is close to air, the inductance determined for intrinsic saliency calculation of the stator shown in Figure 5-3 can be used as a starting point. Accordingly, the magnet thickness (t_{mag}) of the SPM rotor is selected to be 3 mm.

Since both SPM rotor and SyR rotor are expected to be used with the same stator and be driven by the same inverter, it is desirable to tune the PM flux linkage such that the rated voltage of both rotors is equal, i.e., $|V_{SPM}|_{rated} = |V_{SyR}|_{rated}$. Using (3.4) and (3.7),

$$\left(\psi_{nm} + L_{sn} I_{dn-pm}\right)^2 + \left(L_{sn} I_{qn-pm}\right)^2 = \left(L_{dn} I_{dn-rm}\right)^2 + \left(\xi L_{dn} I_{qn-rm}\right)^2 \tag{5.7}$$

Using the approximation of $L_{dn} = L_{sn}$, and rearranging,

$$\left(\frac{\psi_{nm}}{L_{dn}} + I_{dn-pm}\right)^2 + I_{qn-pm}^2 = I_{dn-rm}^2 + \xi^2 I_{qn-rm}^2 \tag{5.8}$$

Expanding the left-hand side of the equation and simplifying,

$$\left(\frac{\psi_{nm}}{L_{dn}}\right)^2 + 2\frac{\psi_{nm}}{L_{dn}} I_{dn-pm} - \left(\xi^2 - 1\right) I_{qn-rm}^2 = 0 \tag{5.9}$$

Equation (5.9) represents a quadratic equation for the characteristic current of the SPM rotor and the roots can be determined as,

$$\frac{\psi_{nm}}{L_{dn}} = -I_{dn-pm} \pm \sqrt{I_{dn-pm}^2 + \left(\xi^2 - 1\right) I_{qn-rm}^2} \tag{5.10}$$

At rated operation, $\gamma = 0$ for SPM rotor and $\gamma = \pi/4$ for SyR rotor, neglecting resistive drop and saturation. Hence,

$$\begin{aligned} I_{dn-pm} &= 0 \\ I_{qn-rm} &= \frac{1}{\sqrt{2}} \end{aligned} \tag{5.11}$$

Substituting into (5.10),

$$\psi_{nm} = L_{dn}\sqrt{\frac{\left(\xi^2 - 1\right)}{2}} \tag{5.12}$$

The desired normalized PM flux linkage of the SPM rotor for a hybrid rotor PMSM can be expressed in terms of the SyR rotor *d*-axis inductance and saliency. For the rated specifications listed in Table 5-1, the base flux linkage and base inductance can be calculated as 0.095 *Wb* and 6.7 *mH*, respectively. Substituting the normalized inductance of 0.52 p.u. and saliency of 3.25 into (5.12), the desired flux linkage is calculated as 1.13 p.u., i.e., 0.11 *Wb*. The PM flux linkage for a given rotor dimension can be expressed as [58],

$$\psi_{PM} = \frac{k_{w1}N_s}{2}\frac{D_g l_e}{p}\frac{\pi}{2}B_g \tag{5.13}$$

where the average airgap flux density (B_g) is related to the magnet remanence (B_r) as,

$$B_g = \frac{B_r}{1 + \frac{g_e}{t_{mag}}} \tag{5.14}$$

The impact of the magnet pole arc angle on the gap flux density is ignored in the above equations. If the magnet span is much less than the pole span, an appropriate correction factor must be introduced to reasonably predict the PM material grade. In this thesis, the magnet arc angle is assumed to be equal to the pole span, i.e., a ring magnet with no gap between poles. Such an assumption is used to make the FEA modeling easier for the hybrid rotor PMSM whilst implementing an arbitrary offset angle on the PM rotor.

The SPM rotor with the magnetization direction of the PM is shown in Figure 5-19. The final t_{mag} and B_r are adjusted to account for saturation effects to achieve the desired

inductance and the flux linkage. The phase voltage waveforms and the voltage harmonic components at rated operation are shown in Figure 5-20 and the rated torque waveform shown in Figure 5-21. The average torque obtained from FEA is 4.12 *Nm*, with a torque ripple of 16%.

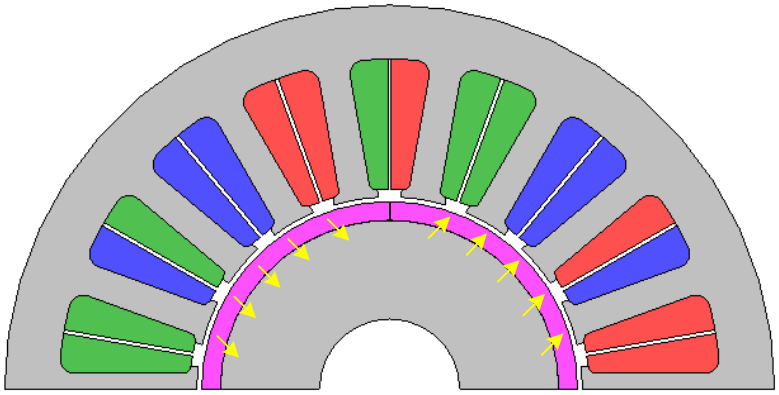

Figure 5-19. SPM rotor design with ring magnet

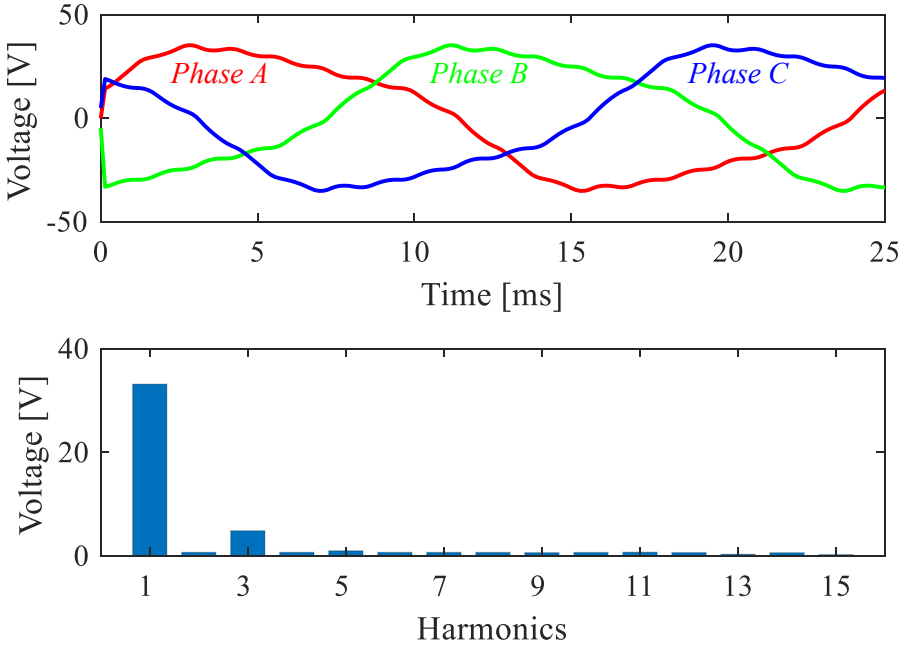

Figure 5-20. Phase voltage waveform and harmonic components at rated operation using SPM rotor

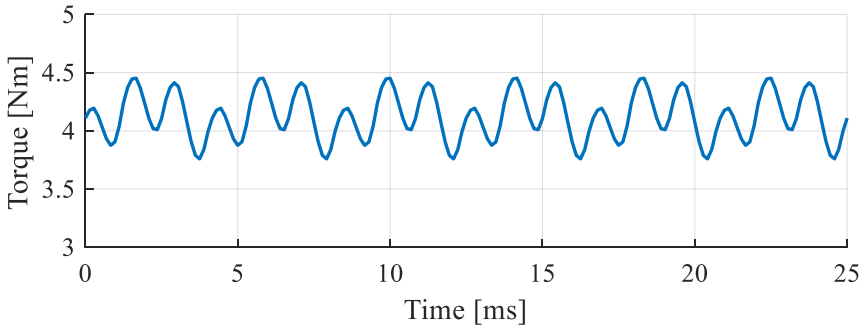

Figure 5-21. Torque waveform at rated operation using SPM rotor

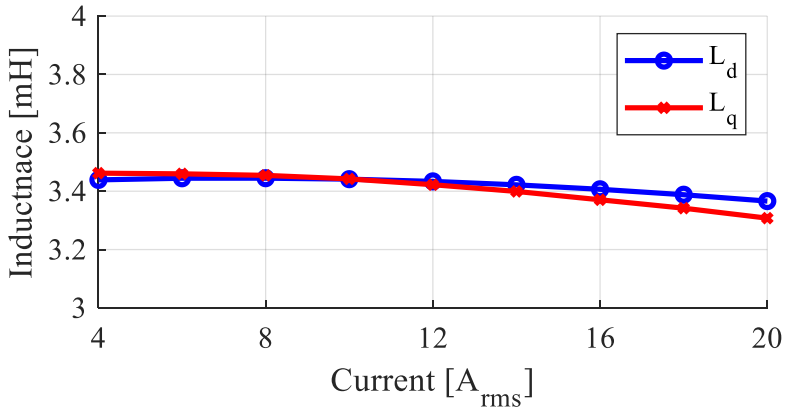

Figure 5-22. Inductance as a function of the current calculated using FEA for SPM rotor

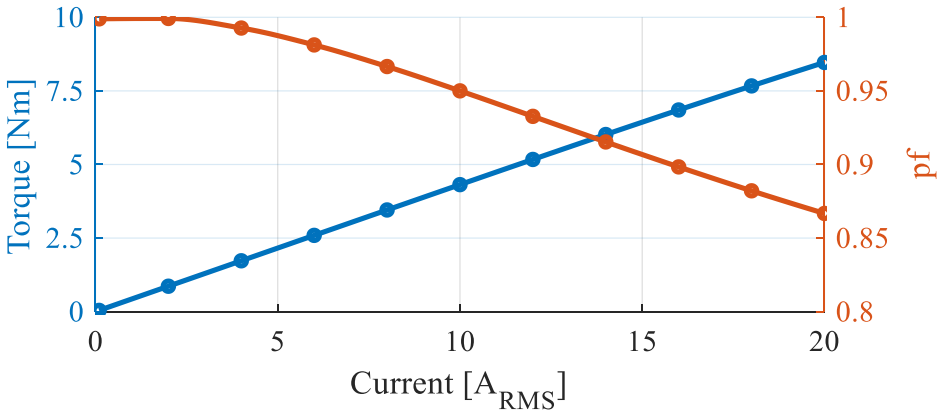

Figure 5-23. Torque and power factor as a function of current in SPM rotor

The inductance of the SPM machine, along with the torque and power factor as a function of the current, are shown in Figure 5-22 and Figure 5-23, respectively. The inductance in both d- and q-axis is almost identical and is equal to the d-axis inductance of the SyR rotor. Due to the selected high PM flux linkage, the SPM machine has high characteristic current and achieves high power factor at rated operation, which implies that the machine will have poor CPSR [8].

5.3. Hybrid Rotor PMSM Design

A hybrid rotor PMSM can now be constructed by combining the SPM and SyR rotor designs developed thus far. For the initial evaluation, a stack length ratio, $k_l = 0.5$ and $\alpha = 0^o$ is chosen. The stator and rotor structure, with cutout on the rotors, is shown in Figure 5-24.

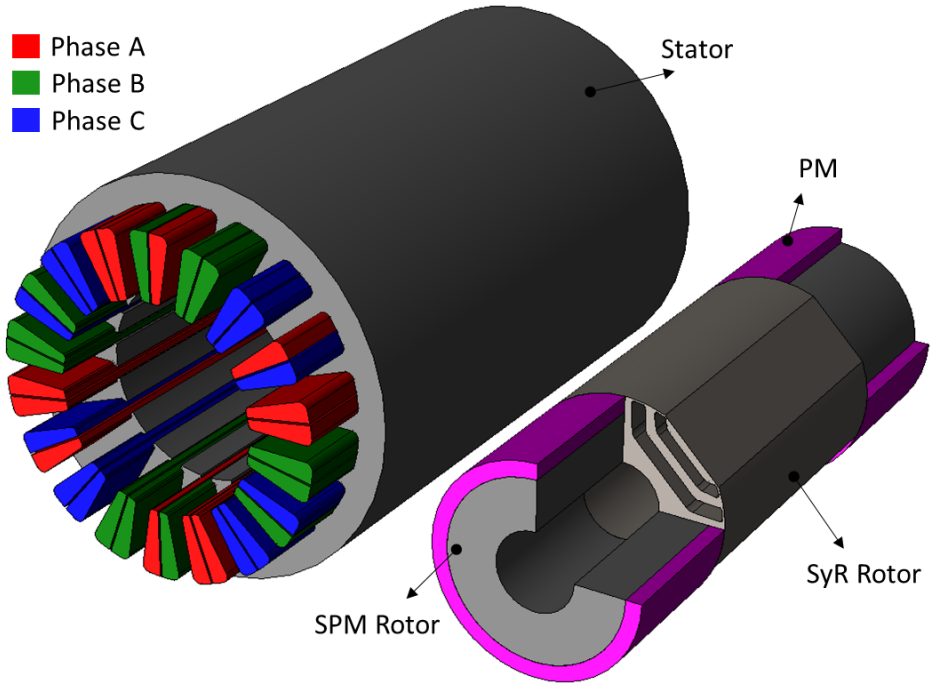

Figure 5-24. Hybrid rotor PMSM exploded view showing rotor structure

The non-uniform nature of the hybrid rotor structure in the axial direction requires the FEA analysis to be performed using 3D models. The burdensome computational requirement of a 3D model was one of the factors for past researchers to limit the exploration of hybrid rotor PMSM models using FEA. Having the three-part rotor, as described in this thesis, as opposed to two-part rotors used by past researchers, introduces an axial symmetry in the model in addition to minimizing axial thrust force on the bearings. Thus the axial symmetry, in

addition to the rotational periodicity of the 18S - 4P can be utilized to understand the performance of this machines using a 1/4th model, as shown in Figure 5-25, and the results can then be converted to the full model.

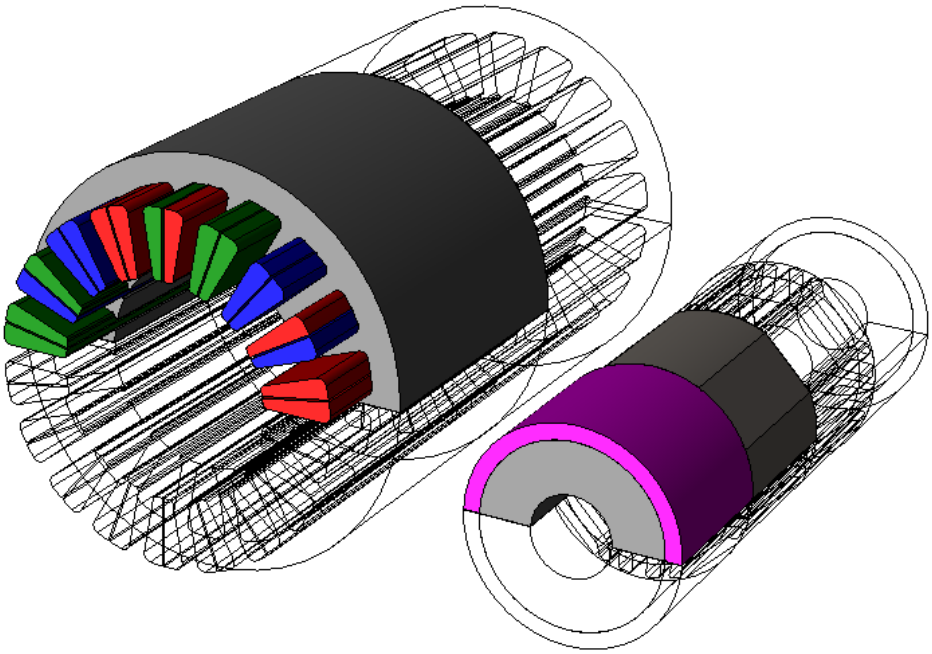

Figure 5-25. Reduced (1/4th) 3D model for hybrid rotor PMSM using axial and rotational symmetry

In addition, applying a relative rotor angle to the SPM rotor and analyzing for various rotor positions requires multiple geometries to be created. However, by utilizing a ring-shaped PM in this analysis makes the process of applying an angular offset to the SPM rotor simpler by changing the magnetization direction of the PM material instead of changing the geometry.

The flux density distribution of the hybrid rotor PMSM at no-load condition is shown in Figure 5-26. Since the PM rotor is only on the end sections, the stator iron at either end has higher flux density while the middle portion of the stator does not have any flux. Although the

FEA model does account for the reduction in the effective stack length due to laminated stator and rotor, it does not account for the axial non-homogeneous distribution of permeability due to laminations. Nevertheless, it is evident that the flux leakage between the SPM and SyR rotor sections is insignificant at no-load operation. Such leakage components will be much lower in a practical machine due to the laminated rotor and stator.

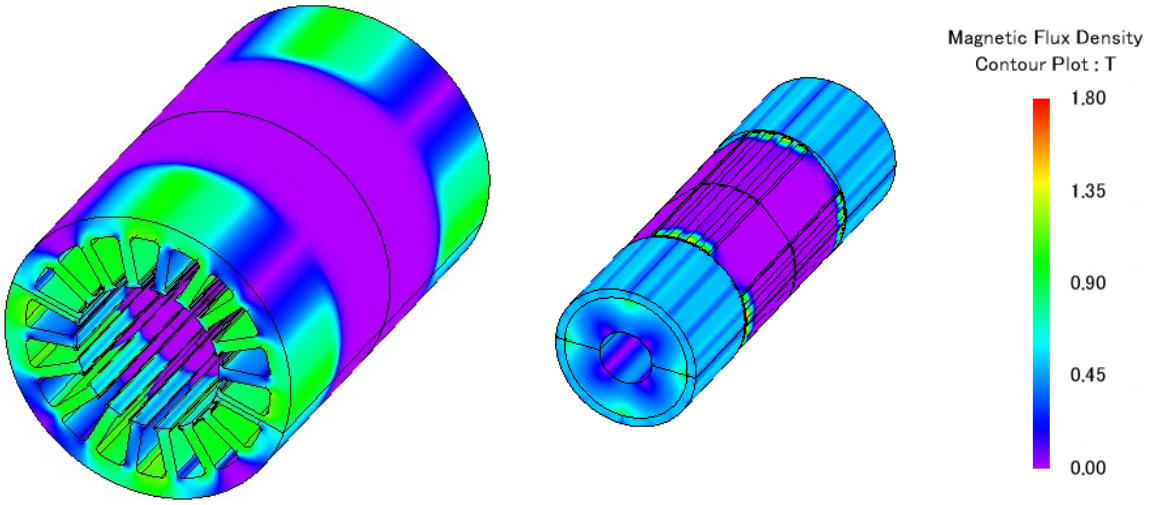

Figure 5-26. No-load magnetic flux density magnitude contour plot for hybrid rotor PMSM

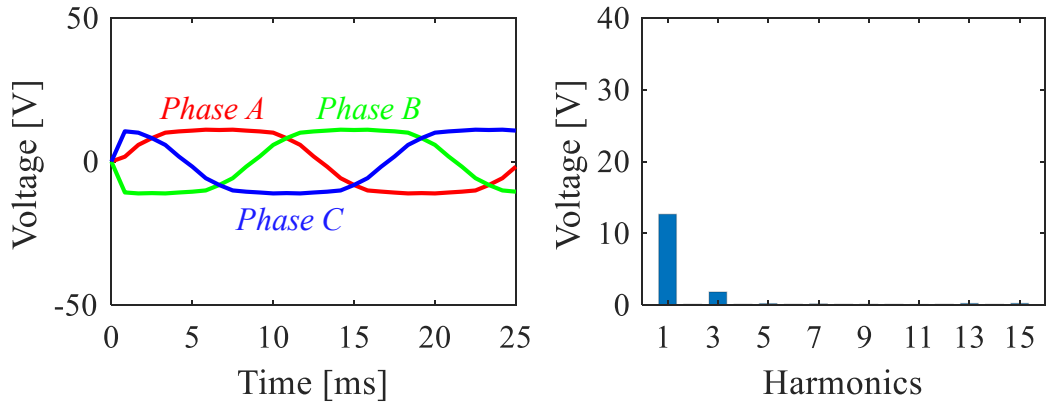

Figure 5-27. No-load voltage waveform and FFT for hybrid rotor PMSM

The back EMF waveforms and harmonic components at no-load operation are shown in Figure 5-27. As expected, the back EMF is scaled down by k_l, i.e., equal to the SPM rotor stack length ratio. The variation of torque with a current angle using rated current excitation is shown in Figure 5-28, the MTPA operation of the hybrid rotor PMSM is in between the MTPA current angle of SyR machine and SPM machine, similar to a conventional IPM machine.

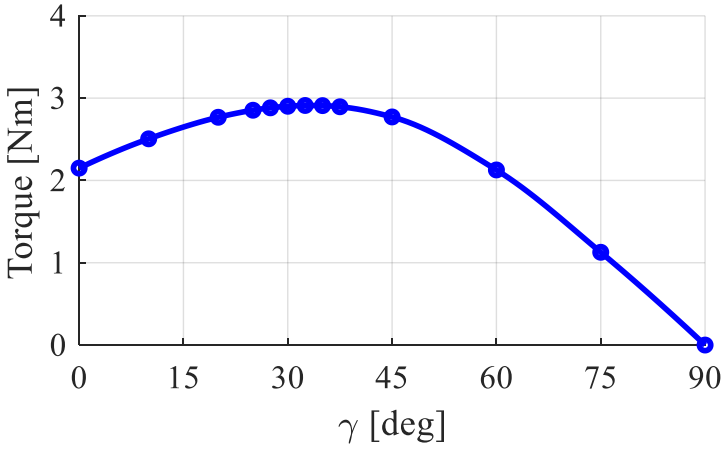

Figure 5-28. Torque vs. current angle (γ) at rated operation for hybrid rotor PMSM

The flux density distribution and voltage with rated current excitation and operating at MTPA for the hybrid rotor PMSM are shown in Figure 5-29 and Figure 5-30, respectively. Once again, from the flux density distribution on the stator back iron, it is evident that the interaction between the SPM and SyR rotor sections through the stator iron is not significant.

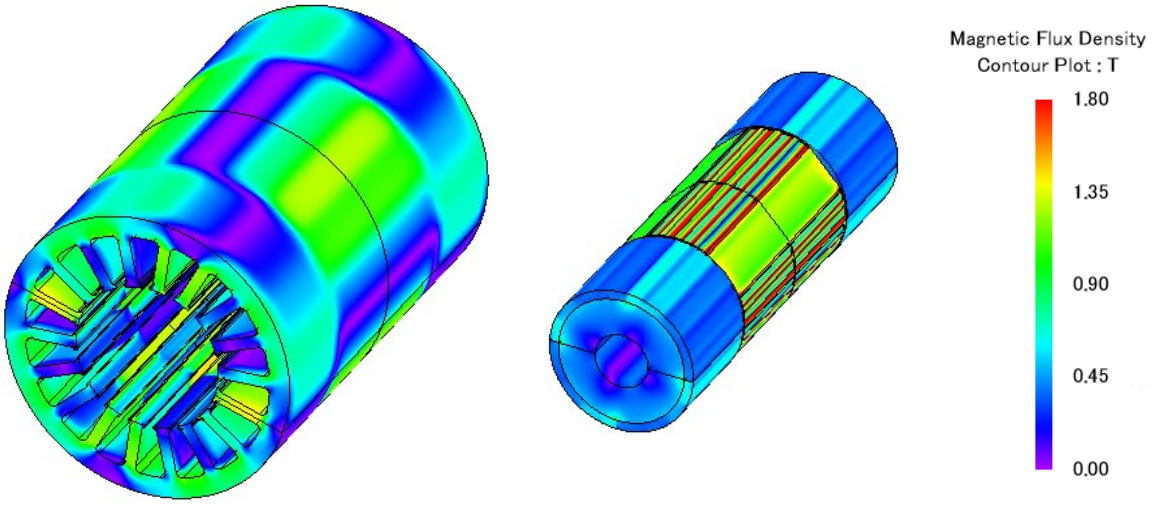

Figure 5-29. Magnetic flux density magnitude contour plot at rated MTPA operation for hybrid rotor PMSM

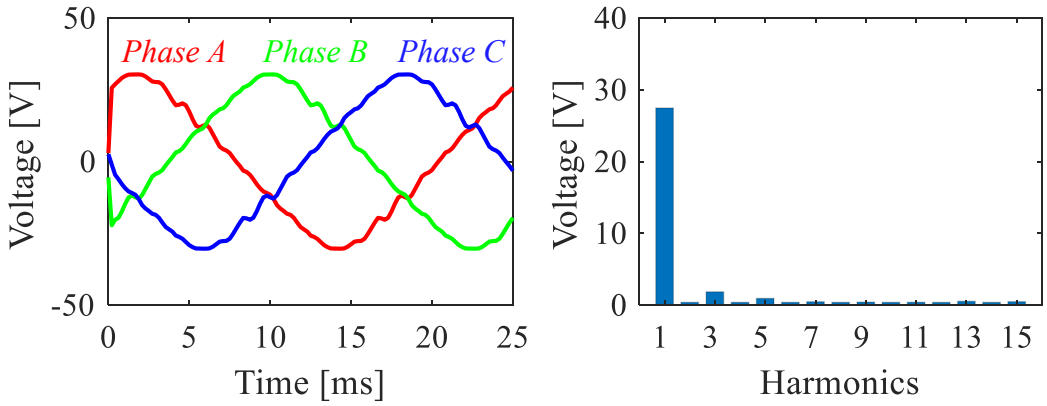

Figure 5-30. Rated MTPA operation voltage waveform and FFT for hybrid rotor PMSM

The torque waveform corresponding to MTPA for the hybrid rotor PMSM with $\alpha = 0^{o}$ is shown in Figure 5-31. The variation of torque and power factor with current are shown, and Figure 5-32, respectively.

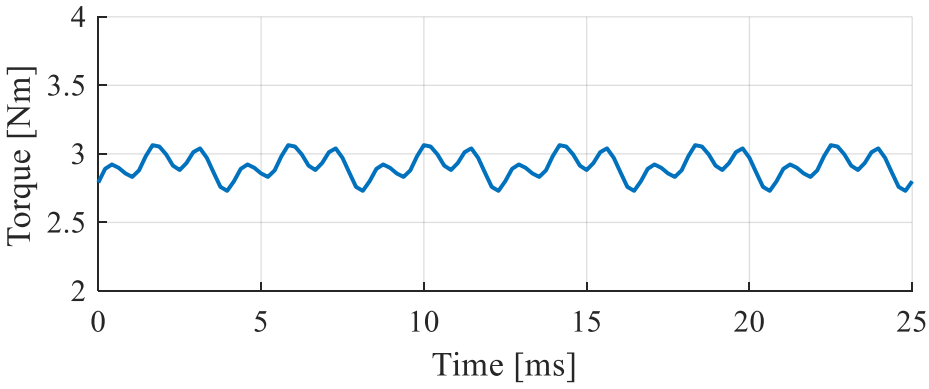

Figure 5-31. Torque waveform at rated operation using HR-PMSM rotor

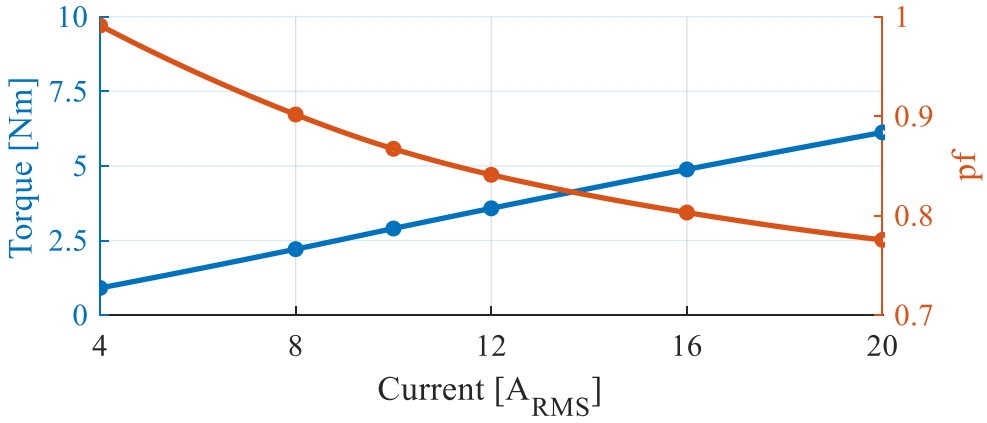

Figure 5-32. Torque and power factor as a function of current in HR-PMSM rotor

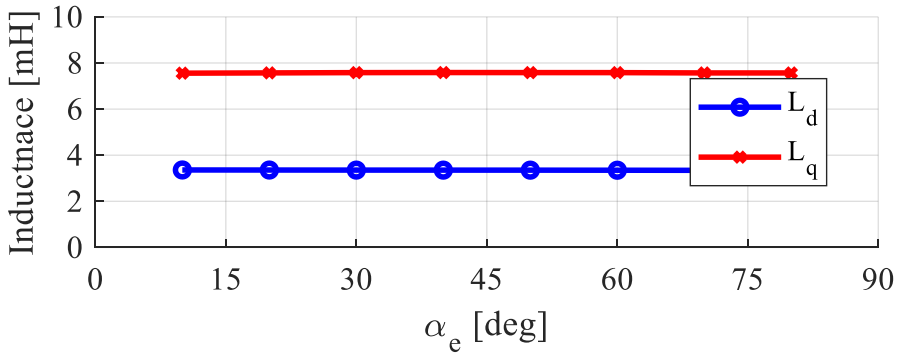

Figure 5-33. Inductance as a function of the rotor offset angle (α) using FEA for HR-PMSM rotor

The dq-axis inductance with rated current of 10 A_{rms}, as a function of α is shown in Figure 5-33. As predicted by the analytical model, the relative rotor angle, α, does not impact the inductances from the SyR rotor reference coordinate system. The analytical equivalent inductance calculation is also validated based on the inductance values from individual SPM and SyR machines.

5.4. Summary

Firstly, it is shown that once the mean airgap radius and stator dimensions are determined, an intrinsic saliency of the possible SyR machine can be estimated through analytical methods. Although such a process uses some simplifying approximations, it is shown through FEA that a good estimate of the *d*-axis inductance can be achieved. The analysis also helps in identifying optimum PM material thickness to achieve desired similar inductance between the SPM and SyR rotors.

The SyR rotor design process based on the slot-pole configuration is presented, and a baseline SyR rotor for a FSDW stator is designed. The baseline rotor is then improved through the implementation of a DE based multi-objective optimization. The PM material selection process of the SPM rotor based on the inductance and saliency of the SyR rotor is developed. Such a process ensures the initial assumptions in developing the hybrid rotor PMSM model, such as equal *d*-axis inductance between SPM and SyR rotor, are held true, and performance characteristics estimated accurately.

A complete 3D FEA model for hybrid rotor PMSM is implemented, and the flux distribution analyzed. It was shown that magnetic separation is not necessary with the use of a

conventional SyR rotor as opposed to axially laminated SyR rotors used in the state-of-the-art due to the lamination direction being orthogonal to the leakage flux between rotor sections. The equivalent machine parameters of hybrid rotor PMSM developed through the analytical model are also validated using the 3D FEA model.

Chapter 6

6. Modeling of Hybrid Rotor PMSM Using Look-Up-Table

Since the rotor structure, and hence the stator electromagnetic circuit of a hybrid rotor PMSM is not homogenous in the axial direction, it necessitates a 3D modeling approach to predict the performance. However, performing FEA using 3D CAD models, despite the use of rotational and axial symmetry to reduce the model size, is still time-consuming and computationally expensive. In this instance, the 3D FEA model analyzed in Chapter 5 required approximately 2 hours of computation time for analyzing one electrical cycle, using 8 core parallel processing. The computational cost is even more apparent in this case due to the wide range of possible combinations stemming from stack length ratios and relative rotor positions. Evaluating the speed-torque characteristics for numerous combinations using 3D FEA is not a practical method. A faster way to analyze hybrid rotor PMSM is necessary. In this chapter, an individual 2D FEA SPM and SyR machine model-based high-fidelity analysis method is proposed. The proposed method is validated with the 3D FEA model developed in the previous chapter. The torque-power, speed characteristics of the hybrid rotor PMSM are then estimated using the proposed method and compared with the analytical model developed in Chapter 3. Furthermore, the rotor combinations to maintain infinite CPSR are calculated and the performance verified.

6.1. Hybrid Rotor PMSM Model Using 2D Look-up-table (LUT)

Since the analytical model, and the preliminary 3D FEA model data indicates that the hybrid rotor PMSM machine parameters and the performance can be decoupled with a proper reference frame, a look-up-table (LUT) based model can be developed that utilizes data from 2D FEA models of SPM and SyR machines separately and can be combined using the equations developed in Chapter 3 to characterize the hybrid rotor PMSM.

Using models of SyR and SPM rotor machines described in sections 5.2.1 and 5.2.2, respectively, LUTs are created by performing 2D FEA at several stator current amplitudes and phase values. The resulting coil flux linkage is stored as a function of the rotor position. This process is achieved using an existing LUT development tool available from commercial FEA software (JMAG-RT). The LUT can then be embedded into a Simulink model that takes rotor position, instantaneous stator current amplitude, and phase as an input and give the corresponding flux linkage. The output torque, voltage, and inductance can then be computed from the current and flux linkage. The LUT based model is implemented using Simulink and shown in Figure 6-1. The outputs from SPM and SyR LUTs are scaled based on the corresponding stack length factors and combined to create the hybrid rotor PMSM. The stationary reference frame outputs are then converted to a synchronous reference frame based on the SyR rotor position.

The LUT generated in this work utilizes 2D FEA models for SPM and SyR machines separately using a total of 1350 test points corresponding to evenly distributed current amplitude and phase values. While the initial LUT generation using FEA took approximately

2.5 hours for each rotor, the analysis time for the hybrid rotor PMSM using the proposed LUT model takes 0.4 seconds. In contrast, analysis using 3D FEA on the same machine with 8-core parallel processing took approximately 2 hours for a single operating point.

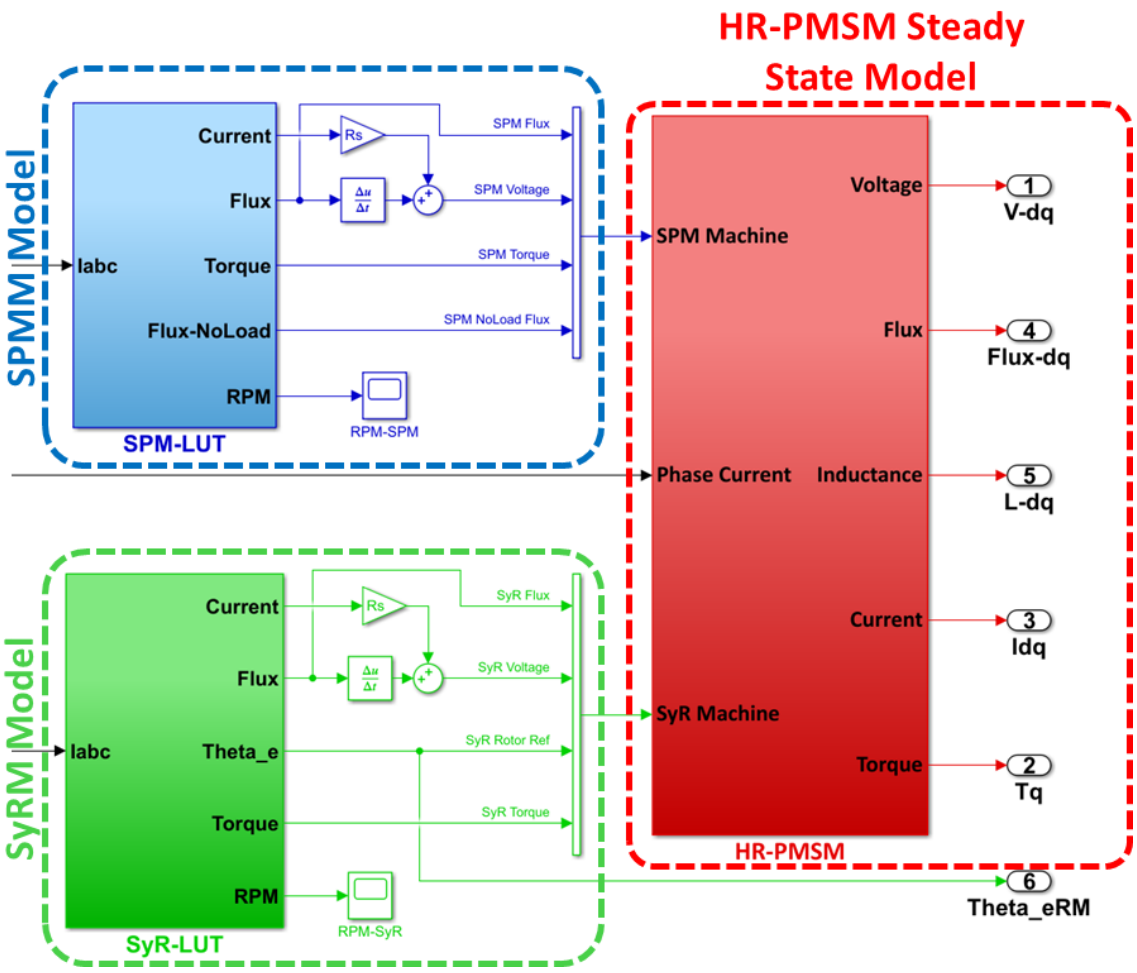

Figure 6-1. Look-up-table (LUT) based model using Simulink for hybrid rotor PMSM

To validate the 2D LUT based model of hybrid rotor PMSM, the voltage and torque waveforms are compared with the waveforms obtained from 3D FEA at MTPA operation, as shown in Figure 6-2 and Figure 6-3, respectively. It can be seen that both models are in good agreement.

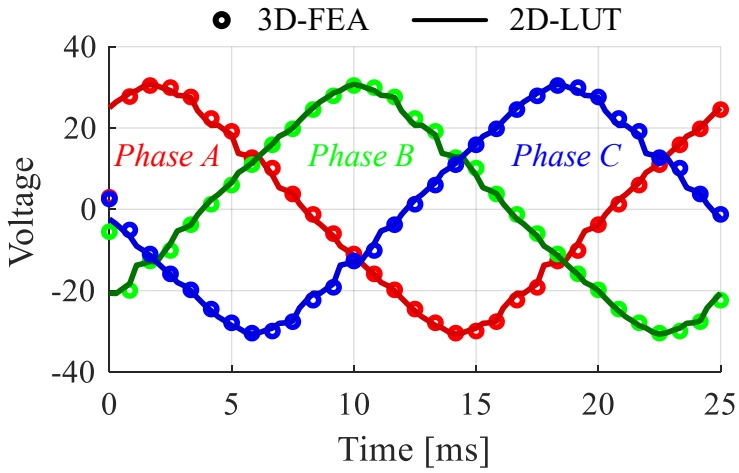

Figure 6-2. Phase voltage comparison of hybrid rotor PMSM with $k_l = 0.5$ and $\alpha = 0^o$ between FEA and LUT based models at rated operation.

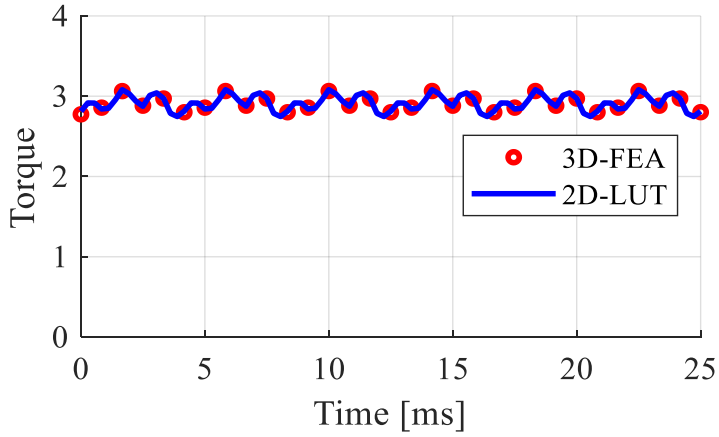

Figure 6-3. Torque comparison of hybrid rotor PMSM with $k_l = 0.5$ and $\alpha = 0^o$ between FEA and LUT based models at rated operation.

The analysis is repeated with multiple current angles to ensure any non-linear saturation effects on individual rotor sections are accounted for in the LUT model. The average torque and RMS phase voltage of the hybrid rotor PMSM as a function of the current angle are calculated and compared, as shown in Figure 6-4 and Figure 6-5, respectively. These plots also

indicate that both models are in good agreement. A similar comparison is also made by keeping the current angle at MTPA of the SyR rotor and changing the SPM rotor relative position angle in both 2D LUT and 3D FEA. The RMS phase voltage and average torque operating with a rated current of 10 A_{rms} are compared, as shown in Figure 6-6 and Figure 6-7, respectively.

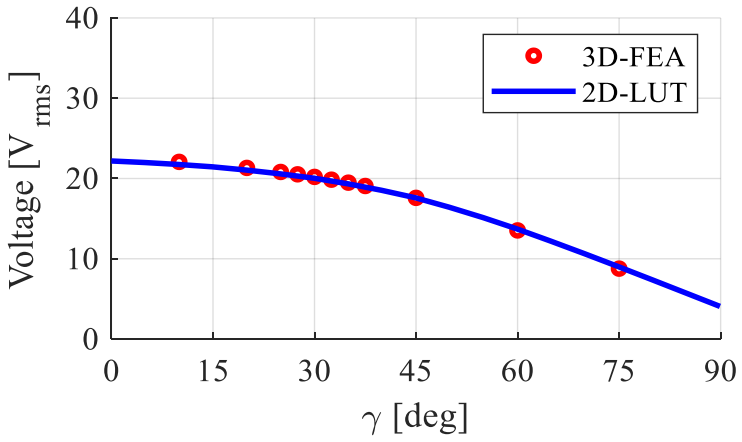

Figure 6-4. Phase RMS voltage vs. current angle comparison of hybrid rotor PMSM with $k_I = 0.5$ and $\alpha = 0^o$ between FEA and LUT based models.

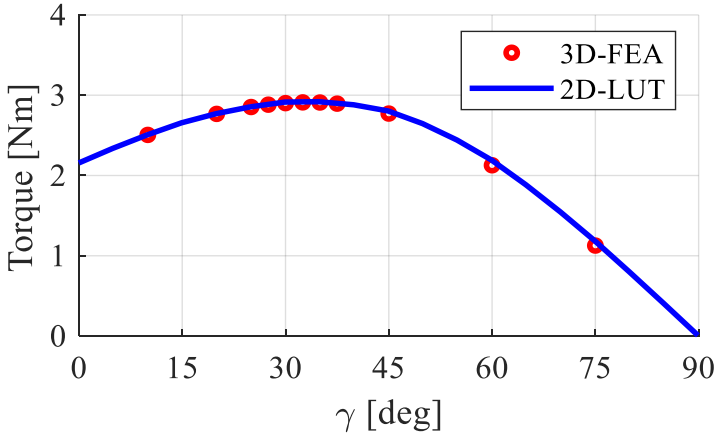

Figure 6-5. Torque vs. current angle comparison of hybrid rotor PMSM with $k_I = 0.5$ and $\alpha = 0^o$ between FEA and LUT based models.

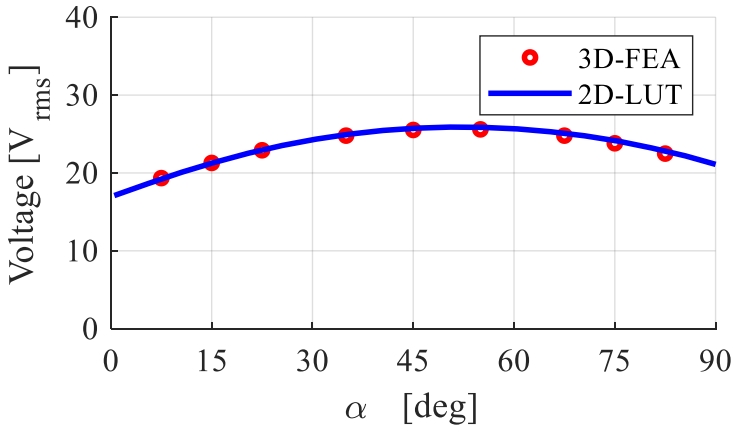

Figure 6-6. Phase RMS voltage vs. α comparison between FEA and LUT based models of hybrid rotor PMSM with $k_I = 0.5$ and operating at rated MTPA of SyR rotor.

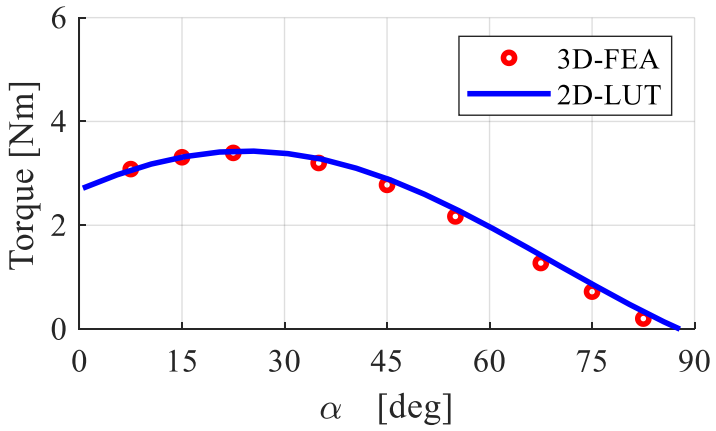

Figure 6-7. Torque vs. α comparison between FEA and LUT based models of hybrid rotor PMSM with $k_I = 0.5$ and operating at rated MTPA of SyR rotor

There is a slight deviation in the average torque as α approaches 90° while there seems to be a good agreement between the voltages obtained from both models. This discrepancy could be due to the fact that as α increases, the SPM rotor is exposed to increasing amplitude of demagnetizing current, thus increasing leakage components and interaction between the two

rotors. Such leakage and cross-coupling between the rotor sections is not captured in LUT model. This could potentially explain the higher degree of deviation in torque at higher offset angles. Despite the slight difference, it is evident that the 2D LUT model captures the hybrid rotor PMSMs performance across a range of operating points with sufficient accuracy. The 2D LUT model, in part, also validates the analytical model developed since the Simulink model is developed based on the analytical equations but uses a high fidelity FEA based LUT. Based on the 2D LUT validations, it can be used to replace the 3D FEA model.

6.2. Operating Characteristics using Hybrid Rotor PMSM LUT

Using the combination of 2D LUT models of SPM and SyR rotors, the LUT for the hybrid rotor PMSM can be generated that corresponds to different values of α and k. This is achieved by utilizing a set of input currents, as shown in Figure 6-8 and evaluate the Simulink model shown in Figure 6-1 and store the corresponding flux linkage and torque values. The flux linkage and torque values from hybrid rotor PMSM LUT for k_I = 0.5 and α = -30^o are shown in Figure 6-9 and Figure 6-10, respectively.

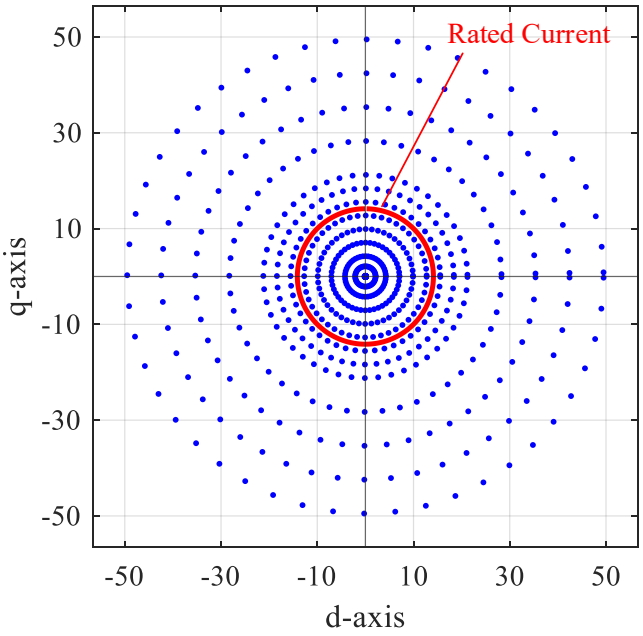

Figure 6-8. Operating points for generation of hybrid rotor PMSM LUT

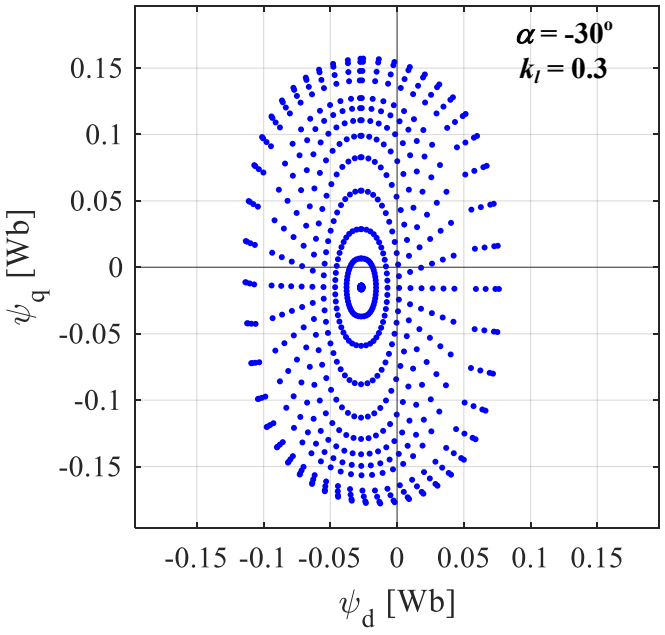

Figure 6-9. Average flux linkage in LUT of hybrid rotor PMSM with $k_I = 0.3$, $\alpha = -30^o$

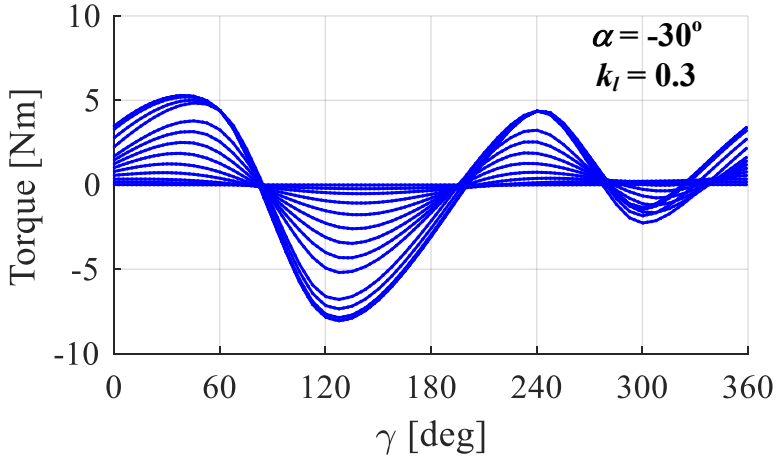

Figure 6-10. Average torque in LUT of hybrid rotor PMSM with $k_l = 0.3$, $\alpha = -30^o$

The field weakening operating characteristics of the hybrid rotor PMSM can then be evaluated for any stack length ratio and offset angle combination. A flow chart of the algorithm designed to determine the operating characteristics is shown in Figure 6-11.

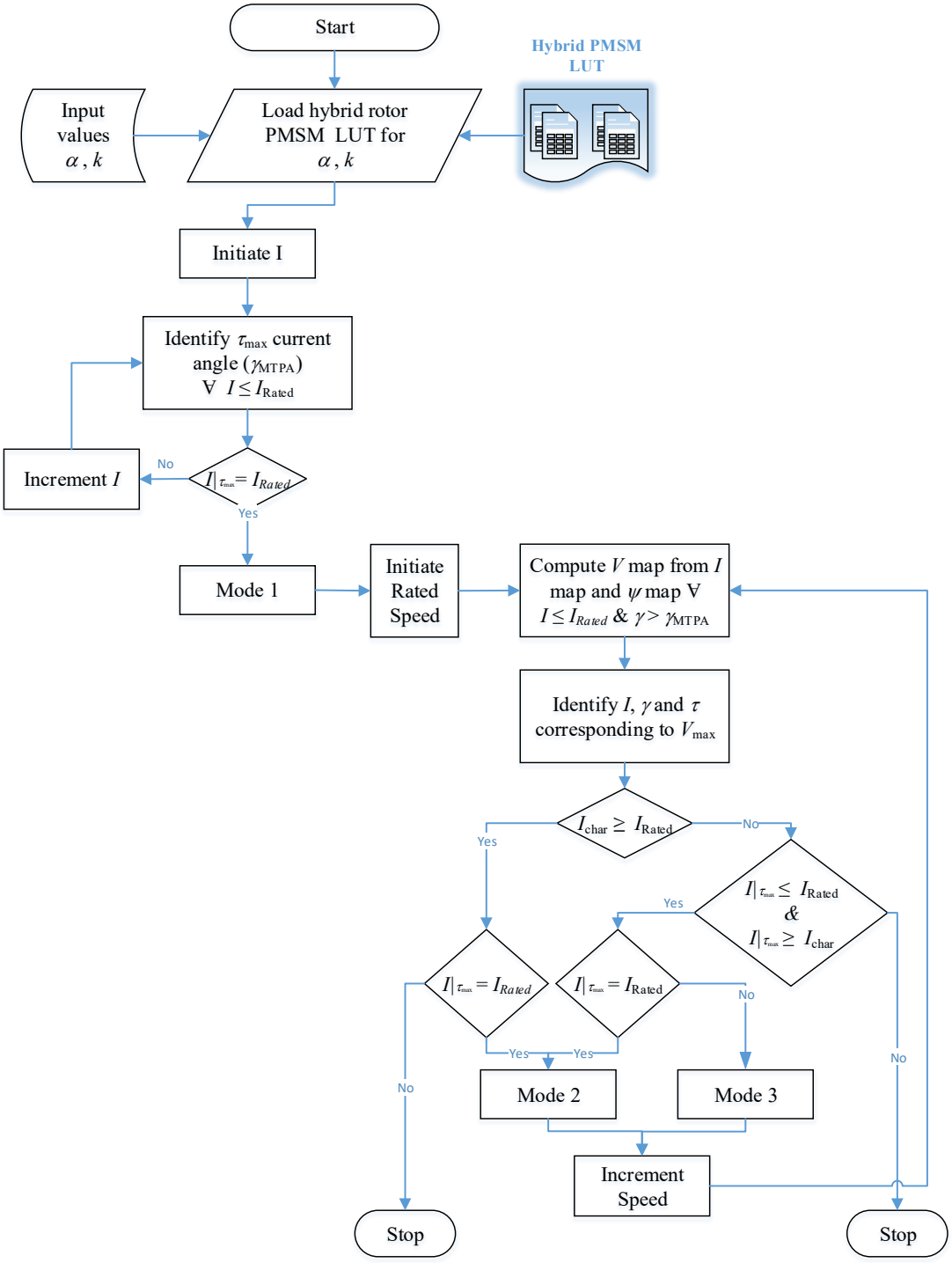

Figure 6-11. Flow chart for identification of current command trajectory and performance characteristics of hybrid rotor PMSM

The current command trajectory obtained from the hybrid rotor PMSM LUT model is overlaid onto the current command trajectories calculated from the unified analytical model described in Chapter 3. The comparison is shown in Figure 6-12. It can be seen that there is a sufficient match between the analytical model and the FEA based LUT model. Similarly, the torque and power vs. speed of the hybrid rotor PMSM determined from both methods is also compared, as shown in Figure 6-13. It can be seen that there is a considerable deviation in the amplitude, but the overall trend of the speed vs. torque and power curves is comparable between the two methods.

The LUT model uses data obtained from FEA modeling that includes resistive losses. Also, the material properties in FEA include non-linearities such as saturation. Although the inductance and PM flux linkage values in the analytical model used in the comparison consider the FEA estimated values from SyR and SPM rotor designs from sections 5.2.1 and 5.2.2, respectively, these are fixed quantities since the analytical model assumes linear material with infinite permeability and a loss-less system. The analytical model can be further improved to include losses and non-linearities.

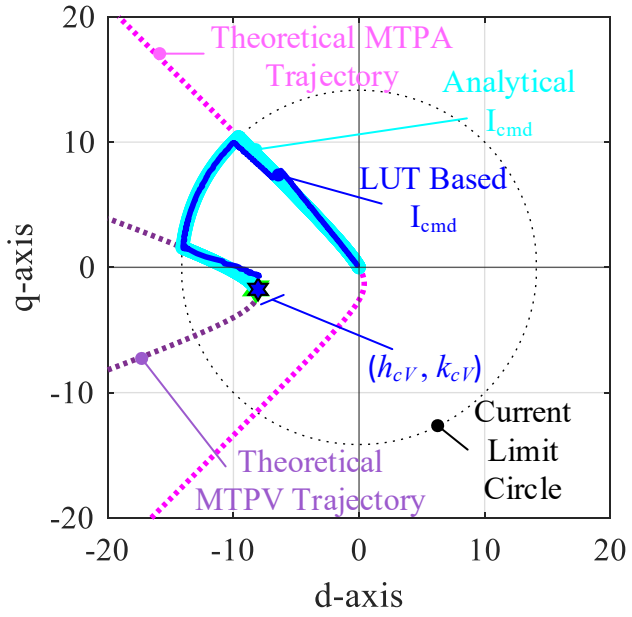

Figure 6-12. Current command trajectories comparison between analytical model and LUT based model of hybrid rotor PMSM with $k_l = 0.3$, $\alpha = 30^o$

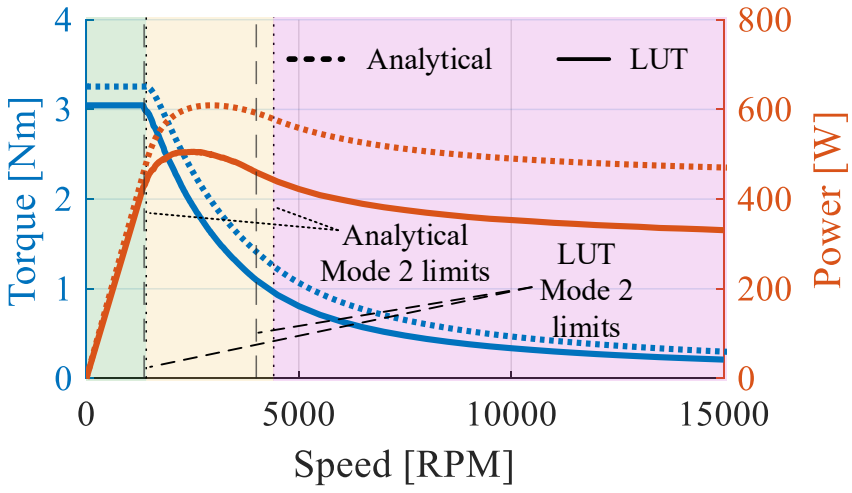

Figure 6-13. Torque and power vs. speed comparison between analytical model and LUT based model of hybrid rotor PMSM with $k_l = 0.3$, $\alpha = 30^o$

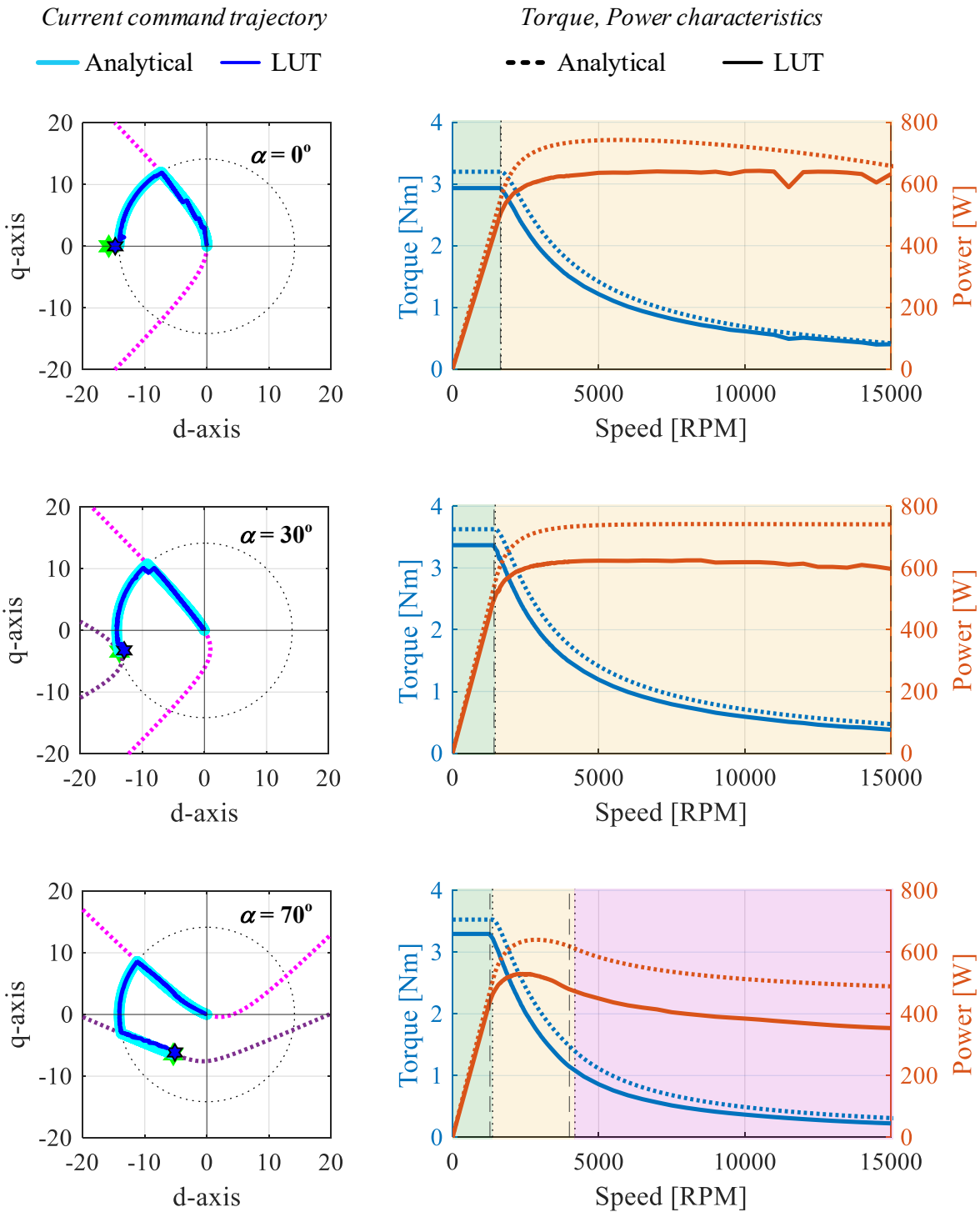

Figure 6-14. Torque and power characteristics of hybrid rotor PMSM with $k_l = 0.5$ and $\alpha = [0, 30, 70]^{\circ}$

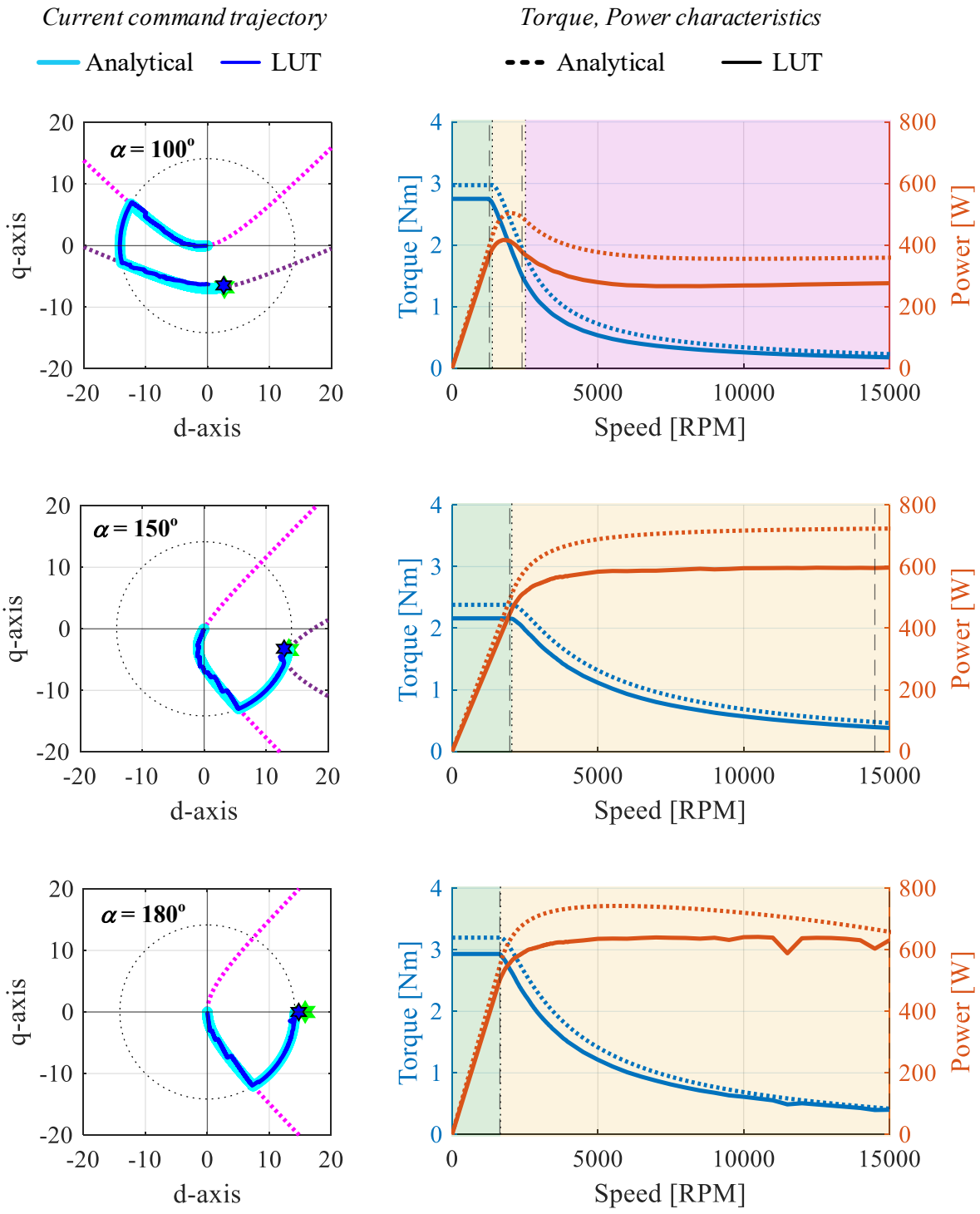

Figure 6-15. Torque and power characteristics of hybrid rotor PMSM with $k_l = 0.5$ and $\alpha = [100, 150, 180]^{\circ}$

A comparison of current command trajectories, as well as torque and power vs. speed for a range of α with k_l = 0.5, are shown in Figure 6-14 and Figure 6-15. Overall, it can be concluded that the analytical model gives a good estimate of the field weakening performance characteristics of a hybrid rotor PMSM. However, the discrepancies in amplitude due to several simplifying assumptions used in the analytical model still need to be addressed.

6.3. Infinite CPSR Hybrid Rotor PMSM - LUT

With the available SPM and SyR rotors, possible stack length ratios and optimum rotor offset values can now be calculated using (3.66) and (3.67). The lower and upper limits of k_l are calculated as 0.447 and 0.774, respectively, for the proof-of-concept hybrid rotor PMSM. The variation of optimum α between the k_l limits to obtain infinite CPSR using the proof-of-concept hybrid rotor PMSM is plotted, as shown in Figure 6-16.

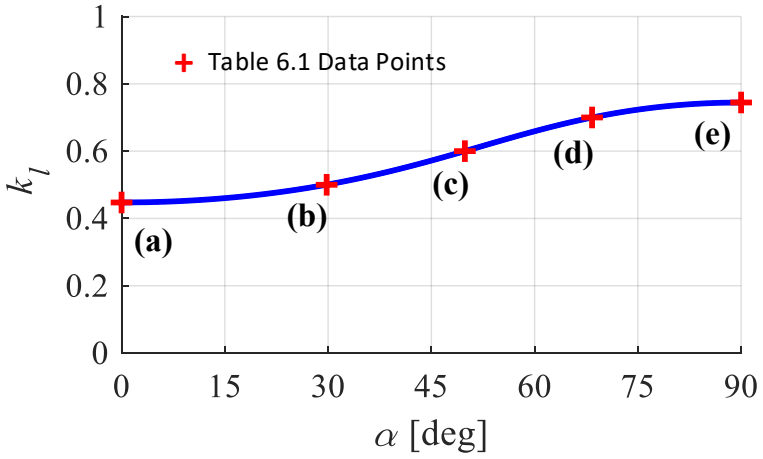

Figure 6-16. Optimum k_l ratio and α for proof-of-concept hybrid rotor PMSM to obtain infinite CPSR

Table 6-1. Optimum parameters for infinite CPSR with proof-of-concept hybrid rotor PMSM

Machine Combination	(a)	(b)	(c)	(d)	(e)
k_I	0.447	0.5	0.6	0.7	0.744
α **[deg]**	0	29.8	49.9	68.35	90

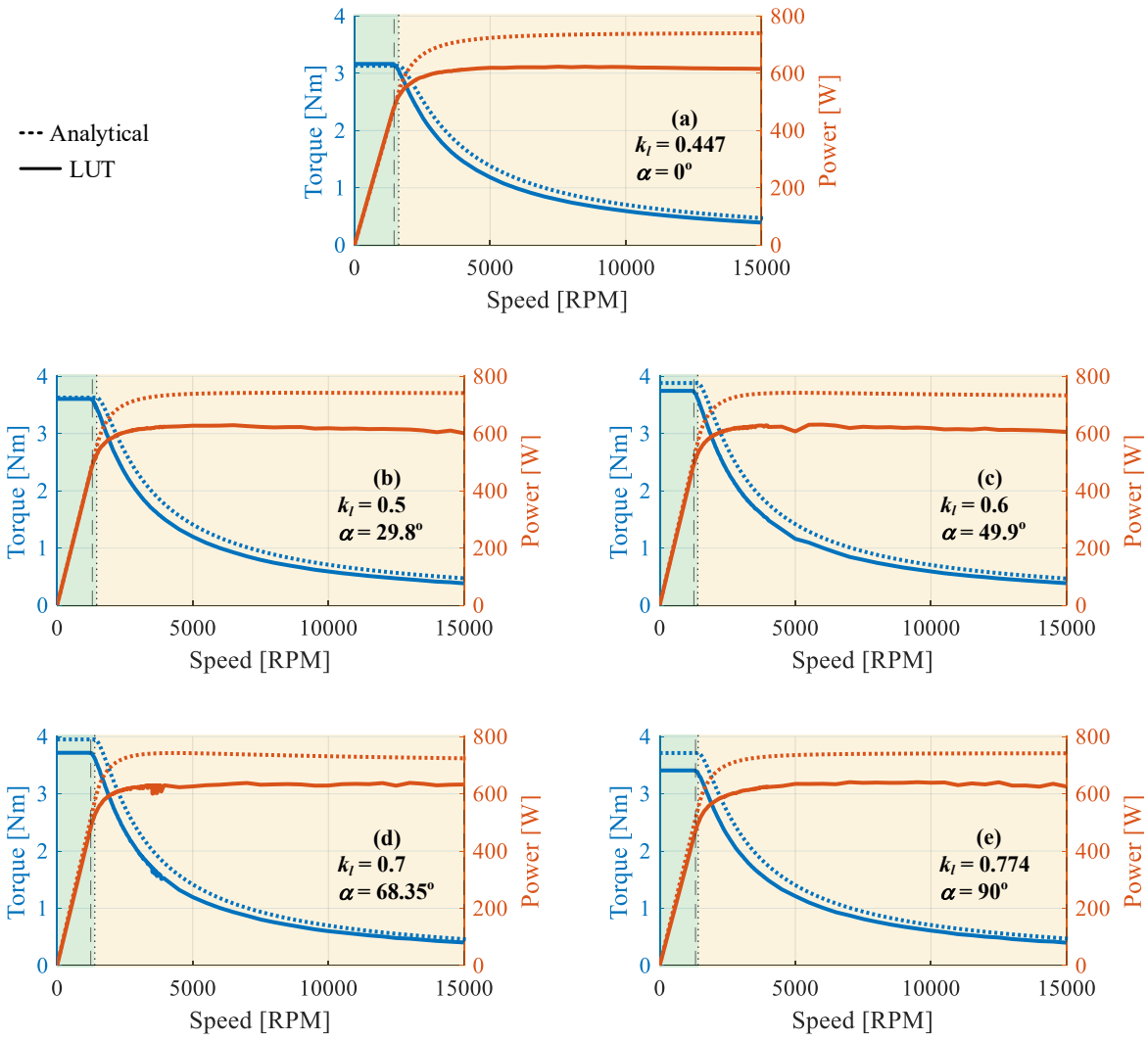

Figure 6-17. Speed and Power characteristics of optimum hybrid rotor PMSM combinations

Few data points from Figure 6-16 are identified and listed in Table 6-1. The torque, power vs. speed characteristics of the machines obtained with parameters from Table 6-1 are shown in Figure 6-17. Although the SyR rotor was designed to withstand only up to 6000 RPM, the torque, power vs. speed characteristics shown above are plotted to 15,000 RPM to show the sustained CPSR capability of the selected hybrid rotor combinations.

It can be observed that all the machine combinations are within the same output power level over extended speed. However, the maximum torque during mode 1 operation and corner speed, i.e., the speed at which mode 2 operation begins, varies depending on the rotor combination selected as observed from Figure 6-17. Depending on the nature of the application's requirement, an optimum CPSR configuration can be selected. The key metrics for this choice can be maximum torque, torque per unit of PM volume and corner speed. The optimum PM volume can be identified using a PM utilization factor that can be defined as,

$$\text{PM Utilization} = \frac{\tau_{\max}\left(k_l\right)}{k_l} \tag{6.1}$$

where $\tau_{max}(k_l)$ is the maximum possible torque as a function of k_l for the CPSR configurations. Since k_l corresponds to the equivalent stack length of the PM rotor section, the PM utilization factor, with the unit of Newton, represents a maximum possible torque per unit length of PM rotor. Hence choosing the highest PM utilization combination gives maximum possible torque with minimum PM volume while maintaining infinite CPSR, for the give SPM and SyR rotor combinations. Similarly, corresponding combinations for maximum torque or desired corner speed can be selected if starting torque or precise corner speed have higher priority. The three

metrics for all possible infinite CPSR configurations from Figure 6-17 are calculated analytically and plotted in Figure 6-18.

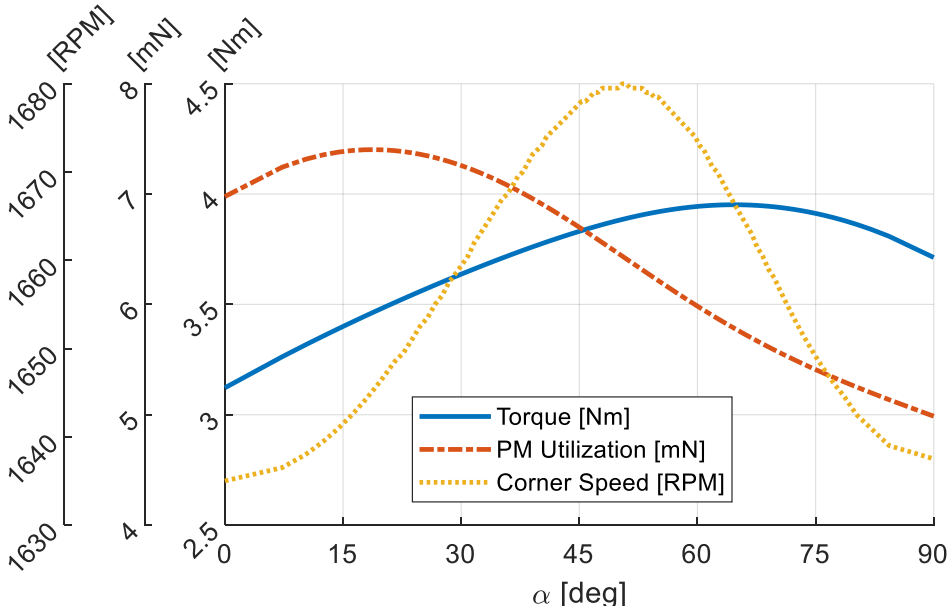

Figure 6-18. Optimum infinite CPSR hybrid rotor PMSM selection metrics

6.4. Summary

Since 3D FEA models are computationally intensive and time-consuming, estimating torque/power-speed characteristics for the hybrid rotor PMSM using 3D FEA is not feasible. A high fidelity LUT based modeling method for hybrid rotor PMSM, that combines LUT obtained from 2D FEA of SPM and SyR machines and equivalent machine parameter calculation from the analytical model is proposed in this chapter.

The proposed high fidelity LUT model is rigorously verified by comparing with 3D FEA results at various operating points and rotor offset angle combinations. Once the LUT based model is validated, a value search algorithm is implemented to estimate the current

command trajectories and associated operation characteristics of a hybrid rotor PMSM in field weakening operation. The results from the LUT based model and analytical model developed in Chapter 3 are compared. Based on the LUT model results, the unified field weakening analytical model for synchronous AC machines is validated. The optimum stack length ratio and offset angles to obtain infinite CPSR were also calculated for the hybrid rotor PMSM and the power-speed characteristics shown from different sample points, thus validating the infinite CPSR capability of hybrid rotor PMSM. An optimum hybrid rotor combination selection parameters based on the application requirements are outlined.

Chapter 7

7. Nonlinearities and Practical Factors

To linearize the model and simplify calculations, the analytical model developed utilizes some assumptions such as, ignoring saturation nonlinearities, leakage inductances, as well as resistive and iron losses. The comparison between the FEA based LUT model and the analytical model partially revealed the impact of these assumptions. In this chapter, each of these non-ideal factors will be added to the analytical model and the impact on field weakening performance quantified. The torque-power vs. speed characteristics are re-evaluated with the nonlinearities included and compared against the linear analytical model as well as the LUT model predictions.

7.1. Losses and Saturation

A typical steady-state equivalent circuit model for a lossy PMSM in *dq* reference frame as shown in Figure 7-1, where R_s is the stator phase resistance, R_c is the equivalent iron loss resistance, and L_{ls} is the stator leakage inductance. The flux linkage components in the *dq* axis can be written as,

$$\begin{aligned} \lambda_{dm} &= I_{dm} L_{dEq} + \psi_{Eq} \cos(\alpha) \\ \lambda_{qm} &= I_{qm} L_{qEq} + \psi_{Eq} \sin(\alpha) \end{aligned} \tag{7.1}$$

where I_{qm} and I_{dm} are the magnetizing current components that are responsible for useful torque output. The magnitude and hence the impacts of stator leakage inductances are typically

negligible with the proposed aspect ratio recommendation, and hence will not be considered in this work.

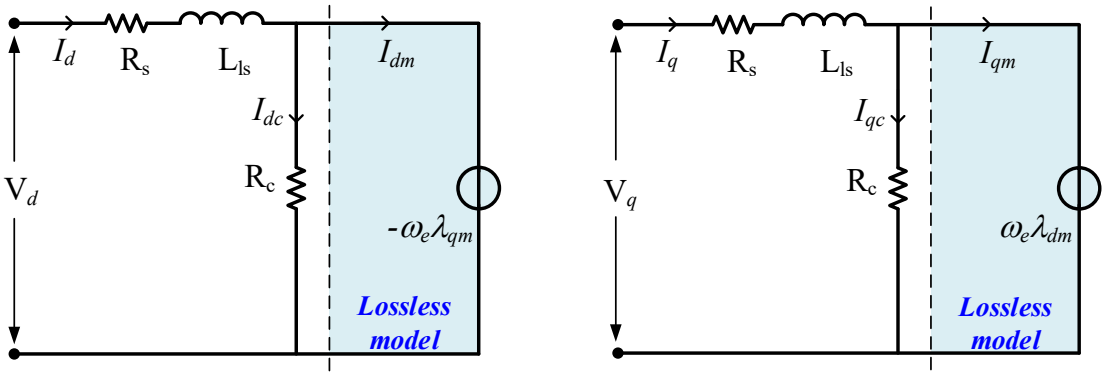

(a) (b)

Figure 7-1. Equivalent circuit models for PMSM with phase resistance, iron loss resistance and leakage inductance added (a) *d*-axis, (b) *q*-axis

7.1.1. Phase Resistance

Adding stator phase resistance to the lossless *dq*-model, the voltage equations will be written as,

$$\begin{aligned} V_d &= R_s I_d - \omega_e I_q L_{qEq} - \omega_e \psi_{Eq} \sin(\alpha) \\ V_q &= R_s I_q + \omega_e I_d L_{dEq} + \omega_e \psi_{Eq} \cos(\alpha) \end{aligned} \tag{7.2}$$

Applying voltage limit constraint and rearranging the terms yields a voltage limit locus as,

$$\left[(I_d - 0)\frac{R_s}{\omega_e L_{qEq}} - \left(I_q + \frac{\psi_{Eq}\sin(\alpha)}{L_{qEq}}\right)\right]^2 \Big/ \left(\frac{V_s}{\omega_e L_{qEq}}\right)^2 + \left[(I_q - 0)\frac{R_s}{\omega_e L_{dEq}} + \left(I_d + \frac{\psi_{Eq}\cos(\alpha)}{L_{dEq}}\right)\right]^2 \Big/ \left(\frac{V_s}{\omega_e L_{dEq}}\right)^2 \leq 1 \tag{7.3}$$

Conventionally, we know that the voltage limit locus forms an ellipse that is centered on the characteristic current while the major and minor axes lengths depend on the *d*-axis and *q*-axis reactance amplitudes, respectively. However, (7.3) does not fit into an easily identifiable standard ellipse equation. Using appropriate coordinate transformations, a standard equation for an ellipse rotated counterclockwise by an arbitrary angle, β, around its center denoted by (h_c, k_c) can be written as,

$$\frac{\left[(x-h_c)\cos(\beta)-(y-k_c)\sin(\beta)\right]^2}{a^2} + \frac{\left[(x-h_c)\sin(\beta)+(y-k_c)\cos(\beta)\right]^2}{b^2} = 1 \qquad (7.4).$$

While there are similarities between (7.3) and (7.4), it is also evident that the locus represented by (7.3) has a rotation center different from the ellipse center. In addition, the rotation is not governed by the familiar trigonometric identities, which makes the rotation in each axis asymmetric. The variation of the shape of voltage limit loci represented by (7.3) at rated speed and different offset angle values is shown in Figure 7-2 as a function of stator resistance.

The observed behavior confirms that the voltage ellipse rotates counterclockwise as the normalized resistance values increases. The rotation of voltage limit ellipse was first observed by Li. et al. in [59] while analyzing the impacts of temperature on the performance of IPM machines. As shown in Figure 7-3, as the temperature increases the voltage limit ellipse rotates counterclockwise. While the reason for the rotation was not identified in Li's work, it is evident that the resistivity of copper increases with temperature, resulting in an increase of phase resistance, and based on (7.3), causes the voltage limit locus to rotate.

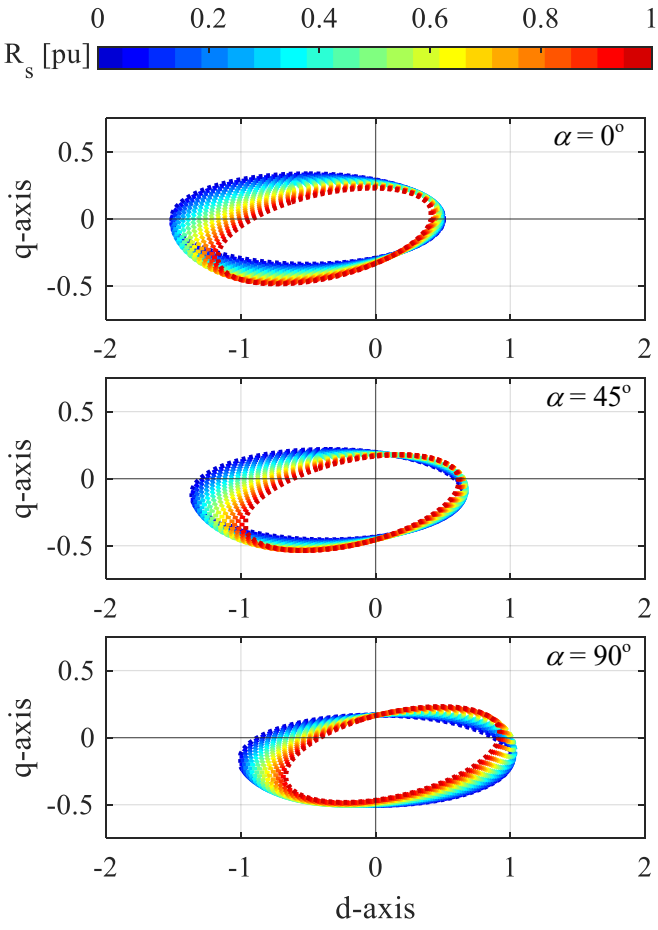

Figure 7-2. Impact of stator resistance on voltage limit loci for a given operating speed

In addition, from (7.3) it can be observed that the scaling term introduced by phase resistance is inversely proportional to the operating speed. Hence, the impact of stator resistance diminishes as operating speed increases, i.e., mode 2 and mode 3 current command trajectories are not significantly impacted by phase resistance.

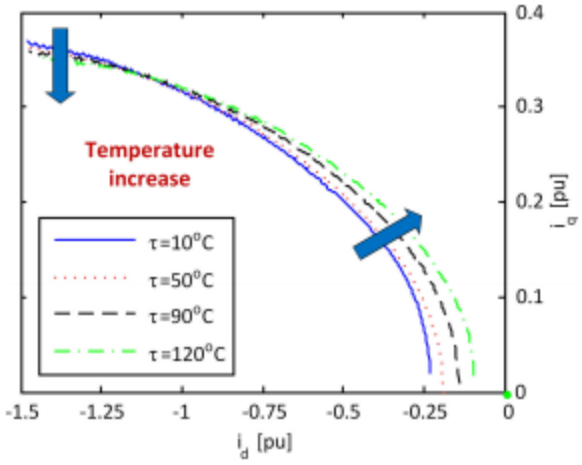

Figure 7-3. Experimental results shown in [59] identifying the counterclockwise rotation of voltage limit ellipse in *dq* plane as temperature increases.

7.1.2. Saturation in Laminations

The effects of magnetic saturation in the stator and rotor laminations are primarily reflected on the torque output as a change in *dq* inductance values. To include the impact of saturation on the machine's performance, the inductances used in the analytical calculation of voltage and torque equations must be modeled as a function of *dq* current amplitudes. While there are analytical methods such as magnetic equivalent circuit (MEC) can be used, these are usually tedious and require in-depth analysis performed for each section of the rotor and stator geometry. Alternatively, the change in inductance as a function of stator current can be estimated using FEA and a look-up-table constructed to be used in the analytical model. The *dq* inductance map constructed using FEA for the proof-of-concept machine along with the analytical current command trajectory overlay is shown in Figure 7-4. It is seen that there is some variation in both *d* and *q* axis inductances of the machine, particularly for mode 3

operation where the current amplitude reduces and hence a higher degree of variation in saturation effects and resulting inductance.

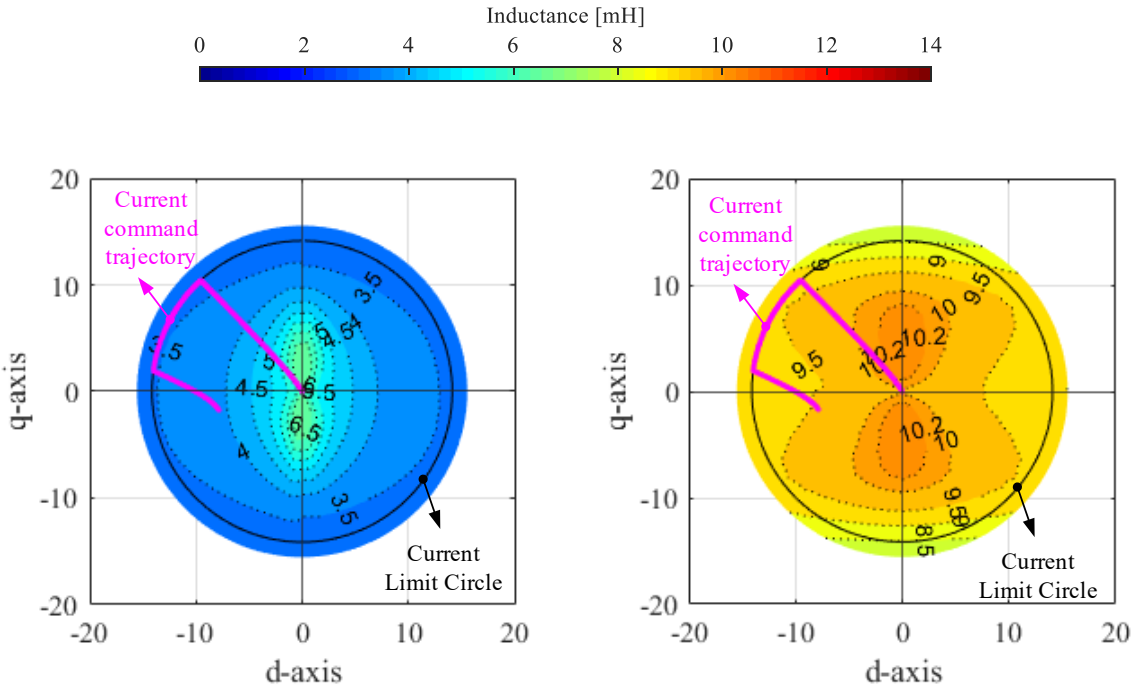

(a) (b)

Figure 7-4. Inductance map as a function of *dq* currents and overlayed current command trajectory for the prototype machine with $k_l = 0.3$ and $\alpha = 30^o$. (a) L_{dEq}, (b) L_{qEq}

7.1.3. Iron Loss

From the equivalent circuits shown in Figure 7-1, the stator current splits into magnetizing component and core loss components, I_{dc}, I_{qc} in the *d* and *q* axis circuits, respectively. Considering the magnetizing component in parallel with the core loss resistance, the current, and applying Kirchhoff's circuit laws,

$$\begin{aligned} I_{dm} &= I_d - \frac{V_{dm}}{R_c} \\ I_{qm} &= I_q - \frac{V_{qm}}{R_c} \end{aligned} \tag{7.5}$$

where,

$$\begin{aligned} V_{dm} &= -\omega_e \lambda_{qm} = -\omega_e I_{qm} L_{qEq} - \omega_e \psi_{mEq} \sin(\alpha) \\ V_{qm} &= \omega_e \lambda_{dm} = \omega_e I_{dm} L_{dEq} + \omega_e \psi_{mEq} \cos(\alpha) \end{aligned} \tag{7.6}$$

Substituting (7.6) into (7.5), the magnetizing currents can be calculated as,

$$\begin{aligned} I_{dm} &= \frac{I_d R_c^2 + \omega_e R_c \left[I_q L_{qEq} + \psi_{Eq} \sin(\alpha) \right] - \omega_e^2 L_{qEq} \psi_{Eq} \cos(\alpha)}{R_c^2 + \omega_e^2 L_{dEq} L_{qEq}} \\ I_{qm} &= \frac{I_q R_c^2 - \omega_e R_c \left[I_d L_{dEq} + \psi_{Eq} \cos(\alpha) \right] - \omega_e^2 L_{dEq} \psi_{Eq} \sin(\alpha)}{R_c^2 + \omega_e^2 L_{dEq} L_{qEq}} \end{aligned} \tag{7.7}$$

Typically, the inductances in (7.7) must correspond to the magnetizing current amplitude and determined iteratively as functions of the magnetizing currents based on the inductance maps shown in Figure 7-4. However, for a well-designed machine, the iron loss resistance (R_c) is usually higher by at least an order of magnitude compared to the phase resistance (R_s). This leads to a minor difference between the stator and magnetizing current components. Thus, the inductance value identified using I_d and I_q can be used as a reasonable approximation for the proof-of-concept machine. However, it is important to note that for machines operating at higher speeds, such approximation may not be suitable. Hence, the inductance must be determined by iteratively solving the two equations in (7.7). Finally, the output torque accounting for the nonlinearities and iron loss can be calculated as,

$$T_{em} = \frac{3}{2}\frac{P}{2}\frac{\left[V_{dm}I_{dm} + V_{qm}I_{qm}\right]}{\omega_e} = \frac{3}{2}\frac{P}{2}\left[I_{qm}\psi_{Eq}\cos(\alpha) - I_{dm}\psi_{Eq}\sin(\alpha) - L_{dEq}I_{dm}I_{qm}\left(\xi_{Eq} - 1\right)\right] \tag{7.8}$$

7.2. Operation Characteristics - Including Nonlinearities

Using the analytical current command trajectory and the inductance LUT, the magnetizing flux linkage and corresponding magnetizing current can be calculated using (7.6) and (7.7) respectively. The magnetizing current is substituted back into (7.3) and iteratively solved to obtain the operating speed. The current command trajectories, as well as torque - power vs. speed for a range of α with k_l = 0.5 of the hybrid rotor PMSM are calculated using the nonlinear model and compared with the linear model, and the LUT model data from Figure 6-14 and Figure 6-15. The comparison results are shown in Figure 7-5 and Figure 7-6. While the current command trajectories for all 3 models are in good agreement, the linear model shows the highest error in torque and power during field weakened operation. The nonlinear model exhibits a reasonably good agreement with the LUT model predicted field weakening performance.

It is to be noted that the phase resistance is considered as constant (0.39 Ω) since temperature effects are not included in LUT model, and iron loss (R_c) neglected in both models. Ideally R_c must be modeled using LUT as a function of current and frequency. For the machine under consideration, most of the difference between linear and nonlinear models is attributed to the saturation effects causing variation in inductance at different operating points.

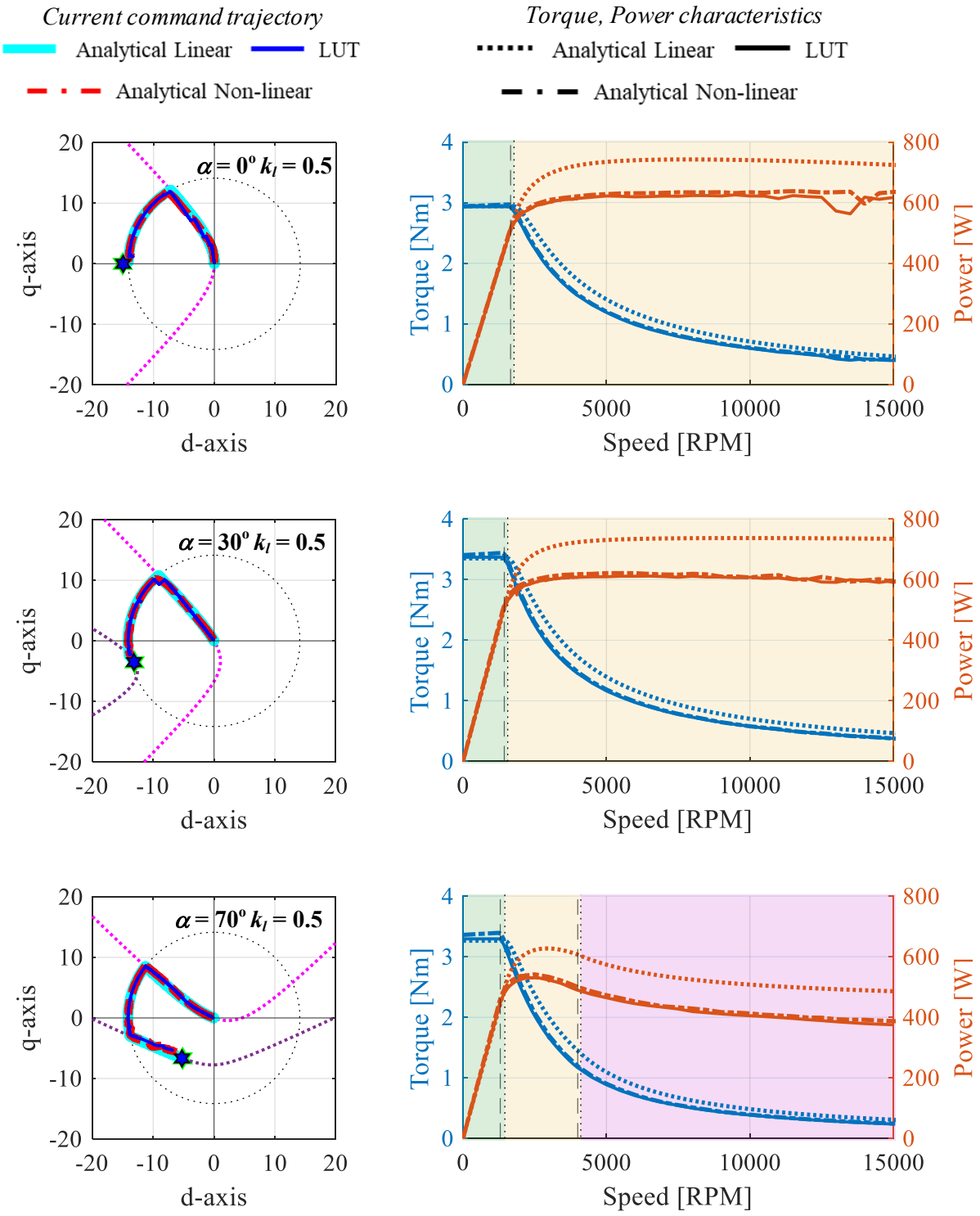

Figure 7-5. Torque and power characteristics of hybrid rotor PMSM with $k_l = 0.5$ and $\alpha = [0, 30, 70]^{\circ}$

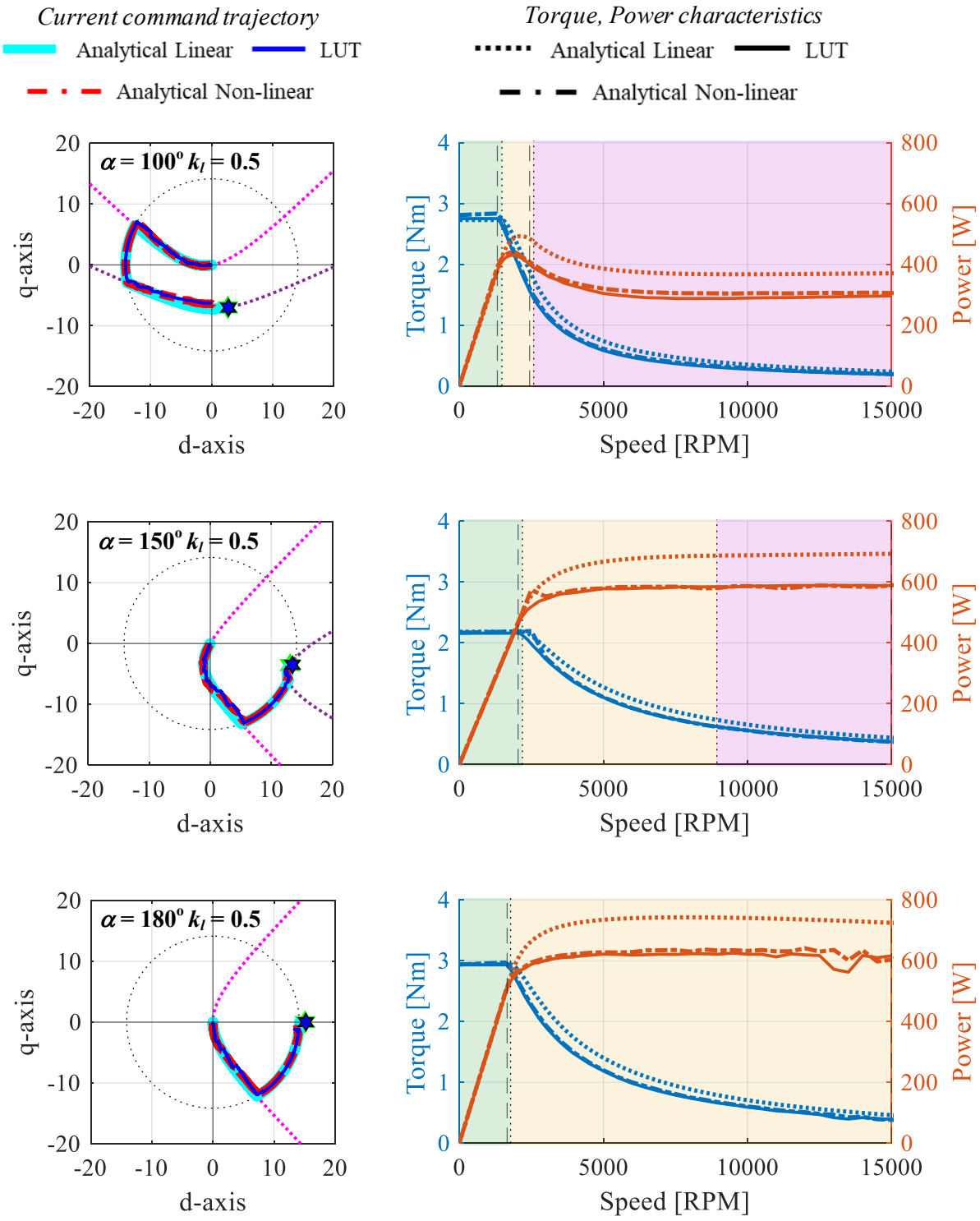

Figure 7-6. Torque and power characteristics of hybrid rotor PMSM with $k_l = 0.5$ and $\alpha = [100, 150, 180]^{\circ}$

7.3. Limitations and Practical Factors

While the analytical nonlinear model shows a reasonably good estimation of the hybrid rotor PMSM's field weakening performance, there are some limitations to the modeling methods used. In addition, there are practical factors that inherently impact the hybrid rotor PMSM due to the asymmetry of the rotor geometry.

7.3.1. Saturation modeling

For the impacts of saturation to be included in analytical model, the inductance must be modeled as a function of the current amplitude. This requires determining the inductance of the machine either using analytical magnetic equivalent circuit (MEC) or FEA. While the developing analytical MEC for SPM is conceivable, developing such detailed model for SyR rotor is possible but laborious task and must be repeated for any new geometric modifications. Alternatively, if FEA is used to generate the inductance map, then the process already provides sufficient information to utilize the LUT based analysis described in Chapter 6. Comparing with the nonlinear analytical model, LUT based model will be a better choice considering the computational costs are comparable and accuracy is higher.

Nevertheless, the developed nonlinear model quantifies the impact of assumptions used in the linear model and further validates the analytical modeling methods developed in this research.

7.3.2. Leakage flux components

The nonlinear analytical model does not explicitly include the leakage inductance component. However, since the inductance map is created using FEA, some of the leakage

components such as, the slot leakage, harmonic leakage components and zig-zag leakage between the rotor and stator teeth are already included. The missing leakage components that are not considered will be the end winding leakage and any interactions between the rotor sections in the hybrid rotor configuration.

As the machines' aspect ratio reduces, the rotor end effects, and end winding leakage will become relatively significant and cannot be neglected. In addition, if the SyR rotor is heavily saturated, there could be higher degree of interaction between the PM and SyR rotor sections. These aspects are not captured either by the nonlinear model or LUT based model. While end winding leakage can be approximated using analytical methods, any interaction between the rotors must be further analyzed thoroughly and is out of the scope of this thesis.

7.3.3. Direction of power flow

Conventional PMSMs can be used for both motoring and generating modes with minor differences. For the hybrid rotor PMSM, motoring and generating modes have similar performance only when $\alpha = n\pi/2$, where n is any real integer number. For the proof-of-concept hybrid rotor PMSM with k_l = 0.5 and α = 30°, the average shaft torque and the individual torque components from the SPM and SyR rotor sections as a function of the current angle are plotted as shown in Figure 7-7. As evident, the PM torque component shifted by α makes the net shaft torque higher and also shifts the motoring mode, i.e., positive shaft torque, past the conventional limit of γ = 90°. Such offset angle aids in producing higher net torque for the same magnet volume and better field weakening operation in the motoring mode. However, as evident from Figure 7-7, in the generating mode, when the SPM torque component reaches its highest magnitude, the SyR torque component is in motoring mode. Hence the net shaft torque

is a difference of both torque components causing it to be less than the peak value in motoring mode operation.

Hence a limitation of the hybrid rotor configurations when designed with, $\alpha \neq n\pi/2$, the machine has a preferred direction of power flow, either motoring or generating mode operation, and cannot be used in both modes with same efficiency. An identical motoring and generating mode operation can be achieved by designing the hybrid rotor PMSM with $\alpha = \{0, \pi/2\}$.

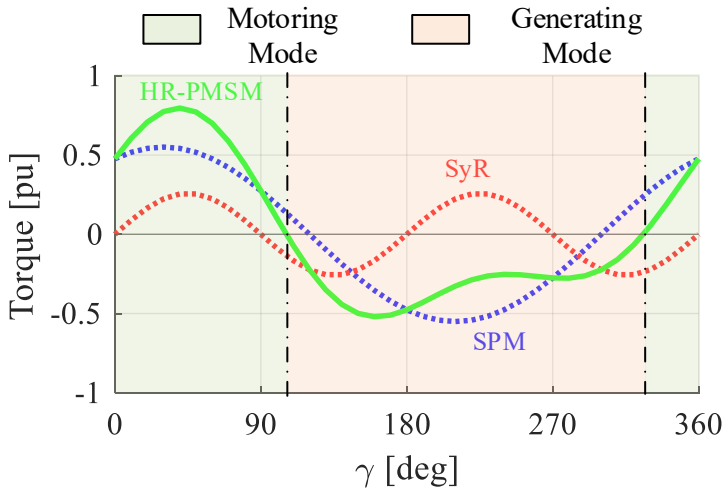

Figure 7-7. Torque components of a hybrid rotor PMSM showing assmetry in motoring and generating mode.

7.3.4. Direction of rotation

Similar to the asymmetry in the direction of power flow, if the hybrid rotor PMSM is manufactured with $\alpha \neq n\pi/2$, then with the change in rotation direction, the torque components do not have the same relation with the current angle due to the angular offset of PM rotor section with respect to the designed reference frame. A comparison of the shaft torque for a hybrid rotor PMSM with $\alpha = 0^o$ and $\alpha = 30^o$ is shown in Figure 7-8. The corresponding MTPA

torque points for positive and negative rotor rotation (ω_r) are also denoted. It can be seen that for a combination with $\alpha = 0^o$, the MTPA operation is identical for both rotation directions while the torque is higher at MTPA for positive ω_r for $\alpha \neq 0^o$. This can also be inferred from the theoretical MTPA trajectories predicted using (3.46) and plotted in Figure 7-5, where the motoring mode of the primary MTPA trajectory is highlighted. The second intersection point of theoretical trajectory with the current limit circle corresponds to either generating mode, or negative ω_r MTPA, depending on the direction of rotor rotation. Hence, similar to the practical limit of direction of power flow, if similar torque performance is desired in both rotation directions, the hybrid rotor PMSM design must be limited to an offset angle of $\alpha = \{0, \pi/2\}$.

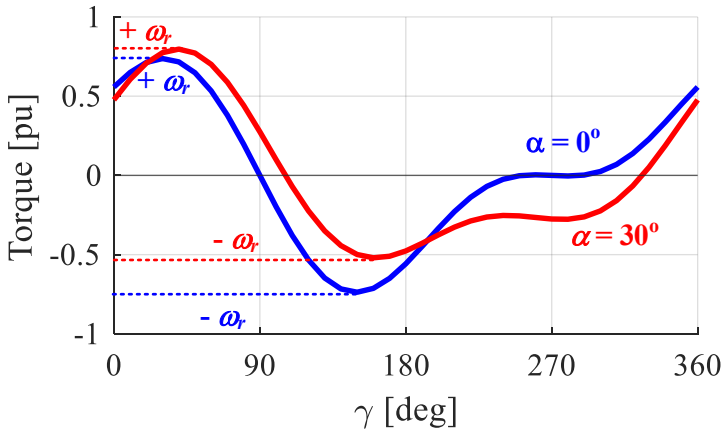

Figure 7-8. Shaft torque comparison for hybrid rotor PMSM with and without offset angle, showing MTPA operation based on direction of rotor rotation.

7.4. Summary

In this chapter, the equivalent steady-state operating circuit of PMSM is used to incorporate the effects of non-linearities and losses to the loss-less linear model developed in

Chapter 3. Firstly, the phase resistance is added to the loss-less equivalent circuit and the voltage constraint equation is derived. The impact of the resistance on the voltage limit ellipse is analytically identified and shown to mimic the behavior experimentally determined in past literature. The nonlinear saturation effects are incorporated by modeling the equivalent inductances as a function of the operating current amplitudes in d, q axes. Lastly, the magnetizing current components are derived in terms of terminal currents and iron loss resistance and the effective output torque calculated. The torque-power vs. speed curves are reevaluated and compared between the analytical linear, analytical non-linear and the LUT based models. It is shown by incorporating the losses and non-linearities, the discrepancy between the analytical model and LUT model is largely mitigated. The limitations of the analytical nonlinear modeling method and LUT modeling methods proposed in this research are identified. The practical limitations for hybrid rotor PMSM regarding the direction of power flow and rotor rotation are also discussed.

Chapter 8

8. Experimental Validation

A prototype is manufactured using full stack length stator and segmented rotor sections to verify the theoretical analysis and FEA models developed for the hybrid rotor PMSM. The prototype is also designed to be easily disassembled and reassembled as necessary to accommodate testing different rotor combinations. The goal of this process is to validate the design and hybrid rotor PMSM modeling methods proposed in this work. Accordingly, this chapter presents the development, manufacturing process, assembly, and experimental results for the proof-of-concept machine and validates the results with both 2D FEA for SPM and SyR machines and the LUT model for hybrid rotor PMSM.

8.1. Permanent Magnet Rotor - Redesign

For simplicity in the modeling of hybrid rotor PMSM concept with angular offset as a parameter, an ideal SPM rotor with ring magnet configuration was used in the FEA models introduced in Chapter 5. However, manufacturing such a ring magnet SPM rotor is not cost-effective for a prototype due to the required tight tolerance on the magnet diameter and the necessity to use a magnet retention mechanism. In addition, using arc-shaped magnets to create a conventional SPM rotor also requires custom manufacturing of magnets to match the outer rotor diameter. To reduce the prototyping cost, a rectangular cross-section PM can be used. However, this requires modifying the PM rotor to embed rectangular cross-section magnets yet have saliency close to unity.

Hence the PM rotor section is redesigned and optimized to achieve the desired inductance and saliency. A cross-section of the redesigned low saliency PM rotor is shown in Figure 8-1. The rotor shape and position of flux barriers are specifically optimized to reduce the inductance in *q*-axis as well as make the *d*-axis inductance equal to SyR rotor. Manufacturing tolerances and ease of assembly are also considered and incorporated into the design process. The PM material is changed to have a B_r of 1.25 T to keep the PM flux linkage and back EMF consistent with the SPM rotor introduced in the previous chapter. The phase voltage waveforms and harmonic components for the low saliency PM rotor are shown in Figure 8-2.

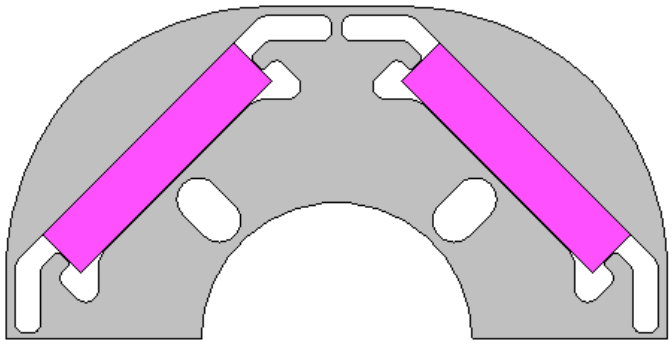

Figure 8-1. Redesigned PM rotor section – low saliency PM rotor

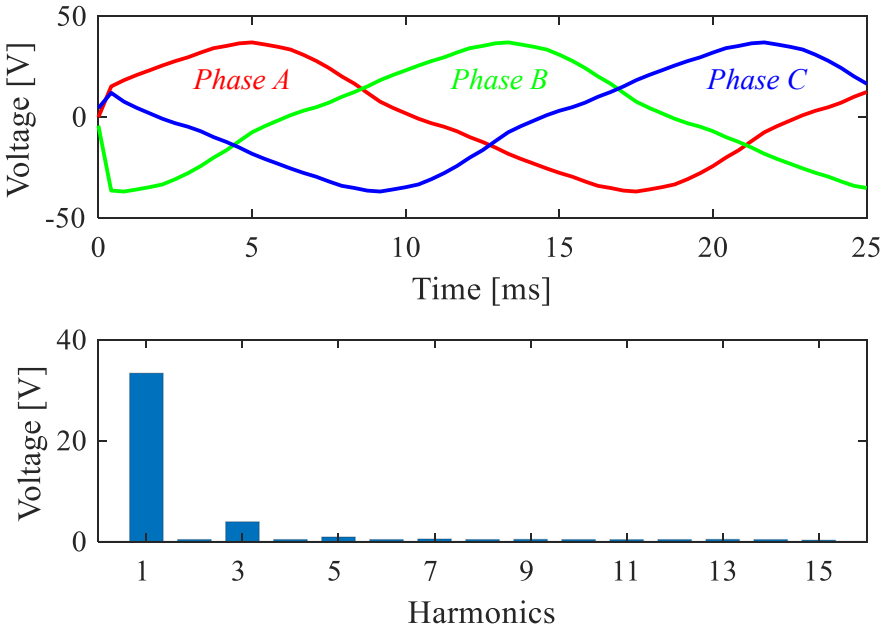

Figure 8-2. Phase voltage waveform and harmonic components at rated operation obtained from FEA for low saliency PM rotor

The torque waveform at rated operation is shown in Figure 8-3. The inductance, along with torque and power factor as a function of the current is plotted, as shown in Figure 8-4 and Figure 8-5, respectively.

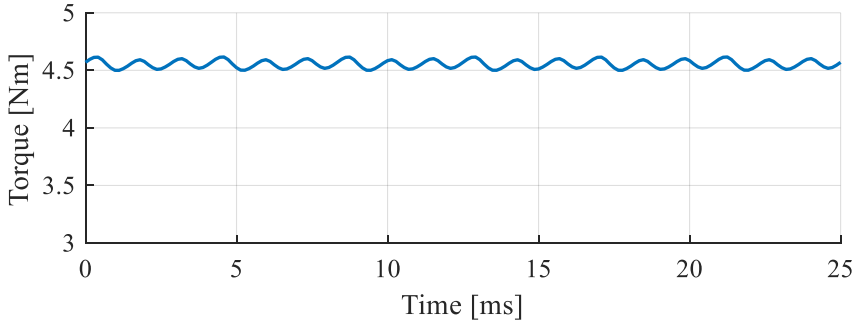

Figure 8-3. Torque waveform at rated operation obtained from FEA for low saliency PM rotor

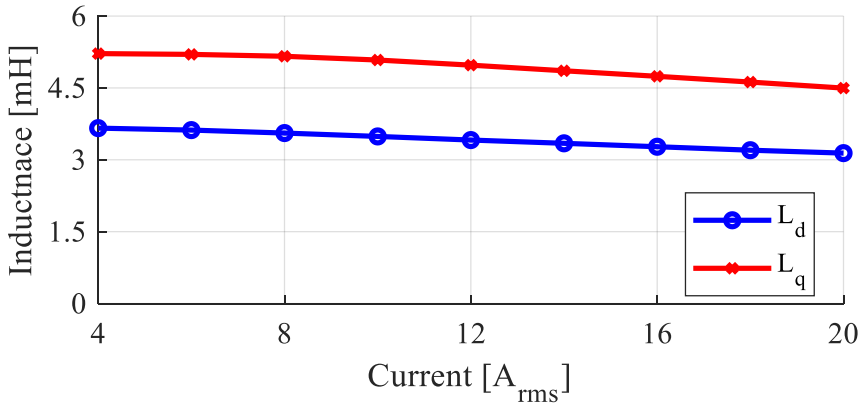

Figure 8-4. Inductance as a function of current calculated from FEA for low saliency PM rotor

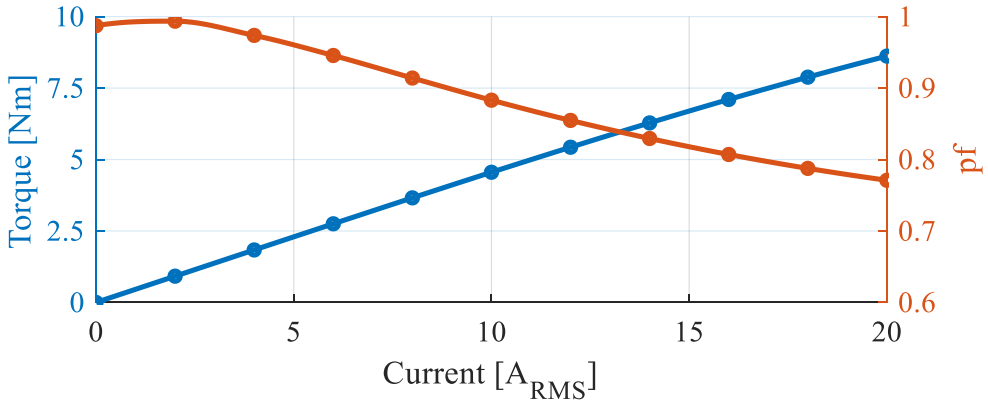

Figure 8-5. Torque and power factor as a function of current obtained from FEA for low saliency PM rotor

It is evident that the average torque and *d*-axis inductance of the redesigned PM rotor section are similar to the ideal SPM rotor shown in Figure 5-21 and Figure 5-22. However, the power factor is lower than the ideal SPM, and the *q*-axis inductance is higher, leading to a saliency of 1.4. Nevertheless, the reluctance torque component is not significant, and hence the redesigned low saliency PM rotor section meets the requirements to test the hybrid rotor PMSM.

8.2. Design and Manufacturing Hybrid Rotor PMSM

8.2.1. Stator and Housing

The stator is obtained from a disassembled servo motor that meets the design requirements. The prototype stator is shown in Figure 8-6. The housing and end plates are designed to fit a standard IEC 100 frame size. Figure 8-7 shows both a CAD drawing of the housing as well as the manufactured components and assembled housing. Housing and stator are assembled with an interference fit.

(a) (b)

Figure 8-6. Stator used for prototype hybrid rotor PMSM

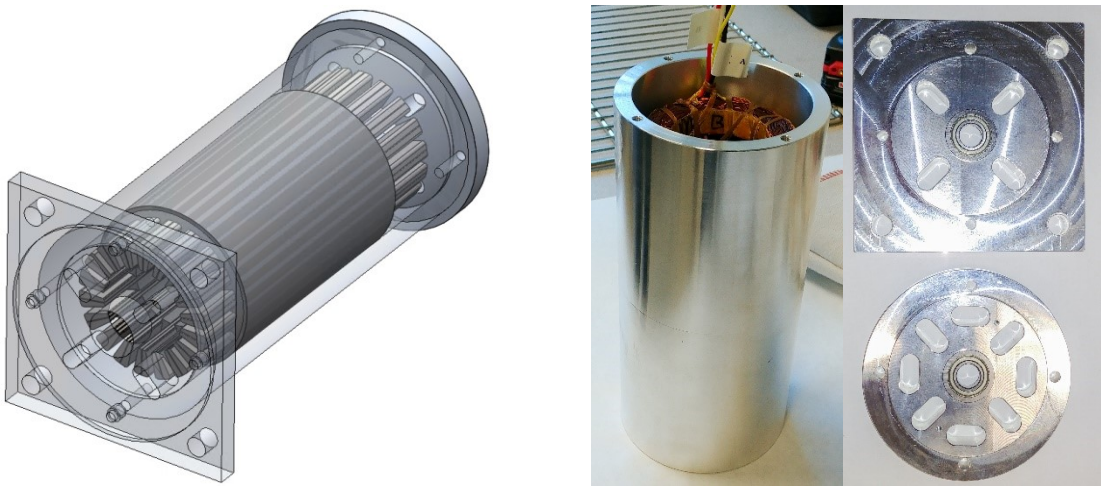

(a) (b)

Figure 8-7. Housing and endplate design (a) CAD model showing stator, housing assembly (b) Manufactured housing and endplates.

8.2.2. Rotor and Shaft

The rotors and shaft must be designed to allow relatively easy disassembly, allowing for the rotor stack length ratio and relative rotor angle to be changed for the proof-of-concept verification. While a spline shaft with matching teeth on the rotor's inner diameter is a practical approach [21], the tolerance requirements and manufacturing costs are prohibitively high. Hence the shaft is designed with a single keyway cut out through the length of the shaft with an end ring to allow removing rotors in either direction. The rotors are designed in 20 mm segments, giving six rotor segments in total for the 120 mm stack length. The CAD model for shaft design and the cross-section lamination shape with an integrated key in the rotor sections are shown in Figure 8-8.

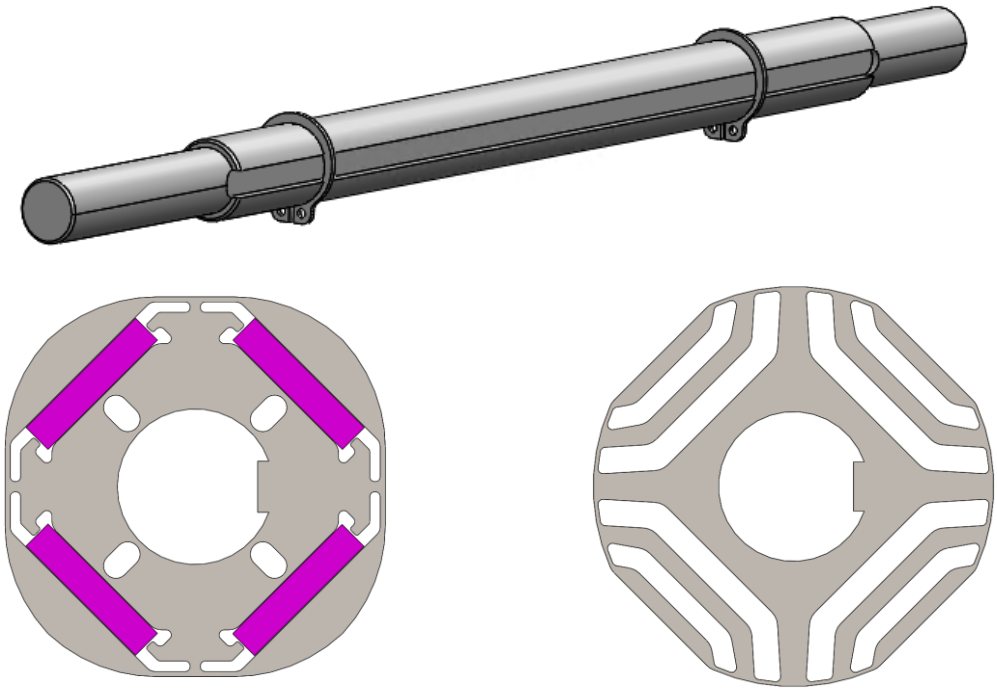

Figure 8-8. CAD models of the shaft, PM, and SyR rotor sections

The rotor laminations are cut using FABLIGHT 4500 laser cutter from 29-gauge (0.014” / 0.356 mm) M19 electrical steel sheets with C5 coating. The laminations are aligned using a dummy shaft and fixtured using clamping plates, as shown in Figure 8-9. A total of 55 laminations per rotor section were used. The clamping plates are spaced to match the desired rotor segment stack length of 20 ± 0.1 mm using metal spacers, and clamping screws tightened using a torque wrench to achieve uniform stack compression. The assembled rotor sections with clamping plates ready for bonding are shown in Figure 8-10. The laminations are bonded using 3M ScotchCast 265 Electrical Resin and cured at 200° C for 1 hour. The bonded rotor sections for low saliency PM rotor and SyR rotor are shown in Figure 8-11. Based on the measurements, a stacking factor of 98% was achieved using this manufacturing process.

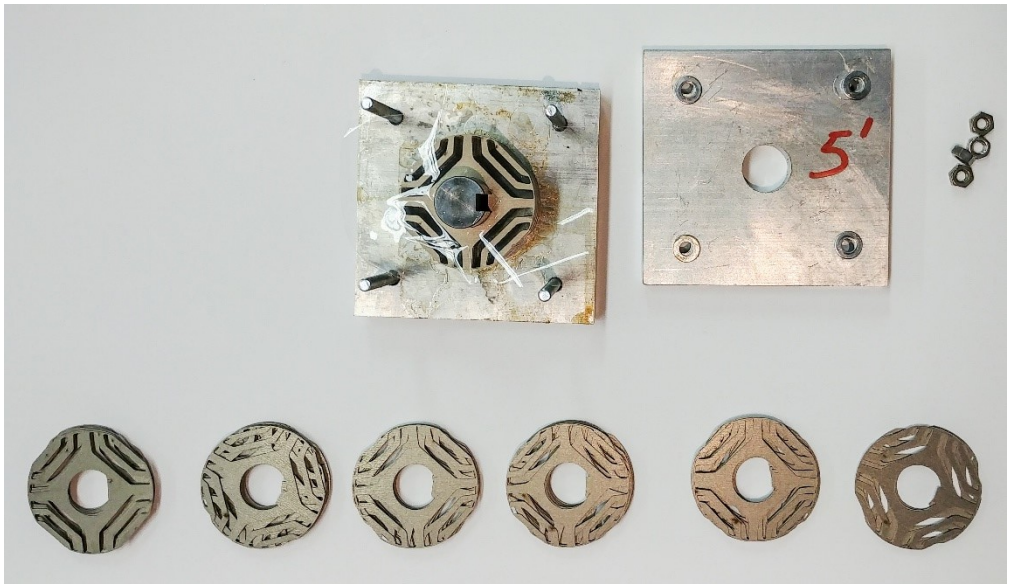

Figure 8-9. Lamination alignment and assembly process

Figure 8-10. Rotor segments prepared for bonding using clamping fixtures

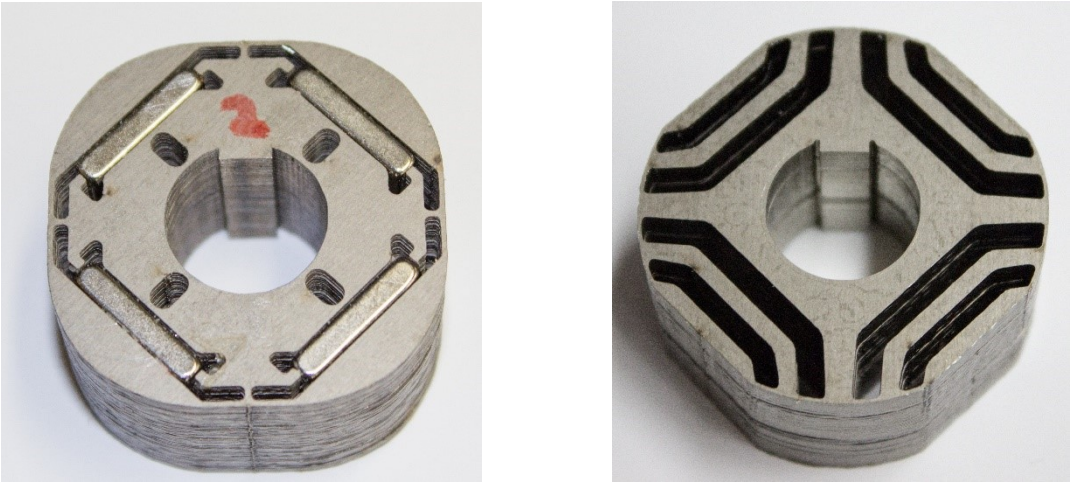

(a) (b)

Figure 8-11. Finished rotor sections (a) Low saliency PM rotor (b) SyR rotor

The PMs are then inserted into the PM rotor slots and held in place using Loctite 332 as a bonding agent and Loctite 7387 as an activating agent, enabling curing at room temperature. The 12 rotor segments, corresponding to 6 each for the PM rotor and SyR rotor, are shown in Figure 8-12 and a picture of the final assembled SyR rotors shown

(a) (b)

Figure 8-12. Assembled individual rotors (a) SPM rotors (b) SyR rotors

Based on the possible infinite CPSR combinations calculated in section 6.3 and shown in Figure 6-16, the stack length ratio (k_l) must be within the bounds of 0.447 and 0.774. With a total stack length of 120 mm and 6 rotor segments, a possible practical k_l value is either 0.33 or 0.66. Hence a stack length ratio of 0.66 is selected, and the corresponding α is calculated to be 57.5° electrical, i.e., 28.75° mechanical. Due to ease of manufacturing and fewer rotor sections, new SyR rotors are manufactured with the integrated rotor key position shifted by 28.75° as shown in Figure 8-13. The top and bottom PM rotor sections of the PM rotor stack are removed and replaced by the offset SyR rotor sections to form the hybrid rotor PMSM. The assembled SyR rotor stack is shown in Figure 8-14(a), and the hybrid rotor stack with k_l = 0.66, α = 57.5° is shown in Figure 8-14(b).

Figure 8-13. Manufactured SyR rotor section with integrated rotor key shifted to achieve an offset angle, α = 57.5°

(a) (b)

Figure 8-14. Assembled rotors (a) SyR rotor (b) Hybrid rotor with $k_l = 0.66$, $\alpha = 57.5^{o}$

8.3. Experimental Results

An SPM servo motor rated at 2.6 kW and 3000 RPM is used as the load machine supplied by a commercially available VFD. The load machine is connected in a back-to-back configuration with the test machine through a HBM T21WN torque transducer capable of measuring up to 20 Nm of torque. The prototype hybrid rotor PMSM (test machine) is excited using a prototype GaN based VFD that is rated for 100 V, 20 A continuous operation and supplied by a 250 V, 80 A Magna DC power supply. Since the test machine will be operated

in all 4 quadrants covering both motoring and generating mode of the hybrid rotor PMSM, an external resistive load bank is connected in parallel with the DC power supply to dissipate power during generating mode operation. The load machine control interface enables speed control operation of the load machine while the test machine control interface allows for *dq* current commands at the given operating speed. The line voltages and currents are measured at the test machine terminals. The voltages, currents and torque measurements are collected using a Teledyne LeCroy 8 Channel MDA for post-processing. The dynamometer test setup for the prototype hybrid rotor PMSM is shown in Figure 8-15, and a close-up view of the testbed setup inside the dyne enclosure is shown in Figure 8-16.

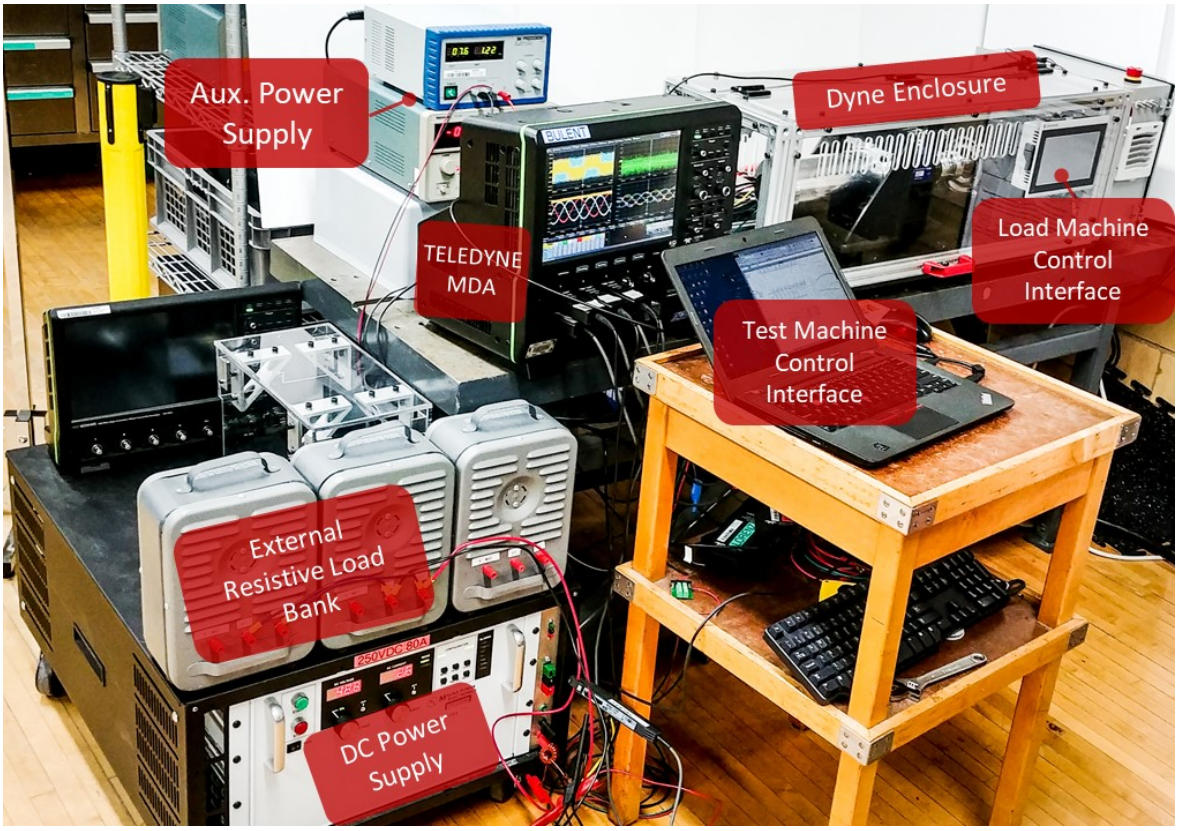

Figure 8-15. Dynamometer setup for prototype hybrid rotor PMSM

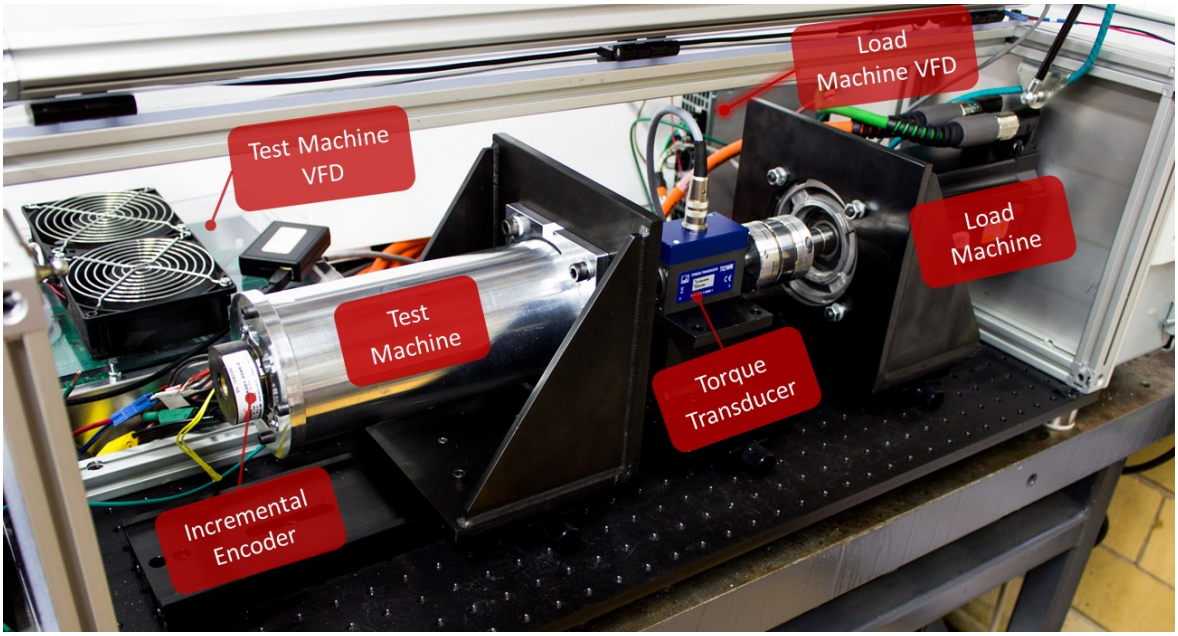

Figure 8-16. Dyne setup for prototype hybrid rotor PMSM

8.3.1. Low Saliency PM Rotor Machine

The test machine is first assembled with a full stack length, i.e., six rotor segments, of low saliency PM rotor. With the test machine mounted on the dyne and disconnected from its VFD, it is driven by the load machine in speed control mode at different speeds to determine the no-load back EMF characteristics. The comparison of peak line voltage at various rotor speeds and the voltage waveforms at the rated speed of 1200 RPM is shown in Figure 8-17. It is evident that the no-load characteristics of the PM machine are in good agreement with the predicted values using FEA modeling and within an error range of 5%. The average PM flux linkage calculated from measured back EMF is 0.106 Wb, corresponding to 3.8% lower than predicted from FEA. This could be attributed to a weaker magnet strength than specification. In addition, it can be observed from Figure 8-11(a) that the PM does not extend the complete

20 mm of each rotor section. An average shortage in the magnet height is measured to be ≈ 0.2 mm per rotor section, i.e., 1% for the total machine stack length. The shorter PM length could also contribute to the reduction in PM flux linkage and back EMF.

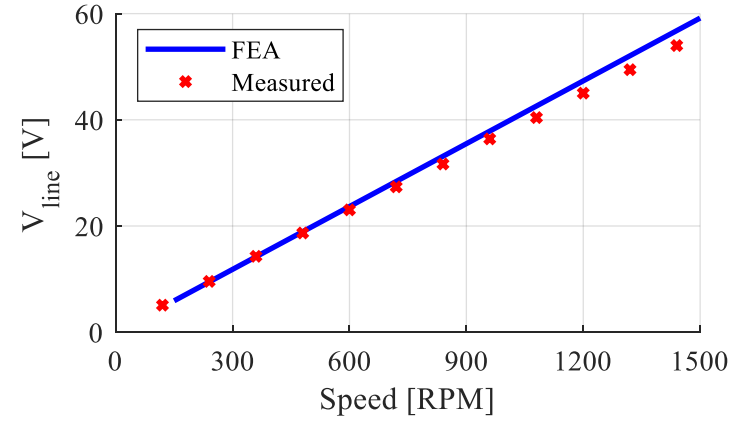

(a)

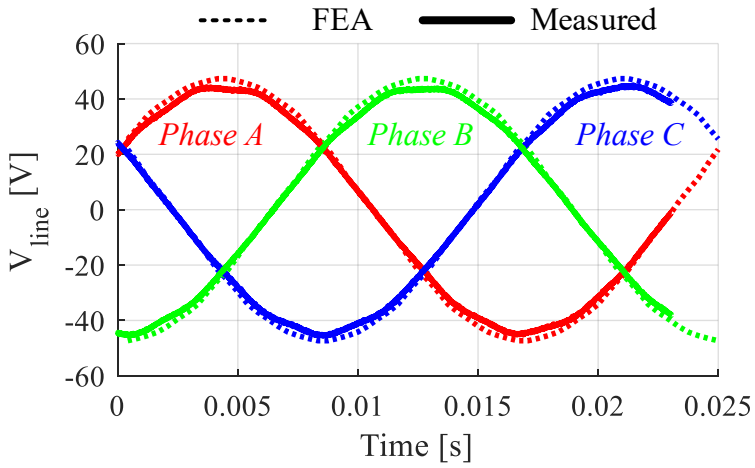

(b)

Figure 8-17. No-Load terminal voltage with low saliency PM rotor comparison between FEA and experimental data (a) Peak line voltage at various speeds (b) Line voltage waveform at 1200 RPM.

With the load machine still in speed control mode and running at a fixed speed, the test machine is then excited with varying values of q-axis current. The measured load torque is compared with FEA and shown in Figure 8-18, and there is good agreement with the expected torque. The measurement error is calculated to be 4.2%, which is in line with the back EMF error and lower PM flux linkage pointing to weaker PM material.

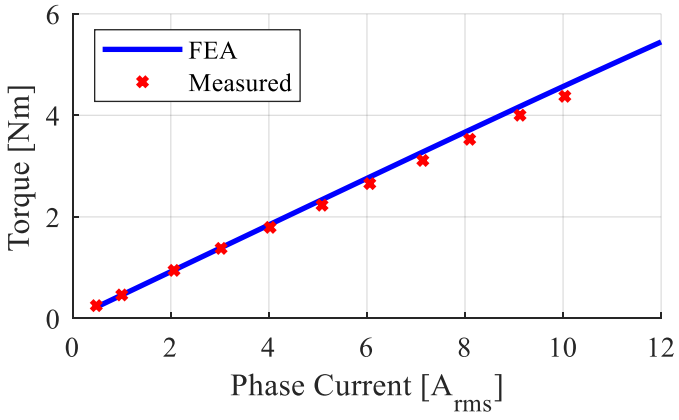

(a)

Figure 8-18. Average torque comparison between FEA and measured values with low saliency PM rotor

The *d* and *q* axis inductances are measured by aligning the rotor to corresponding *d* and *q* axis positions using stator current and then locking the rotor using a mechanical brake on the machine shaft. The machine is then exciting with an increasing frequency voltage signal, also referred to as a chirp signal, that ranges from 1 Hz to 500 Hz. A frequency response function (FRF) analysis is performed using the resulting current and voltage waveforms. Through this method, both the phase resistance and inductance of the PM machine can be accurately estimated.

The FRF amplitude, along with an overlay of FRF transfer function amplitude using the estimated resistance and *d*-axis inductance measured with a *d*-axis current offset of 4 A_{rms} is shown in Figure 8-19. This process is repeated with different offset current values for both *d* and *q* axis rotor positions. The measured inductances are compared with FEA and shown inFigure 8-20.

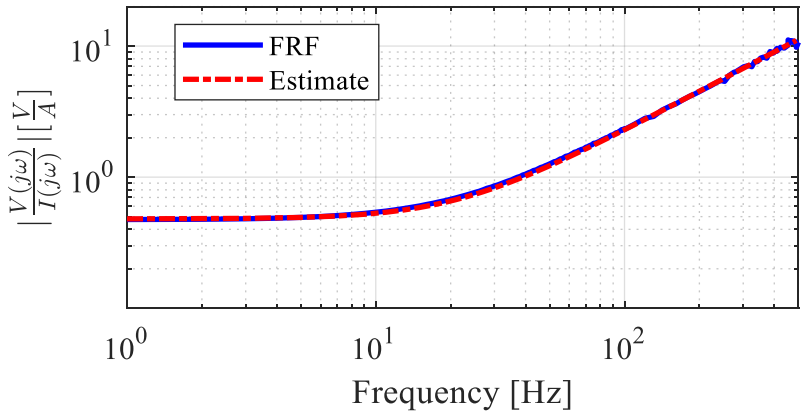

Figure 8-19. Measured and estimated magnitude of frequency response function with low saliency PM rotor

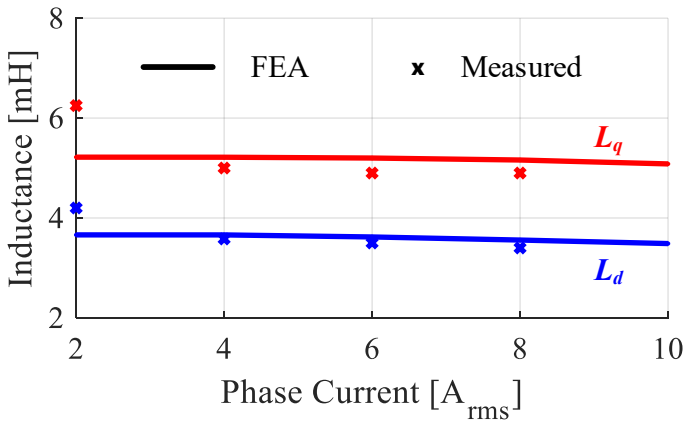

Figure 8-20. Inductance comparison between FEA and measured values with low saliency PM rotor

It can be seen that the inductance measurement has a reasonable agreement with FEA except at low current amplitude. Multiple measurements were performed at this current amplitude, all yielding similar results. The discrepancy is most likely due to the rotor bridges being unsaturated due to weaker PM flux, leading to additional leakage flux paths. In addition, the measurement noise in the current waveform has a dominant effect at lower current amplitudes leading to calculation errors.

8.3.2. SyR Rotor Machine

The test machine is disassembled, and the PM rotor sections on the shaft are replaced with the SyR rotor sections for the full stack length. The FRF test procedure for the inductance is repeated by locking the rotor similar to the PM machine, and the measured inductances are compared with FEA as shown in Figure 8-21.

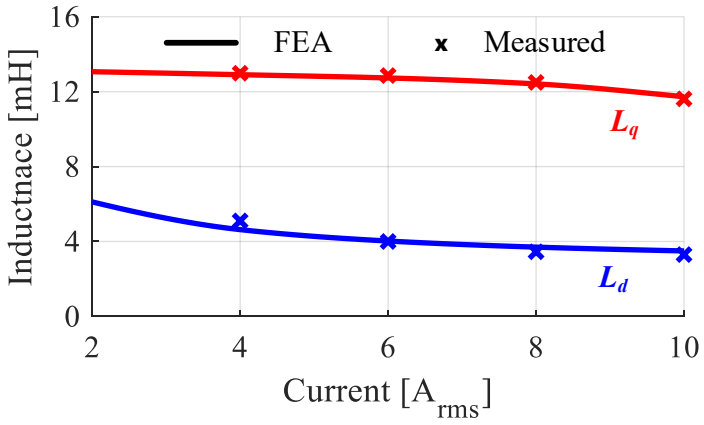

Figure 8-21. Inductance comparison between FEA and measured values with SyR rotor

Similar to PM machine, the inductance measurement at lower current amplitudes had a higher error. Particularly for a SyR machine, there is no inherent rotor flux to saturate the

bridges which act as leakage paths. As the stator MMF increases, the bridges are saturated, and the rotor saliency can be measured. The minimum current necessary to saturate these rotor bridges is approximately 4 A_{rms}.

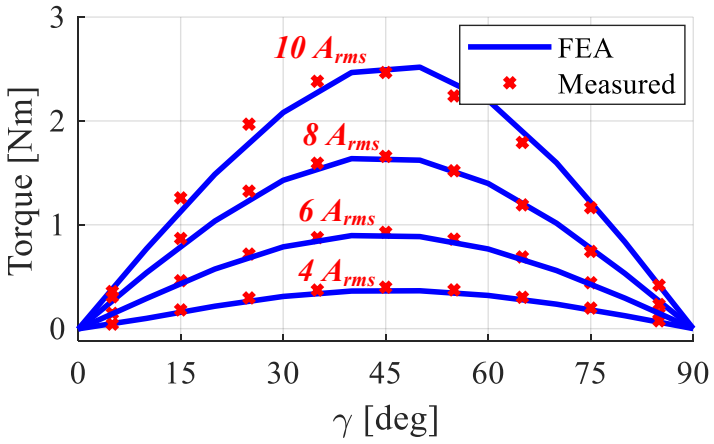

(a)

Figure 8-22. Average torque comparison between FEA and measured values SyR rotor

The torque as a function of the current amplitude and advance angle is measured using the test machine, and the comparison with FEA is shown in Figure 8-22. The measured torque is in very good agreement with the prediction. It can be seen that there is a slight deviation at 10 A_{rms} operation, i.e., rated current. The error in torque output at MTPA operation is calculated to be 3.7%, which is well within an acceptable margin.

8.3.3. Hybrid Rotor PMSM

The machine is disassembled, and the rotor was modified to the hybrid rotor configuration shown in Figure 8-14(b). The test procedures are repeated to characterize the hybrid rotor machine. With the test machine disconnected from the VFD and rotating at

different pre-set speeds using the load machine, the terminal voltage is measured, and the peak values are plotted in comparison with FEA as shown in Figure 8-23. The measured voltage trend is similar to the low saliency PM rotor and shows an average error of 3.6%. The calculated PM flux linkage from the measured back EMF is 0.069 Wb, approximately 4.9% lower than the value estimated using LUT based model.

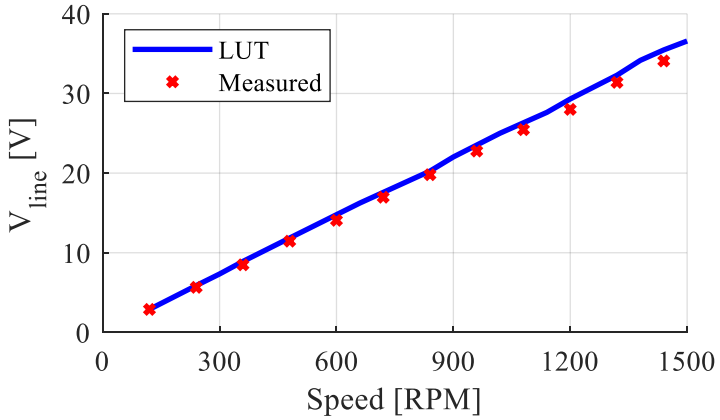

Figure 8-23. No-Load terminal voltage of hybrid rotor PMSM, comparison between FEA and experimental data

In order to perform the load test by applying appropriate *d* and *q* axis currents, the rotor position must be known. In this test setup, an incremental encoder was used, which requires initializing the rotor *d*-axis position with respect to the encoder index position. The initialization is achieved by uncoupling the test machine from the dyne, let the rotor align itself by applying DC current across phases B and C and reset the index position of the encoder to match with the rotor aligned position. This would be a common procedure for either SPM or SyR machines when using an incremental encoder.

For the hybrid rotor machine, the developed modeling method assumes a SyR rotor reference frame, i.e., the encoder must be initialized with the SyR rotor *d*-axis position. With a non-zero α, and a dominant PM rotor section, the rotor tends to align more towards the PM rotor reference frame using the above-mentioned initialization procedure. If the rotor strictly aligns with PM rotor, an external encoder offset angle can be added manually to offset the rotor position and align with SyR rotor reference frame. However, during the experimental test, it was observed that the rotor appears to align slightly off from the PM *d*-axis, which can only be interpreted as an equilibrium position between the two-competing *d*-axes represented by each rotor section. This phenomenon led to further difficulty in precisely identifying the SyR rotor reference frame. This difficulty can be avoided by either using an absolute encoder that can be mounted to align with the SyR reference frame or using additional sensing coils in the stator design to detect either of the rotor reference frame accurately.

The load torque of the hybrid rotor PMSM was measured by incrementally changing the current advance angle from 0^o to 360^o. The entire range of current angle is used for this test to ensure the performance is captured for all 4 quadrants, given the possibility of operation beyond the conventional 2nd quadrant for hybrid rotor machines, as shown in section 6.2. The measured torque as a function of the current angle is compared with the LUT based model estimated values, as shown in Figure 8-24. It is evident that the measured torque values are in good agreement with the expected performance between $0^o \leq \gamma \leq 180^o$ with a maximum error of 3.3%. The data between $240^o \leq \gamma \leq 330^o$ however, shows a higher degree of error, particularly with a current of 10 A_{rms}, where the measured torque is 6.1% higher in magnitude at $\gamma = 240^o$. This operating region corresponds to the generating mode for the SPM (negative

torque), but the reluctance rotor is in motoring mode (positive torque). As observed from Figure 8-22, the saturation effects in SyR rotor are slightly higher than predicted, causing the torque curve to shift. Since the SyR torque is maximum at $\gamma \approx 225^{o}$, and negating the PM torque component, the error could be more apparent in this operating region.

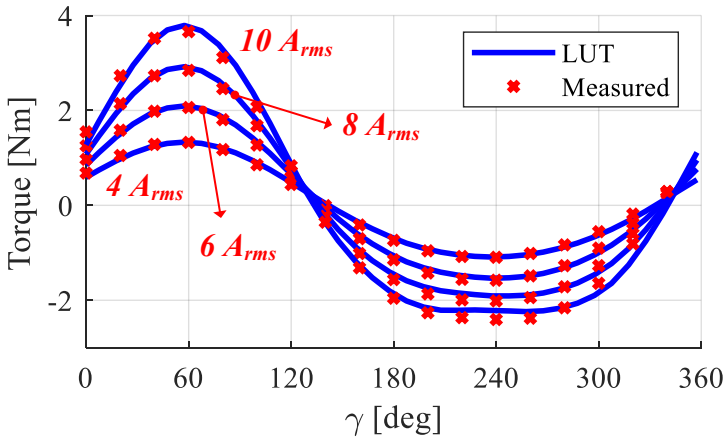

Figure 8-24. Average torque comparison between FEA and measured values for proof-of-concept hybrid rotor PMSM

While adding a manual offset value to rotor position worked well for the torque measurement, the inductance measurement in SyR rotor reference frame posed additional challenges since minor rotor position error could lead to significant error in inductance. Hence the locked rotor inductance measurement in SyR reference frame using the FRF method could not be performed with sufficient rotor position accuracy. In the absence of inductance estimate from FRF method, the coil flux linkage estimated from voltage measurements could give a sufficient representation of the machines' inductance characteristics.

With the machine rotating at low speed, the measured line voltage values and the calculated *dq* voltages are compared with the LUT based model as shown in Figure 8-25 and

Figure 8-26, respectively. The maximum error is found to be 3.1%, occurring at the operating point corresponding to phase current of 10 A_{rms} and $\gamma = 90^{o}$.

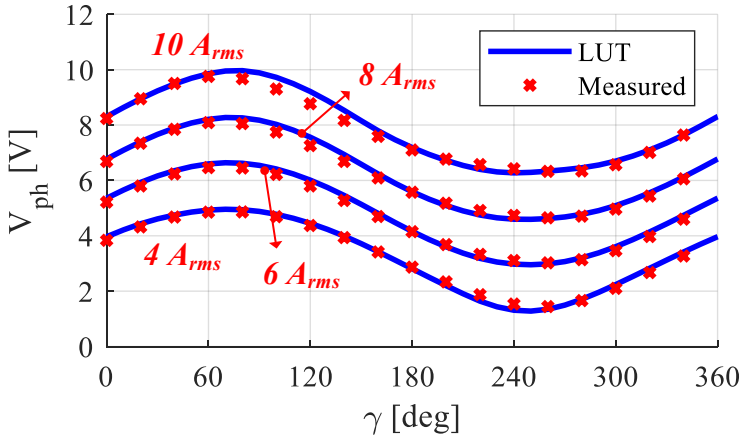

Figure 8-25. Phase voltage vs. current angle comparison between measured and LUT based models of proof-of-concept hybrid rotor PMSM.

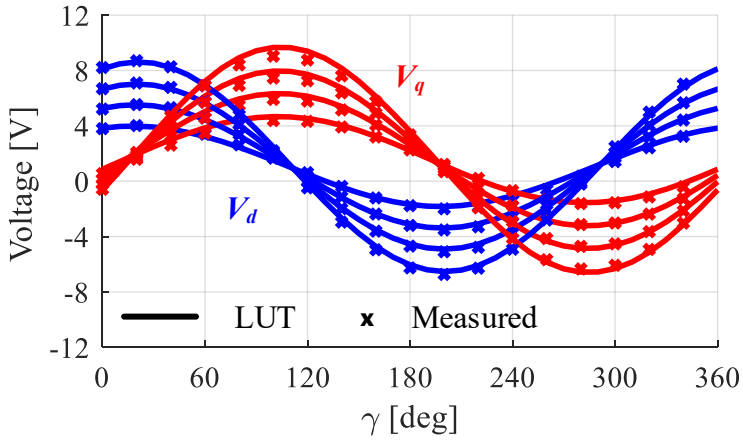

Figure 8-26. *dq* voltage vs. current angle comparison between measured and LUT based models of proof-of-concept hybrid rotor PMSM

The flux linkages are calculated from measured *dq* voltages using equations (7.1), (7.2) and compared with LUT based model as shown in Figure 8-27. Unlike the voltage

measurement, the flux linkage shows a considerable mismatch between predicted and measured values. The calculation of flux-linkage from terminal voltage also requires an accurate value of phase resistance, as evident from equation (7.2).

While the additional resistance due to the long leads between the inverter and the test machine was measured and accounted for in the calculation, the prolonged testing time caused the machine temperature to rise noticeably. With the negligible iron loss due to low-speed operation, the joule losses in the phase winding are the primary source for rise in temperature. Since there was no thermocouple used in the test machine, the winding temperature was not measured. This difference in phase resistance could contribute to a calculation error in the winding flux linkage.

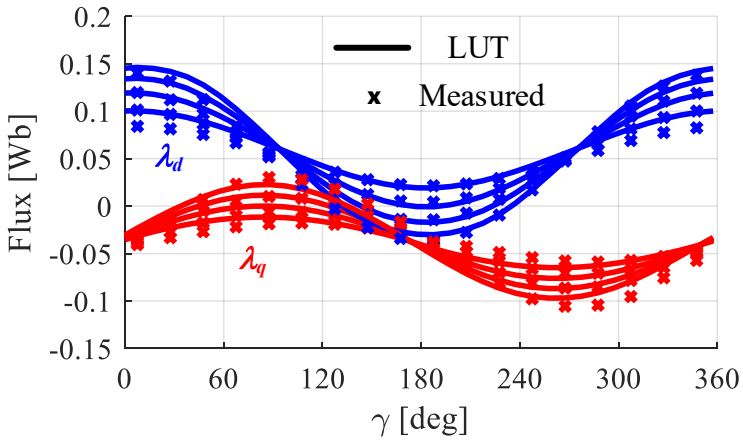

Figure 8-27. Flux linkage comparison between LUT and calculated values for measured voltage for proof-of-concept hybrid rotor PMSM

8.4. Prototype Manufacturing Lessons

The design and manufacturing process of the prototype rotor presented practical issues and offered several lessons learned. Some of the manufacturing issues faced, and solution trade-offs are summarized:

- The initial proof-of-concept SPM rotor used a ring magnet, which offered ease in design and analyzing different offset angles for the PM rotor. The SPM rotor offset was achieved by simply offsetting the magnetization vector instead of the CAD model, thus reducing meshing and computation time. However, manufacturing the SPM rotor with ring magnet was expensive, mainly due to the tolerance requirement on PM dimensions as well as the custom manufacturing required to meet the design specifications. The PM rotor section was modified to an IPM configuration to fit a simpler bar magnet shape for the prototype. The rotor core shapes of the PM and SyR sections had to be modified to tune the effective airgap in the *d* and *q* axes individually. As a trade-off, both the PM and SyR rotor sections deviated from the conventional cylindrical shape.

- During manufacturing of the rotor sections, several issues with the laser current tolerance were identified. Firstly, it was observed that at times the cut on the laminations indicated periodic oscillations as shown in Figure 8-28(a), which led to small ledges on the slots designed for PM rotor shown in Figure 8-28(b). These ledges caused PM assembly difficulty and, even fracturing the bar magnet at time due to excessive stress. The tolerance on the slot was adjusted several times to achieve sufficient clearance between the PM material and rotor slot. Effectively this led to slightly higher effective airgap and lower *d*-axis inductance for PM rotor than desired.

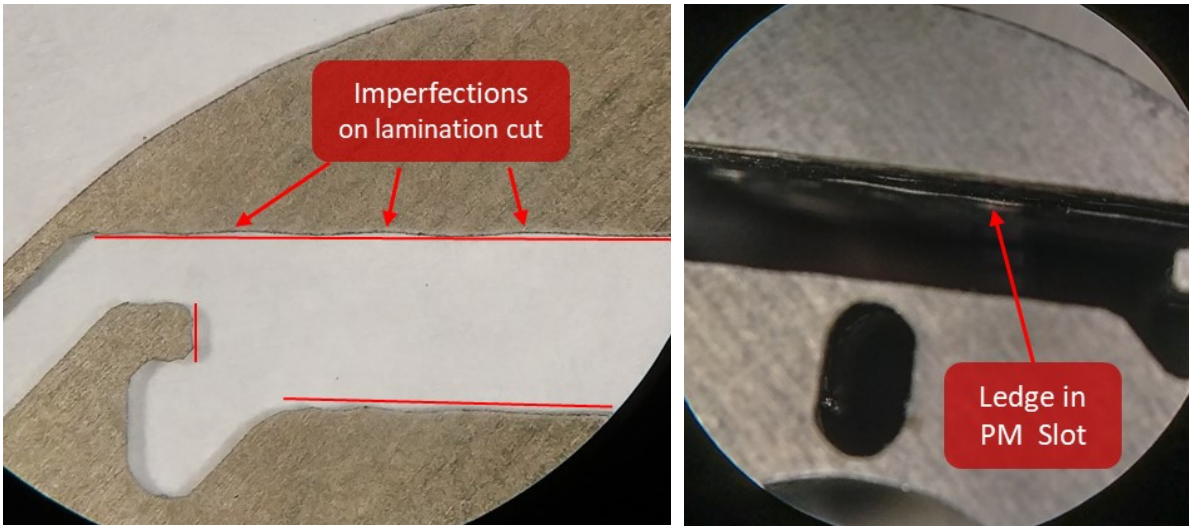

(a) (b)

Figure 8-28. Tolerance issues and imperfections on lamination (a) Laser head motion dynamics appear of lamination (b) Uneven magnet slot

- Upon further investigation, the periodic oscillations appeared on the laminations were found to have some correlation with the orientation of the cutting direction with respect to the 2-axis motion of the laser cutter head, as well as the position of the cut on the laser cutter bed. A view of the laser cutter bed with the laser head and the motion axes identified is shown in Figure 8-29. Firstly, it was identified that if the orientation of the slot is diagonal to the reference laser head axes, as found in Figure 8-29, the laser head motion during that cut is controlled by two servo motors moving in both x and y directions simultaneously. This appears to have caused some of the laser head motion dynamics to show up on the lamination cut. Since the prototype rotor is comprised of 4 poles, this issue was easily solved by rotating the rotor template to ensure the slot cut is dependent on only one axis motion. Secondly, the molten metal on the lamination during the cut is removed

by blowing compressed air through a nozzle adjacent to the laser head. If the lamination sheet is not properly secured to the bed, or if there is not adequate support beneath the lamination sheet, the compressed air induced minute oscillation in the sheet, causing the uneven cut. This effect was more apparent near the edges of the lamination sheet, where adding more support is not feasible. As a result, some of the rotor laminations obtained from the edges of the sheet had to be discarded, increasing material wastage.

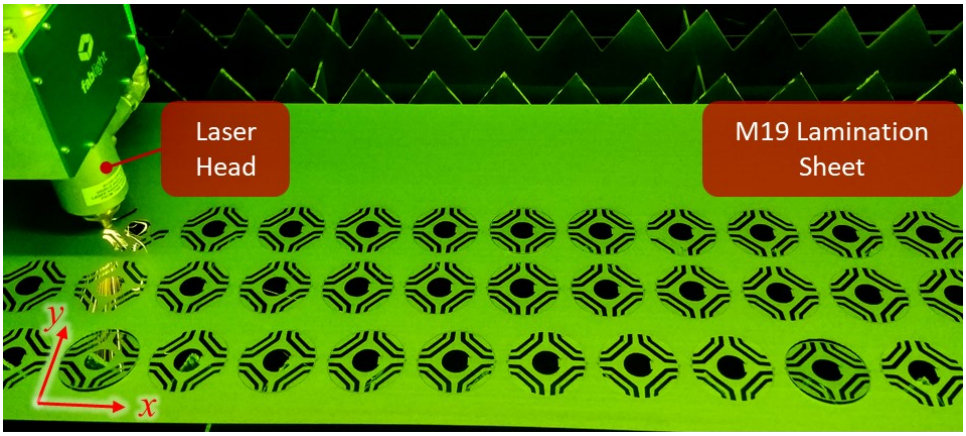

Figure 8-29. View of laser cutter bed during SyR rotor lamination cutting process with the laser head and axes of motion identified

- The stator housing, end plates and the bearing position must be strictly concentric to ensure a uniform airgap between the rotor and stator. However, after assembly, it was observed that the rotor exhibited some eccentricity due to a mismatch in the concentricity of the end plate. While the nature and magnitude of eccentricity were not big enough to hinder the experimental measurements at low-speed operation, the resulting dyne shaft misalignment and vibrations limited the speed to ≈ 1,400 RPM. This eccentricity and misalignment also resulted in encoder position issues due to a torsion effect on the encoder that was mounted

on the end plate while the shaft had slight orbital motion. The encoder mounting position had to be carefully adjusted to avoid position error due to torsional effects causing the shaft position to slip with respect to the encoder, and the measurement was limited to low speeds.

- While deep grooved and double shielded bearings were selected to reduce friction and maintain consistent lubrication of the bearings, the shaft eccentricity, as well as repeated disassembly and assembly to change the rotor configurations, lead to additional stress on the bearings. In addition, due to the long aspect ratio, small physical airgap, and strong NdFeB magnets, the assembly process for the PM rotor was particularly tricky and had to rely upon bearings and endplate to nudge the rotor into position while mounting the end plate to the housing. This could have caused unintended axial force on the bearings leading them to fail prematurely. As a result, the bearings had to be replaced midway through the experimental testing process.

8.5. Summary

This chapter presented the experimental data from the prototype hybrid rotor PMSM machine and compared the measurements with predicted FEA and LUT model data. To account for manufacturing complexity and cost considerations, a low saliency PM rotor section was designed to replace the SPM rotor section of the proof-of-concept hybrid rotor PMSM. The design, fabrication, and assembly of the components for a prototype hybrid rotor PMSM is documented, and the experimental setup is described.

The prototype machine is tested with a full stack length of PM and SyR rotors separately and the measured voltages, torque and inductance are compared with predicted FEA

modeling. The PM machine back EMF and torque measurements were within an error margin of ≈ 4%. This is most likely due to a generous tolerance specification on the PM length leading to shorter than expected magnets as well as lower strength PM material than specifications. Similarly, the torque measurement of the SyR rotor revealed ≈ 3.7% error, which could also indicate material property difference for the lamination steel used in rotor construction.

The tests are repeated for a hybrid rotor configuration with $k_l = 0.66$, $\alpha = 57.5^o$ and the torque, voltage, flux linkage are compared with the LUT model. Good agreement was observed with ≈ 3% error for torque and voltage in the motoring mode operation and a higher but acceptable degree of error in generating mode operation. Hence the validity of the hybrid rotor PMSM operation and the proposed LUT modeling method is verified.

Chapter 9

9. Performance Comparison of Hybrid Rotor PMSM for Traction Application

The ability to design for theoretical infinite CPSR being one of the attractive advantages of the hybrid rotor configuration, a practical application for such configuration would be as a traction machine. Such machines tend to be in the power range of 50 kW to 150 kW and operate to a maximum of 11,000 to 15,000 RPM in the field weakening region. In this chapter, to validate the proposed design principle as well as the viability of using hybrid rotor PMSM for traction applications, a suitable traction machine is selected, and the design details are summarized as the baseline. The sizing and design methodologies developed in Chapters 4 and 5 are applied and a hybrid rotor PMSM design developed to meet the baseline specifications. The LUT based model from Chapter 6 is extended to include iron losses as well as joule losses from PM and rotor sleeve. The field weakening performance of the designed hybrid rotor PMSM is compared with the baseline machine. Inherent advantages of hybrid rotor machines with torque ripple mitigation and to avoid demagnetization are discussed.

9.1. Baseline Traction Machine

Over the years, Oak Ridge National Laboratories' (ORNL) National Transportation Research Center had undertaken benchmarking numerous commercially available EV and HEV components as a part of providing strategic planning of state-of-the-art technologies projects by US Dept. of Energy (DOE). A wealth of benchmarking reports are publicly

available that have a detailed breakdown of the components and comprehensive performance metrics. At the time of this research, the latest report with detailed performance metrics is available for first generation 2016 BMW i3 [60]. Being one of the newest generation traction machines, the IPM machine in production for a BMW i3 with a published rating of 125 kW is selected as the baseline to compare the performance of an equivalent hybrid rotor PMSM designed using the modeling and analysis methods proposed in this research.

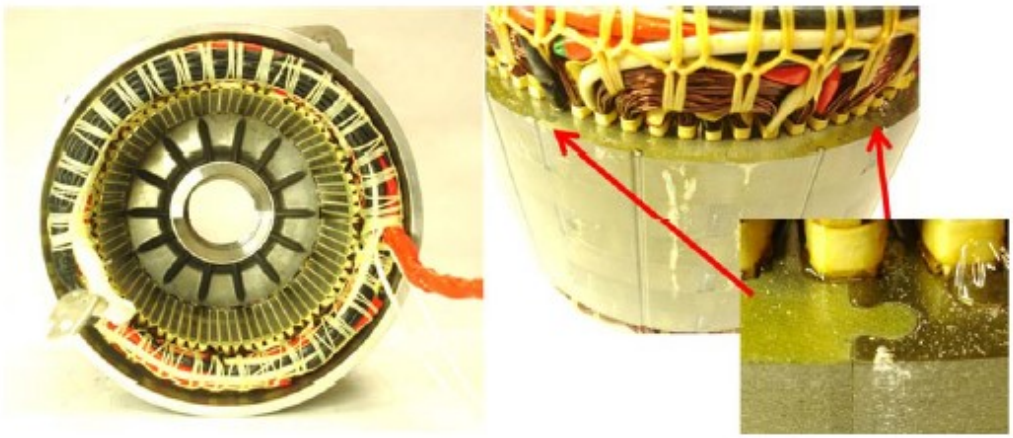

Figure 9-1. Baseline machine (BMW i3) stator construction [60]

The baseline machine is a 72 Slot – 12 Pole (SPP = 2) machine with an aspect ratio of 0.74. The stator is constructed using segmented lamination sections per pole pair, as shown in Figure 9-1. The stator is encompassed in a shrunk fit aluminum housing with spiral channels for liquid cooling. The stator winding is connected in 6 parallel paths, with 9 turns per coil and 12 parallel strands of wire size 21 AWG per turn. The current density of the machine at max torque can be calculated as 12.7 A_{rms}/mm^2, which is within the nominal range for the liquid cooling technique employed. Since the slot cross-section area is not known, the slot fill factor

cannot be estimated. However, considering the cost of manufacturing and practicality, a good estimate would be between 30% to 40% fill factor.

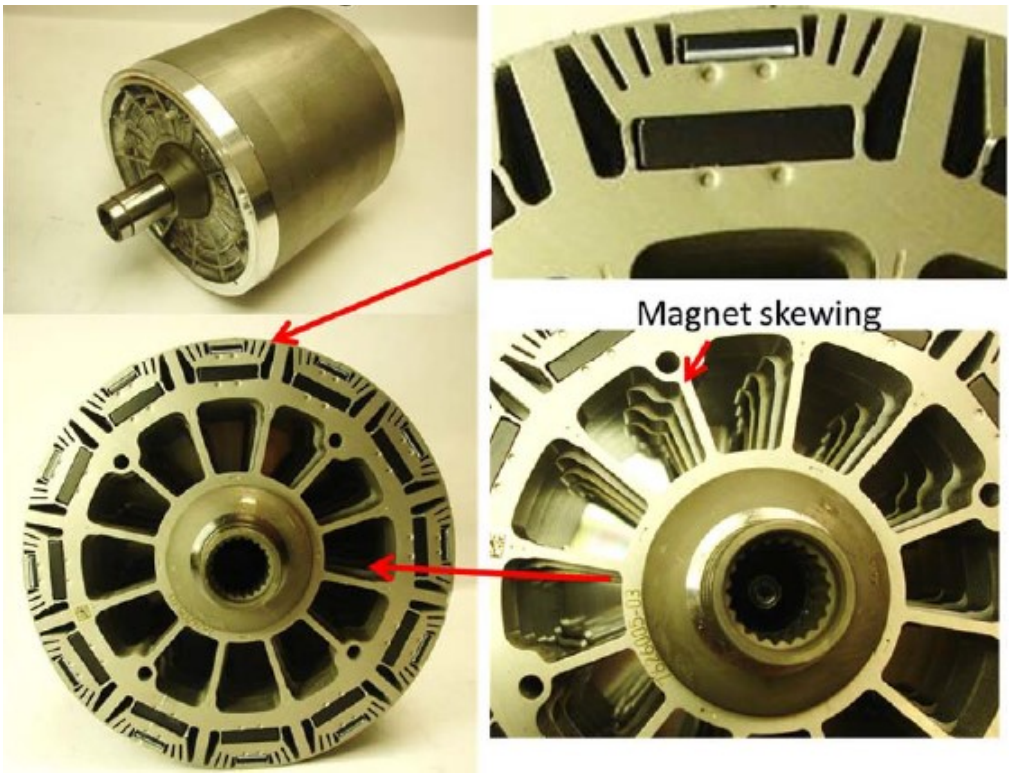

Figure 9-2. Baseline machine (BMW i3) rotor showing PM placement and step-skew arrangement [60]

The rotor in the baseline machine resembles a synchronous reluctance rotor with multiple flux barriers, along with one large and one small NdFeB magnets per pole as shown in Figure 9-2. The segregated PM and reluctance torque components are not available. The rotor is shown to employ a step-skew by segmenting the rotor into 6 sections. The total skew angle and precise material properties were not reported.

Some key dimensions and specifications available for the baseline machine are summarized in Table 9-1, and the torque-speed curve with an overlayed efficiency map for the

motor is shown in Figure 9-3. The baseline machine achieves a constant 125 kW power over a wide range of operating speeds. Based on the torque-speed curve, the maximum speed appears to be 11,400 RPM.

Table 9-1. Baseline machine parameters

Parameter	Value
Max. Power [kW]	125
Rated Speed [RPM]	4500
Phase Current (I_s) [A_{rms}]	375
DC Bus [V_{DC}]	360
Stack Length (l_e) [mm]	132.3
Stator Outer Diameter [mm]	242.1
Stator Inner Diameter [mm]	180
Air gap [mm]	0.7

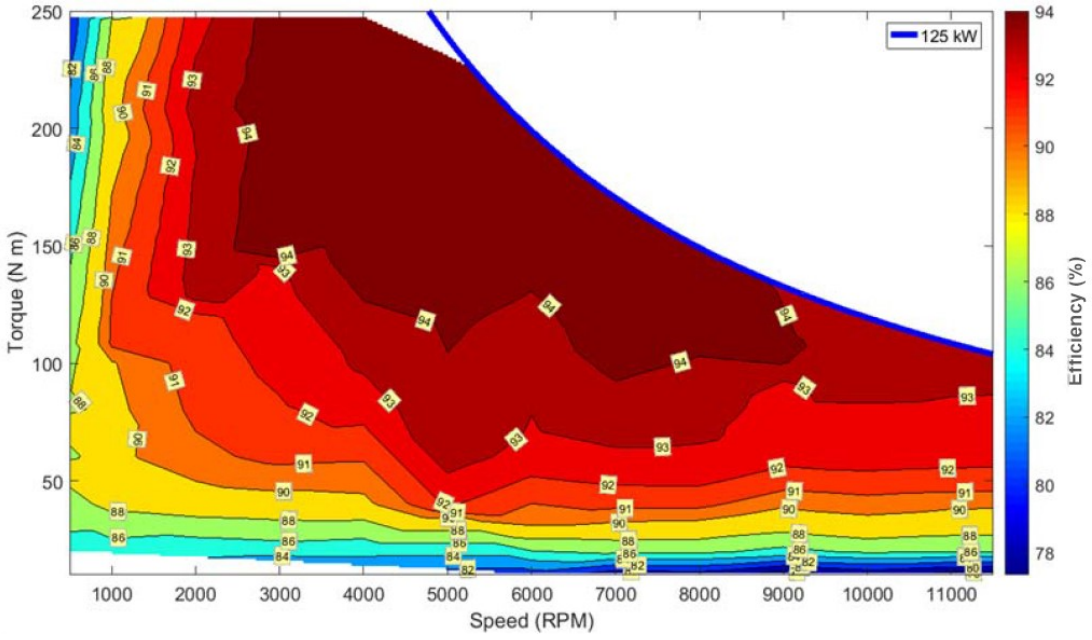

Figure 9-3. Baseline machine (BMW i3) torque-speed curve and efficiency map [60]

9.2. Hybrid Rotor PMSM for Traction Application

Following the design considerations described in Chapter 4, an optimum SPP for the hybrid rotor PMSM is between 1 to 3 with an aspect ratio of 1 or higher. Since the aspect ratio of the baseline machine is less than 1, similar frame size and stack length will not be used. In addition, the baseline machine uses a 12-pole rotor, which is detrimental to the achievable saliency for an SyR rotor. However, choosing a 4-pole configuration for the rotor will produce a wide pole arc for the magnet, which complicates the manufacturing and magnetization process. Hence a 72 Slot – 8 Pole configuration (SPP = 3) is selected for the hybrid rotor machine. Assuming an aspect ratio of 1 and considering the same DC bus voltage limit of 360 V_{DC} as well as phase current of 375 A_{rms} set by the baseline machine, a PMSM machine stator is analytically sized.

Due to the periodic nature of an 8-pole machine and SPP of 3, only $1/8^{th}$ portion of the machine geometry is necessary in FEA, i.e., half pole-pair. The stator winding configuration for the $1/8^{th}$ model implemented in FEA is shown in Figure 9-4. Assuming a slot fill factor of 0.35, the stator winding phase resistance is calculated as 5.6 $m\Omega$ (at 120^{o} C), and a slot current density of 13.5 A_{rms}/mm^2, which is in a similar range with the baseline machine and hence can be cooled with similar liquid cooling infrastructure. While the lamination material for the baseline is not specified, considering the aggressive material cost reduction targets of the automotive industry, a standard Si steel of 0.35 mm thickness lamination is assumed. For the hybrid rotor PMSM design in this work, 35JN230 electrical steel is used for both stator and rotor laminations. Key design parameters of the HR-PMSM machine are summarized in Table 9-2.

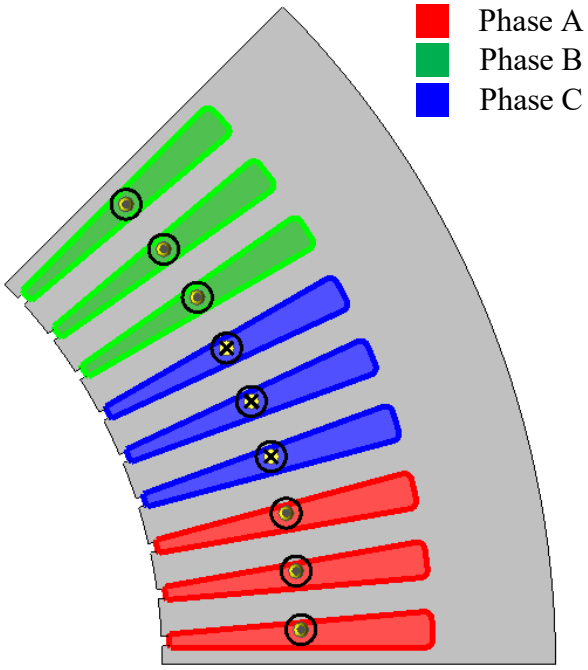

Figure 9-4. Stator design and winding configuration for 72 slot – 8 pole configuration

Table 9-2. Design parameters of HR-PMSM for traction application

Parameter	Value
Max. Power [kW]	125
Rated Speed [RPM]	4500
Phase Current (I_s) [A_{rms}]	375
DC Bus [V_{DC}]	360
Stack Length (l_e) [mm]	130
Stator Outer Diameter [mm]	176.7
Stator Inner Diameter [mm]	130
Air gap [mm]	0.6
Turns per coil	5
# parallel path per phase	4
Phase Resistance (R_s) [mΩ] @ 120° C	5.6

9.2.1. SyR Rotor Design

Following a similar design procedure established in Chapter 5, the intrinsic saliency of the machine is estimated and an initial SyR rotor designed. Multi-objective optimization, as described in section 5.2.1, is performed on the SyR machine with objectives to maximize torque and power factor, while minimizing torque ripple. A total of 6,500 designs were analyzed and the corresponding scatter plots for objectives with Pareto curves are shown in Figure 9-5. Considering a permissible torque ripple of 5%, an optimum design is selected from the Pareto points. The rotor geometry is further parametrically analyzed to ensure structural integrity at the maximum expected operating speed. The initial and optimized SyR rotor geometries are shown in Figure 9-6, and the optimized rotor stress distribution is shown in Figure 9-7. It can be seen that the stresses in the central bridges are around 350 MPa, which gives ≈ 18% safety margin on the stress limit.

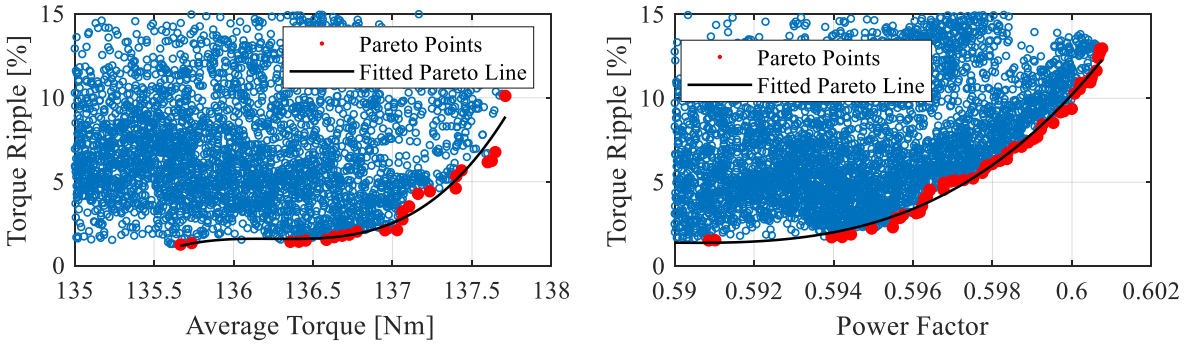

Figure 9-5. Scatter plots for objectives with pareto curve (a) Average torque vs. Torque ripple (b) Power factor vs. Torque ripple

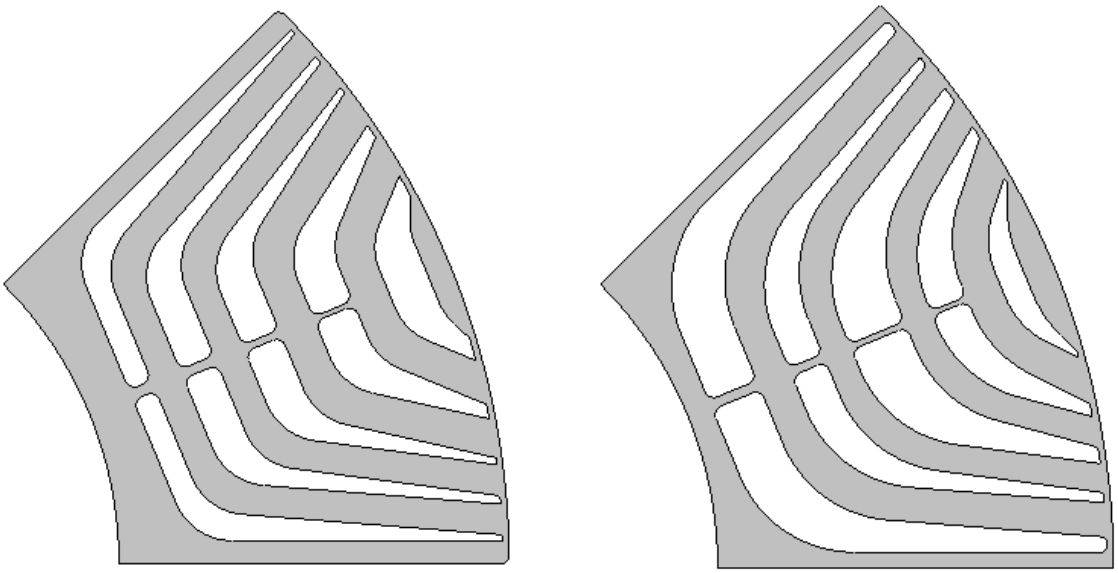

(a) (b)

Figure 9-6. SyR rotor design (a) Initial rotor (b) Optimized rotor

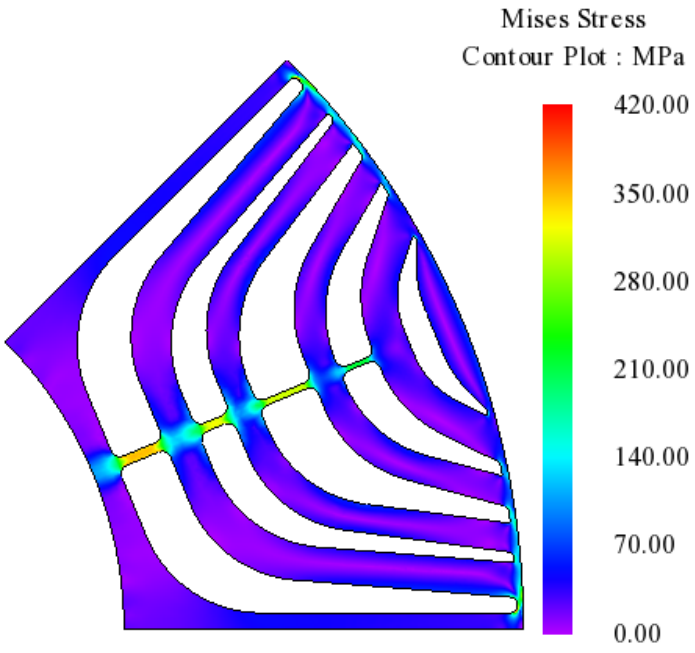

Figure 9-7. Mises stress distribution for the optimized SyR rotor at 12,000 RPM

The SyR machine torque as a function of phase current and current angle is determined using FEA and plotted, as shown in Figure 9-8. It can be seen that the MTPA operation shifts as the stator current increases due to saturation. The MTPA operation for rated current is found to be at $\gamma = 60^{o}$.

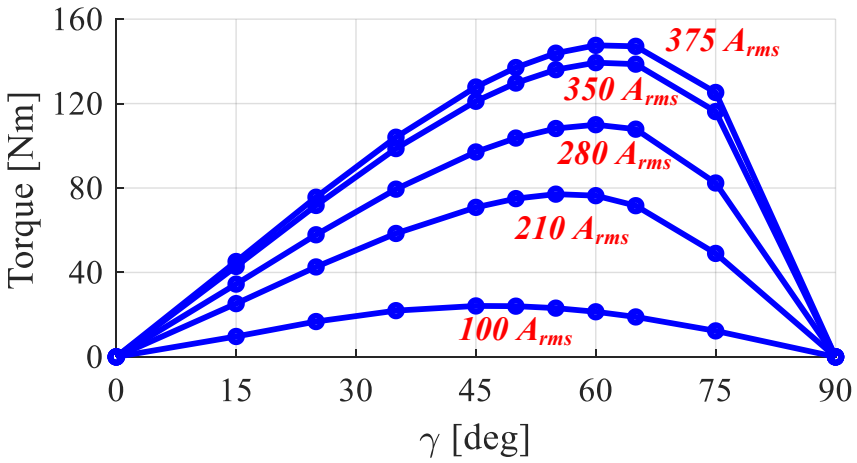

Figure 9-8. Torque as a function of current amplitude and phase optimized SyR rotor design

The phase voltage and torque waveforms at rated MTPA operation are shown in Figure 9-9 and Figure 9-10, respectively. The optimized SyR rotor achieves an average torque of 147.5 Nm with a torque ripple of 3.5%. The calculated inductance from FEA as a function of the stator current is shown in Figure 9-11. At rated operation, the optimized SyR rotor achieves a saliency ratio of 3.2 and a power factor of 0.6.

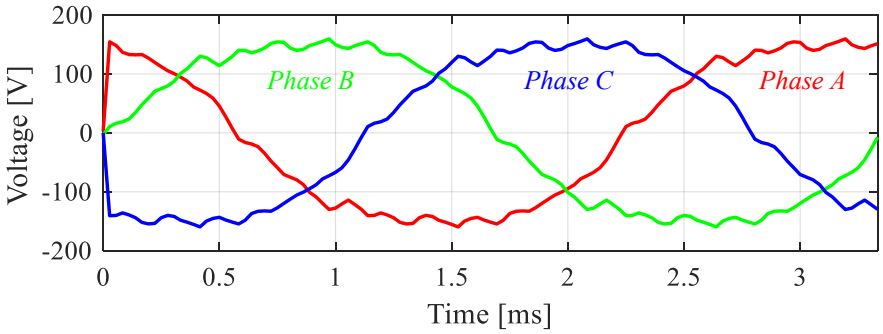

Figure 9-9. Phase voltage waveform at rated MTPA operation for optimized SyR rotor

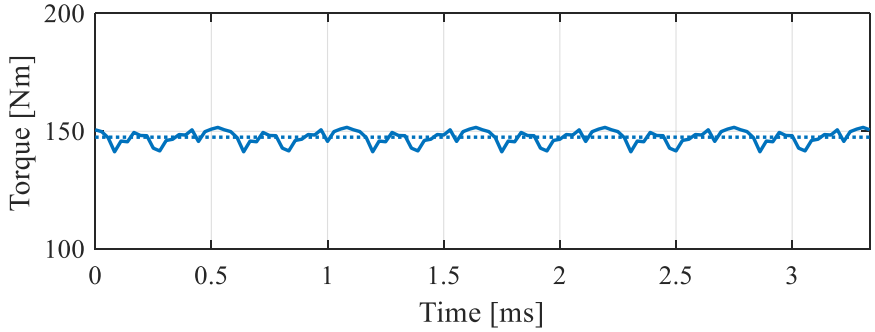

Figure 9-10. Torque waveform at rated MTPA operation for optimized SyR rotor

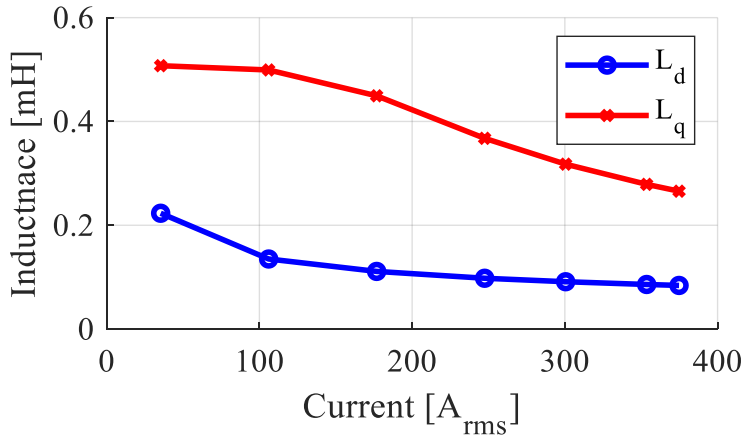

Figure 9-11. Inductance as a function of current calculated using FEA for optimized SyR rotor

9.2.2. SPM Rotor Design

The PM flux linkage and thickness are calculated using equations (5.12) to (5.14) for the SPM rotor. Given the maximum operation speed of around 12,000 RPM, PM retention is necessary for this PM rotor. Conventional practice is to use a rotor sleeve with an interference fit to apply pre-stress in the PM material. The pre-stress counters the centrifugal force experienced by the magnets, thus maintaining PM material contact with the back iron up to the designed speed range. Along with the maximum operating speed of the rotor, the rotor outer diameter, the magnet thickness and material density, and the material properties of the sleeve influence the sleeve design.

Inconel, a Nickel-Chromium-Iron alloy, is a typical sleeve material used in high volume production machines due to its high structural strength and corrosion resistance. Provided the thickness of the sleeve is small relative to the rotor outer diameter, an analytical model to accurately estimate the sleeve thickness was presented by Binder et al. in [61] . The two necessary conditions for the mechanical stability of the sleeve are described by,

$$\begin{aligned} p_{c-prestress} - \left(p_{\omega-m} + p_{\omega-s} \right) > 0 \\ \left(\sigma_{t-prestress} + \sigma_{t-\omega} \right) < \sigma_{t-\max} \end{aligned} \tag{9.1}$$

where $p_{c\text{-}prestress}$ and $\sigma_{t\text{-}prestress}$ are the residual contact pressure between the magnets and rotor surface and residual tangential tensile stress in the sleeve material respectively due to prestress, $p_{\omega\text{-}m}$ and $p_{\omega\text{-}s}$ are the outward pressure generated by the magnet and sleeve material respectively due to the rotation speed of ω, $\sigma_{t\text{-}max}$ is the maximum permissible tangential tensile stress of the sleeve material, and $\sigma_{t\text{-}\omega}$ is the tangential stress experienced by the material due to rotation.

An analytical iterative solver based on the two simultaneous equations described by (9.1) is implemented to determine the minimum sleeve thickness required for the designed SPM rotor assuming Inconel 718 material. A safety factor of 10% overspeed is considered, and the required sleeve thickness is determined to be 0.7 mm for a magnet thickness of 8.3 mm. The magnet grade N48H is selected, which has a B_r of 1.25 T, assuming a peak operating temperature of 80° C under rated operating conditions. The SPM rotor with the components and corresponding dimensions identified is shown in Figure 9-12.

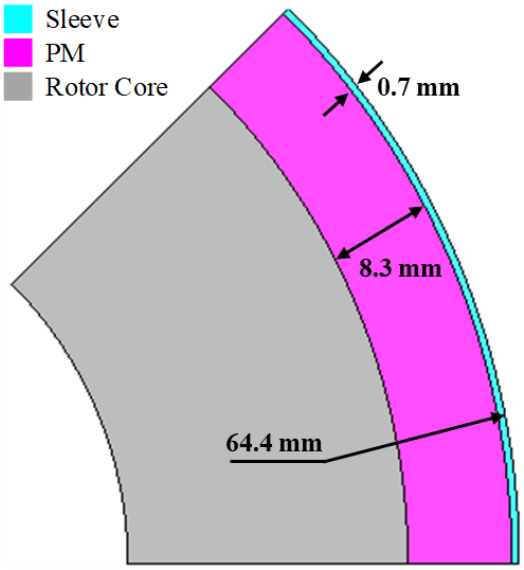

Figure 9-12. SPM rotor design with ring magnet

The torque as a function of current is plotted as shown in Figure 9-13. It can be seen that the torque response is fairly linear up to the rated current, indicating low saturation effects.

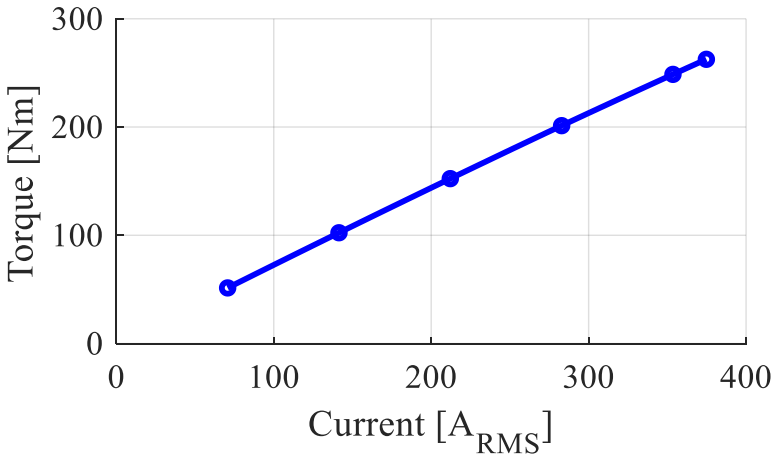

Figure 9-13. Torque as a function of current in SPM rotor

The phase voltage and torque waveforms at rated MTPA operation for the SPM rotor are shown in Figure 9-14 and Figure 9-15, respectively. At rated operation, the SPM rotor achieves an average torque of 262.9 Nm with a torque ripple of 5.9%, slightly higher than the target of 5% ripple. The calculated inductance from FEA as a function of the stator current is shown in Figure 9-16.

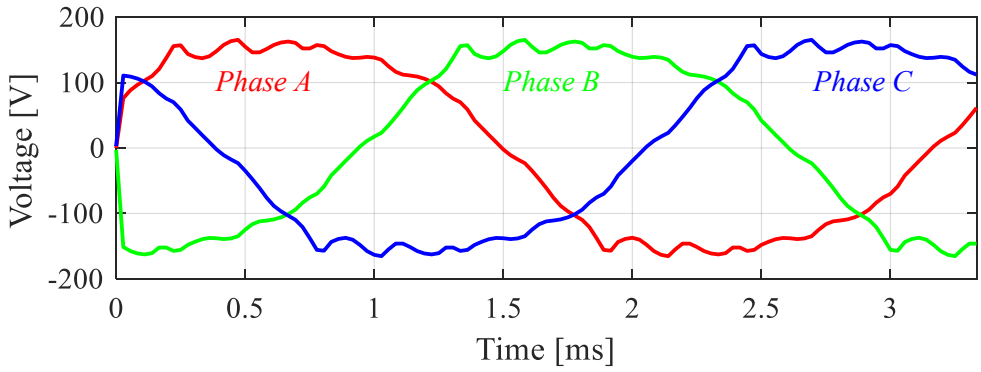

Figure 9-14. Phase voltage waveform at rated MTPA operation for SPM rotor

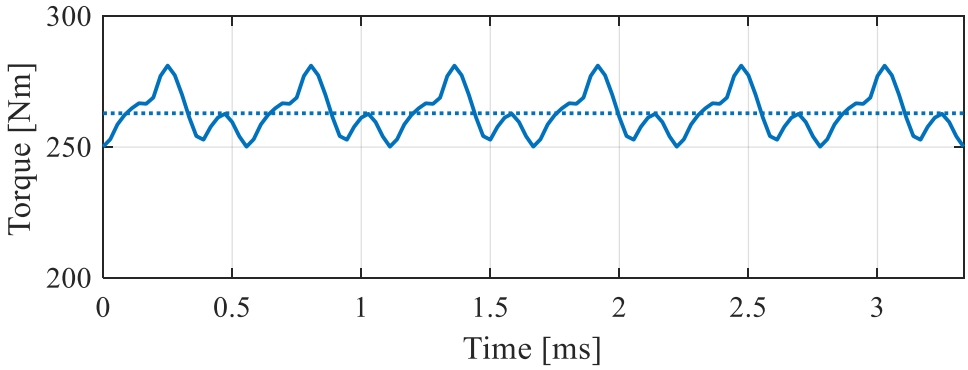

Figure 9-15. Torque waveform at rated MTPA operation for SPM rotor

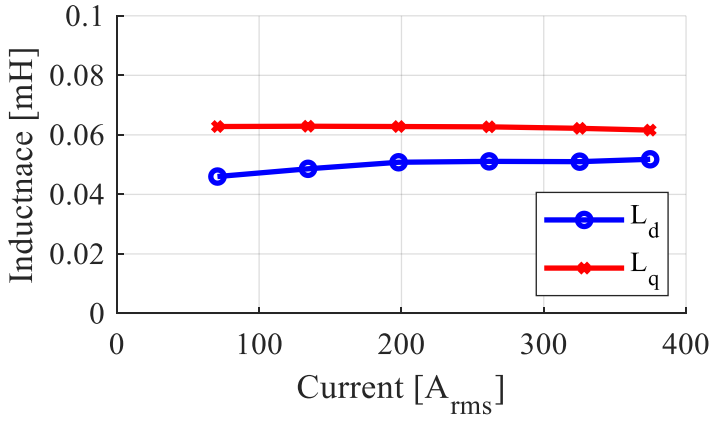

Figure 9-16. Inductance as a function of the current calculated using FEA for SPM rotor

9.2.3. Hybrid Rotor

Compared to the *q*-axis inductance of the SyR rotor, the *d*-axis inductance of both rotors is around 0.6 mH set by the SyR rotor. Hence the assumption of $L_{dpm} \approx L_{drm}$ is valid for this design, and the proposed analytical modeling methods can be used to calculate the optimum combination of the individual rotor sections to achieve an ideal infinite CPSR design. Using

equations (3.66) and (3.67), the bounds for α and k_l to achieve theoretical infinite CPSR are calculated as,

$$\begin{aligned} 0.296 \le k_l \le 0.614 \\ 5.9^o \le \alpha \le 66.74^o \end{aligned} \tag{9.2}$$

As discussed in Section 6.3, any combination of the rotor sections that satisfy both equations (3.66) and (3.67) simultaneously will maintain constant power during field weakening operation. Targeting high starting torque, the combination that gives maximum starting torque is selected, which occurs at α = 56° and k_l = 0.584, i.e., 58.4% of the stack length will be PM rotor at an electrical offset angle of 56°. An exploded view of the reduced axisymmetric and periodic 1/16th CAD model is shown in Figure 9-17, and the magnetic flux density distribution contour plot for the complete model is shown in Figure 9-18.

LUT's for both SPM and SyR machines are generated and assembled in Simulink as described in section 6.1. The rated torque and voltage waveforms obtained from 3D FEA and LUT model are plotted and compared as shown in Figure 9-19. It can be observed that there is a slight mismatch between the LUT and 3D FEA results, particularly in the torque waveform with the LUT model overestimating the average torque by 2.3%. This could be due to the higher degree of saturation and leakage components in the 3D model, which are not accounted for in the LUT based model.

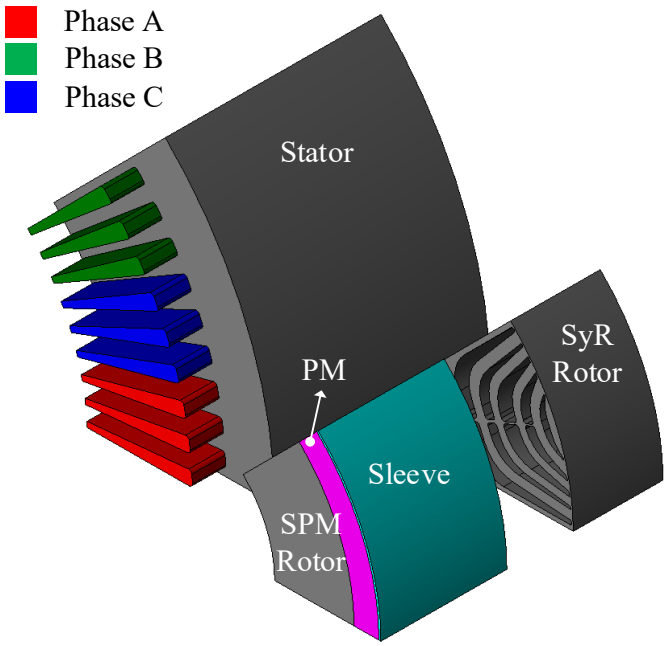

Figure 9-17. Reduced (1/16th) 3D model for hybrid rotor PMSM using axial and rotational symmetry

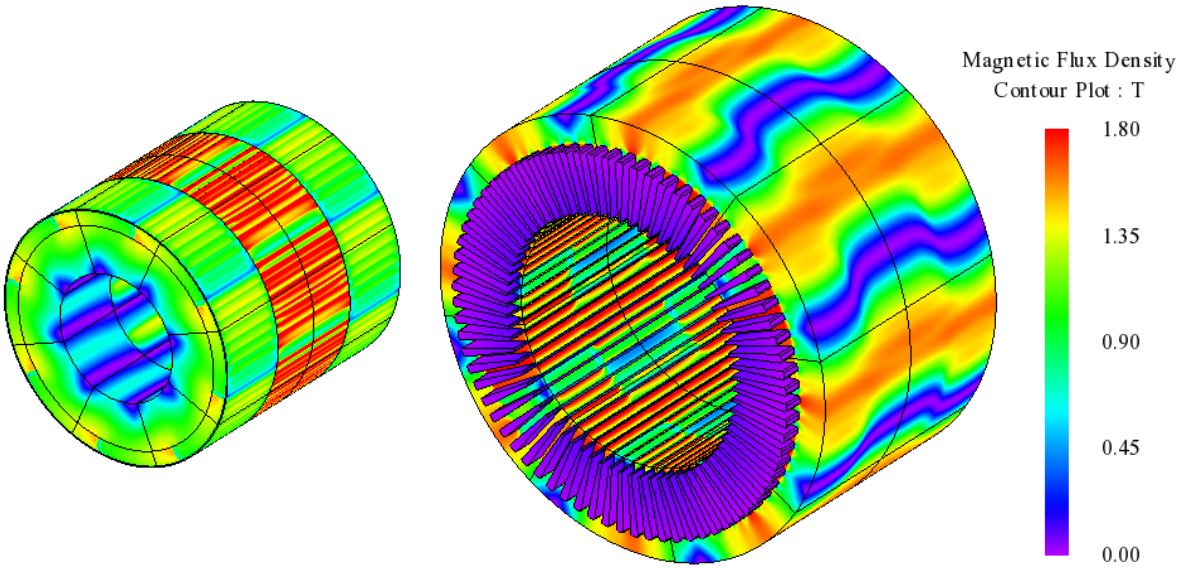

Figure 9-18. Flux density contour plot at rated MTPA operation for hybrid rotor PMSM

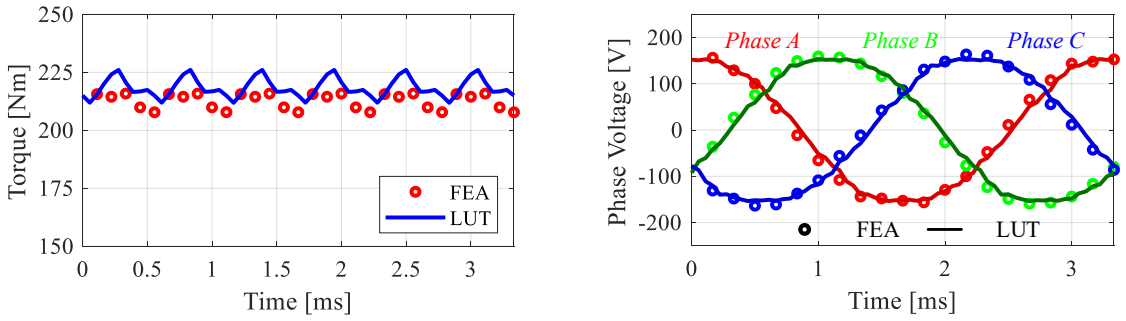

(a) (b)

Figure 9-19. Rated MTPA operation waveforms comparison between 3D FEA and LUT model for hybrid rotor PMSM (a) Torque (b) Phase voltage

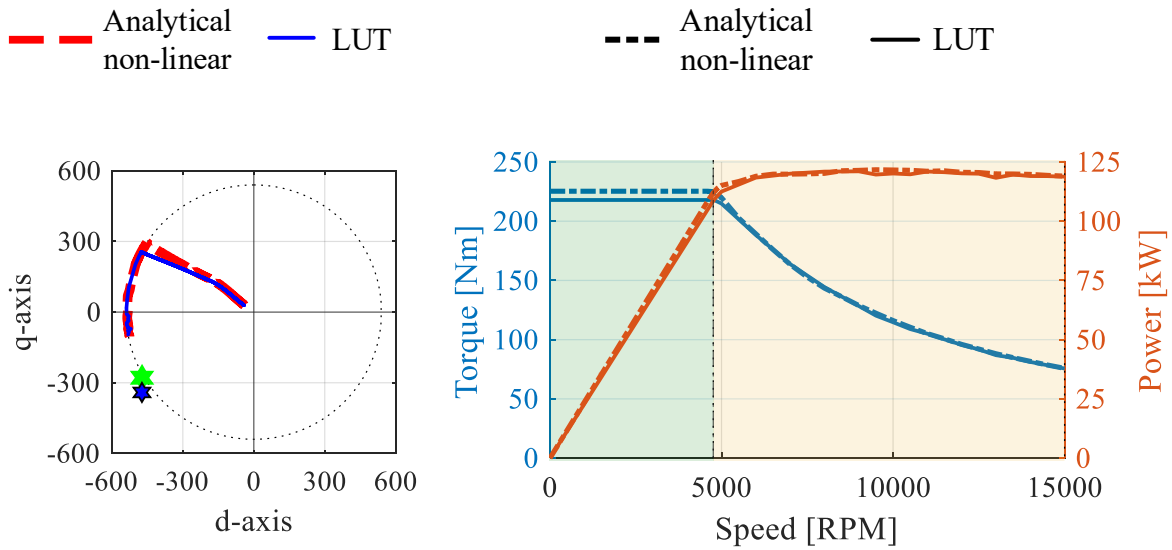

(a) (b)

Figure 9-20. Torque and power characteristics of the hybrid rotor PMSM (a) Current command trajectory (b) Speed-torque and speed-power curves

The current command trajectory as well as the torque-speed and power-speed curves are estimated using both analytical non-linear model and the LUT model, as shown in Figure

9-20. It is important to note that both models do not include iron loss component. The developed hybrid rotor machine achieves a peak power of 121.6 kW, which is 2.72% lower than the baseline machine. However, it is evident that the developed hybrid rotor PMSM achieves wide CPSR operation over the desired operating speed range.

9.3. Efficiency Map Generation and Performance Comparison

In order to compare the performance with the baseline traction machine, along with the torque, power – speed characteristics, an efficiency map over the complete operating region of the hybrid rotor PMSM must be developed. The 2D LUT developed in Chapter 6 is focused on assembling the torque and flux linkage as a function of the stator current amplitude and phase angle. For a given input of current amplitude and rotation speed limits, the algorithm extracts the torque and flux linkage and computes the corresponding voltage using flux linkage. The machine losses are dependent on the operation speed and the flux density distribution in the machine as a result of the current command and not captured in the existing LUT model.

Due to the nature of the lamination direction and the segmented rotor sections, the magnetic flux from each rotor section has minimal interaction through the stator core as discussed in section 5.3, and a clear differentiation in the phase of the stator flux density contour corresponding to each rotor section in Figure 9-18. This also allows for the losses to be separated into each rotor section, similar to the torque and flux linkage, and determine using 2D FEA. The results can then be recombined based on the values of k_I and α. Accordingly, a secondary LUT is developed that comprises of core loss data obtained from 2D FEA of SPM

and SyR machines individually at different operating speeds and current commands. The iron loss LUT data for each rotor section as a function of rotor speed is plotted in Figure 9-21.

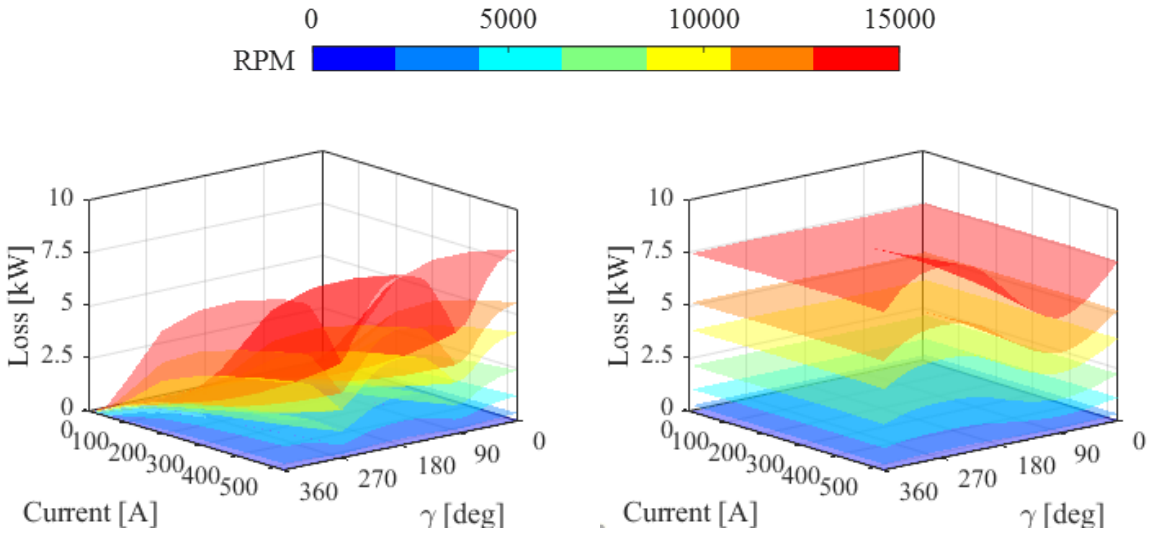

(a) (b)

Figure 9-21. Iron loss LUT data obtained from 2D FEA as a function of rotor speed (a) SyR rotor (b) SPM rotor

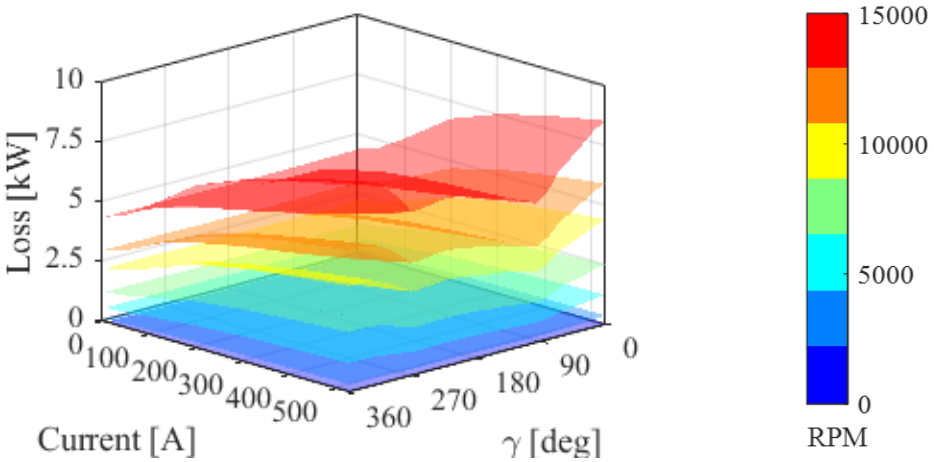

Figure 9-22. Reconstructed iron loss LUT data as a function of rotor speed for the hybrid rotor PMSM

The loss data for the SPM section shown in Figure 9-21(b) is shifted on the γ axis based on the α value, in this case, 56°, and combined by scaling with the corresponding stack length ratios. The combined LUT for the hybrid rotor PMSM is shown in Figure 9-22. From the iron loss LUT data, the loss corresponding to any operating point defined by rotor speed and current command can be computed through interpolation.

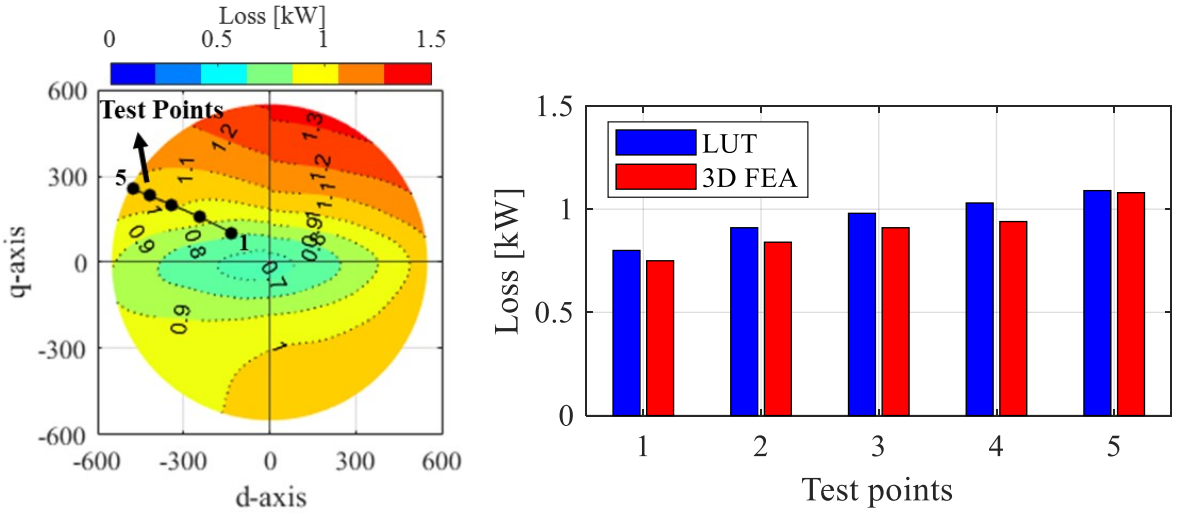

(a) (b)

Figure 9-23. Validation of iron loss estimation from LUT model (a) LUT generated loss map at 4,500 RPM with overlayed test points (b) Comparison with FEA at test points

To verify the validity of this model, the iron loss map for an operating speed of 4,500 RPM is calculated using interpolation and extracted from the LUT and plotted on the *dq*-plane as shown in Figure 9-23(a). Various [i_d, i_q] test points corresponding to MTPA operation are selected and overlayed on the loss map in Figure 9-20(a). The corresponding losses are also determined using 3D FEA model and compared with the results from LUT based model, as shown in Figure 9-23(b). The LUT model is slightly over-predicting the losses compared to

3D FEA since the 3D analysis more accurately models the end effects and leakage components. The losses are overestimated at low current values by at most 7.2%, while in good agreement with the 3D FEA predicted values at rated operation.

While the iron losses can be predicted with reasonable certainty using 2D FEA to develop a LUT, the eddy currents generated in the SPM rotor sleeve and magnets flows axially and require 3D FEA modeling. In addition, the eddy currents are typically generated close to the surface of the rotor outer diameter, i.e., the radially outer surface of the sleeve and the magnet, thus requiring high mesh density on the surface. Due to the high computational cost associated with 3D FEA, it is not practical to create LUT similar to iron losses.

The proportionality of eddy current losses (P_e) can be expressed as,

$$P_e \propto f_e^2 B_{pk}^2 \tag{9.3}$$

where f_e and B_{pk} are the frequency and peak flux density, respectively. While f_e is determined by the rotation speed, the value of B_{pk} is dependent on the current amplitude and current angle (γ). Since the highest joule losses will be at peak current amplitude, an initial study is performed at peak current and rated speed to identify the impact of current angle on the rotor eddy current losses for the current hybrid rotor under consideration, i.e., k_l = 0.584. Since the SPM rotor is segmented, the stack length for the magnet and sleeve is set to 37.96 mm. The eddy current losses from sleeve and PM as a function of γ in the PM rotor reference frame are plotted in Figure 9-24.

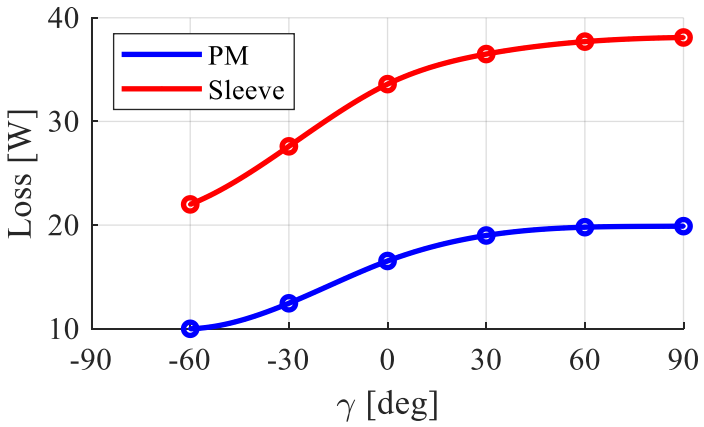

Figure 9-24. Rotor eddy losses as function of current angle using FEA for SPM rotor with rated current and rated speed.

It is evident that the losses are highest when the current angle is at 90°, where the demagnetizing flux from the stator is the highest. Considering the machine will be in the field weakening region during high-speed operation, i.e., $\gamma > 0$ in the PM rotor reference frame, the rotor eddy losses are calculated using 3D FEA at various operating speeds and $\gamma = 90^{o}$ and plotted as shown in Figure 9-25. Due to the naturally segmented nature of the PM rotor arrangement in the hybrid rotor PMSM, the losses in both the PM and sleeve are found to be not significant.

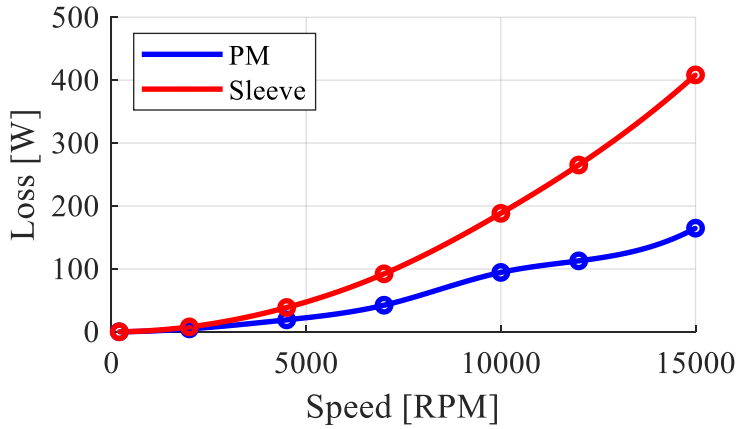

Figure 9-25. Rotor eddy losses as function of operating speed using FEA for SPM rotor with rated current and γ= 90°.

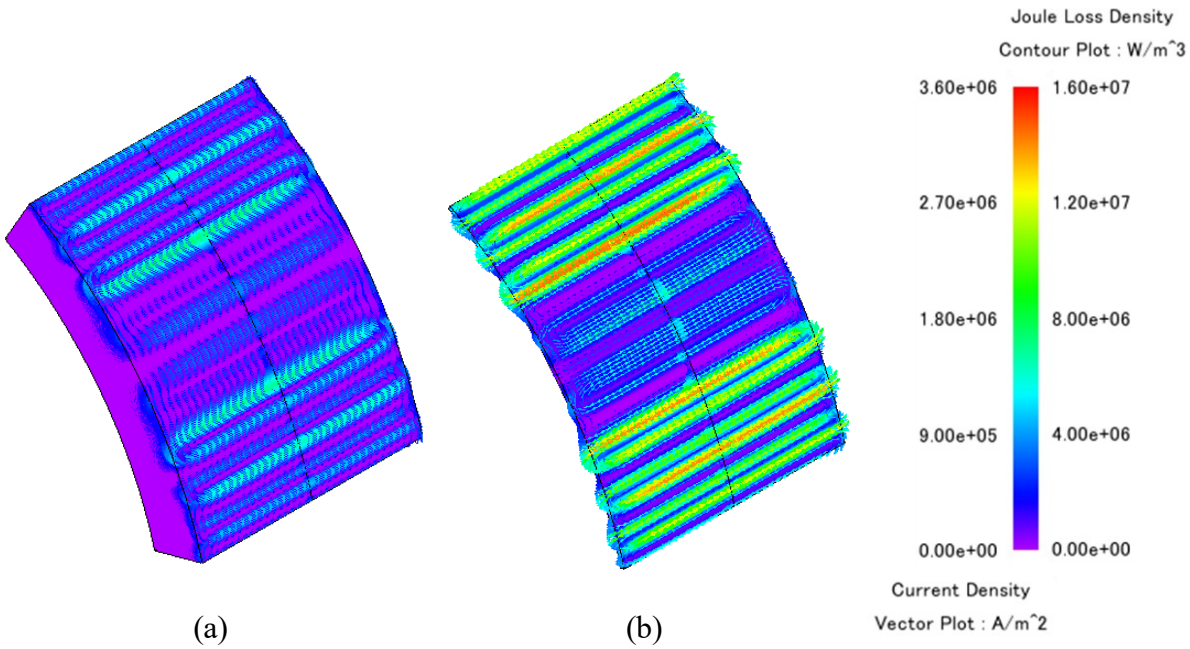

Figure 9-26. Joule loss density distribution and eddy current vectors for SPM rotor components at MTPA operation and 4800 RPM (a) Magnet (b) Inconel sleeve

The joule loss density contour along with the eddy current vector plots for the PM and sleeve at rated speed and current with $\gamma = 90^{o}$ are shown in Figure 9-26. It can be seen that the presence of a rotor sleeve actively shields the magnet from experiencing high eddy current losses. It is evident that the rotor eddy current losses are not significant compared to the iron loss, particularly at higher operating speeds. This is expected due to the highly sinusoidal MMF with the adopted distributed winding configuration and high SPP. This leads to reduced higher-order harmonic components interacting with the rotor in the synchronous reference frame. However, it is important to note that the analysis presented here is assuming an ideal sinusoidal current excitation. While it is possible to achieve close to sinusoidal excitation using current source inverters (CSI), a typical traction machine, along with the baseline machine selected for comparison, are exited using voltage source inverters (VSI) and introduce significant high frequency switching harmonics, potentially increasing both iron and joule losses. Hence the loss estimates obtained from FEA are assumed to be optimistic.

The joule losses in the stator winding can be calculated at any operating point with the corresponding current amplitude and the phase resistance. Hence a LUT based loss calculation model is developed that utilizes the output from the algorithm described in Figure 6-11. For every operating point on the speed-torque curve, the iron loss, stator winding loss and rotor eddy losses are determined using the loss LUT model, and the efficiency calculated. This process is repeated for several speed-torque curves corresponding to different phase current amplitudes, and an efficiency map is generated, as shown in Figure 9-27. The torque lines corresponding to the maximum constant power achieved by the developed hybrid rotor PMSM as well as the target power of 125 kW are overlayed on the efficiency map. As indicated by the efficacy map, the developed hybrid rotor PMSM can reach a peak efficiency of over 97%.

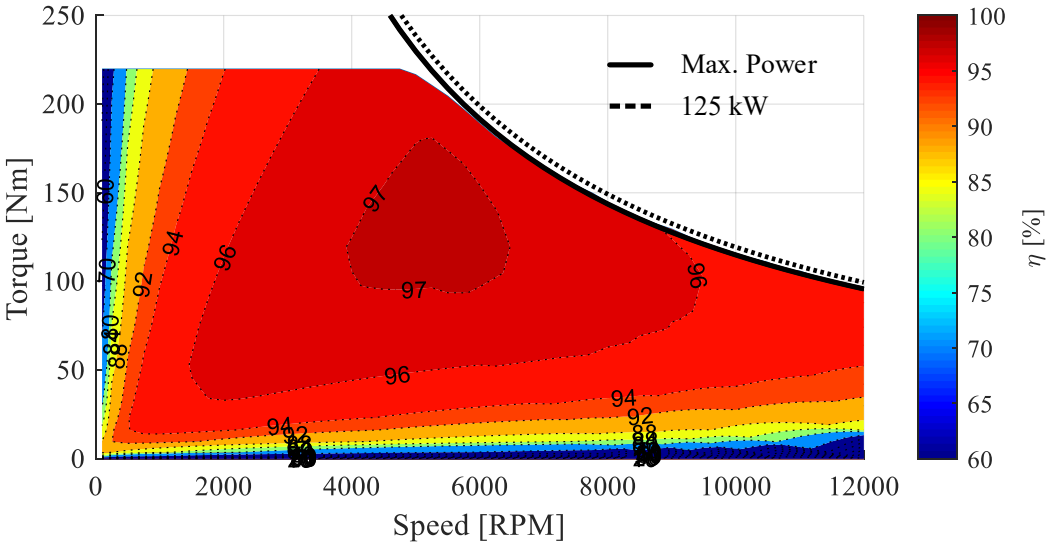

Figure 9-27. Efficiency map for the hybrid rotor PMSM

To compare the power density of the developed hybrid rotor PMSM with the baseline machine, the active mass of the machine components is calculated. The mass breakdown of the baseline BMW i3 machine is available in [60], where the active mass of the stator was clearly indicated. The rotor mass, however, includes the shaft and end plates. To account for these components, a 50% weight penalty is added to the rotor mass of the developed hybrid rotor PMSM. The performance metrics, as well as the power and torque densities of the machines are summarized in Table 9-3. While the baseline machine has slightly higher torque density, both machines have similar power densities and peak efficiency.

In addition, since PM material has the highest cost per unit mass it is important to ensure the magnet volume (or) mass is similar for both machines. While the magnet dimension or mass of the baseline machine is not specifically available, the dimensions of two individual magnets are approximately estimated from the available images by comparing with the known

dimensions. The total magnet volume is calculated to be ≈ 24 × 10^{-5} m^3, while the magnet volume of the hybrid rotor PMSM is 23.82 × 10^{-5} m^3, which gives a similar cost estimate for the PM material in both machines.

Table 9-3. Performance comparison of HR-PMSM for traction application with baseline BMW i3 IPM machine

Parameter		Baseline	HR-PMSM
Max. Power [kW]		125	121.6
Max. Torque [Nm]		250	218.75
Peak efficiency [%]		94	97.3
Coil current density [A_{rms}/mm^2]		12.7	13.5
Stator OD [mm]		241	176.7
Rotor OD [mm]		178.6	128.8
Stack length (l_e) [mm]		132	130
Rotor mass [kg]	Active	- -	7.72
	× 150%	14.2	11.58
Stator mass [kg]		20.8	22.16
Torque density [Nm/kg]		7.1	6.6
Mass power density [kW/kg]		3.57	3.6

Finally, the estimated performance of the individual SPM, SyR and the hybrid rotor configurations are determined and summarized in Table 9-4. The power-speed curves for the three rotor configurations are also determined and compared, as shown in Figure 9-28. It can be seen that while the SPM rotor exceeds the desired maximum power rating, there is no CPSR operation. The SyR rotor can maintain a CPSR but with a very low power rating. By combining the two rotor geometries, a wide range of performance characteristics between the two rotors can be obtained with the same stator design and relatively no additional tooling costs.

Table 9-4. Estimated performance range of HR-PMSM for traction application using LUT modeling

Parameter	SPM	SyR	HR-PMSM
Max. Power [kW]	128.6	73.1	121.6
Max Power Speed [RPM]	4750	4850	5800
Max. Torque [Nm]	268.7	147.6	218.75
Corner Speed [RPM]	4400	4500	4750
Phase Current (I_s) [A_{rms}]		375	
Stack Length (l_e) [mm]		130	
Stack length ratio (k_l)	1	0	0.584
Rotor offset angle (α) [deg]	-	-	56

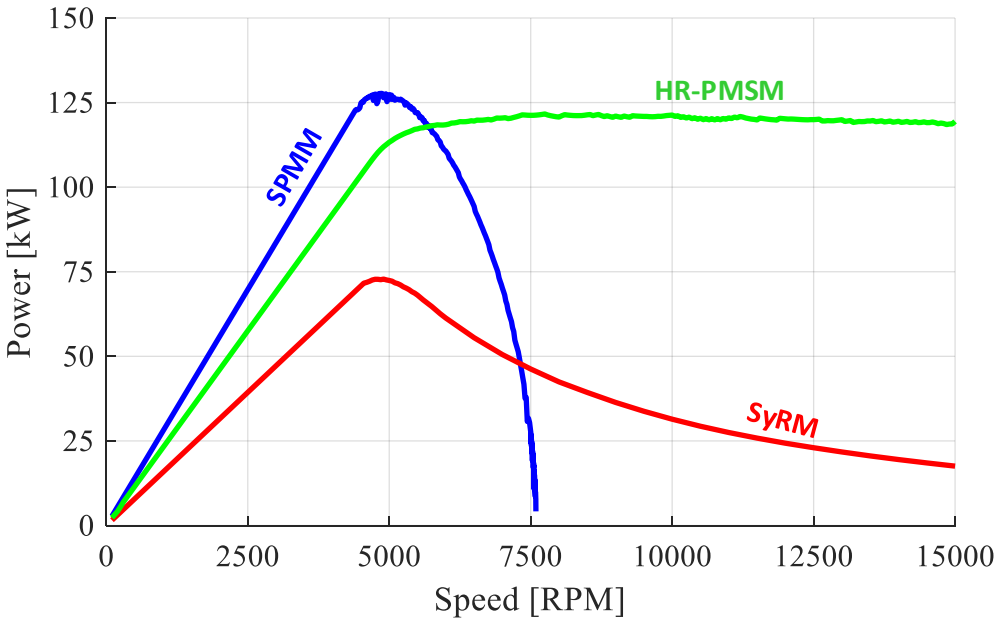

Figure 9-28. Speed-power curve comparison for the designed SPMM, SyRM and optimum HR-PMSM

9.4. Torque Ripple Mitigation

While it is observed that the SPM rotor itself has a torque ripple of 5.9%, the hybrid rotor PMSM comprises of only 58.4% stack length of PM rotor. Also, the torque ripple components of the SPM rotor section are combined with SyR rotor torque components, and hence the net torque ripple is lower than the 5.9% from SPM rotor.

As observed in Figure 9-2, the baseline machine has a step skewed rotor with 6 segments. This arrangement helps in mitigating the torque ripple, which could cause unwanted vibration in the drive system. The segmented nature of the hybrid rotor PMSM naturally allows for implementing such step skew. From the rated torque waveform of the designed hybrid rotor PMSM shown in Figure 9-19, the torque ripple appears as a 6^{th} order component. With the 72S - 8P configuration, the appropriate skew angle (ε) can be calculated as,

$$\varepsilon = \frac{2\pi}{P}\left(\frac{1}{h_\tau}\right) \tag{9.4}$$

where h_τ is the dominant harmonic component for the torque ripple. Hence the skew angle to obtain minimum torque ripple is π/24 (or) 7.5°.

This step skew can be implemented by offsetting the top section of the SPM rotor by (α + ε/2) and the bottom section of SPM rotor by (α – ε/2) as shown in Figure 9-29. An LUT based analysis is performed with multiple step skew angles, and the average torque along with torque ripple percentage as a function of the skew angle are plotted in Figure 9-30. As expected, a minimum torque ripple of 1.1% is obtained at ε = 7.5°. A comparison of the torque waveforms with and without the skew is shown in Figure 9-30.

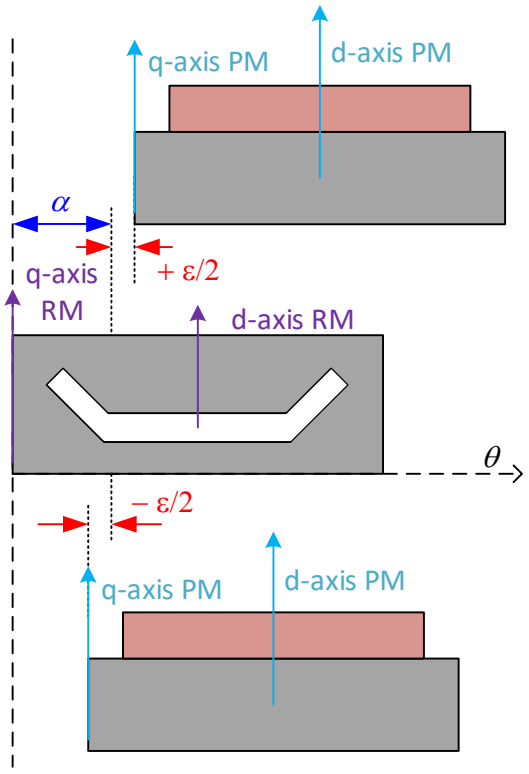

Figure 9-29. Hybrid rotor PMSM interpretation with step skew on the SPM rotor sections

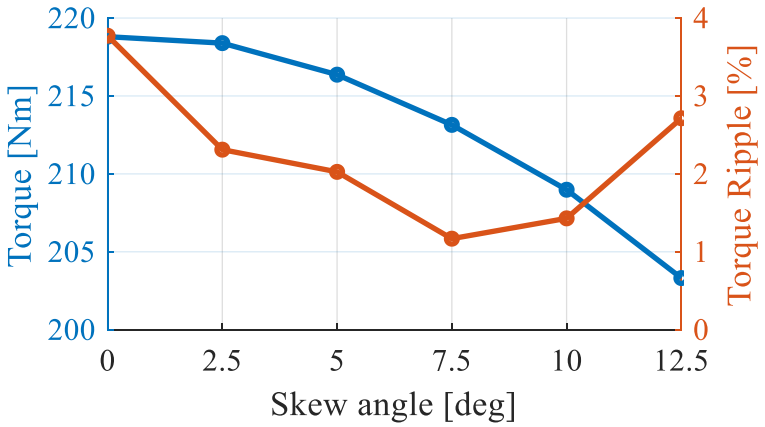

Figure 9-30. Average torque and torque ripple percentage as a function of skew angle for hybrid rotor PMSM.

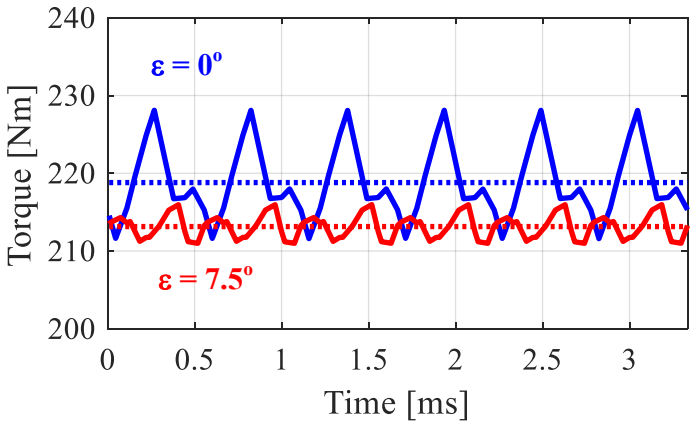

Figure 9-31. Torque waveform of the hybrid rotor PMSM with and without step skew

With the step skew, torque ripple reduced from 3.8% to 1.1%, while the average torque reduced from 218.75 Nm to 213.15 Nm, a 2.5% reduction.

9.5. Demagnetization

The operation point of the PM material is determined by the intersection point of the load line and the BH curve of the PM material at its operating temperature. The slope of the load line, also known as the permeance (P_c) is determined by the machine geometry, and the offset of the load line is determined by the amplitude of the external field applied by the stator MMF. A series of BH curves for different temperatures from the manufacturer data sheet for the selected PM material, and an interpretation of the load line that is displaced by an external magnetic field are shown in Figure 9-32. If the PM operating point goes below the knee point of the BH curve due to the external field, the PM material will be permanently demagnetized and will not return to its original strength.

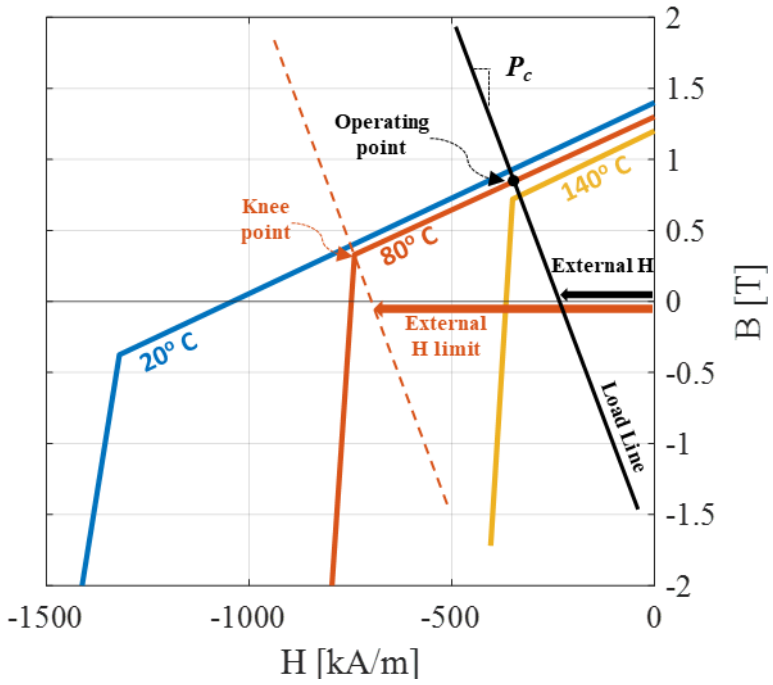

Figure 9-32. Selected PM material BH curves and operating point

Considering the nominal operating temperature of 80°C, a 1 p.u. demagnetizing current, i.e., $\gamma = 90^{o}$ in PM rotor reference frame which corresponds to field weakening operation at theoretical infinite speed, is applied for one electrical cycle, and the H field inside the PM material of the SPM rotor was extracted using FEA. This is achieved by individually recording the amplitudes of field vectors in the direction of initial magnetization inside each mesh element of the PM material and categorizing the mesh element as either healthy or demagnetized depending on if the operating field amplitude is lower than the field amplitude set by knee point at any time in the 1 electrical cycle. Each mesh element is color-coded and plotted, as shown in Figure 9-33. It can be observed that there are no demagnetized zones on the magnet under the rated current operation.

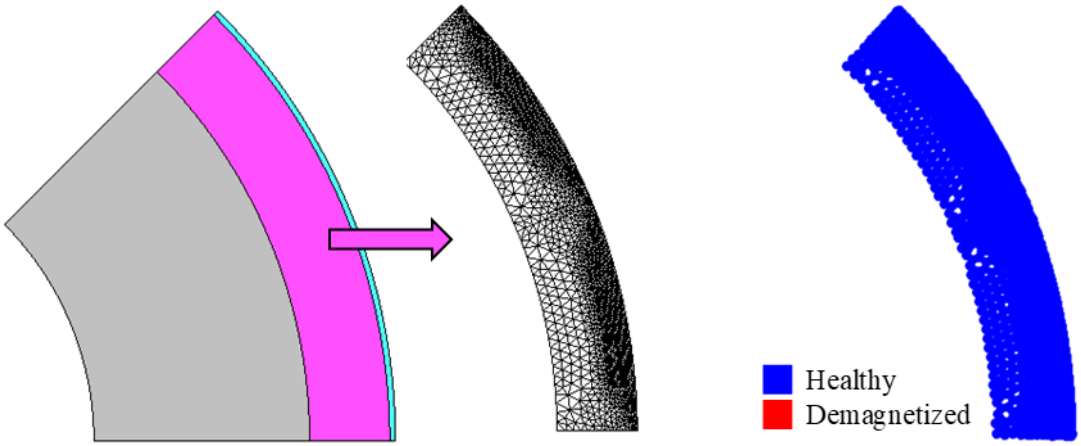

(a) (b) (c)

Figure 9-33. Demagnetization analysis of SPM rotor section using magnetic field strength (H) of PM material (a)Rotor (b) Meshed PM (c) Mapped demagnetization zones for 1 pu demagnetizing current.

From Figure 9-32, the PM material has a BH curve that changes depending on the operating temperature. The selected magnet material, N48H, has a manufacturer recommended maximum operating temperature of 120^{o} C. Hence the process is repeated for different temperatures and the impact of demagnetization shown in Figure 9-34. It can be seen that for the developed machine geometry, the PM material can withstand up to 140^{o} C before the effects of demagnetization are observed.

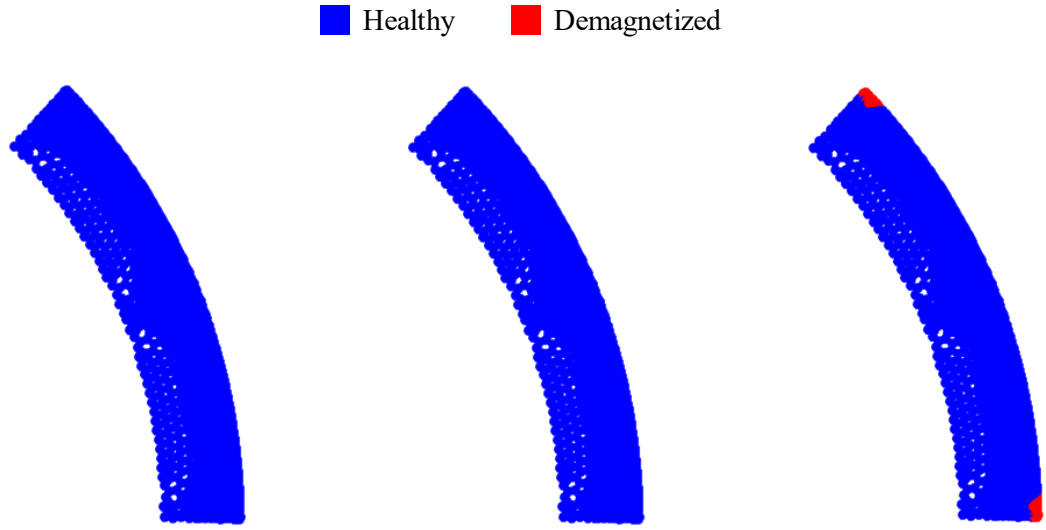

Figure 9-34. Mapped demagnetization zones for 1 pu demagnetizing current at different operating temperatures (a) 95° C (b) 110° C (c) 140° C.

In addition to the field weakening current during extended speed operation, a potential winding short circuit can also cause severe demagnetization. Ideally, a characteristic current of 1 p.u. is a necessary condition for an infinite CPSR machine. Accordingly, the steady state short circuit current of the designed hybrid rotor PMSM is expected to be 1 p.u. However, the transient effects at the instance of a short circuit can reach much higher, causing a potential for demagnetization. The phase current obtained from a 3-phase short circuit analysis performed using FEA is shown in Figure 9-35. While the steady state current is close to 1 p.u., a maximum of 3 p.u. current is observed.

Hence a 3 p.u. demagnetizing current applied, and the demagnetization analysis is repeated for different temperatures. The observed impact of demagnetization is shown in Figure 9-36. While there is negligible impact at the nominal operating temperature of 80°C,

the outer surface of the magnet begins to show demagnetization if the material is at 95° C when the short occurs, and mostly demagnetized at 110° C.

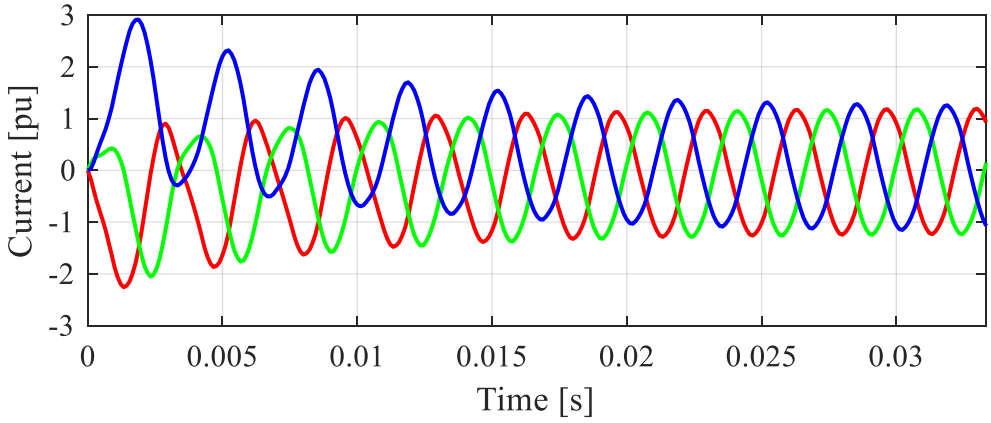

Figure 9-35. Phase current with a 3-phase short circuit of the hybrid rotor PMSM

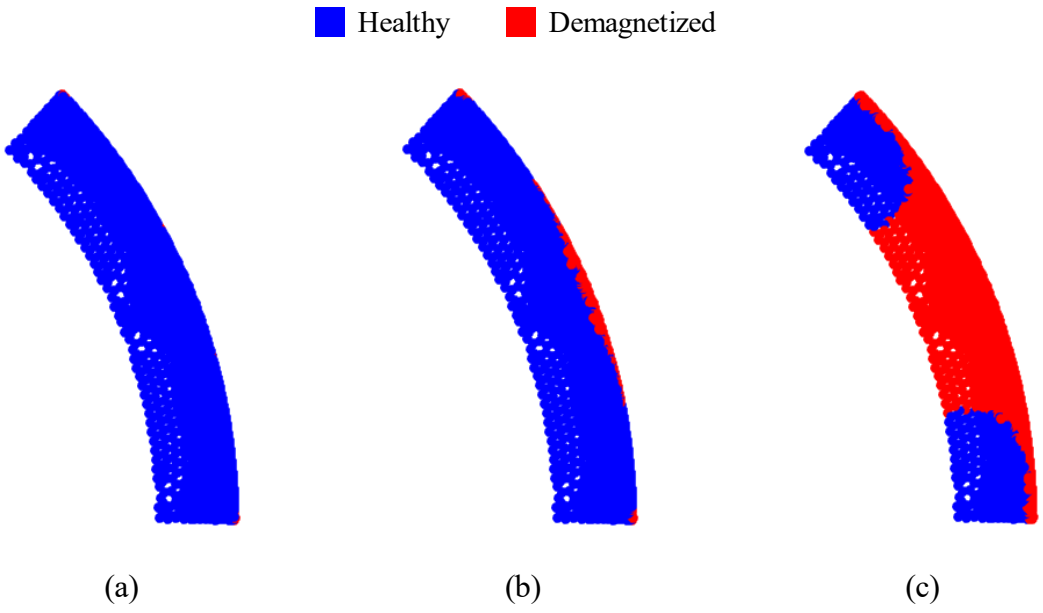

Figure 9-36. Mapped demagnetization zones for 3 pu demagnetizing current at different operating temperatures (a) 80° C (b) 95° C (c) 110° C.

While the above analysis shows the demagnetization tolerance of the specific hybrid rotor PMSM developed in this chapter, a more general comparison between conventional machines and hybrid rotor machines can be performed by analyzing the design requirements and sizing equations. The magnitude of the characteristic current can be calculated as,

$$I_{char} = \frac{\psi_{PM}}{L_d} \tag{9.5}$$

To maintain wide CPSR, the characteristic current must be 1 pu. For a typical SPM machine, both the *d*-axis inductance and PM flux linkage are dependent on the air gap diameter and stack length of the rotor. Assuming the magnet thickness (t_m) and mechanical airgap thickness (g_m) follow the relation $t_m >> g_m$, the proportionality can be written as,

$$\begin{aligned} \psi_{PM} &\propto D_g l_e \\ L_d &\propto \frac{D_g l_e}{t_m} \end{aligned} \quad \Rightarrow \quad I_{char} \propto t_m \tag{9.6}$$

Hence, for a machine with a given air gap diameter and stack length, the characteristic current is inversely proportional to the magnet thickness.

To avoid demagnetization, the slope of the load line (P_c) shown in Figure 9-32 must be as high as possible. The proportionality of the load line slope can be written as,

$$P_c \propto \frac{t_m}{D_g} \tag{9.7}$$

Equations (9.6) and (9.7) establish simultaneous constraints for the thickness of the magnet to maintain the characteristic current at 1 p.u. while also increasing the slope of the load line, thus restricting the scope of demagnetization tolerance.

For a hybrid rotor PMSM with a stack length ratio of k_l, and a rotor offset angle of α, the magnitude of the characteristic current can be written using equations (3.33) to (3.36) as,

$$I_{char} = \frac{k_l \psi_{PM}}{L_d} \sqrt{\cos^2(\alpha) + \frac{1}{\xi}\sin^2(\alpha)} \propto t_m k_l \sqrt{\cos^2(\alpha) + \frac{1}{\xi}\sin^2(\alpha)} \quad (9.8).$$

Hence the load line slope, i.e., the magnet thickness, can be independently tuned to improve the demagnetization tolerance while maintaining the characteristic current magnitude using the parameters k_l and α.

9.6. Summary

With a goal of verifying the viability of using hybrid rotor PMSM for a practical, high-power application, an existing commercial EV (BMW i3) IPM machine is selected as the baseline. The traction application is suitable for this analysis due to the sustained wide CPSR operating region for hybrid rotor PMSM.

Using the design considerations and analysis procedure proposed in this research, a hybrid rotor PMSM is sized and designed for the specifications of the baseline machine. A LUT based iron loss estimation method that utilizes individual SPM and SyR iron loss tables obtained form 2D FEA is proposed and validated using 3D FEA models. Both the torque and iron loss estimation show ≈ 2.5% error at rated operation compared to 3D FEA. This error is due to a higher degree of end effects compared to the low power proof-of-concept machine and not captured in 2D FEA. The joule losses in PM material and the PM rotor sleeve are estimated using 3D FEA and incorporated into the loss LUT model. An efficiency map is

generated, and the performance of the designed high power hybrid rotor PMSM compared with the baseline BMW-i3 IPM machine.

While the max. torque and max. power of the designed hybrid rotor PMSM are12.6% and 2.6% lower, respectively, it was shown that the overall torque and power densities are comparable with the baseline machine, and the peak efficiency is 3.3% higher. It has to be noted that while the efficiency map of the baseline machine was generated using measured losses, the developed efficiency map is from FEA and ignores switching harmonic components. Typically, FEA tends to under-estimate the losses. However, it was observed that the LUT model was over-estimating the losses, as well as the PM rotor joule losses are only evaluated at peak operation due to the computational cost of 3D FEA. Considering these simplifications and inherent error in FEA, it can be concluded that both machines have similar practical efficiencies with a conservative approach.

Finally, the segmented nature of the PM rotor is utilized to implement step skew and achieve a minimum torque ripple of 1.1% with a 2.5% reduction in average torque as a trade-off. This can be avoided by further optimizing the PM shape or magnetization distribution instead of the uniform ring magnet used in this research.

The demagnetization tolerance of the hybrid rotor PMSM is also studied and it was shown that the developed design can withstand a field weakening current of 1 pu, up to 140^{o}C, far exceeding the suggested operating temperature limit of the PM material. However, in the case of a 3-phase short circuit, it was shown that the PM material starts to demagnetize at 95^{o}C, only 18.8% thermal margin from the nominal 80^{o}C operation. It was analytically shown that the hybrid rotor PMSM design gives a separate handle on tuning the demagnetization tolerance

while designing for the 1 p.u. characteristic current, which is an added advantage over the conventional PM machines since both characteristic current and the demagnetization tolerance depend on the magnet thickness.

Chapter 10

10. Conclusions, Contributions and Future Work

10.1. Conclusions

Based on the state-of-the-art literature review, it was identified that IPM machines are predominantly used in present-day traction applications due to a better PM material utilization ratio and high-speed, field weakening operation characteristics. However, designing IPM machines for such high speed – constant power operation requires significant fine-tuning of rotor geometry using optimization techniques. Different rotor arrangements and use of active magnetization state change techniques were investigated in the recent past to overcome some of the challenges in designing for precise operation characteristics. In addition, achieving modular design strategies to efficiently scale the machine design with minimal tooling costs is also gaining attraction in the aerospace and traction fields. Examples of a conventional approach of linear scaling of stack length are found in both cases.

Hybrid rotor machines that combine different rotor types on a single shaft were hypothesized to meet a wide range of load profile and system characteristic requirements. However, due to the perceived complexity in modeling and lack of understanding in the field weakening characteristics, hybrid rotor machines did not draw enough attention.

In this research, an analytical modeling method and a high fidelity LUT based modeling method for a hybrid rotor PMSM are proposed. FEA models are initially used to validate both

analytical and LUT based methods. Analytical calculation and design procedure to achieve an ideal infinite CPSR desired by traction loads is developed using hybrid rotor PMSM. A proof-of-concept prototype is manufactured, and the proposed models are experimentally validated. A high-power hybrid rotor PMSM is also designed and compared with an existing traction application machine. Some of the key research conclusions are summarised below:

10.1.1. Hybrid rotor PMSM analytical model

- Hybrid rotor PMSMs are truly a combination of individual characteristics of SPM and SyR machines with additional degrees of freedom available to combine the characteristics into a single machine. By controlling the nature of the rotor combinations, hybrid rotor PMSMs represent the possible performance profiles of a family of synchronous AC machines.
- With appropriate design constraints on individual rotor inductances, a complete unified machine model and a unified field weakening theory can be developed that encompasses the maximum torque performance characterization of synchronous AC machines, including the hybrid rotor PMSMs. The field weakening characteristics of conventional synchronous machines can be obtained from a unified field weakening model developed in this thesis by simply reducing the appropriate order. Hence, it can be interpreted that the conventional synchronous machines are only a subset of a broader scope of possible machine designs.
- If the initial SPM and SyR rotors meet the developed minimum criterion in terms of saliency and PM flux linkage, a theoretical infinite CPSR operation could be achieved

by appropriate selection of the rotor combination parameters, i.e., the stack length ratio (k_l) and rotor offset angle (α).

- The assumptions used to simplify and linearize the analytical model contributed to the discrepancy in the predicted field weakening performance using analytical modeling. However, the performance trend and the capability of CPSR operation were both accurately predicted by the analytical model. Furthermore, the analytical predictions were made more accurate by incorporating the non-linearities and loss components, thus validating the proposed linearized analytical modeling approach for the initial design.

10.1.2. Design of hybrid rotor PMSM

- The slot-pole combination and the aspect ratio selection are more dependent on the nature of the application requirements. However, to better utilize the individual rotor section strengths in a hybrid rotor PMSM, a DW configuration with a low pole number and an aspect ratio between 1 to 3 is beneficial.

- While very high saliency in the SyR rotor section is beneficial, it is not necessary to obtain desired power-speed characteristics. Although the conventional radial laminated SyR rotor structures produce lower saliency than axially laminated SyR rotor structures, the 20× magnetic gap separation required by the axially laminated rotor in hybrid rotor configuration would impact the overall performance, particularly if the machine does not have a small electromagnetic airgap.

- Contrary to the hypothesized claim of hybrid rotor PMSMs ability to achieve better power density due to the rotor offset angle in the past literature, the generalized sizing

equations for hybrid rotor PMSM developed in this research indicate that the hybrid rotor PMSM can achieve a similar power density of an equivalent SPM machine depending on the PM material strength and SyR rotor saliency and power factor.

- Designing the hybrid rotor PMSM for the desired field weakening performance, however, offers better modularity and manufacturing flexibility compared to conventional PMSM. This is possible since the same PM, and SyR rotor laminations can be combined in different ratios and offset angles to obtain a wide range of peak power and field weakening performance.

10.1.3. LUT based modeling of hybrid rotor PMSM

- The axial asymmetry of a hybrid rotor configuration requires 3D CAD models to perform detailed FEA. This was one of the key inhibiting factors for a through FE based analysis in the past. Combining the proposed analytical unified machine model with 2D FEA based LUT modeling methods provides a viable path for high fidelity and fast computation methods for hybrid rotor PMSM with a minimal trade-off in modeling accuracy.

- While the LUT generation requires moderately high computation resources, once a LUT is assembled for any given PM, and SyR rotor designs, numerous possible rotor combinations and their field weakening performance can be analyzed with minimal computational resources.

- The rotor joule losses, as well as stator and rotor iron losses, can also be separately evaluated using 2D FEA and combined into the LUT based model to predict the machine losses and efficiency over the complete range of operation. Similar to the

field weakening performance estimates, the loss estimation LUT requires moderate computational resources, but once LUT is assembled, the modeling method can analyze efficiencies of numerous combinations and operating scenarios with a minimal computational cost.

10.1.4. Scalability and advantages of hybrid rotor PMSM

- Compared to a conventional PMSM, where axial length is the only modular and scalable parameter with no additional tooling cost, hybrid rotor PMSMs' introduces additional dimensions to the machine scalability and provides a greater degree of modularity for an industrial supplier. The PM and SyR rotor cross-sections can be standardized and rotor modules combined based on application requirements to achieve different machine and performance characteristics, thus reducing redesign and retooling costs.
- The modular nature of a hybrid rotor PMSM also allows for appropriately fine-tuning the machine to meet desired performance characteristics post-manufacturing while accounting for production line efficacy and tolerances.
- Due to the segmented nature of hybrid rotor PMSM, the SyR and PM rotors can be individually optimized for desired saliency and PM flux linkage, respectively. Such independent design choice available on the two crucial parameters for determining characteristic current offers a strong advantage in achieving and maintaining the ideal CPSR operation with hybrid rotor PMSM.
- The inherent segmented nature of the SPM rotor in the hybrid rotor PMSM aids in reducing the rotor eddy current losses and allows for applying step skew to reduce

torque ripple. In addition, the fractional stack length of the PM rotor also allows for independently designing the PM thickness to better tolerate demagnetization while maintaining the desired characteristic current and hence field weakening performance.

10.2. Research Contributions

The primary contribution of this research is the development of an analytical methodology to analyze the field weakening performance of a hybrid rotor PMSM, including the arbitrary relative rotor offset angle and rotor section stack length ratios. A concise summary of contributions from this research are listed below:

- Established an analytical method for the determination of equivalent machine parameters of the hybrid rotor PMSM using the SyR rotor reference frame.
- Developed the analytical formulation of field weakening current command trajectories of hybrid rotor machines for maximum torque production within the current and voltage vector limits.
- Unified the field weakening analysis of different types of PMSMs that have been studied either using separate theoretical models or by numerical methods due to lack of analytical process.
- Established the criterion and methodology to determine optimum rotor offset angle for a hybrid rotor PMSM based on individual SPM and SyR rotor parameters to achieve ideal constant power speed characteristics.

- Proposed optimum CPSR design selection criterion based on application requirements form a range of possible infinite CPSR designs that all have the same output power but different corner torque, corner speed and PM volume.
- Developed sizing equations and extended guidelines for the selection of appropriate slot-pole combination and aspect ratio selection for the hybrid rotor PMSM. Established scalability criterion to maintain field weakening performance.
- Proposed the use of a conventional SyR rotor in place of an axially laminated SyR rotor to eliminate the non-magnetic separation between rotor sections.
- Proposed a high fidelity and rapid modeling method using a combination of look-up-tables (LUT) derived from 2D FEA of individual SPM and SyR machines with the analytical equivalent hybrid rotor machine model and validated using 3D FEA.
- Developed algorithms to generate performance characteristics, loss estimation and efficiency map generation for a hybrid rotor PMSM from LUT based models, and the validity of the proposed methods verified using 3D FEA.
- Identified manufacturing methods that can be used to build hybrid rotor PMSM configurations to meet either various load characteristics or fine-tune for manufacturing tolerances without a significant electromagnetic redesign.
- Designed a low power – low speed hybrid rotor PMSM suitable for servo application and demonstrated the ability to achieve wide CPSR operation along with variable range of performance characteristics to satisfy a range of application requirements.

- Manufactured a proof-of-concept prototype hybrid rotor PMSM and experimentally verified the 2D FEA models as well as the LUT based modeling methods for hybrid rotor PMSM.
- Designed a high power – high speed hybrid rotor PMSMs suitable for traction application and compared the performance with an existing traction machine showing similar performance, power density and efficiency but with better modularity and capable of meeting a wide range of operating characteristics.
- Demonstrated the ability for hybrid rotor machines to integrate torque ripple mitigation strategies and design for better demagnetization resistance.

10.3. Recommended Future Work

This thesis demonstrates that hybrid rotor machines performance, despite the added degree of complexity, can be practically modeled and analyzed analytically as well as with high fidelity LUTs using an equivalent machine model. It is shown that in fact the additional degrees of design freedom can be beneficial in standardizing the machine cross-section and yet have the flexibility to customize for system specifications with minimal tooling and manufacturing costs.

Nevertheless, there are other potential benefits of hybrid rotor configurations that are not investigated as part of this research. Accordingly, some potential recommended future work is summarized below:

- The analytical model and analysis in this work is focused only on maximum torque performance. There are several applications and use case scenarios where maximum

efficiency or maximum power factor operation strategies are beneficial. The modular nature of the hybrid rotor could offer opportunities to design specifically for such operation strategies.

- While the modeling in this research is focused on the SyR rotor reference frame to avoid a rotating saliency term, this is only required in order to generalize the analytical model. In the PM rotor reference frame, it was identified that the *dq* inductance can be tuned to operate in flux intensifying mode. This opens opportunities for hybrid rotor machines with variable magnetization state.
- The machine designs analyzed in this work are using NdFeB PM material. A similar case study of hybrid rotor machines with non-rear earth PM material can offer different design guidelines and optimum CPSR selection criteria.
- While the impacts of non-linearities and saturation were addressed in this research, a closed-form solution including nonlinearities could not be resolved. Further analysis may present a complete analytical model including nonlinearities in *dq* equivalent circuit. Particularly, the impacts of change in resistance, flux linkage and inductance due to temperature are of high importance for control aspects, and a closed-from solution could vastly reduce the control algorithm complexity and computation time.
- Both analytical model and LUT based modeling method developed in this research avoided designs with significant end effects or leakage components. However, small aspect ratio machines still have some practical applications. Expanding the analytical and LUT model to include leakage inductance could reduce the limitations and expand the design space for hybrid rotor PMSM.

- This analytical model developed in this work is focused on steady state operation and important for gaining insights into understanding the working principles and develop design guidelines. The rotor dynamics and cross-coupling effects need further investigation to gain a better understanding of the transient behaviour of the hybrid rotor structure.

Bibliography

[1] A. M. Bazzi, Y. Liu, and D. S. Fay, "Electric machines and energy storage: Over a century of technologies in electric and hybrid electric vehicles," *IEEE Electrif. Mag.*, vol. 6, no. 3, pp. 49–53, Sep. 2018.

[2] P. Ramesh and N. C. Lenin, "High power density electrical machines for electric vehicles-comprehensive review based on material technology," *IEEE Trans. Magn.*, vol. 55, no. 11, 2019.

[3] J. Hendershot, "Electric traction machine choices for hybrid & electric vehicles," 2014. [Online]. Available: https://site.ieee.org/miami/?p=1437.

[4] "Tesla Model 3 Teardown," *Bloomberg Technology*, 2018. [Online]. Available: https://www.youtube.com/watch?v=Lj1a8rdX6DU.

[5] A. Extance, "Toyota promises cheaper electric car motor magnets within a decade," 2018. [Online]. Available: https://www.chemistryworld.com/news/toyota-promises-cheaper-electric-car-motor-magnets-within-a-decade/3008716.article.

[6] K. Sakai, K. Yuki, Y. Hashiba, N. Takahashi, and K. Yasui, "Principle of the variable-magnetic-force memory motor," in *Proceedings - The 12th International Conference on Electrical Machines and Systems, ICEMS 2009*, 2009, pp. 1–6.

[7] S. Morimoto, Y. Takeda, T. Hirasa, and K. Taniguchi, "Expansion of operating limits for permanent magnet motor by current vector control considering inverter capacity," *IEEE Trans. Ind. Appl.*, vol. 26, no. 5, pp. 866–871, 1990.

[8] W. L. Soong, "Field-weakening performance of brushless synchronous AC motor drives," *IEEE Proc. - Electr. Power Appl.*, vol. 141, no. 6, p. 331, 1994.

[9] L. Alberti, N. Bianchi, and S. Bolognani, "Lamination design of a set of induction motors for elevator systems," in *2007 IEEE International Electric Machines & Drives Conference*, 2007, vol. 1, pp. 514–518.

[10] "IAV - Automotive Engineering," 2020. [Online]. Available: https://www.iav.com/en/services/engineering/. [Accessed: 12-Dec-2020].

[11] "magniX Aero - Products," 2020. [Online]. Available: https://www.magnix.aero/products. [Accessed: 11-Aug-2020].

[12] D. F. Gosden, "Drive system design for an electric vehicle based on alternative motor types," in *Proceedings of 5th International Conference on Power Electronics and Variable-Speed Drives*, 1994, no. 399, pp. 710–715.

[13] B. J. Chalmers, L. Musaba, and D. F. Gosden, "Synchronous machines with permanent magnet and reluctance rotor sections," in *International Conference on Electrical Machines*, 1994, pp. 185–189.

[14] B. J. Chalmers, L. Musaba, and D. F. Gosden, "Variable-frequency synchronous motor drives for electric vehicles," *IEEE Trans. Ind. Appl.*, vol. 32, no. 4, pp. 896–903, 1996.

[15] B. J. Chalmers, R. Akmeşe, and L. Musaba, "Design and field-weakening performance of permanent-magnet/reluctance motor with two-part rotor," *IEE Proc. - Electr. Power Appl.*, vol. 145, no. 2, p. 133, 1998.

[16] C. L. Gu, B. J. Chalmers, and C. W. Lu, "Rotor design optimization of synchronous machine with two-part rotor," *EEE Int. Electr. Mach. Drives Conf. Rec.*, vol. 7, p. TB2/6.1-TB2/6.3, 1997.

[17] C. L. L. Gu, B. J. Chalmers, and B. J. Chalmet, "New approach to longitudinal magnetic field in drum type machine," *IEEE Trans. Magn.*, vol. 33, no. 2, pp. 2041–2044, Mar. 1997.

[18] S. A. Randi and S. Astier, "Parameters of salient pole synchronous motor drives with two-part rotor to achieve a given constant power speed range," in *PESC Record - IEEE Annual Power Electronics Specialists Conference*, 2001, vol. 3, pp. 1673–1678.

[19] X. Chen, "Analysis on different rotor structure synchronous motor vector control," *2nd Int. Conf. Intell. Comput. Technol. Autom.*, vol. 3, pp. 14–17, 2009.

[20] X. Chen, C. Gu, X. He, and H. Shao, "Experimental research on the ALA+SPM hybrid rotor machine," *Int. Conf. Electr. Mach. Syst.*, pp. 2–5, 2011.

[21] E. K. Beser, S. Camur, B. Arifoglu, and E. Beser, "Analysis and application of a hybrid motor structure convenient to modify the magnet and reluctance torques on the rotor," *J. Electr. Eng. Technol.*, vol. 7, no. 3, pp. 349–357, 2012.

[22] E. K. Beser, S. Camur, B. Arifoglu, and E. Beser, "Comparison of two rotor configurations by changing the amount of magnet and reluctance components," *J. Electr. Eng. Technol.*, vol. 10, no. 1, pp. 155–164, 2015.

[23] H. Yang *et al.*, "Novel reluctance axis shifted machines with hybrid rotors," *IEEE Energy Convers. Congr. Expo.*, vol. 2017-Janua, pp. 2362–2367, 2017.

[24] W. Zhao, F. Xing, X. Wang, T. A. Lipo, and B. Il Kwon, "Design and analysis of a novel PM-assisted synchronous reluctance machine with axially integrated magnets by the finite-element method," *IEEE Trans. Magn.*, vol. 53, no. 6, 2017.

[25] D. Kelly, "Double-rotor induction motor," *IEEE Trans. Power Appar. Syst.*, vol. PAS-88, no. 7, pp. 1086–1092, Jul. 1969.

[26] R. Qu, M. Aydin, and T. A. Lipo, "Performance comparison of dual-rotor radial-flux and axial-flux permanent-magnet BLDC machines," in *IEEE International Electric Machines and Drives Conference*, 2003, vol. 3, pp. 1948–1954.

[27] T. Guo, N. Schofield, and A. Emadi, "Double Segmented Rotor Switched Reluctance Machine With Shared Stator Back-Iron for Magnetic Flux Passage," *IEEE Trans. Energy Convers.*, vol. 31, no. 4, pp. 1278–1286, Dec. 2016.

[28] Y. H. Yeh, M. F. Hsieh, and D. G. Dorrell, "Different arrangements for dual-rotor dual-output radial-flux motors," *IEEE Trans. Ind. Appl.*, vol. 48, no. 2, pp. 612–622, Mar. 2012.

[29] Y. Li, D. Bobba, and B. Sarlioglu, "A novel dual-rotor hybrid machine with synchronous

reluctance and surface permanent magnet rotors," in *IEEE International Electric Machines and Drives Conference (IEMDC)*, 2017, pp. 1–8.

[30] Y. Li, D. Bobba, and B. Sarlioglu, "Design and optimization of a novel dual-rotor hybrid PM machine for traction application," *IEEE Trans. Ind. Electron.*, vol. 65, no. 2, pp. 1762–1771, Feb. 2018.

[31] M.-H. Hwang, J.-H. Han, D.-H. Kim, and H.-R. Cha, "Design and analysis of rotor shapes for ipm motors in EV power traction platforms," *Energies*, vol. 11, no. 10, p. 2601, Sep. 2018.

[32] N. Bianchi, S. Bolognani, and B. J. Chalmers, "Salient-rotor PM synchronous motors for an extended flux-weakening operation range," *IEEE Trans. Ind. Appl.*, vol. 36, no. 4, pp. 1118–1125, 2000.

[33] N. Bianchi and S. Bolognani, "Performance analysis of an IPM motor with segmented rotor for flux-weakening applications," in *Ninth International Conference on Electrical Machines and Drives*, 1999, pp. 49–53.

[34] N. Limsuwan, Y. Shibukawa, D. D. Reigosa, and R. D. Lorenz, "Novel design of flux-intensifying interior permanent magnet synchronous machine suitable for self-sensing control at very low speed and power conversion," *IEEE Trans. Ind. Appl.*, vol. 47, no. 5, pp. 2004–2012, Sep. 2011.

[35] N. Limsuwan, "Concurrent Design of FI-IPM Machines for Self-Sensing and Electromechanical Power Conversion," 2013.

[36] A. Athavale, K. Sasaki, B. S. Gagas, T. Kato, and R. D. Lorenz, "Variable flux permanent magnet synchronous machine (VF-PMSM) design to meet electric vehicle traction requirements with reduced losses," in *IEEE Energy Conversion Congress and Exposition (ECCE)*, 2016, pp. 1–8.

[37] M. Ibrahim, L. Masisi, and P. Pillay, "Design of variable-flux permanent-magnet machines using AlNiCo magnets," *IEEE Trans. Ind. Appl.*, vol. 51, no. 6, pp. 4482–4491, Nov. 2015.

[38] C.-Y. Yu, T. Fukushige, N. Limsuwan, T. Kato, D. D. Reigosa, and R. D. Lorenz, "Variable-flux machine torque estimation and pulsating torque mitigation during magnetization state manipulation," *IEEE Trans. Ind. Appl.*, vol. 50, no. 5, pp. 3414–3422, Sep. 2014.

[39] W. Zhao, F. Zhao, T. A. Lipo, and B. Il Kwon, "Optimal design of a novel v-type interior permanent magnet motor with assisted barriers for the improvement of torque characteristics," *IEEE Trans. Magn.*, vol. 50, no. 11, pp. 1–4, 2014.

[40] G. Xu, G. Liu, S. Jiang, and Q. Chen, "Analysis of a hybrid rotor permanent magnet motor based on equivalent magnetic network," *IEEE Trans. Magn.*, vol. 54, no. 4, pp. 1–9, 2018.

[41] H. Yang, W. Wang, H. Lin, Z. Q. Zhu, S. Lyu, and S. Niu, "A novel hybrid-pole interior PM machine with magnet-axis-shifting effect," in *IEEE International Electric Machines & Drives Conference (IEMDC)*, 2019, pp. 273–279.

[42] R. F. Schiferl and T. A. Lipo, "Power capability of salient pole permanent magnet synchronous motors in variable speed drive applications," *IEEE Trans. Ind. Appl.*, vol. 26, no. 1, pp. 115–123, 1990.

[43] W. L. Soong, "Design and modelling of axially-laminated interior permanent magnet motor drives for field-weakening applications," University of Glasgow, 1993.

[44] B. Gagas, T. Fukushige, N. Limsuwan, C.-Y. Yu, K. Akatsu, and R. D. Lorenz, "Suggested design space in a PMSM parameter plane for variable flux machines," in *International Electric Machines & Drives Conference (IEMDC)*, 2013, pp. 549–556.

[45] Z. Q. Zhu, Z. P. Xia, L. J. Wu, and G. W. Jewell, "Influence of slot and pole number combination on radial force and vibration modes in fractional slot PM brushless machines having single- and double-layer windings," in *IEEE Energy Conversion Congress and Exposition (ECCE)*, 2009, pp. 3443–3450.

[46] F. Libert and J. Soulard, "Investigation on pole-slot combinations for permanent-magnet machines with concentrated windings," in *International Conference on Electrical Machines*, 2004, no. January 2004, pp. 5–8.

[47] R. Krall, J. Krenn, and A. Schmid, "Comparison of leakage inductance between fractional slot winding and distributed winding," in *16th International Power Electronics and Motion Control Conference and Exposition*, 2014, pp. 276–282.

[48] B. J. Chalmet, R. Akmese, and L. Musaba, "Design and field-weakening performance of permanent-magnet/reluctance motor with two-part rotor," *IEE Proc.-Electr. Power Appl.*, vol. 145, no. 2, p. 133, 1998.

[49] X. Chen, "Combined ALA+PM rotor synchronous motor," *2nd Int. Conf. Intell. Comput. Technol. Autom.*, vol. 3, pp. 30–33, 2009.

[50] D. Bobba, T. A. Burress, J. Pries, and B. Sarlioglu, "Three-part hybrid rotor PM machine with variable magnetization state," in *IEEE Energy Conversion Congress and Exposition (ECCE)*, 2017, pp. 1240–1246.

[51] W. Zhao, H. Shen, T. A. Lipo, and X. Wang, "A new hybrid permanent magnet synchronous reluctance machine with axially sandwiched magnets for performance improvement," *IEEE Trans. Energy Convers.*, vol. 33, no. 4, pp. 2018–2029, 2018.

[52] O. Ocak and M. Aydin, "A new hybrid permanent magnet synchronous motor with two different rotor sections," *IEEE Trans. Magn.*, vol. 53, no. 11, pp. 1–5, Nov. 2017.

[53] T. A. Lipo, *Introduction to AC Machine Design*. Hoboken, NJ, USA: John Wiley & Sons, Inc., 2017.

[54] D. Ban, D. Zarko, and I. Mandic, "Turbogenerator end-winding leakage inductance calculation using a 3-D analytical approach based on the solution of Neumann Integrals," *IEEE Trans. Energy Convers.*, vol. 20, no. 1, pp. 98–105, Mar. 2005.

[55] A. Schramm and D. Gerling, "Analytical calculation of the end winding leakage inductance based on the solution of Neumann integrals," in *IEEE International Symposium on Industrial Electronics, ISIE*, 2005, vol. 2, pp. 851–855.

[56] R. Lin and A. Arkkio, "Calculation and analysis of stator end-winding leakage inductance of an induction machine," *IEEE Trans. Magn.*, vol. 45, no. 4, pp. 2009–2014, Apr. 2009.

[57] A. Vagati, M. Pastorelli, G. Franceschini, S. C. Petrache, G. Francheschini, and S. C. Petrache, "Design of low-torque-ripple synchronous reluctance motors," *IEEE Trans. Ind. Appl.*, vol. 34, no. 4, pp. 758–765, 1998.

[58] N. Bianchi and S. Bolognani, "Unified approach to the analysis and design of an AC motor drive for flux-weakening operations," *Conf. Rec. - IAS Annu. Meet. (IEEE Ind. Appl. Soc.*, vol. 1, no. 4, pp. 95–102, 1998.

[59] S. Li, B. Sarlioglu, S. Jurkovic, N. R. Patel, and P. Savagian, "Analysis of temperature effects on performance of interior permanent magnet machines for high variable temperature applications," *IEEE Trans. Ind. Appl.*, vol. 53, no. 5, pp. 4923–4933, Sep. 2017.

[60] "FY2016 electric drive technologies annual progress report," United States, Jul. 2017.

[61] A. Binder, T. Schneider, and M. Klohr, "Fixation of buried and surface mounted magnets in high-speed permanent magnet synchronous motors," in *Fourtieth IAS Annual Meeting. Conference Record of the Industry Applications Conference.*, 2006, vol. 4, no. 4, pp. 2843–2848.